830-H-B

NASI·60:1533

NASA Technical Paper 1533

Longitudinal Aerodynamic Characteristics of a Vectored-Engine-Over-Wing Configuration at Subsonic Speeds

Laurence D. Leavitt

OCTOBER 1979

NASA

(136)

Longitudinal Aerodynamic Characteristics of a Vectored-Engine-Over-Wing Configuration at Subsonic Speeds

Laurence D. Leavitt
Langley Research Center
Hampton, Virginia

SUMMARY

An investigation has been conducted in the Langley V/STOL tunnel to deter-
mine the effects of vectoring exhaust flow on the longitudinal aerodynamic char-
acteristics of a vectored-engine-over-wing configuration. Vectoring was accom-
plished by blowing from over-wing-mounted engines over a variable trailing-edge
flap. Effects of varying canard geometry and wing leading-edge geometry were
investigated. Wind-tunnel data were obtained at a Mach number of 0.186 for an
angle-of-attack range from -2^O to 24° and engine nozzle pressure ratios from 1.0
(jet off) to approximately 3.75.

The results of the investigation indicate that significant lift and drag
polar improvements can be achieved by vectoring nozzle exhaust flow over the
wing trailing-edge flaps. Maximum lift coefficients in excess of 4.0 were
achieved. These lift improvements generally increased with increasing nozzle
pressure ratio and trailing-edge flap deflection (up to 30°). However, because
vectoring occurred aft of the moment reference center, these same lift increases
were accompanied by large nose-down pitching moments.

The close-coupled canard generally increased lift, improved the drag polar
at high angles of attack, and reduced nose-down pitching moment for all condi-
tions tested. Increases in canard incidence provided reductions in nose-down
pitching moment but degraded overall performance.

INTRODUCTION

Several promising concepts for augmenting the lift capabilities of modern
fighter-type configurations have been investigated in recent years. It has been
shown in previous studies (refs. 1 to 15) that the potential benefits (including
increased maneuverability, improved survivability, and improved take-off and
landing performance) derived from enhancing external aerodynamic performance are
significant. Many of these concepts, including upper-surface blowing (refs. 16
and 17), internally and externally blown flaps (refs. 18 to 20), primary exhaust
nozzle deflection (refs. 2 to 15 and 21 to 27), and vectored-engine-over-wing
blowing (refs. 28 to 33), utilize vectored exhaust nozzle flow as the primary
mechanism for augmenting lift capabilities. Vectoring of the exhaust nozzle
flow provides a direct thrust vector term in the lift direction and, with proper
integration with the airframe, may also provide an additional jet-induced term.

The VEO-wing concept is unique in that it combines upper-surface blowing
with primary nozzle exhaust deflection to achieve thrust vectoring. Exhaust
flow momentum from over-wing-mounted engines is turned internally in the non-
axisymmetric convergent-divergent nozzles. Additional turning or deflection
back to the horizontal is accomplished by blowing the exhaust flow over a vari-
able trailing-edge flap. Previous tests, using the VEO-wing concept (refs. 28
to 33), illustrated that significant aerodynamic performance improvements could
be achieved with this system at both subsonic and transonic speeds. However,

1

additional tests were required to more completely explore the advantages of the VEO-wing concept especially at take-off and landing conditions as a method of obtaining good STOL performance.

Consequently, an investigation was conducted in the Langley V/STOL tunnel to determine the effects on model longitudinal aerodynamic characteristics of vectoring exhaust flow from over-wing-mounted engines by blowing over a variable trailing-edge flap. Wing trailing-edge flap deflection angles from -25° to 35° were tested. In addition, the effects of canard, canard planform, canard incidence, canard trailing-edge flap deflection, wing leading-edge flap deflection, and spanwise blowing were investigated in conjunction with the over-wing blowing. The effects of spanwise blowing on the longitudinal aero-dynamic characteristics of this configuration are presented in reference 32. Wind-tunnel data were obtained at a Mach number of 0.186 for an angle-of-attack range from -2° to 24°. A high-pressure air system was used to simulate jet-exhaust flow and to provide engine nozzle pressure ratios from 1.0 (jet off) to approximately 3.75.

SYMBOLS

All aerodynamic coefficients are referenced to the stability axis system and are nondimensionalized with respect to $q_\infty S$ or $q_\infty S \bar{c}$ except at static conditions ($M = 0$), where p_a was substituted for q_∞. Coefficients denoted as total coefficients include thrust effects. The moment reference center was located at a point 110.025 cm rearward of the fuselage nose and in the chord plane of the wing located at -3.53 cm below the model center line. (See fig. 1(a).) All dimensions presented are in the International System of Units (SI).

A_B fuselage base area, 197.933 cm^2

A_e nozzle exit area, cm^2

A_t nozzle throat area, cm^2

$C_{A,B}$ fuselage base axial-force coefficient, $\dfrac{p_B - p_\infty}{q_\infty}\left(\dfrac{A_B}{S}\right)$

$C_{A,j}$ static thrust along body-axis coefficient

$C_{A,N}$ nozzle base axial-force coefficient, $\dfrac{p_N - p_\infty}{q_\infty}\left(\dfrac{A_e}{S}\right)$

C_D drag coefficient (eq. (6))

$C_{(D-T)}$ total drag-minus-thrust coefficient, $\dfrac{D - T}{q_\infty S}$

$C_{F,g}$ wind-on gross thrust coefficient, $\dfrac{F_g}{q_\infty S}$

C_L total lift coefficient (including thrust component)

$C_{L,aero}$ lift coefficient with effects of thrust removed (eq. (5))

$C_{L,C_T=0}$ jet-off total lift coefficient

$C_{L,j}$ jet-reaction lift coefficient

$C_{L,\Gamma}$ jet-induced lift coefficient

ΔC_L incremental lift coefficient, $C_{L,\Gamma} + C_{L,j}$

C_m total pitching-moment coefficient (including thrust component)

$C_{m,aero}$ pitching-moment coefficient with effects of thrust removed (eq. (7))

$C_{m,j}$ static (M = 0) pitching-moment coefficient

$C_{N,j}$ static (M = 0) normal-force coefficient

$\bar{c}$ wing mean geometric chord, 31.25 cm

D drag force, N

F_g resultant gross thrust force, N

F_i ideal isentropic gross thrust, N

h_e nozzle exit height, cm (fig. 1(f))

h_t nozzle throat height, cm (fig. 1(f))

M Mach number

$\dot{m}$ measured mass flow rate, kg/sec

$\dot{m}_i$ ideal mass flow rate, kg/sec

p_a ambient pressure, Pa

p_B fuselage base pressure, Pa

p_N nozzle base pressure, Pa

$p_{t,j}$ jet total pressure, Pa

$(p_{t,j}/p_\infty)_{av}$ average nozzle pressure ratio

p_∞	free-stream static pressure, Pa
q_∞	free-stream dynamic pressure, Pa
S	wing reference area including projection of leading- and trailing-edge sweep to model center line, 3251.63 cm^2 (fig. 1(a))
T	thrust force, N
α	angle of attack, deg
δ_c	canard incidence angle, positive leading edge up, deg
$\delta_{c,TE}$	canard trailing-edge flap angle, positive trailing edge down, deg
δ_j	resultant thrust vector angle, deg (eq. (1))
δ_{LE}	wing leading-edge flap deflection angle, positive leading edge down, deg
δ_{TE}	wing trailing-edge flap deflection angle, positive trailing edge down, deg
ε	nozzle expansion ratio, A_e/A_t
θ	nozzle roof angle, deg (fig. 1(f))
ϕ	nozzle wedge angle, deg (fig. 1(f))

Abbreviations:

BL	buttock line, cm
C-D	convergent-divergent
conf	configuration
FS	fuselage station, cm
MRC	model reference center, WL -3.53 cm
WL	water line, cm

APPARATUS AND PROCEDURE

Model

Details of the VEO-wing model are presented in figure 1, and a photograph of the model installed in the Langley V/STOL tunnel is shown in figure 2. The model consists of a canard-wing-body-nozzle configuration which is representative of a high-performance fighter-type aircraft. Some compromises were made

in the external lines of the model. The inlets were faired over since inlet flow could not be accommodated, and space to house the propulsion simulator hardware and sting support system was required.

The wing shown in figure 1(b) had a leading-edge sweep of 40° and a cranked trailing edge. It incorporated a full-span leading-edge flap and inboard and outboard trailing-edge flaps. The inboard trailing-edge flap was located directly behind the engine exhaust nozzle and was used for thrust vectoring. Both the inboard and outboard flaps were deflected together during the current investigation.

The VEO-wing configuration was tested without and with either of two canard planforms (fig. 1(c)). Both canards had essentially the same exposed area; however, the leading-edge sweep of the H_3 canard was larger.

Propulsion System

A sketch of the key features of the model propulsion system is shown in figure 1(d). These features are similar to those shown in references 31 to 33. An external high-pressure air system provided air for exhaust flow simulation at a controlled temperature of about 388 K. This high-pressure air is brought through the sting support strut into a high-pressure plenum and air line arrangement. The air line was designed to minimize tare forces on the balance caused by the transfer of high-pressure air across the balance to the model plenum. This air line was connected to a high-pressure plenum which split the flow and directed it into two U-shaped air supply pipes. (See fig. 1(d).) Two valves located on the supply pipes allowed the flow rate to be controlled to each nozzle for balancing purposes.

The nonaxisymmetric nozzle shown in figures 1(e) and 1(f) represents a half-wedge two-dimensional convergent-divergent (C-D) nozzle with a nominal aspect ratio of 4.0 (the aspect ratio being defined as the throat width divided by the throat height). Nozzle configurations shown in figure 1(f) were obtained by changing nozzle wedge ramp angle and location (simulates translating wedge). These changes resulted in varying nozzle expansion ratio and, in addition, design nozzle pressure ratio.

Wind Tunnel and Support System

This investigation was conducted in the Langley V/STOL tunnel, which is a single-return atmospheric wind tunnel with a 4.4-m by 6.6-m rectangular test section. The wind tunnel has a continuously variable capability up to M = 0.30.

The model was supported by a sting as shown in figures 1(d) and 2. The tunnel sting support pivots and translates in such a manner that the model remains on or near the test-section center line throughout the angle-of-attack range. The test data were not corrected for blockage or flow angularity since these were considered negligible.

Instrumentation

External aerodynamic forces and moments and nozzle thrust forces and moments were measured with a six-component strain-gage balance. Four internal base cavity pressure orifices were located approximately 90° apart in the cylindrical base region at about model fuselage station 175 cm. These measurements were used to calculate and remove base pressure tares (referenced to free-stream static pressure) from the balance readings. In addition, one total-pressure probe in each engine exhaust nozzle was connected through a remotely controlled solenoid valve to a lower pressure range, more accurate pressure transducer and was used for measurement of nozzle base cavity pressure during jet-off operating conditions. Nozzle cavity base tares, referenced to free-stream static pressure, were calculated from these measurements and removed from the jet-off balance data. Typical examples of the magnitude of both fuselage and nozzle base cavity pressure are shown in figure 3. Note that the fuselage base cavity pressure correction was a strong function of trailing-edge flap deflection and, hence, the angle at which the thrust is directed past the fuselage base region. At $\delta_{TE} = 0^{\circ}$, a significant portion of the nozzle exhaust flow washes the fuselage cavity. As a result, large base pressure corrections were measured. As trailing-edge flap deflections increased (up to $\delta_{TE} = 25^{\circ}$), the magnitude of the jet-on base pressure correction decreased as a larger percentage of the nozzle exhaust flow was directed away from the fuselage base region.

A venturi flowmeter (external to the test section) was used to measure the total mass flow rate to the nozzles. Three total-pressure probes, illustrated in figure 1(e), and one thermocouple, measuring static temperature at the wall, were located forward of each engine nozzle throat and were used to measure nozzle internal flow characteristics.

Model angle of attack was measured with an accelerometer located in the nose cavity of the model fuselage. This attitude transmitter recorded changes in model attitude with respect to the horizontal independent of any deflection of the sting and balance under aerodynamic loads.

Tests

The wind-tunnel tests were conducted at $M = 0.186$ in the Langley V/STOL tunnel. The free-stream dynamic pressure was 2394 Pa, and the stagnation temperature was approximately 358 K. The average Reynolds number was 1.26×10^6 based on $\bar{c}$. All configurations were tested with fixed boundary-layer transition strips on the model wings, canards, and nose. These transition strips consisted of No. 80 silicon carbide grit located 2.54 cm aft of wing and canard leading edges and 4.06 cm aft of the nose. These transition strips were used to insure a turbulent boundary layer over the nozzles and aft portion of the wing. Force and moment data were obtained for each configuration at angles of attack ranging from -2° to 24° and nozzle pressure ratios from 1.0 (jet off) to approximately 3.75.

Data Acquisition and Reduction

Data for both the model conditions and the wind-tunnel test conditions were recorded simultaneously on magnetic tape. At each test point, multiple data samples were recorded. The samples were averaged, and the averaged values were used for all computations.

Total aerodynamic and nozzle thrust forces and moments measured by an internal six-component strain-gage balance (as shown in fig. 1(d)) were corrected for presence of the air line (and the air pressure associated with the air line) across the balance. To obtain corrected thrust-minus-axial force, it was necessary to make momentum tare corrections for forces induced on the model by the nozzle exhaust flow simulation system. The momentum tares are usually associated with transfer of the high-pressure air, required for propulsion simulation, across the balance. Momentum tares were calculated using standard calibration nozzles and the technique described in reference 21.

Static characteristics.- Prior to wind-on investigation, the static ($M = 0$) nozzle characteristics were determined for the various nozzle configurations. From the measured axial and normal force components of the resultant thrust, the static resultant thrust vector angle, gross thrust coefficient, and jet-reaction lift coefficient are defined as follows:

$$\delta_j = \tan^{-1} \frac{C_{N,j}}{C_{A,j}} \tag{1}$$

$$(C_{F,g})_{M=0} = \sqrt{C_{N,j}^2 + C_{A,j}^2} \tag{2}$$

$$C_{L,j} = C_{F,g} \sin (\alpha + \delta_j) \tag{3}$$

Thrust removal.- Since all the forces and moments measured by the model balance were total forces and moments (thrust contribution included) and there was no independent measurement of thrust during tunnel runs, the static nozzle performance data were used to remove thrust components from the wind-on data. The static gross thrust coefficient was related to wind-on conditions by

$$C_{F,g} = \frac{p_\infty}{q_\infty} (C_{F,g})_{M=0} \tag{4}$$

The thrust coefficient for a given configuration at a given set of tunnel conditions was then used to remove the thrust components from the total force and moment wind-on data by the relationships:

$$C_{L,aero} = C_L - C_{F,g} \sin (\alpha + \delta_j) \tag{5}$$

$$C_D = C_{(D-T)} + C_{F,g} \cos (\alpha + \delta_j) \tag{6}$$

$$C_{m,aero} = C_m - C_{m,j} \left(\frac{p_\infty}{q_\infty} \right) \tag{7}$$

Note that the use of static nozzle data for thrust removal assumes no effect of the external flow on the jet-turning characteristics. As shown in reference 21, the external flow can have an effect on jet turning.

Incremental lift.- As shown in reference 18, the total lift measured by the force balance can be divided into three components: (1) jet-off lift, (2) jet-induced lift, and (3) jet-reaction lift. In coefficient form this relation can be stated as

$$C_L = C_{L,C_T=0} + C_{L,\Gamma} + C_{L,j} \tag{8}$$

where $C_{L,C_T=0}$ is the jet-off lift coefficient, $C_{L,\Gamma}$ is the jet-induced term, and $C_{L,j}$ is the jet-reaction lift coefficient

$$C_{L,j} = C_{F,g} \sin (\alpha + \delta_j)$$

The incremental lift coefficient ΔC_L is determined by subtracting the measured jet-off lift coefficient from the measured total lift coefficient

$$\Delta C_L = C_L - C_{L,C_T=0} \tag{9}$$

and is therefore defined as the sum of the induced and jet-reaction lift terms

$$\Delta C_L = C_{L,j} + C_{L,\Gamma} \tag{10}$$

RESULTS

An index of configurations tested and the figure numbers for their basic data are listed in table I. The results of this investigation are presented in plotted coefficient form in the following figures:

8

An outline of comparison data figures presenting longitudinal aerodynamic characteristics for a nozzle pressure ratio of 3.25 is as follows:

DISCUSSION

Static Data

The static (M = 0) characteristics of two nozzle configurations under varying trailing-edge flap conditions were obtained. These data are presented in figure 4. Nozzle discharge $\dot{m}/\dot{m}_i$, mass flow $\dot{m}$, and internal nozzle performance F_g/F_i are plotted as a function of nozzle pressure ratio for nozzle configurations 1 and 2 in figures 4(a) and (b). No mass-flow data were obtained for nozzle configurations 3 and 4 or for $\delta_{TE} = 35^O$ on configurations 1 and 2, primarily as a result of instrumentation problems with the flowmeter. Note that nozzle discharge coefficient and mass flow do not vary with trailing-edge flap deflection. It is also evident that measured mass flow $\dot{m}$ is essentially the same for nozzle configurations 1 and 2, as would be expected when nozzle throat area remains constant.

As seen in figure 4(a), however, trailing-edge flap deflection (vectoring) does have a significant impact on nozzle performance. Best performance was obtained when the trailing-edge flap angle ($\delta_{TE} = 15^O$) was approximately equal to the nozzle wedge angle ($\phi = 20^O$). It is felt that the highest performance would be obtained at this 15° trailing-edge flap deflection because a majority of the flow turning is the result of an internal flow turning mechanism. Internal turning is achieved in the VEO-wing nozzle by expansion of nozzle exhaust flow down the nozzle wedge. Since the wedge angle is 20° and the blown surface of the trailing-edge flap is approximately 20° with respect to the horizontal (flap chord line is 15° to the horizontal and upper flap surface is an additional 5°), the amount of supersonic exhaust flow deflection and supersonic exhaust flow Coanda turning is a minimum. In contrast, the $\delta_{TE} = 0^O$ case results in relatively large amounts of supersonic exhaust flow deflections (to turn the flow from approximately 20° off the wedge back to the horizontal), which result in performance losses. For $\delta_{TE} = 25^O$ and above, the exhaust flow turning mechanism is supersonic flow Coanda turning, which is also seen to produce significant losses in nozzle performance.

Also note in figure 4(a) that internal performance is increased as nozzle pressure ratio is increased. This is a result of not being able to attain nozzle pressure ratios equal to or above the design nozzle pressure ratio (which is approximately 5.0) at wind-off test conditions.

Static (wind-off) forces and moments and measured static resultant thrust vector angles are presented in figure 5 for the four nozzle configurations tested. The turning characteristics were generally excellent for all nozzle configurations. Note that for nozzle configuration 1, $\delta_{TE} = 0^O$, a turning angle δ_j of approximately 5° was measured. This 5° turning results from the approximately 5° slope on the trailing-edge flap upper surface.

Basic Longitudinal Characteristics

The basic longitudinal aerodynamic data (thrust included) for all configurations tested are presented in figures 7 to 10 for several nozzle pressure

ratios. Plotted in each figure are angle of attack, drag-minus-thrust coefficient, and pitching-moment coefficient as a function of total lift coefficient. The basic coefficient data (without thrust removed) are presented because they are representative of the specific excess power for each configuration. It should be noted that drag-minus-thrust coefficients presented in figures 7 to 10 are drag values defined as positive in the drag direction. Thus, negative values of $C_{(D-T)}$ indicate an excess thrust, $C_{(D-T)} = 0$ indicates thrust equals drag, and positive values of $C_{(D-T)}$ indicate a drag level higher than the thrust level. Of course, positive values of excess power (negative $C_{(D-T)}$) can be converted into an acceleration or an increased rate of climb.

In general, for positive trailing-edge flap deflections, the basic longitudinal data show an increase in lift coefficient as nozzle pressure ratio is increased. The total model drag-minus-thrust coefficient decreases with increasing nozzle pressure ratio (primarily as a result of increased thrust); and, since the thrust effects occur aft and slightly above the configuration reference center-of-gravity location, the pitching-moment coefficient becomes more negative (larger nose-down moments).

The lift-curve slope generally increased and the pitching-moment-curve slope decreased with increasing nozzle pressure ratio. Large negative values of trailing-edge flap deflection, $\delta_{TE} = -25^\circ$, provided a decrease in lift coefficient and an increase in positive (nose-up) pitching moment as nozzle pressure ratio increased. (See fig. 7(k).) However, for $\delta_{TE} = -10^\circ$ (fig. 7(l)), lift coefficient decreased only at angles of attack below about 6°. Above $\alpha = 6^\circ$, lift coefficient increased and pitching moment decreased. This results from the effective turning angle being relatively small. As angle of attack increased beyond 6°, the thrust reaction component in the lift direction increased as nozzle pressure ratio increased.

Induced and Incremental Lift

As discussed previously, the incremental lift ΔC_L is defined as the sum of the induced lift $C_{L,\Gamma}$ and the jet-reaction lift $C_{L,j}$. The variation of ΔC_L, $C_{L,j}$, and $C_{L,\Gamma}$ with angle of attack for all positive wing trailing-edge flap and nozzle combinations is presented in figures 11 to 14.

In general, for all configurations tested, jet-reaction lift increased with increasing angle of attack and nozzle pressure ratio. This observation is expected as $C_{L,j}$, by definition, increases with increasing α and $C_{F,g}$. Since jet-reaction lift is the major contributor to incremental lift (as evidenced by the relatively small induced lift terms), incremental lift also increases with angle of attack and nozzle pressure ratio.

As seen in figures 11(a) and (b), there is an increase in induced lift with increasing angle of attack and trailing-edge flap deflection angle. However, for cases where $\delta_{TE} > 15^\circ$, induced lift appears to be relatively insensitive to either angle of attack or trailing-edge flap deflection angle. These observations concerning the effects of model angle of attack on induced lift are characteristic of other thrust vectoring concepts such as reported in refer-

ence 21. Relatively small effects on induced lift as a result of trailing-edge flap deflection (above $\delta_{TE} = 15^O$) may be the result of some separation of the nozzle exhaust flow as it is turned over the flap; however, exact causes are not known at this time.

A summary of the variation of incremental lift with angle of attack and nozzle pressure ratio is presented in figure 15 for five trailing-edge flap deflections (nozzle configuration 1). The top half of the figure indicates, as discussed previously, that incremental lift increases with increasing nozzle pressure ratio. In addition, increases in incremental lift do occur for increases in trailing-edge flap deflection up to $\delta_{TE} = 30^O$. Note, however, that the relative magnitude of the lift increments resulting from a given trailing-edge flap deflection decreases with increasing trailing-edge flap deflection. This effect is probably a result of some exhaust flow separation over the trailing-edge flap, resulting in less efficient vectoring performance. The $\delta_{TE} = 35^O$ case which results in a decrease in incremental lift is believed to have a more significant flow separation problem.

The lower half of figure 15 presents a summary of the incremental lift effects as a function of model angle of attack for several trailing-edge flap positions. It is seen that for a constant nozzle pressure ratio of 3.25, incremental lift increased with increasing angle of attack and trailing-edge flap deflection. Again, however, the $\delta_{TE} = 35^O$ case was the exception for the same reasons previously mentioned.

Aerodynamic Lift and Drag

The aerodynamic (or thrust-removed) lift and drag characteristics of the VEO-wing model are presented in figures 16 to 19 for all configurations tested. Note that these thrust-removed data are actually a combination of the jet-off aerodynamic characteristics and the jet-induced characteristics.

These data in general show increases in lift and improvements in the drag polar (especially at the higher angles of attack) at jet-on conditions. Increases in nozzle pressure ratios above choke pressure ratio (approximately $P_{t,j}/P_\infty = 2.0$) had little additional effect on lift or drag in most cases. As trailing-edge flap deflection was increased, the magnitude of improvements in lift and drag also increased. These observations are seen up to $\delta_{TE} = 30^O$, after which payoffs are diminished, primarily because of the reduced turning efficiency at $\delta_{TE} = 35^O$.

Comparisons

Summary figures showing the effects of various configuration changes including wing trailing-edge flap deflections; nozzle expansion ratio; canard planform, incidence, and trailing-edge flap deflections; and wing leading-edge flap deflections are presented in figures 20 to 31. Both total-coefficient data and thrust-removed data are presented for each comparison. All comparisons were made at a nominal nozzle pressure ratio of 3.25.

12

Trailing-edge flap effects.- The effects of deflecting the wing trailing-edge flaps on model aerodynamic characteristics are presented in figures 20 and 21. The data have general characteristics of increased lift as trailing-edge flap deflection increases (up to $\delta_{TE} = 30^\circ$) throughout the angle-of-attack range and improvements in polar shape at the higher lift coefficients. An envelope drag polar can be faired as the locus of the optimum trailing-edge flap deflections. These trends are valid for both power-on and power-off (not shown) conditions; however, the rate of change in the aerodynamic characteristics is much larger with power on. The pitching-moment characteristics show that increases in trailing-edge flap deflection tend to increase the negative (nose-down) moment with little or no change in longitudinal stability.

Nozzle expansion ratio effects.- Data presenting the effects of various nozzle expansion ratios for $\delta_{TE} = 30^\circ$ are shown in figure 22. The large changes in aerodynamic performance shown in figure 22(a) are primarily the result of changes in nozzle performance. At $p_{t,j}/p_\infty = 3.23$, nozzle configuration 2 exhibits the best performance simply because it is operating closer to its design nozzle pressure ratio than any of the other nozzles; hence, at $M = 0.186$, it provides the best polar characteristics. Based on nozzle expansion ratio alone, nozzle configurations 1, 3, and 4 would follow configuration 2 in order of highest internal performance at $p_{t,j}/p_\infty = 3.23$. The thrust-removed data (fig. 22(b)) highlights these observations as there is little difference in the four nozzle configurations once the effects of thrust are removed.

Canard effects.- The effects resulting from the presence of a close-coupled canard are shown in figures 23 to 25. As seen in figure 23, the canard has only small effects on lift or drag at low angles of attack. This indicates that the additional lift associated with a close-coupled canard is probably being counteracted by a comparable loss in lift on the wing due to the downwash flow field from the canard as reported in references 34 and 35. At high angles of attack, however, the addition of the canard increases lift, improves the drag polar, and reduces the nose-down pitching moment. Also note that the benefits are even more pronounced at the $\delta_{TE} = 30^\circ$ case in figure 25. These favorable effects are felt to be a result of favorable interference effects between the wing and canard flow fields which result in delay of the wing flow separation.

Canard planform effects.- Data showing the effects of the two different canard geometries are also shown in figures 23 to 25. For $\delta_{TE} = 0^\circ$ and 15°, there is little difference between the two geometries. However, at $\delta_{TE} = 30^\circ$, the H_3 canard, which has 5° of leading-edge sweep more than the H_2 canard, provided improvements in lift and drag at angles of attack greater than 12°. It is felt that this is probably a result of a stronger canard vortex interacting on the wing flow field.

Canard incidence effects.- The effects of canard incidence are presented in figures 26 to 29. In general, increases in canard incidence provided significant reductions in nose-down pitching moment. In addition, however, these deflections provided reductions in overall lift and significantly degraded the drag polars in all cases tested.

Canard trailing-edge flap effects.- The effects of canard trailing-edge flap deflection are presented in figure 30. Note that while small reductions in nose-down pitching moment occur with increasing $\delta_{c,TE}$, there are no significant effects on lift or drag.

Wing leading-edge flap effects.- The effects of deflecting the wing leading-edge flaps in the presence of a canard are shown in figure 31. As seen at lower angles of attack, both lift and drag are degraded, but between $\alpha = 8^o$ and $\alpha = 20^o$, the polar is significantly improved. Above $\alpha = 20^o$ there are small effects. The favorable effects at high angles of attack normally associated with leading-edge flap deflection most likely are suppressed by the interaction of the canard on the wing flow field.

CONCLUSIONS

An investigation has been conducted in the Langley V/STOL tunnel to determine the effects of vectoring exhaust flow from over-wing-mounted engines by blowing over a variable trailing-edge flap. Effects of varying canard geometry and wing leading-edge geometry were investigated. Wind-tunnel data were obtained at a Mach number of 0.186 for an angle-of-attack range from -2° to 24° and engine nozzle pressure ratios from 1.0 (jet off) to approximately 3.75. Results from this study indicate the following:

1. Static (wind-off) nozzle internal performance is highest when trailing-edge flap angle is approximately equal to nozzle wedge angle. When this condition exists, a majority of the exhaust flow turning occurs internally by expansion down the nozzle wedge.

2. Static turning characteristics were generally good for all nozzle configurations tested.

3. Significant lift and drag polar improvements were achieved by vectoring nozzle exhaust flow over the wing trailing-edge flaps. These were, however, accompanied by large nose-down pitching moments.

4. Incremental lift increased with increasing nozzle pressure ratio, angle of attack, and trailing-edge flap deflection except for $\delta_{TE} = 35^o$, where separation of the nozzle exhaust flow was suspected.

5. Addition of canard increased lift, improved the drag polar at high angles of attack, and reduced nose-down pitching moment for all conditions tested.

6. Increases in canard incidence provided significant reductions in nose-down pitching moment but degraded overall performance.

7. Increasing canard leading-edge sweep seemed to have a favorable effect on lift and drag, especially at high angles of attack.

8. Deflecting canard trailing-edge flaps or wing leading-edge flaps (in the presence of a canard) generally had small effects on aerodynamic characteristics.

Langley Research Center
National Aeronautics and Space Administration
Hampton, VA 23665
August 31, 1979

REFERENCES

1. Pennington, Jack E.: Simulation Study of Effects of Thrust Vectoring and Induced Lift Due to Thrust Vectoring on Combat Effectiveness of a Fighter Aircraft. NASA TM X-3202, 1975.

2. Martens, Richard E.: F-15 Nozzle/Afterbody Integration. AIAA Paper No. 74-1100, Oct. 1974.

3. Pendergraft, O. C.: Comparison of Axisymmetric and Nonaxisymmetric Nozzles Installed on the F-15 Configuration. AIAA Paper 77-842, July 1977.

4. Capone, Francis J.: A Summary of Experimental Research on Propulsive-Lift Concepts in the Langley 16-Foot Transonic Tunnel. AIAA Paper No. 75-1315, Sept.-Oct. 1975.

5. Berrier, Bobby L.; Palcza, J. Lawrence; and Richey, G. Keith: Nonaxisymmetric Nozzle Technology Program - An Overview. AIAA Paper 77-1225, Aug. 1977.

6. Berrier, B. L.; and Re, R. J.: A Review of Thrust-Vectoring Schemes for Fighter Aircraft. AIAA Paper No. 78-1023, July 1978.

7. Schnell, W. C.; and Grossman, R. L.: Vectoring Non-Axisymmetric Nozzle Jet Induced Effects on a V/STOL Fighter Model. AIAA Paper 78-1080, July 1978.

8. Hiley, P. E.; Kitzmiller, D. E.; and Willard, C. M.: Installed Performance of Vectoring/Reversing Nonaxisymmetric Nozzles. AIAA Paper 78-1022, July 1978.

9. Sedgwick, T. E.: Investigation of Nonaxisymmetric Two-Dimensional Nozzles Installed in Twin-Engine Tactical Aircraft. AIAA Paper No. 75-1319, Sept.-Oct. 1975.

10. Goetz, Gerald F.; Young, John H.; and Palcza, J. Lawerence: A Two-Dimensional Airframe Integrated Nozzle Design With Inflight Thrust Vectoring and Reversing Capabilities for Advanced Fighter Aircraft. AIAA Paper No. 76-626, July 1976.

11. Hiley, P. E.; Wallace, H. W.; and Booz, D. E.: Study of Non-Axisymmetric Nozzles Installed in Advanced Fighter Aircraft. AIAA Paper No. 75-1316, Sept.-Oct. 1975.

12. Culpepper, Richard G.: A Summary of Research on Thrust Vectoring in Forward Flight (VIFF). NASA TM-74048, 1977.

13. Paulson, John W., Jr.; Thomas, James L.; and Winston, Matthew M.: Transition Aerodynamics for Close-Coupled Wing-Canard Configuration. AIAA Paper 79-0336, Jan. 1979.

14. Lander, J. A.; Nash, D. O.; and Palcza, J. Lawrence: Augmented Deflector Exhaust Nozzle (ADEN) Design for Future Fighters.   AIAA Paper No. 75-1318, Sept.-Oct. 1975.

15. Stevens, H. L.:   F-15/Nonaxisymmetric Nozzle System Integration Study Support Program.   NASA CR-135252, 1978.

16. Phelps, Arthur E., III; Johnson, Joseph L., Jr.; and Margason, Richard J.: Summary of Low-Speed Aerodynamic Characteristics of Upper-Surface-Blown Jet-Flap Configurations.   Powered-Lift Aerodynamics and Acoustics, NASA SP-406, 1976, pp. 63-87.

17. Johnson, Joseph L., Jr.; and Phelps, Arthur E., III: Low-Speed Aerodynamics of the Upper-Surface Blown Jet Flap.   [Preprint] 740470, Soc. Automot. Eng., Apr.-May 1974.

18. Lowry, John G.; Riebe, John M.; and Campbell, John P.:   The Jet-Augmented Flap.   Preprint No. 715, S.M.F. Fund Paper, Inst. Aeronaut. Sci., Jan. 1957.

19. Campbell, John P.:   Overview of Powered-Lift Technology.   Powered-Lift Aerodynamics and Acoustics, NASA SP-406, 1976, pp. 1-27.

20. Osborn, R. F.; and Oates, G. S.:   Wind Tunnel Investigation of Three Powered-Lift STOL Concepts.   V/STOL Aerodynamics, AGARD-CP-143, Apr. 1974, pp. 4-1 - 4-12.

21. Capone, Francis J.:   The Effects on Propulsion-Induced Aerodynamic Forces of Vectoring a Partial-Span Rectangular Jet at Mach Numbers From 0.40 to 1.20.   NASA TN D-8039, 1975.

22. Corson, Blake W., Jr.; Capone, Francis J.; and Putnam, Lawrence E.:   Lift Induced on a Swept Wing by a Two-Dimensional Partial-Span Deflected Jet at Mach Numbers From 0.20 to 1.30.   NASA TM X-2309, 1971.

23. Capone, Francis J.:   Static Performance of Five Twin-Engine Nonaxisymmetric Nozzles With Vectoring and Reversing Capability.   NASA TP-1224, 1978.

24. Capone, Francis J.:   Supercirculation Effects Induced By Vectoring a Partial-Span Rectangular Jet.   AIAA Paper No. 74-971, Aug. 1974.

25. Maiden, Donald L.:   Performance of an Isolated Two-Dimensional Variable-Geometry Wedge Nozzle With Translating Shroud and Collapsing Wedge at Speeds Up to Mach 2.01.   NASA TN D-7906, 1975.

26. Maiden, Donald L.:   Performance of an Isolated Two-Dimensional Wedge Nozzle With Fixed Cowl and Variable Wedge Centerbody at Mach Numbers Up to 2.01. NASA TN D-8218, 1976.

27. Willard, C. M.; Capone, F. J.; Konarski, M.; and Stevens, H. L.: Static Performance of Vectoring/Reversing Nonaxisymmetric Nozzles. AIAA Paper 77-840, July 1977.

28. Woodrey, R. W.; Whitten, P. D.; Smith, C. W.; and Bradley, R. G.: An Experimental Investigation of a Vectored-Engine-Over-Wing Powered-Lift Concept. Volume I - Low Speed and Transonic Tests. AFFDL-TR-76-92, Vol. I, U.S. Air Force, Sept. 1976.

29. Bradley, R. G.; Jeffries, R. R.; and Capone, F. J.: A Vectored-Engine-Over-Wing Propulsive-Lift Concept. AIAA Paper No. 76-917, Sept. 1976.

30. Huffman, Jarrett K.; and Fox, Charles H., Jr.: Subsonic Longitudinal Aerodynamic Characteristics of a Vectored-Engine-Over-Wing Configuration Having Spanwise Leading Edge Vortex Enhancement. NASA TM X-73955, 1977.

31. Whitten, Perry D.: An Experimental Investigation of a Vectored-Engine-Over-Wing Powered-Lift Concept. Volume II - High Angle of Attack and STOL Tests. AFFDL TR-76-92-VOL-2, U.S. Air Force, Mar. 1978. (Available from DDC as AD B033 094L.)

32. Leavitt, Laurence D.; and Yip, Long P.: Effects of Spanwise Nozzle Geometry and Location on the Longitudinal Aerodynamic Characteristics of a Vectored-Engine-Over-Wing Configuration at Subsonic Speeds. NASA TP-1215, 1978.

33. Leavitt, Laurence D.; Whitten, P. D.; and Stumpfl, S. C.: Low Speed Aerodynamic Characteristics of a Vectored-Engine-Over-Wing Configuration. AIAA Paper No. 78-1081, July 1978.

34. Henderson, William P.: The Effect of Canard and Vertical Tails on the Aerodynamic Characteristics of a Model With a 59° Sweptback Wing at a Mach Number of 0.30. NASA TM X-3088, 1974.

35. Re, Richard J.; and Capone, Francis J.: Longitudinal Aerodynamic Characteristics of a Fighter Model With a Close-Coupled Canard at Mach Numbers From 0.40 to 1.20. NASA TP-1206, 1978.

TABLE I.- INDEX TO BASIC DATA

Nozzle conf	δ_{TE}, deg	δ_{LE}, deg	δ_C, deg	$\delta_{C,TE}$, deg	Canard planform	Figure Total-coefficient data	Thrust-removed data
1	Off	Off	Off	Off	Off	7(a)	
↓	Off	Off	0	0	H_2	7(b)	
	0	0	Off	Off	Off	7(c)	16(a)
	0	↓	0	0	H_2	7(d); 7(e)	16(b); 16(c)
	15		↓	↓	↓	7(f)	16(d)
	25					7(g)	16(e)
	30					7(h); 7(i)	16(f); 16(g)
	35					7(j)	16(h)
	-25					7(k)	16(i)
	-10		↓			7(l)	16(j)
	15		10			7(m)	16(k)
	15		20			7(n)	16(l)
	0		0	10		7(o)	16(m)
	↓			20		7(p)	16(n)
				30		7(q)	16(o)
	15		↓	20		7(r)	16(p)
	↓		20	20		7(s)	16(q)
			0	0		7(t)	16(r)
	0		↓	↓	H_3	7(u)	16(s)
2	30				H_3	8(a)	17(a)
	35				H_2	8(b)	17(b)
	35		20		↓	8(c)	17(c)
	30		0		H_3	8(d)	17(d)
			20		H_3	8(e)	17(e)
		20	0		H_2	8(f)	17(f)
		20	20		H_2	8(g)	17(g)
↓		0	Off	Off	Off	8(h)	17(h)
3	↓	↓	0	0	H_2	9	18
4			0	0	H_2	10	19

(a) Basic model with H_2 canard.

Figure 1.- Drawing of model components. (All dimensions in cm unless noted.)

Wing Geometry

Mean geometric chord 31.250
Aspect ratio   3.750
Taper ratio   0.40
Airfoil Sections:
  Root (BL 17.780) to BL 24.658   NACA 64A205
  Tip (BL 55.212)   NACA 64A204

40°

FS 93.294

7.572

19.855

51.486

42.067

$\bar{c}$

Wing leading-edge flap

5.047

6.309

16.828

4.577

BL 55.212

BL 43.180

BL 24.658

BL 23.662

BL 7.938   BL 0

Outboard trailing-edge flap

Inboard trailing-edge flap

(b) Wing details.

Figure 1.- Continued.

21

FS 91.796
Canard axis
of rotation

H₂ Canard Geometry

Mean geometric chord	17.738
Aspect ratio	2.50
Taper ratio	0.30
Airfoil section	4% biconvex
Exposed area,	654.129 cm²

24.884

11.024

6.502

BL 17.780

50°

16.177

20.221

3.048

BL 38.001

24.097

7.465

H₂ CANARD

FS 91.796
Canard axis
of rotation

H₃ Canard Geometry

Mean geometric chord	19.598
Aspect ratio	2.102
Taper ratio	0.268
Airfoil section	4% biconvex
Exposed area,	654.217 cm²

27.818

11.400

BL 17.780

55°

18.542

BL 36.332

26.480

7.465

H₃ CANARD

(c) H₂ and H₃ canard details.

Figure 1.- Continued.

22

Nozzle choke plate

Half-wedge 2-D C-D
exhaust nozzle

Fuselage

U-shaped model
air supply tube

High-pressure
plenum

Inboard trailing-edge
flap

Manual air supply
flow control valve

Sting

Sting air supply tube

Strain-gage balance
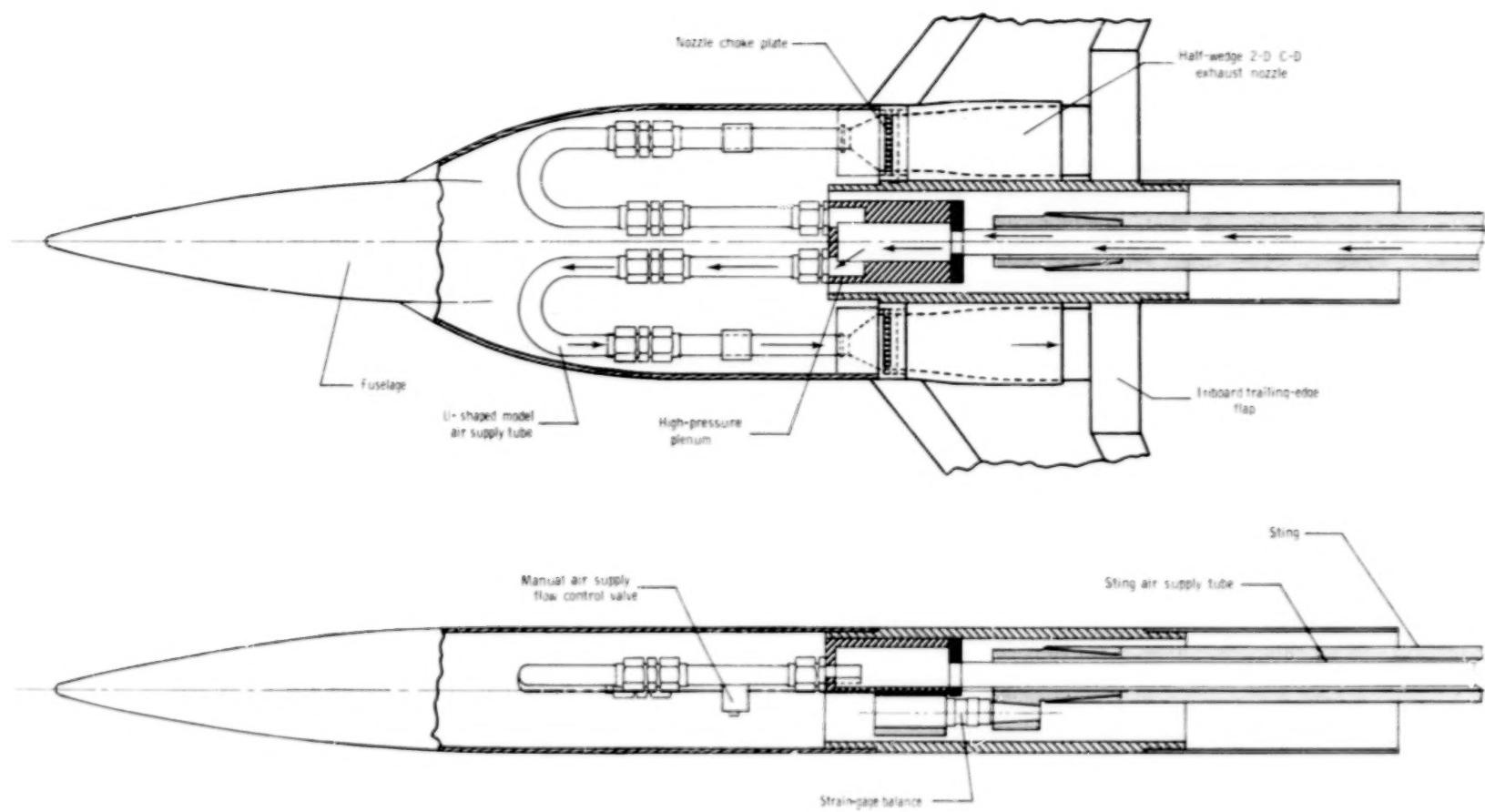
(d) Model air supply system and balance arrangement.

Figure 1.- Continued.

23

External nozzle geometry		
FS	Y_1	Z_1
113.030	17.780	7.620
114.300	17.818	
115.570	17.907	
116.840	18.072	
118.110	18.186	
119.380	18.288	
121.920		
124.460		
127.000		7.417
129.000		6.934
132.000		6.274
135.677		5.105
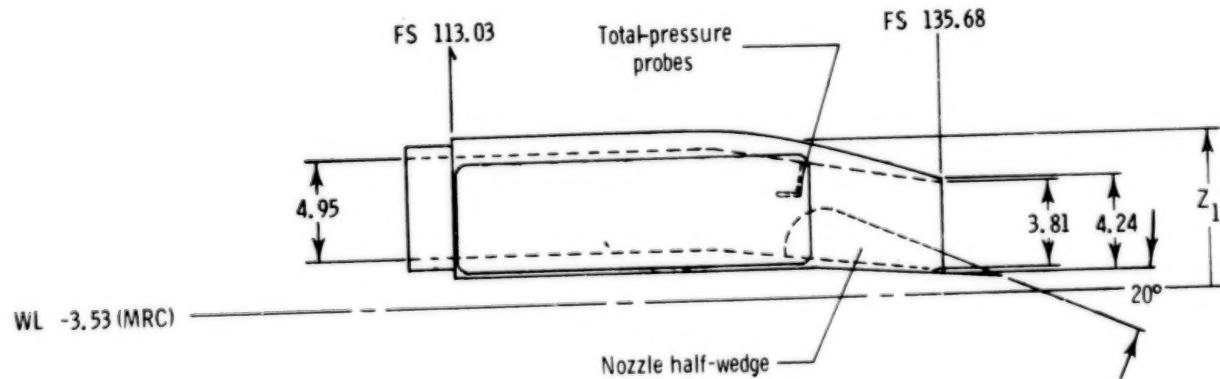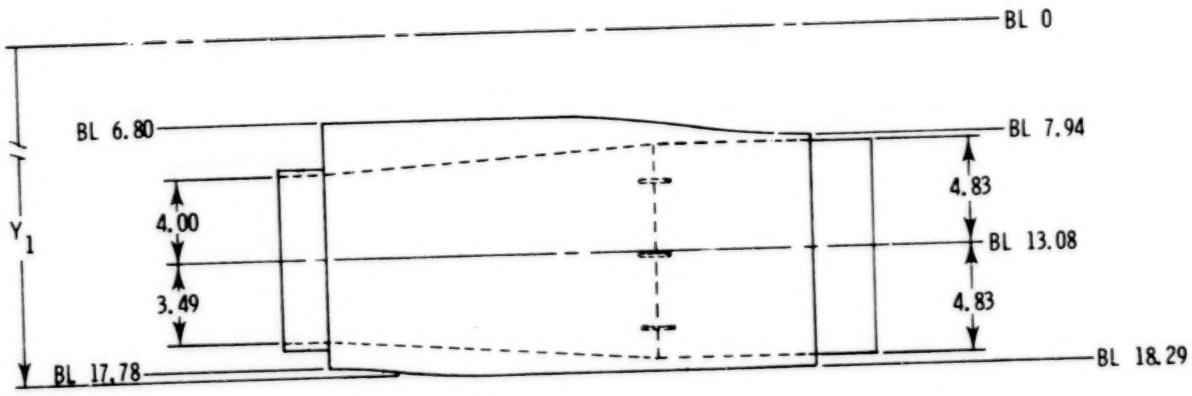
(e) Half-wedge two-dimensional C-D exhaust nozzle. Conf 1 (no spanwise blowing); total exhaust nozzle throat area of 46.26 cm^2.

Figure 1.- Continued.
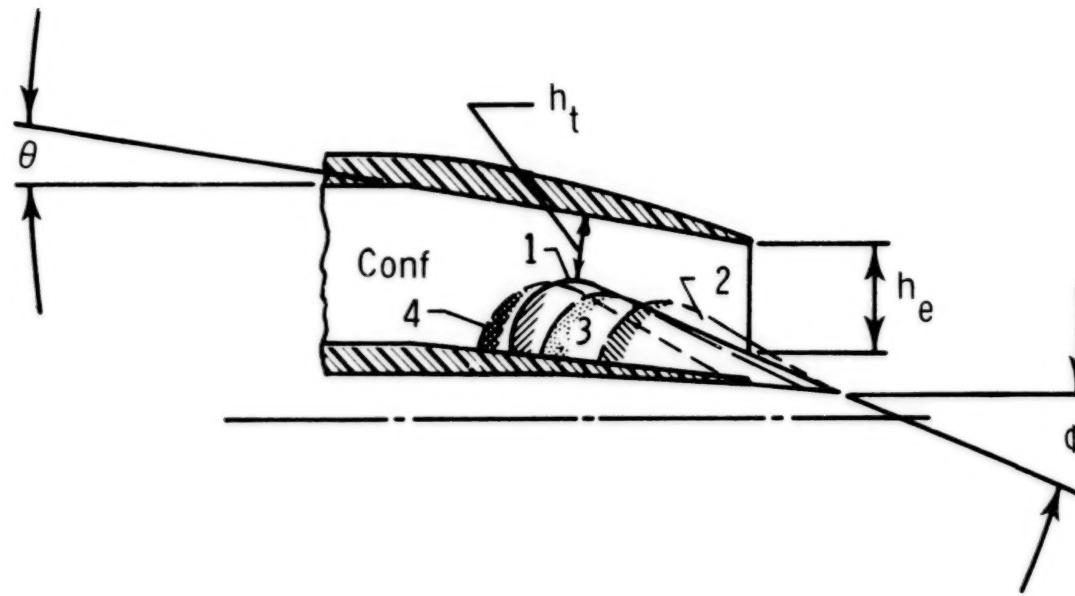
Nozzle conf	Aspect ratio	A_t, cm^2/side	A_e, cm^2/side	ε	h_t, cm	h_e, cm	θ, deg	Φ, deg
1	4.03	23.132	31.148	1.35	2.395	3.224	10	20
2	4.04	23.097	27.461	1.19	2.391	2.843		25
3	4.10	22.771	32.300	1.42	2.357	3.344		
4	3.98	23.471	39.484	1.68	2.430	4.087		

(f) Exhaust nozzle internal geometry characteristics.

Figure 1.- Concluded.
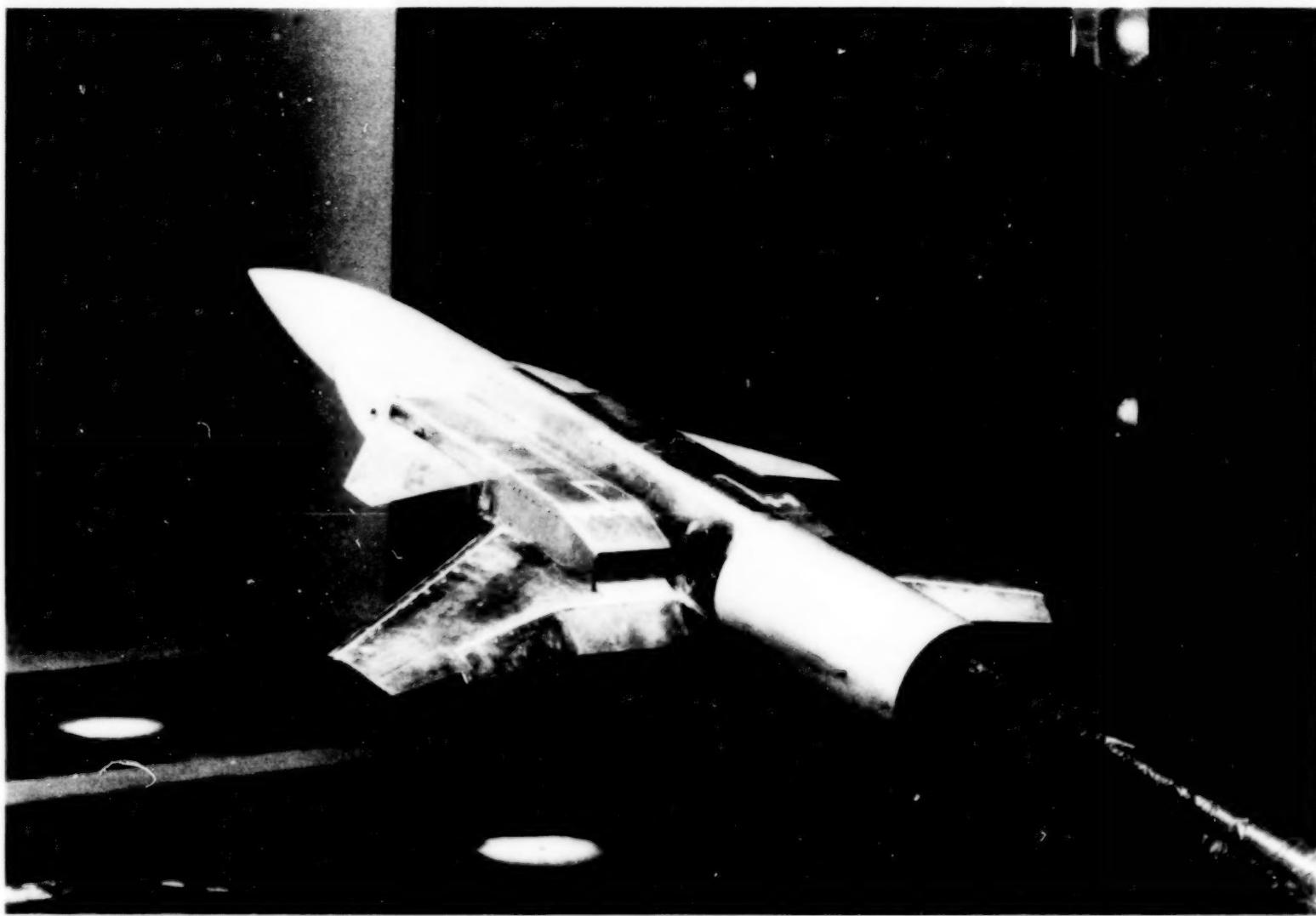
L-78-46.1

Figure 2.- VEO-wing model installed in Langley V/STOL tunnel test section.
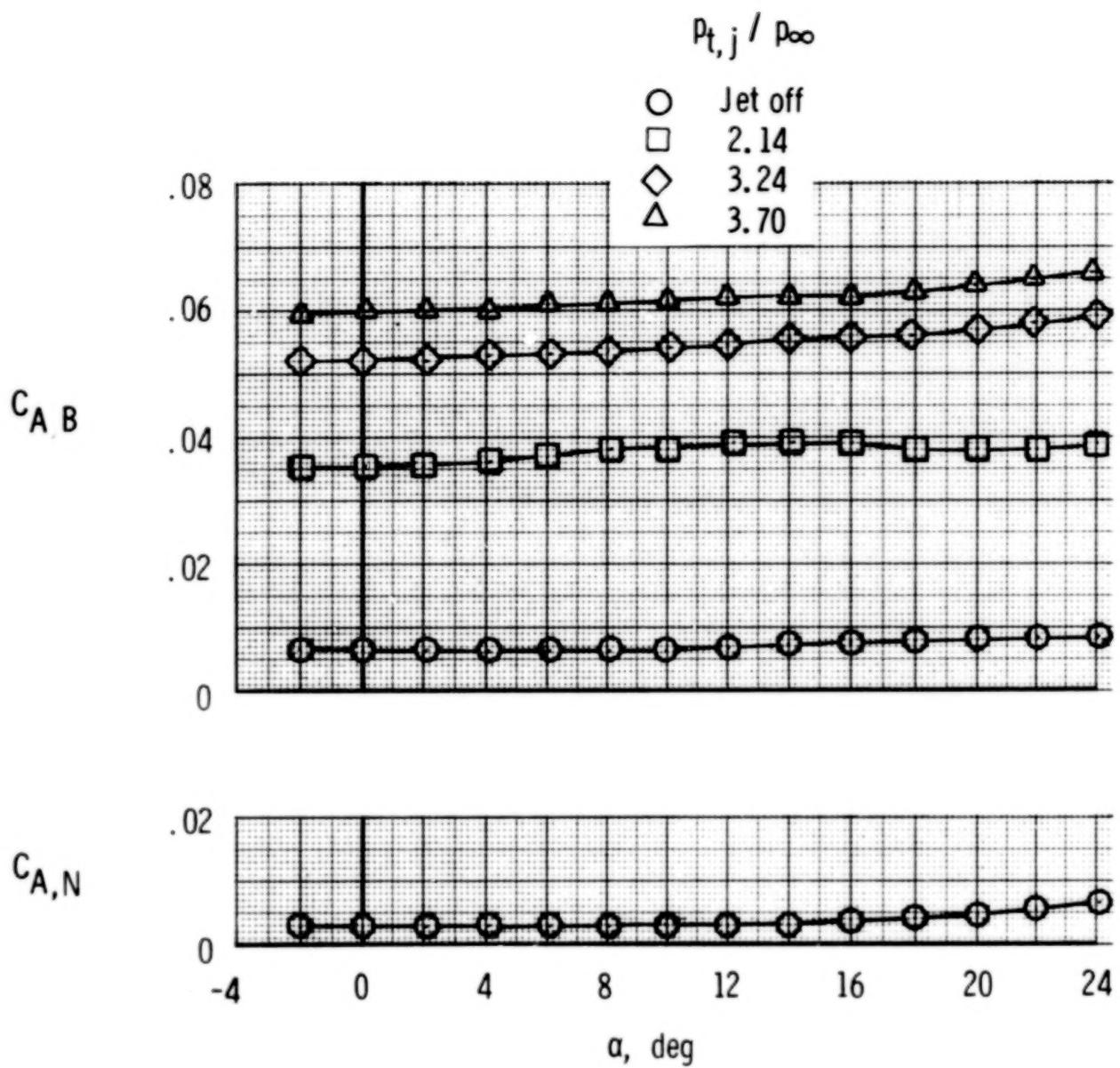
(a) $\delta_{TE} = 0^{\circ}$.

Figure 3.- Typical base pressure correction data.
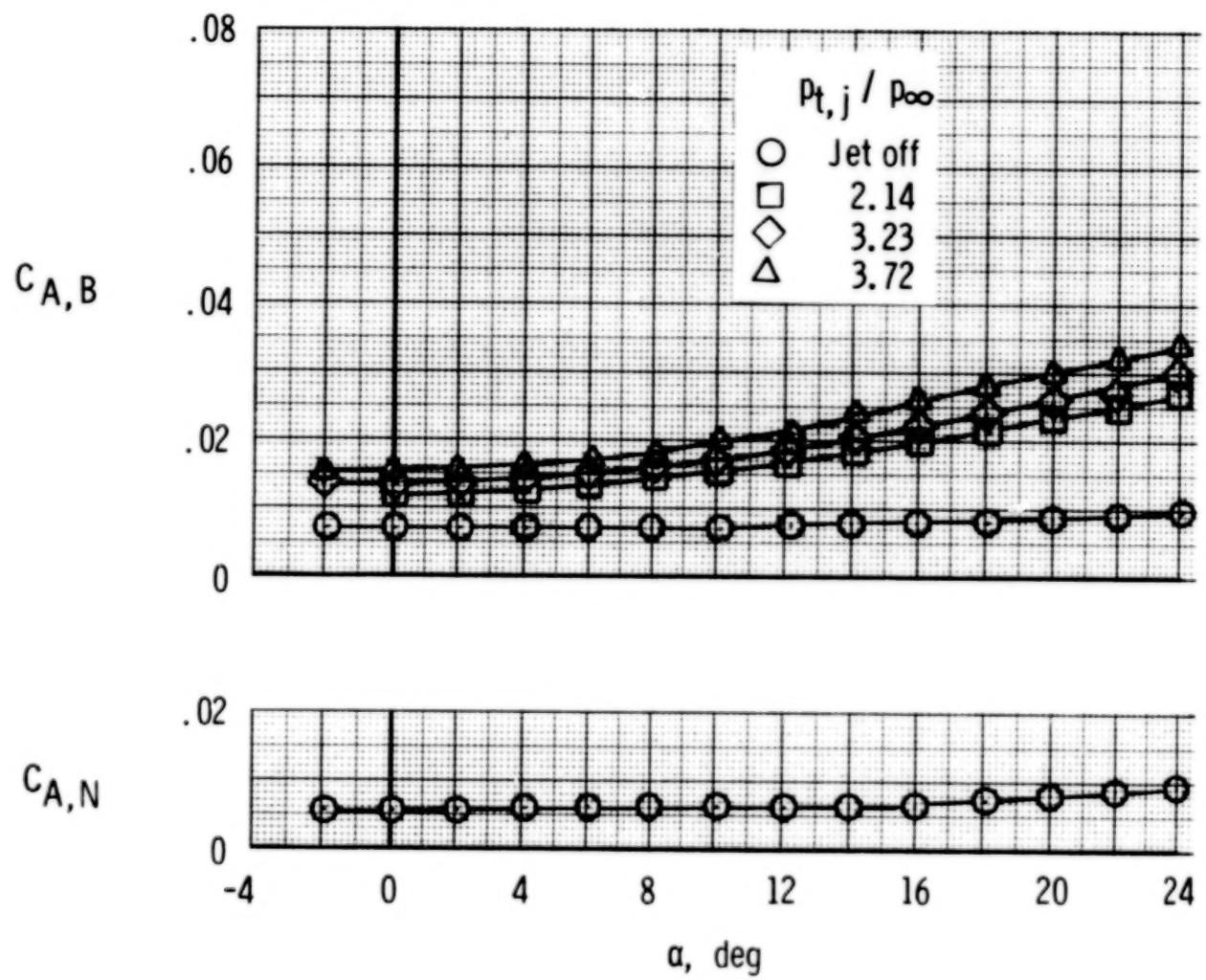
(b) $\delta_{TE} = 15°$.
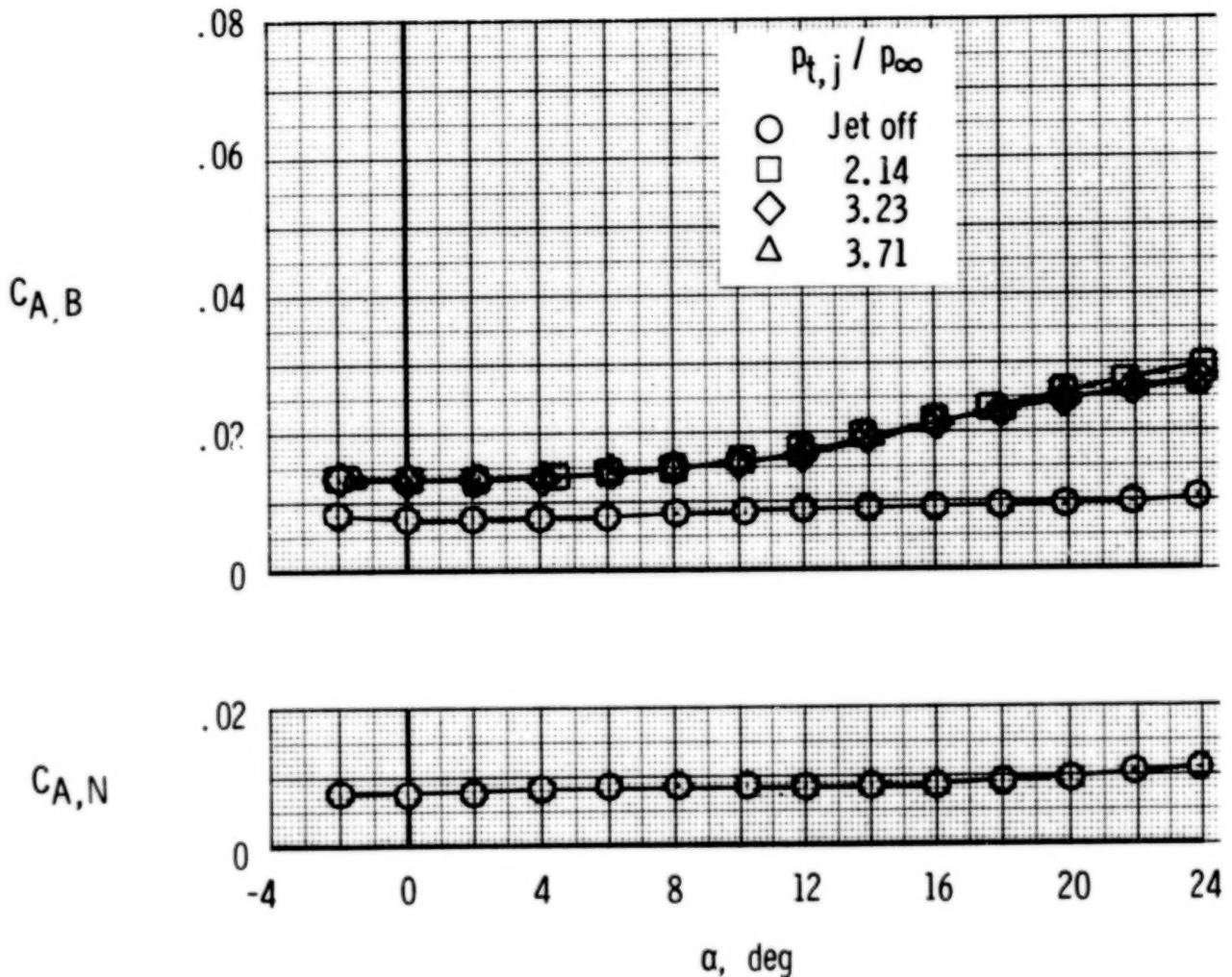
Figure 3.- Continued.

(c) $\delta_{TE} = 25^{o}$.

Figure 3.- Continued.

29

(d) $\delta_{TE} = 30^\circ$.
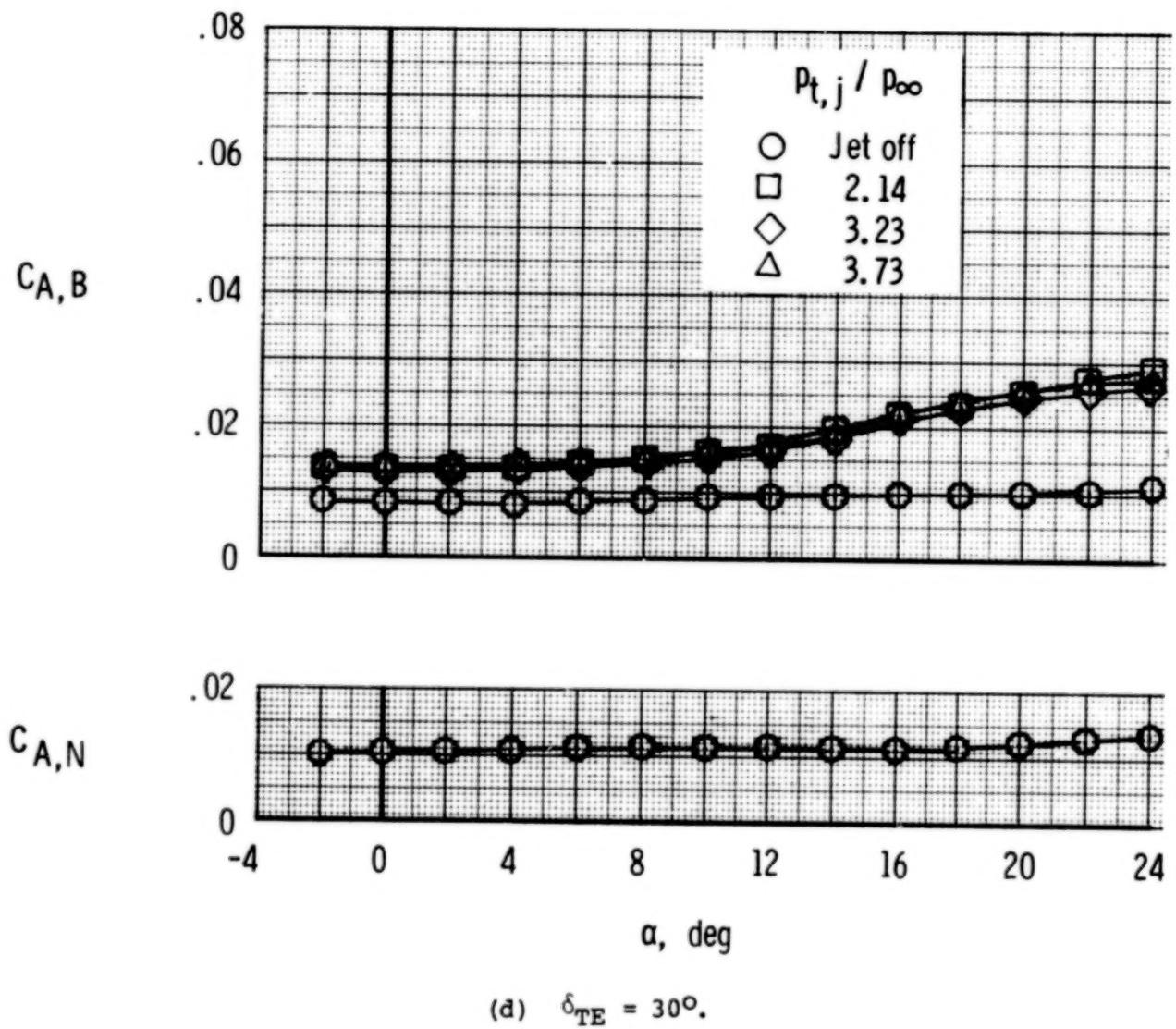
Figure 3.- Continued.
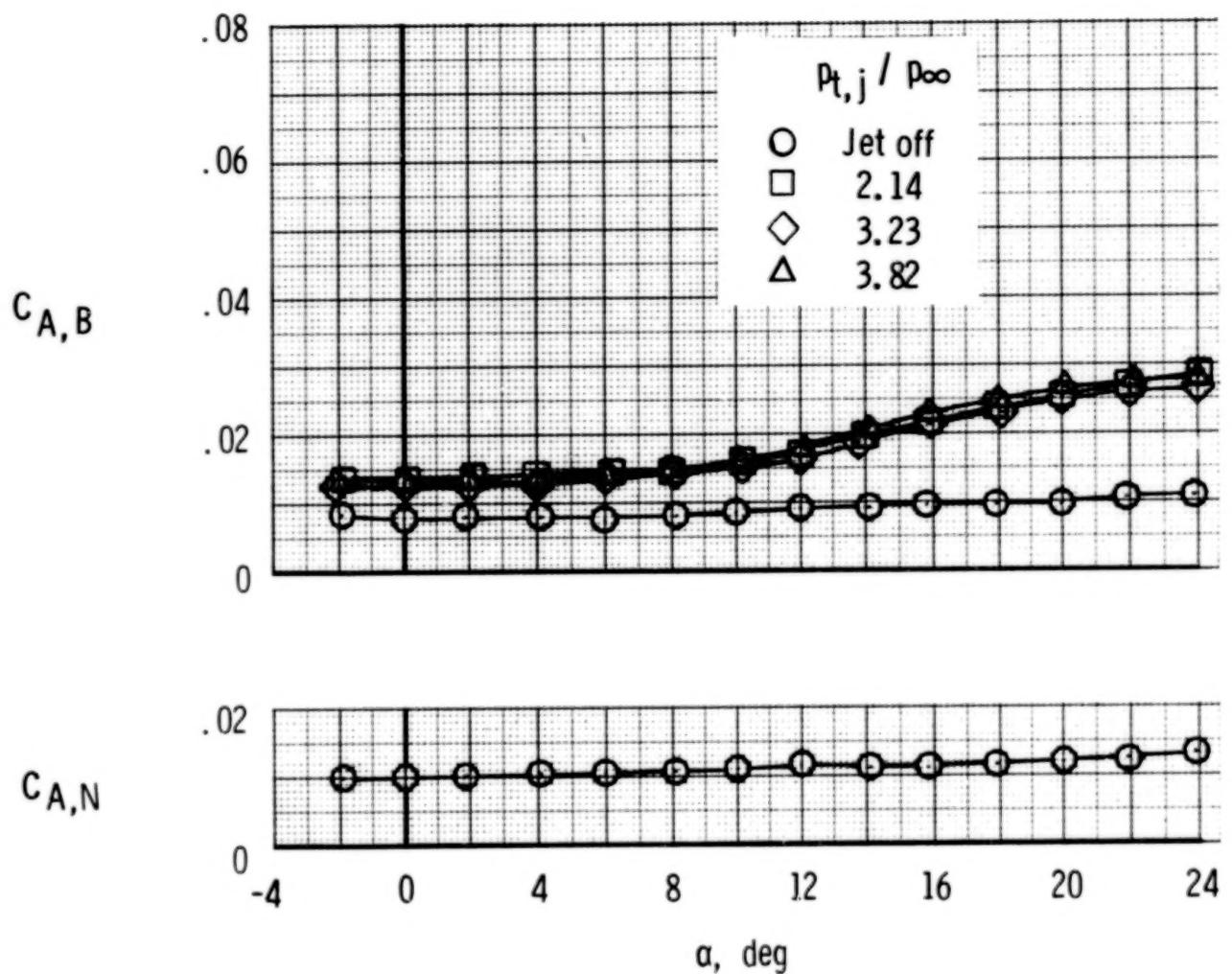
(e) $\delta_{TE} = 35^\circ$.

Figure 3.- Concluded.

δ_{TE}, deg

○   0
□   15
◇   25
△   30
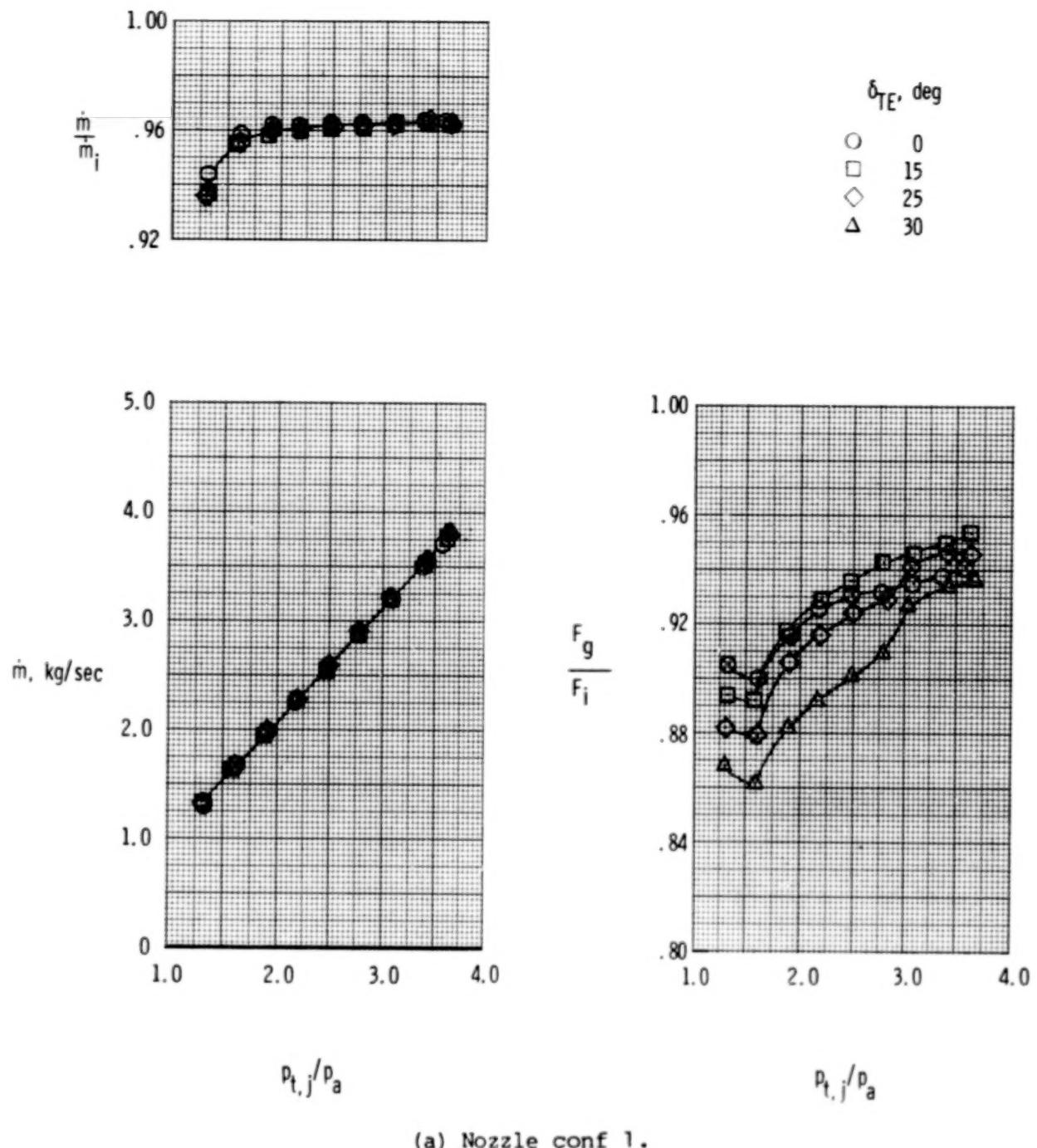
(a) Nozzle conf 1.

Figure 4.- Static internal performance and nozzle discharge
coefficient characteristics.
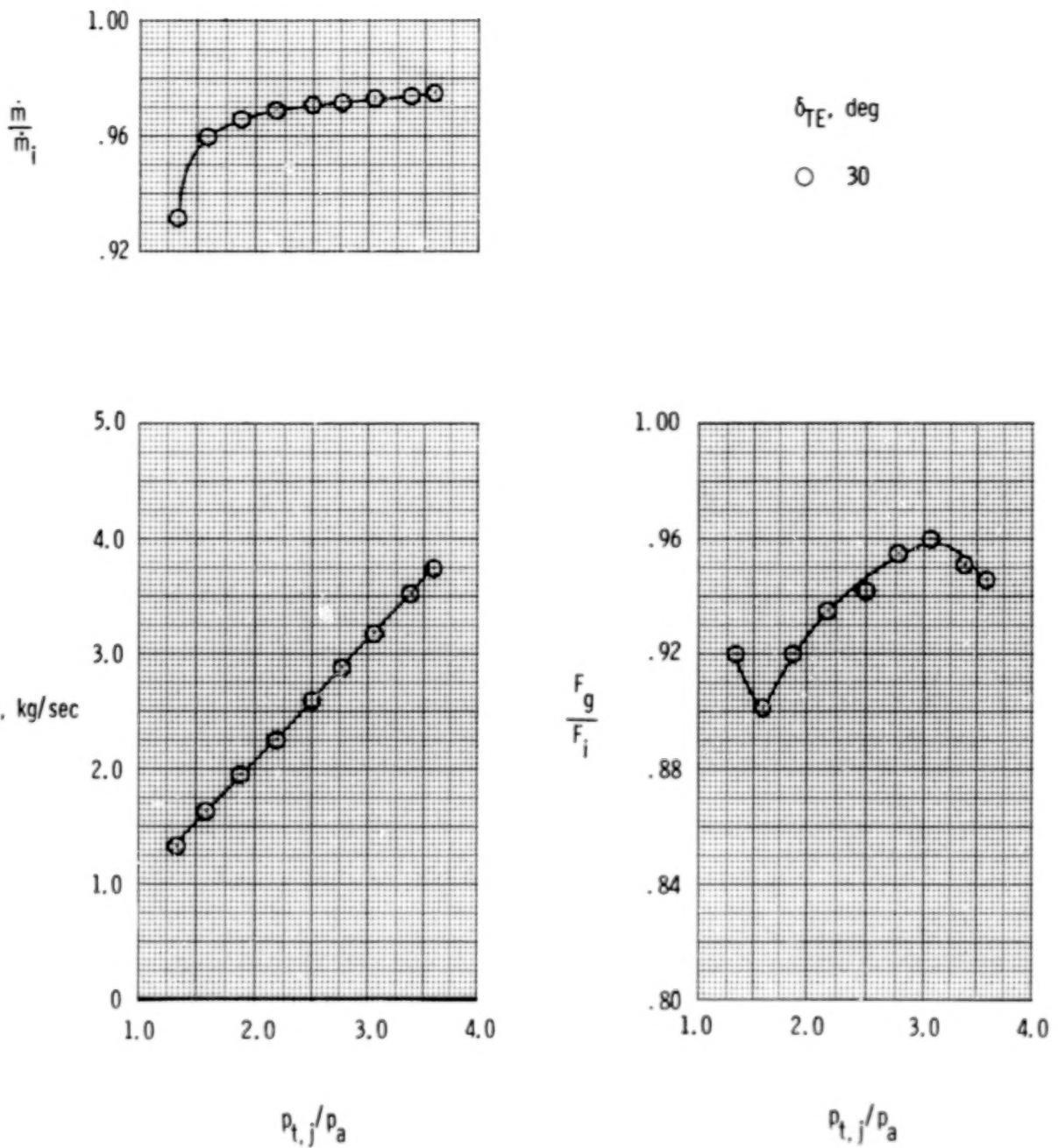
(b) Nozzle conf 2.

Figure 4.- Concluded.
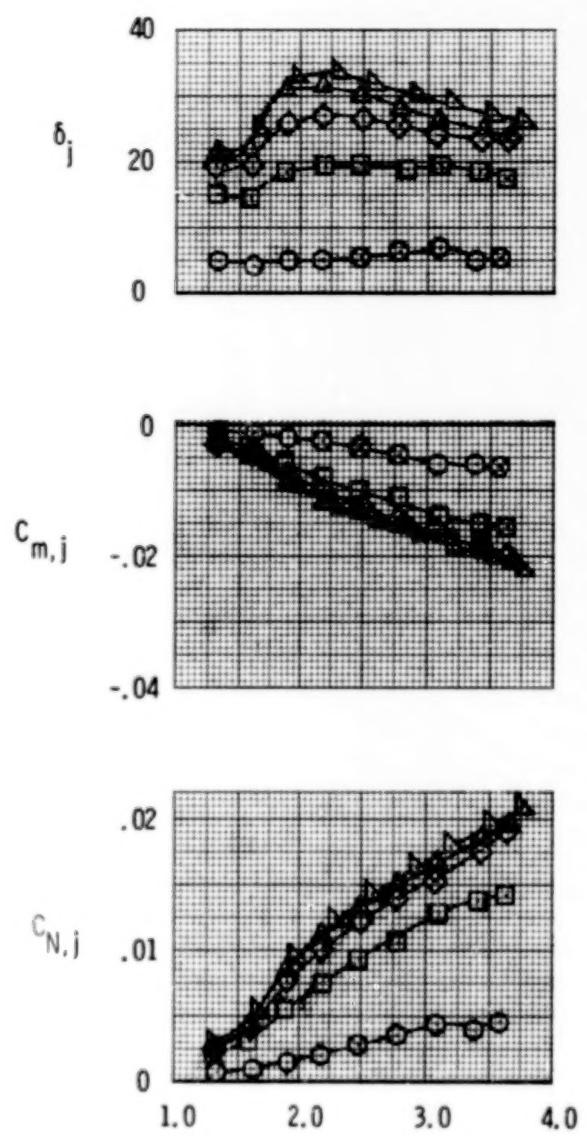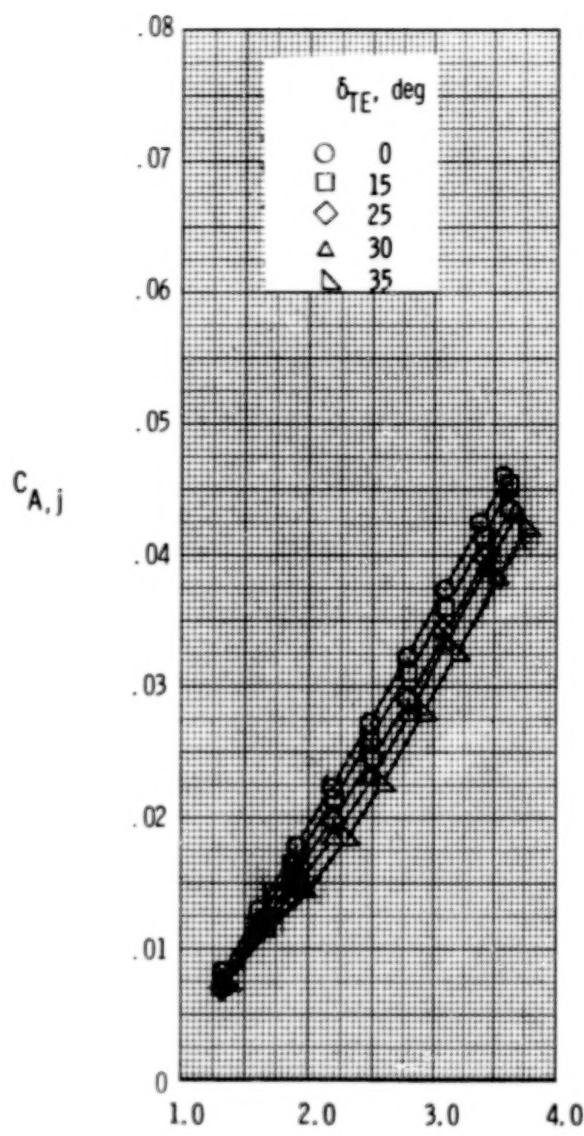
(a) Nozzle conf 1.

Figure 5.- Static thrust and turning-angle characteristics.
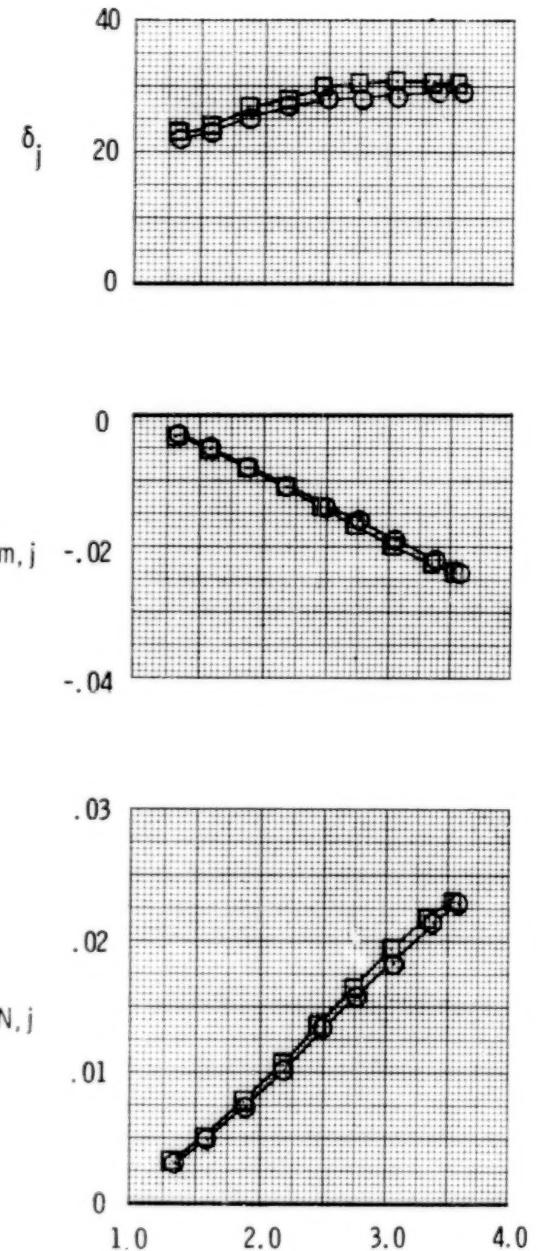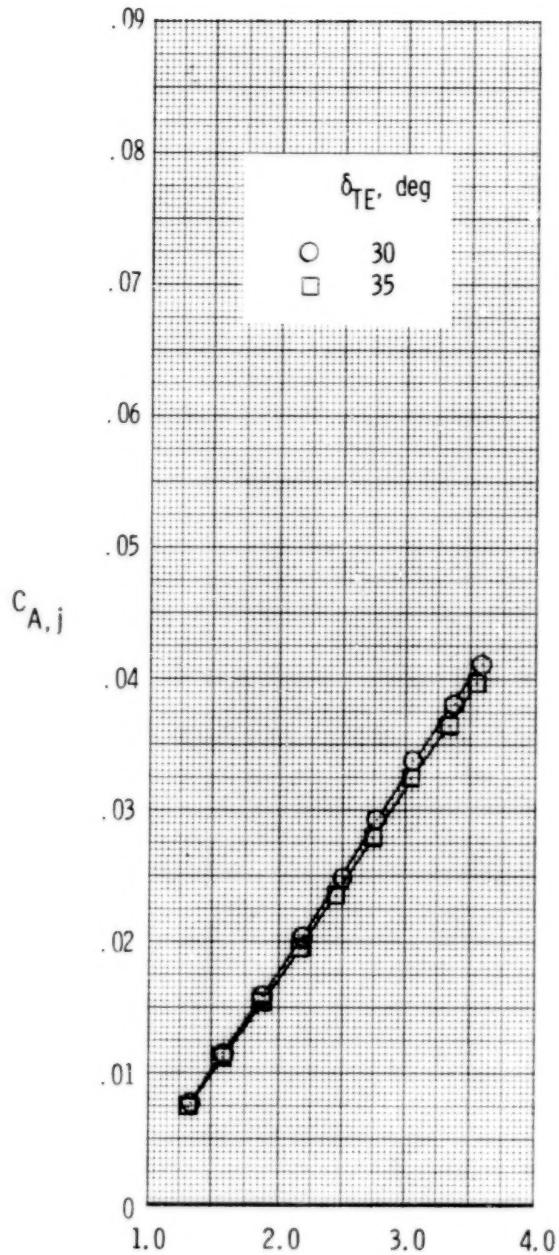
(b) Nozzle conf 2.

Figure 5.- Continued.
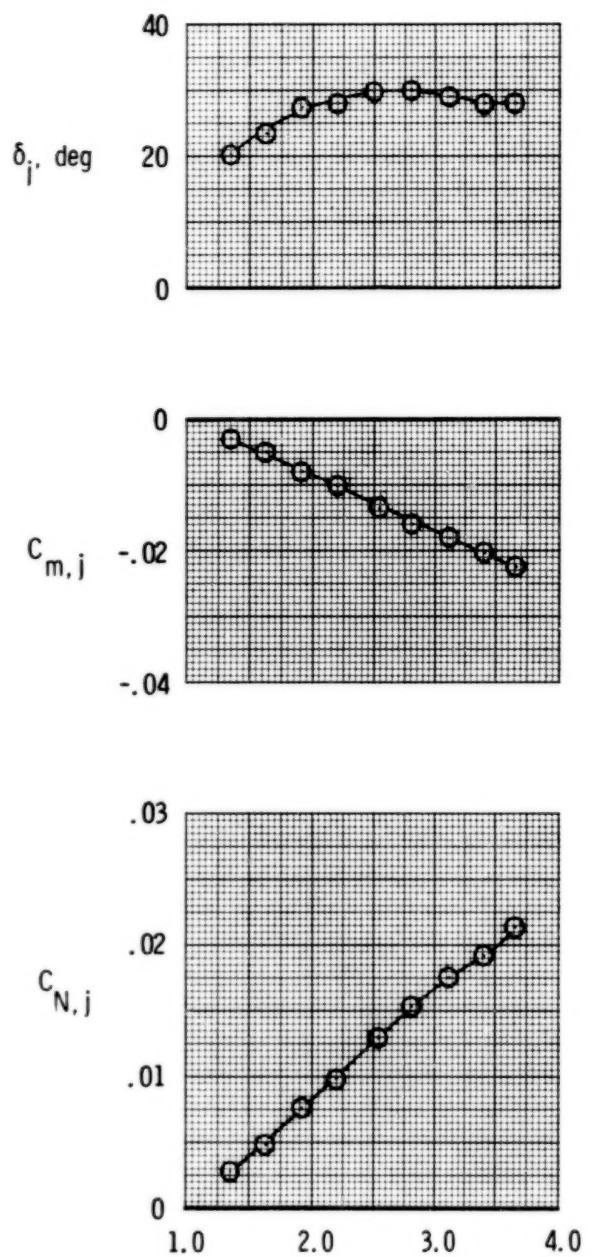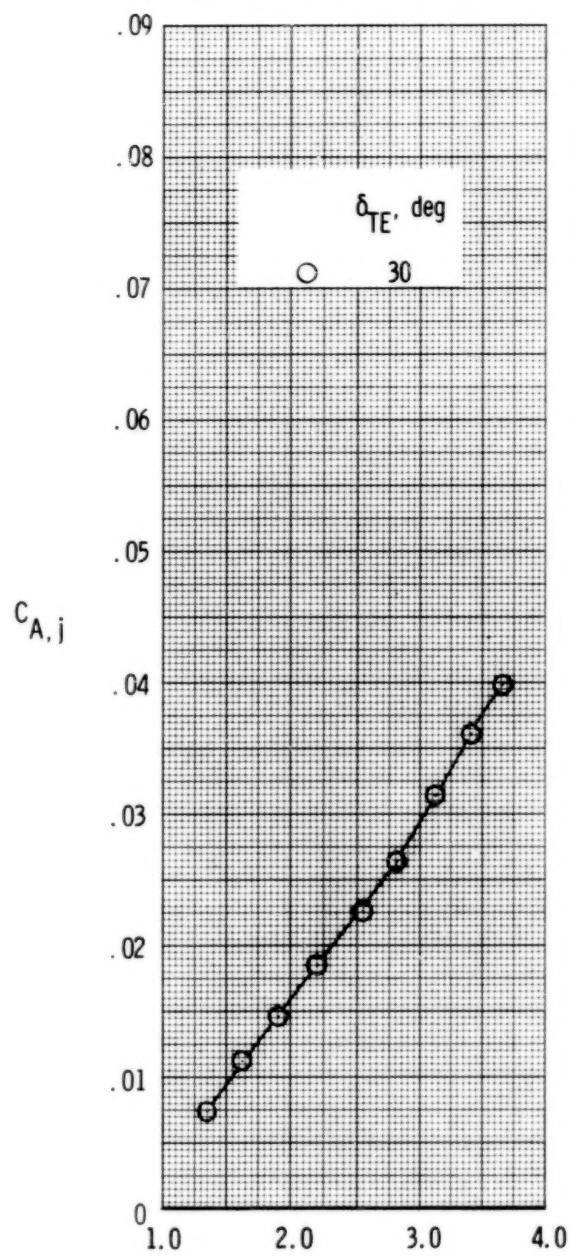
(c) Nozzle conf 3.

Figure 5.- Continued.
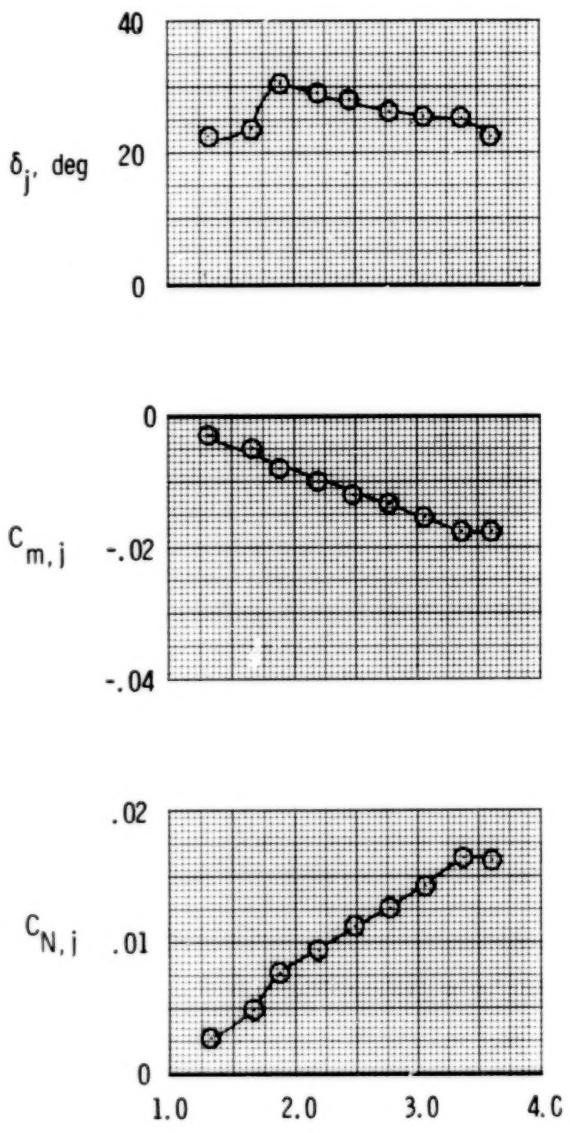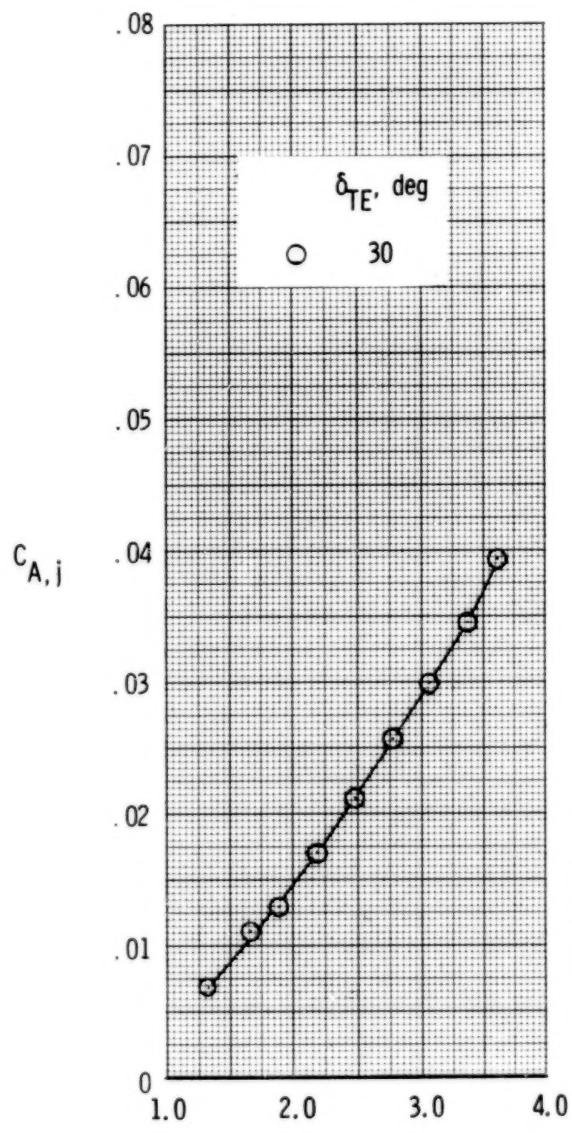
(d) Nozzle conf 4.

Figure 5.- Concluded.
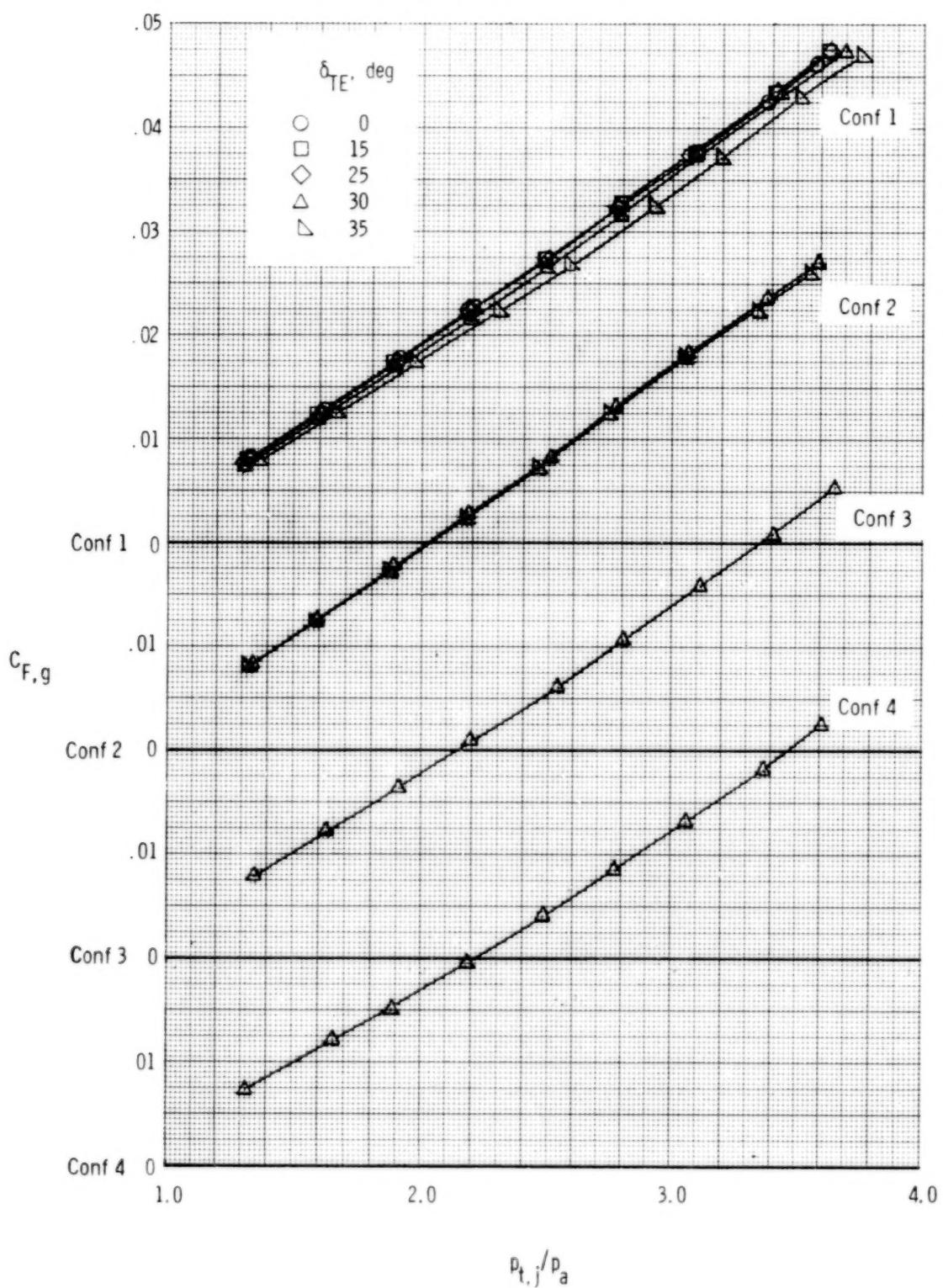
(a) M = 0.

Figure 6.- Gross thrust characteristics.
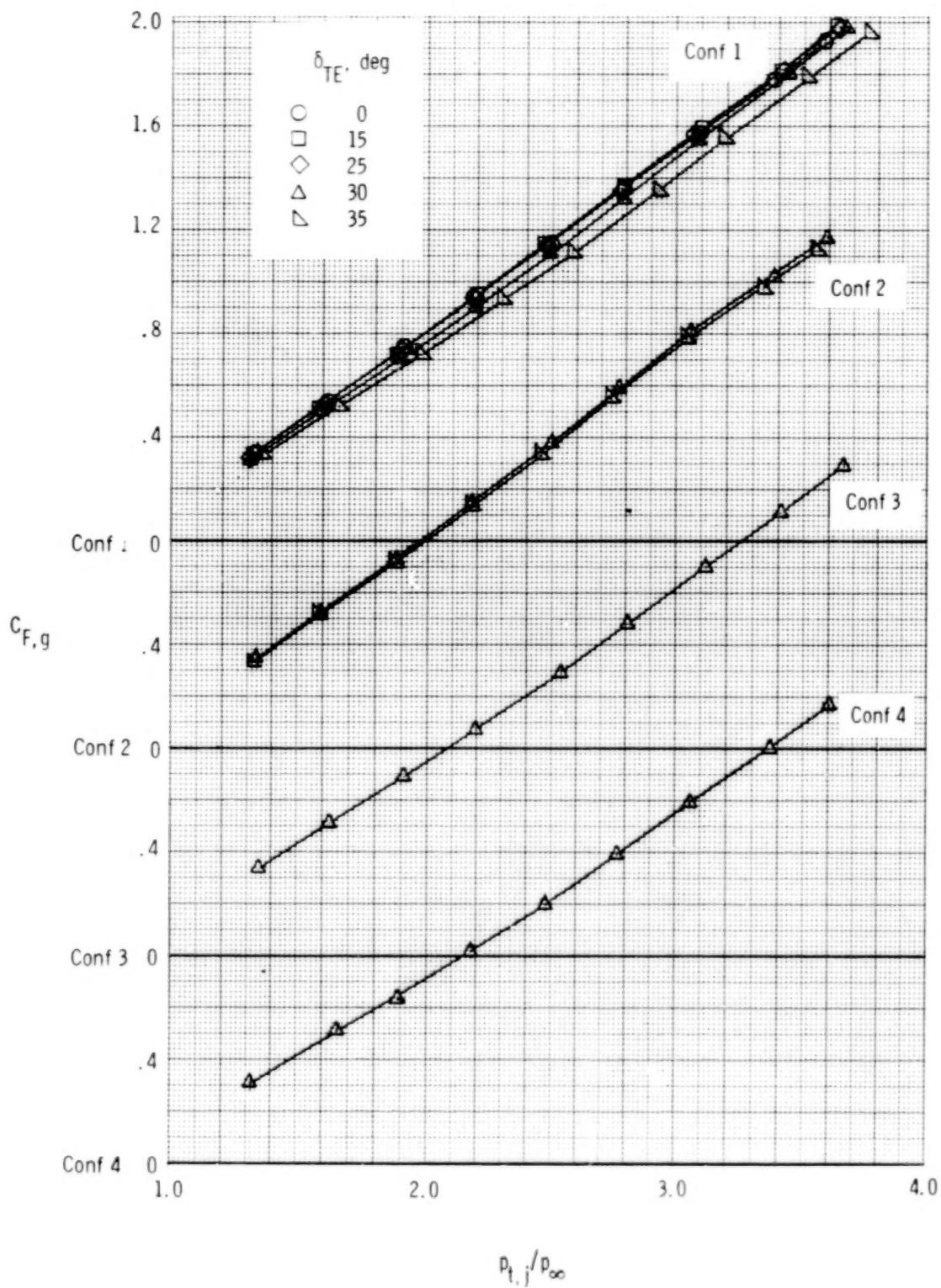
(b)   M = 0.186.

Figure 6.- Concluded.
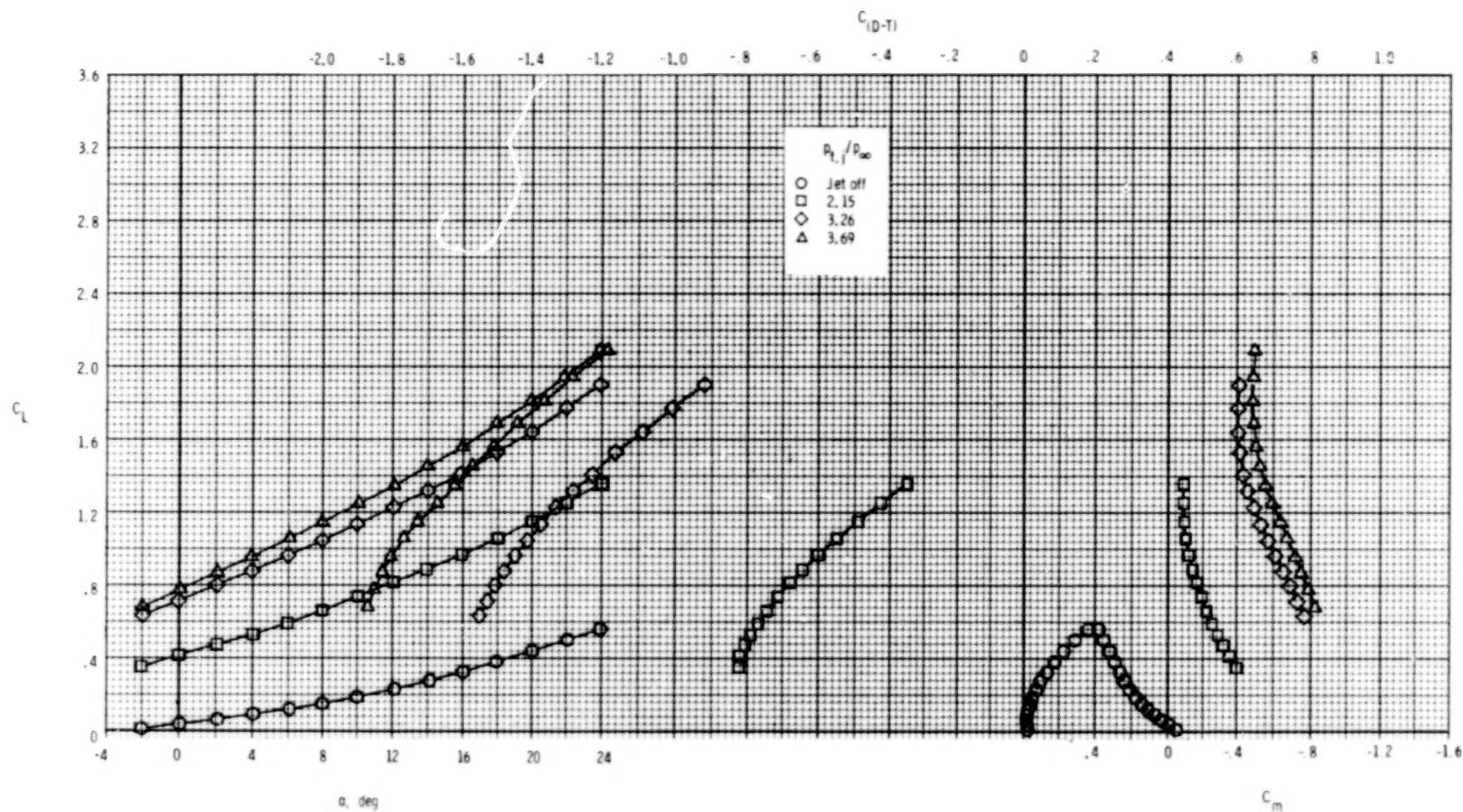
(a) Wing and canard removed.

Figure 7.- Basic longitudinal aerodynamic characteristics at M = 0.186 for nozzle conf 1.

(b) Wing off; $\delta_C = \delta_{C,TE} = 0^O$; H_2 canard.

Figure 7.- Continued.

41
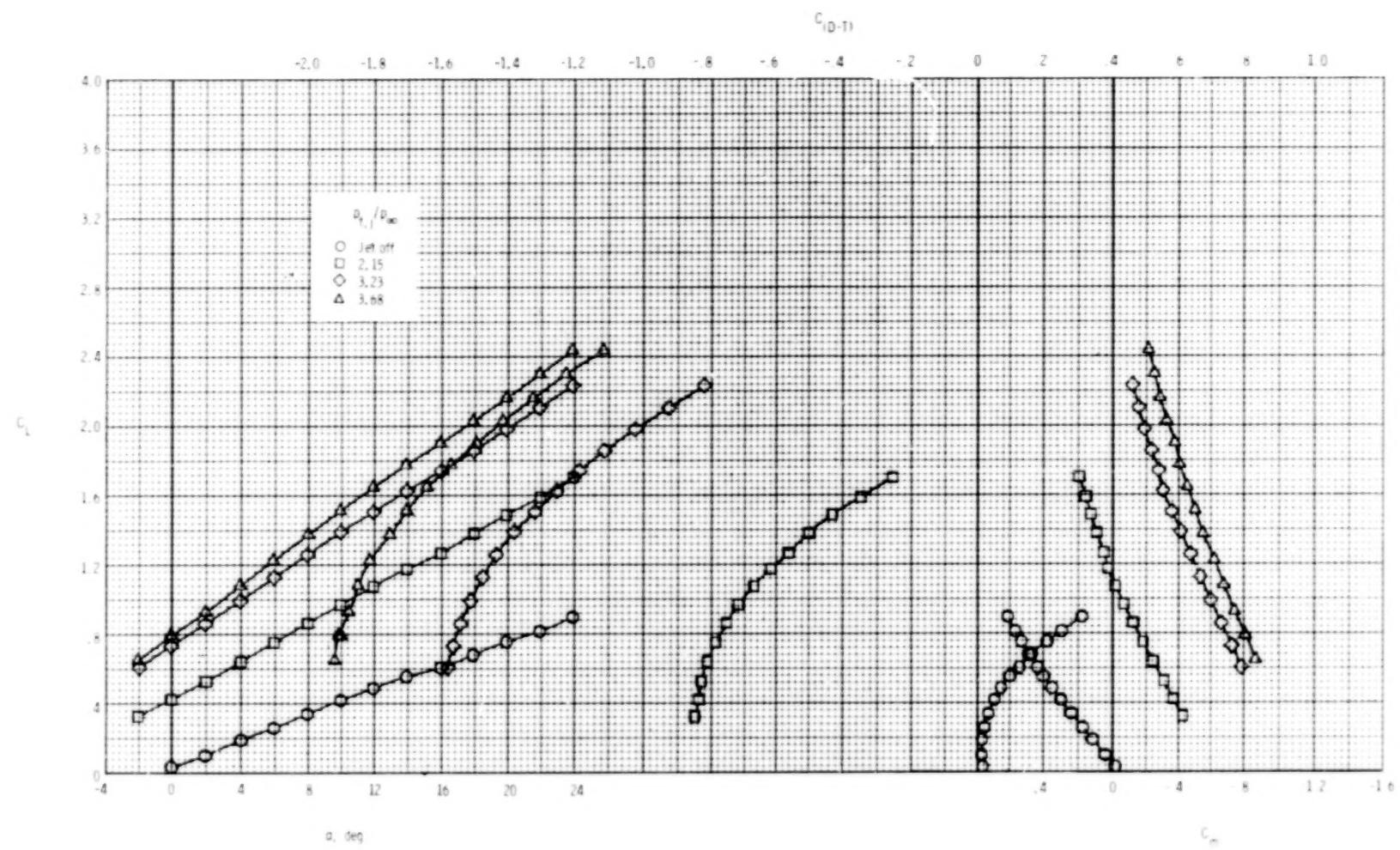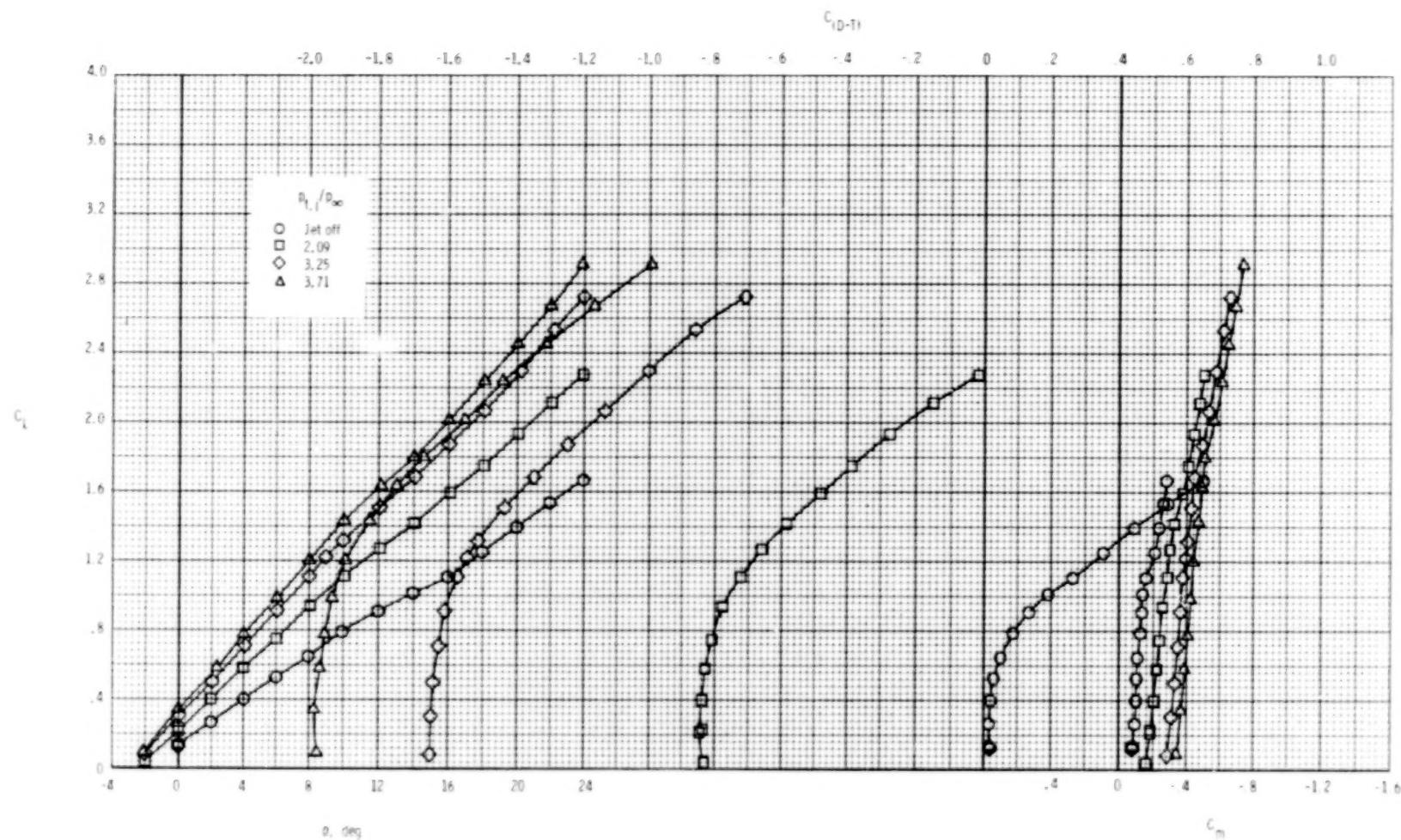
(c) $\delta_{TE} = \delta_{LE} = 0^o$; canard off.

Figure 7.- Continued.
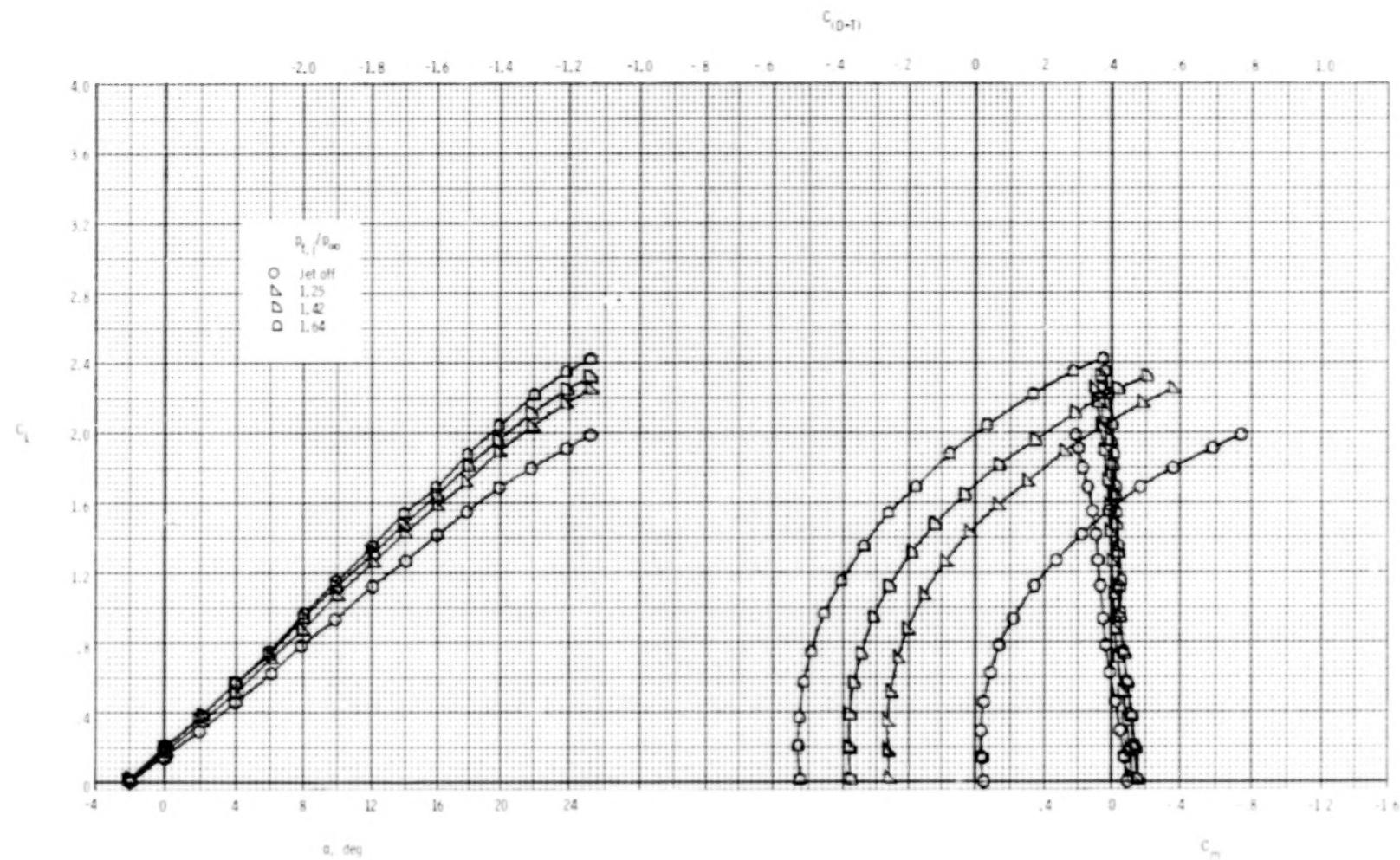
(d) $\delta_{TE} = \delta_{LE} = \delta_C = \delta_{C,TE} = 0°$; H_2 canard; $P_{t,j}/P_\infty = 1.25$ to 1.64.

Figure 7.- Continued.

BLANK PAGE

BLANK PAGE
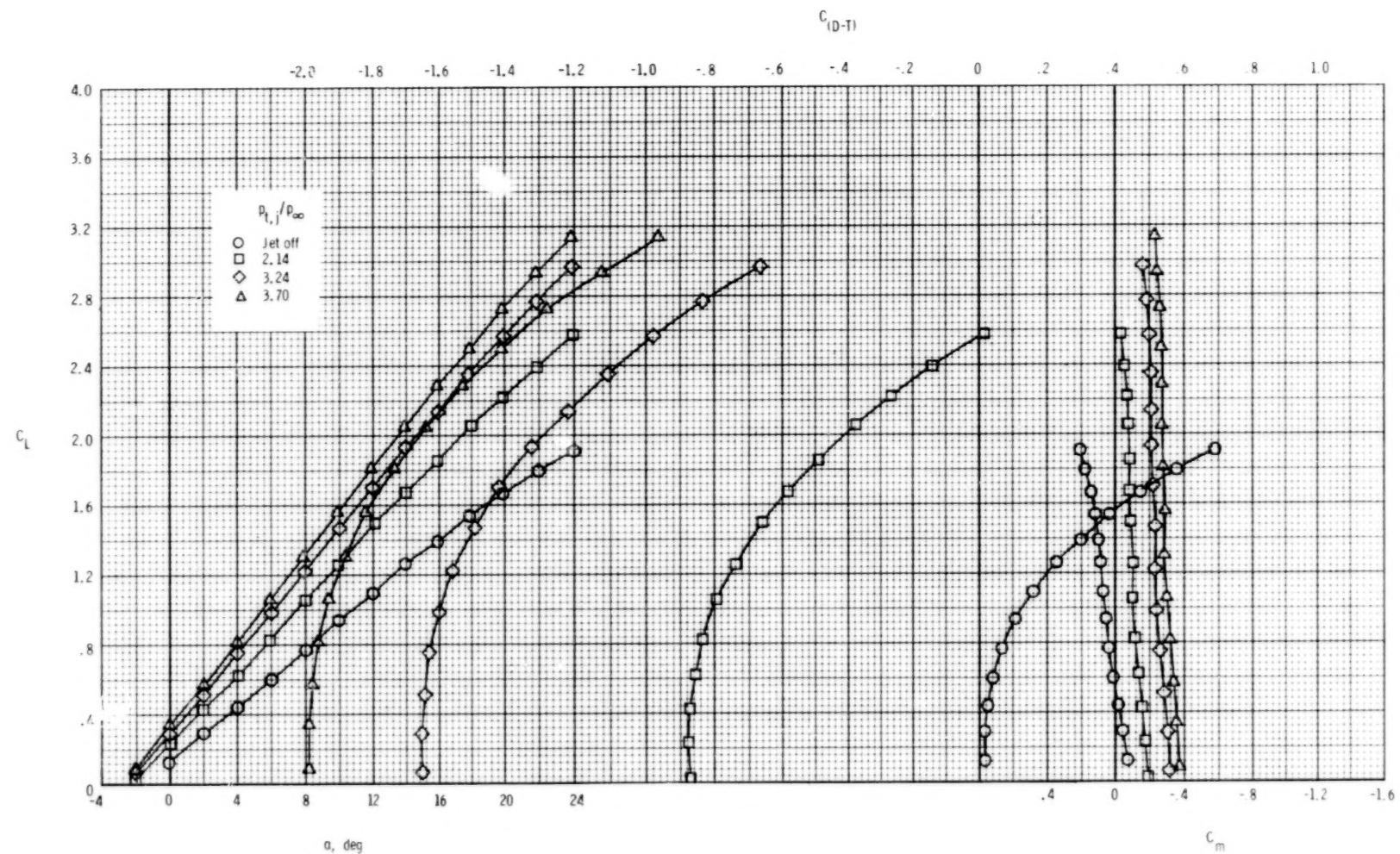
(e) $\delta_{TE} = \delta_{LE} = \delta_C = \delta_{C,TE} = 0^o$; H_2 canard; $p_{t,j}/p_\infty = 2.14$ to 3.70.

Figure 7.- Continued.

(f) $\delta_{TE} = 15^o$; $\delta_{LE} = \delta_c = \delta_{c,TE} = 0^o$; H_2 canard.

Figure 7.- Continued.

45

(g) $\delta_{TE} = 25^o$; $\delta_{LE} = \delta_C = \delta_{C,TE} = 0^o$; H_2 canard.
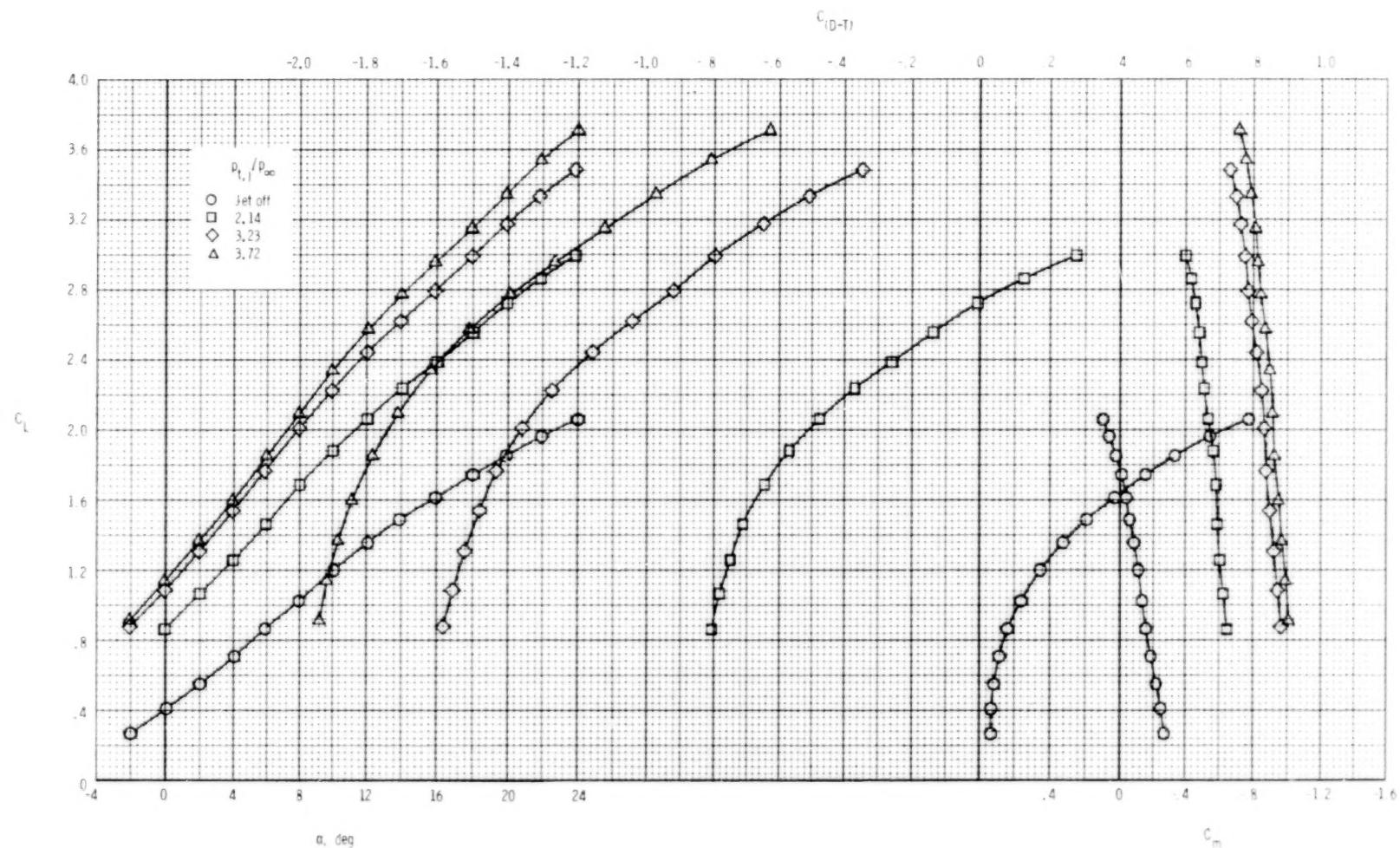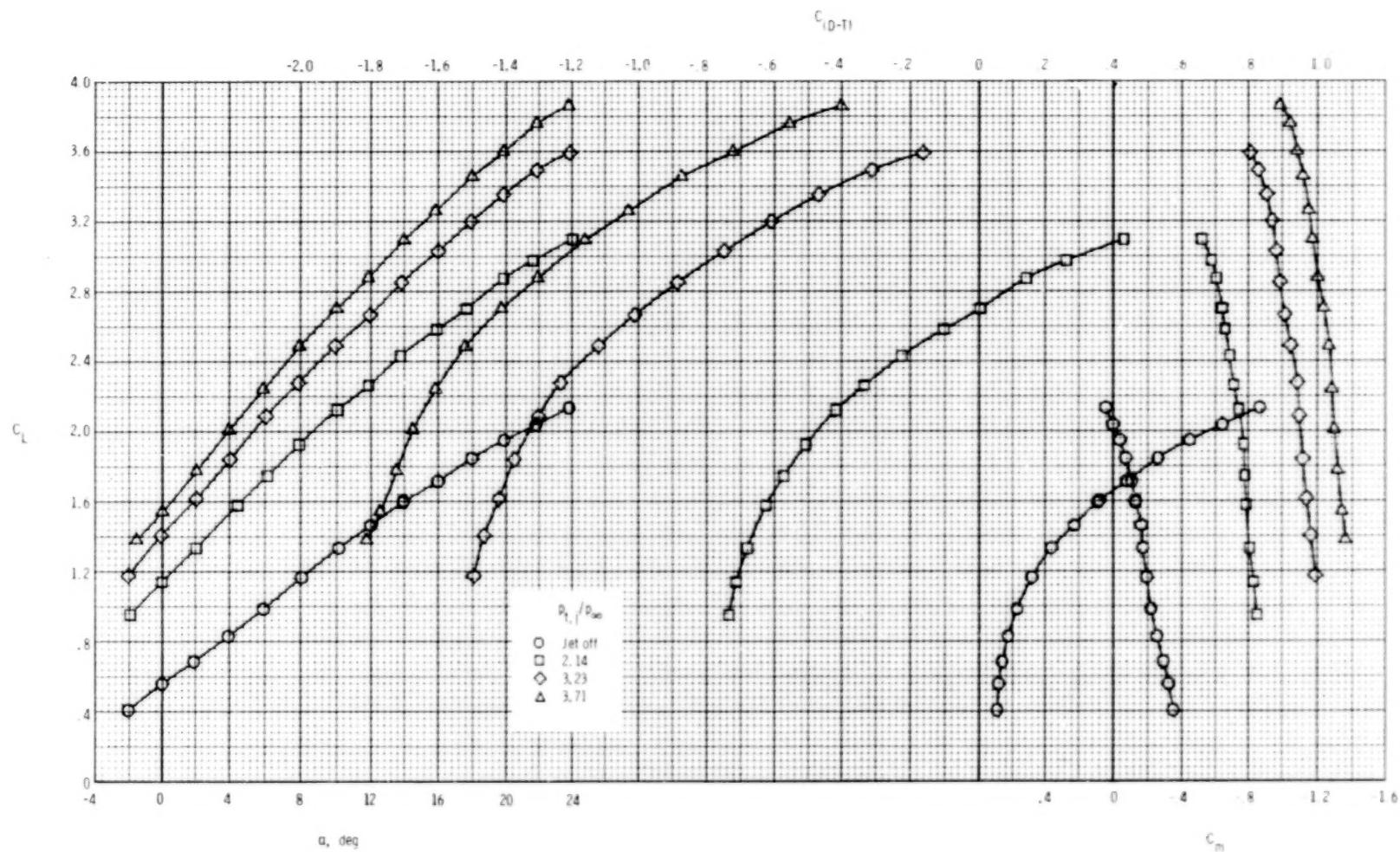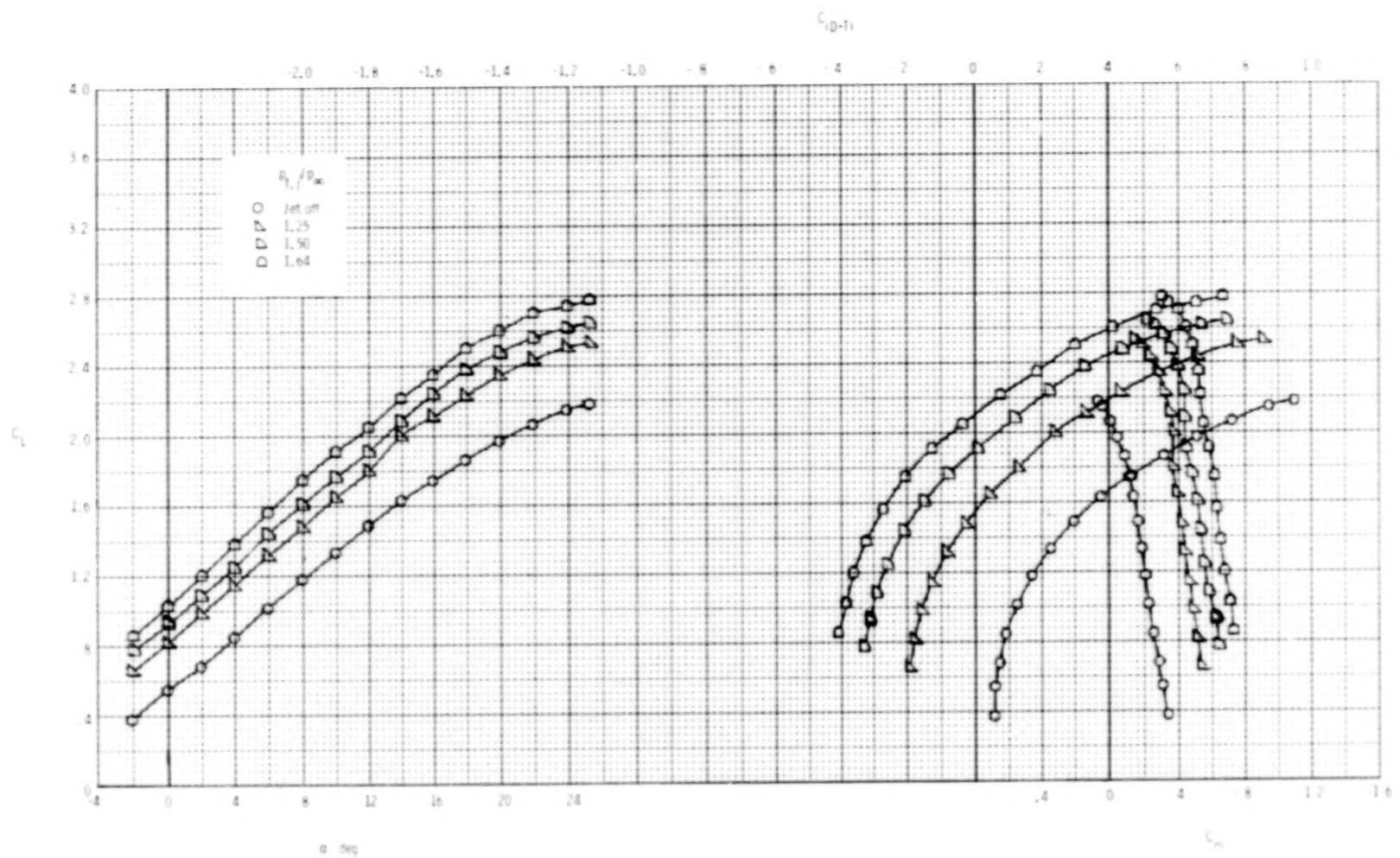
Figure 7.- Continued.

(h) $\delta_{TE} = 30^\circ$; $\delta_{LE} = \delta_c = \delta_{c,TE} = 0^\circ$; H_2 canard; $P_{t,j}/P_\infty = 1.25$ to 1.64.

Figure 7.- Continued.

47
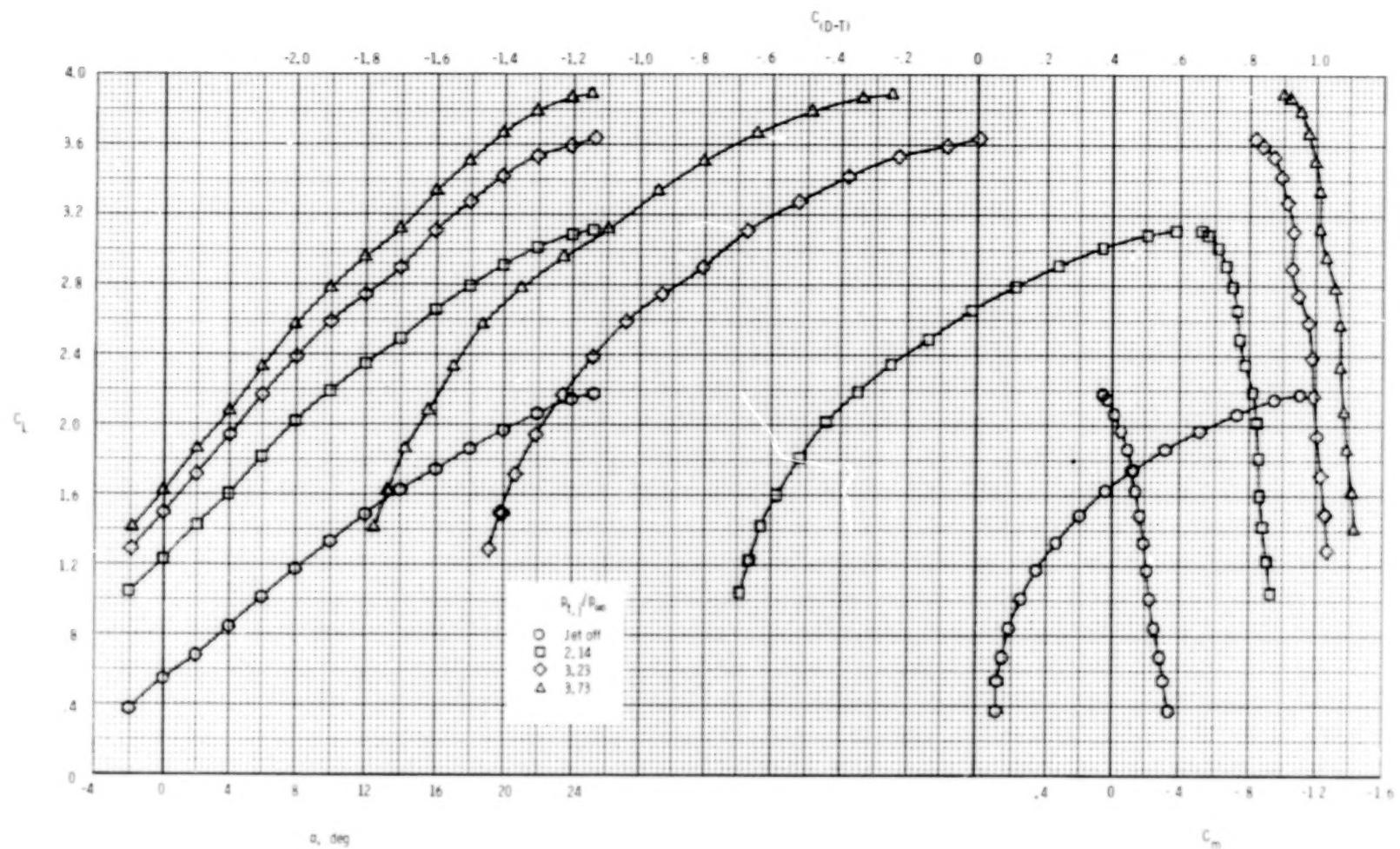
(i) $\delta_{TE} = 30^{\circ}$; $\delta_{LE} = \delta_C = \delta_{C,TE} = 0^{\circ}$; H_2 canard; $p_{t,j}/p_{\infty} = 2.14$ to 3.73.

Figure 7.- Continued.

(j) $\delta_{TE} = 35^o$; $\delta_{LE} = \delta_C = \delta_{C,TE} = 0^o$; H_2 canard.

Figure 7.- Continued.

49
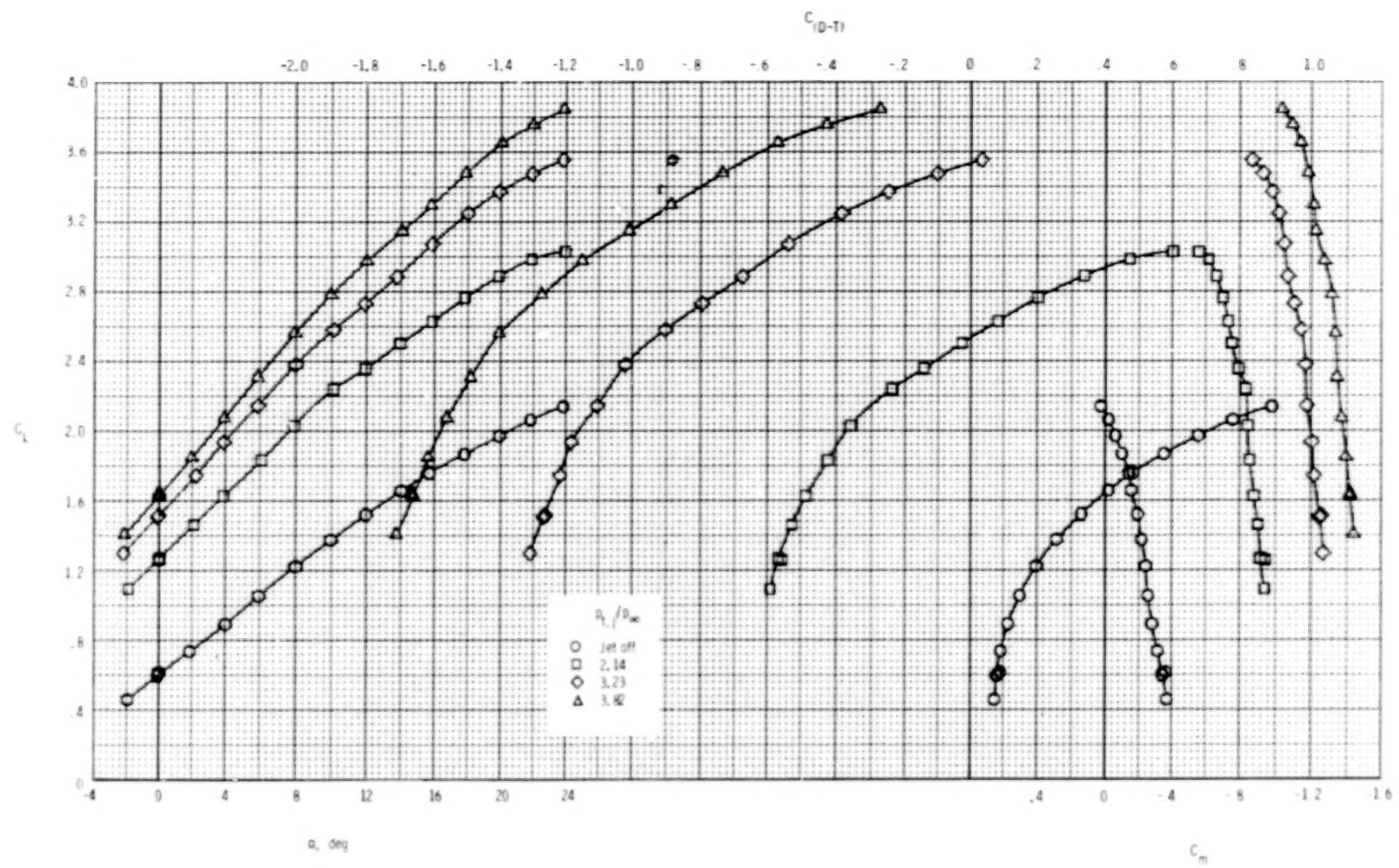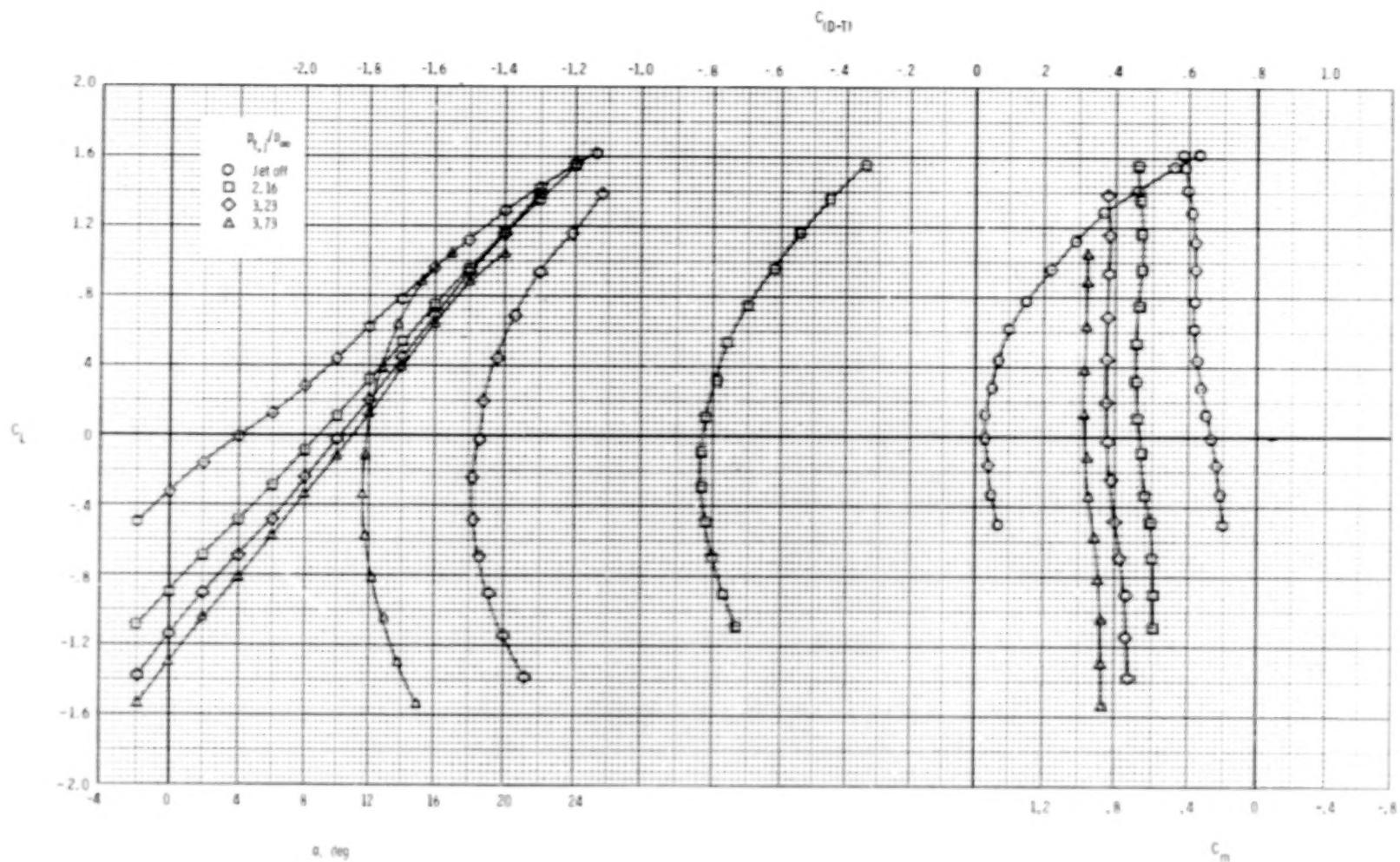
(k) $\delta_{TE} = -25^{\circ}$; $\delta_{LE} = \delta_C = \delta_{C,TE} = 0^{\circ}$; H_2 canard.
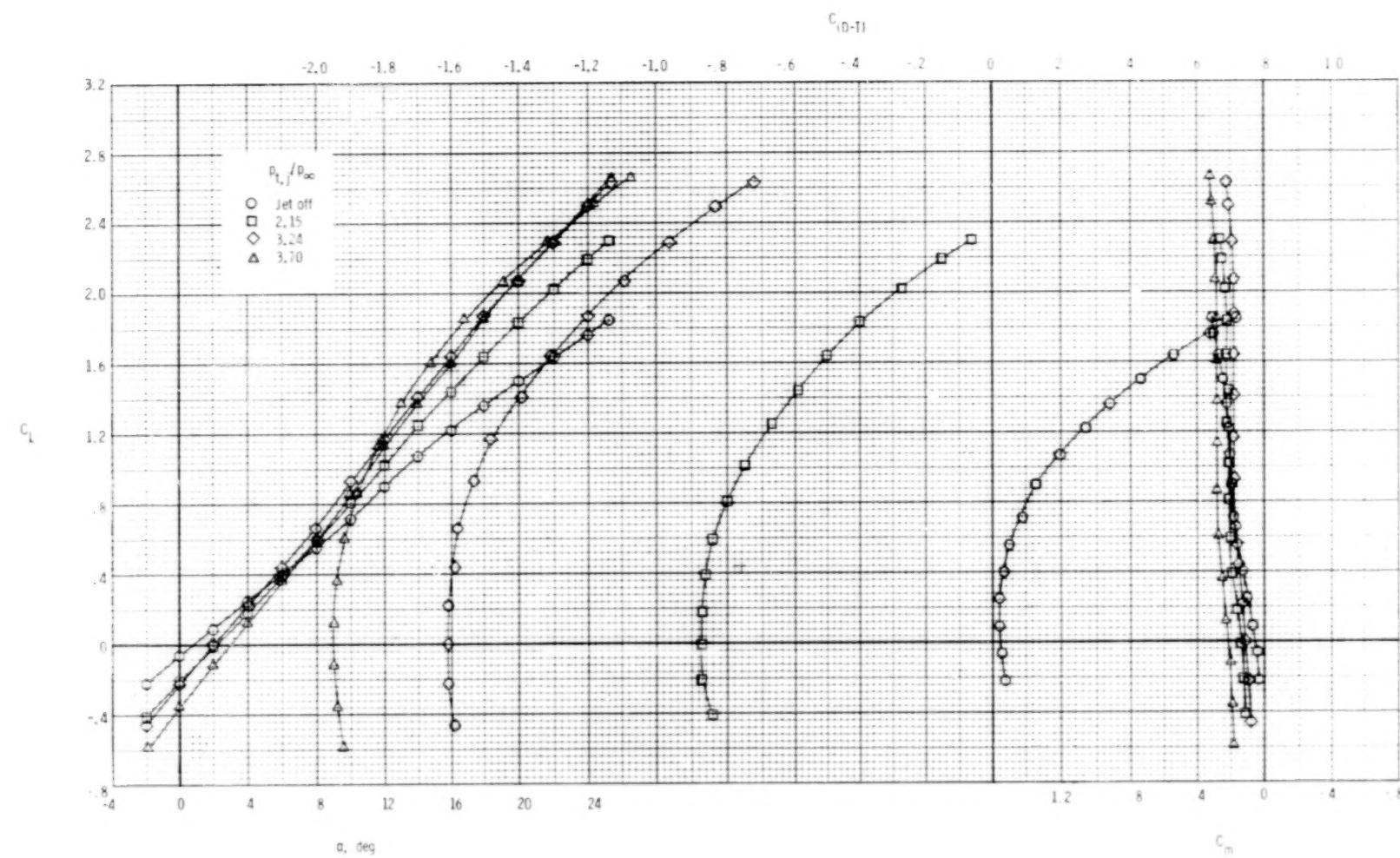
Figure 7.- Continued.

(1) $\delta_{TE} = -10^{\circ}$; $\delta_{LE} = \delta_C = \delta_{C,TE} = 0^{\circ}$; H_2 canard.

Figure 7.- Continued.

(m) $\delta_{TE} = 15^o$; $\delta_{LE} = 0^o$; $\delta_C = 10^o$; $\delta_{C,TE} = 0^o$; H_2 canard.
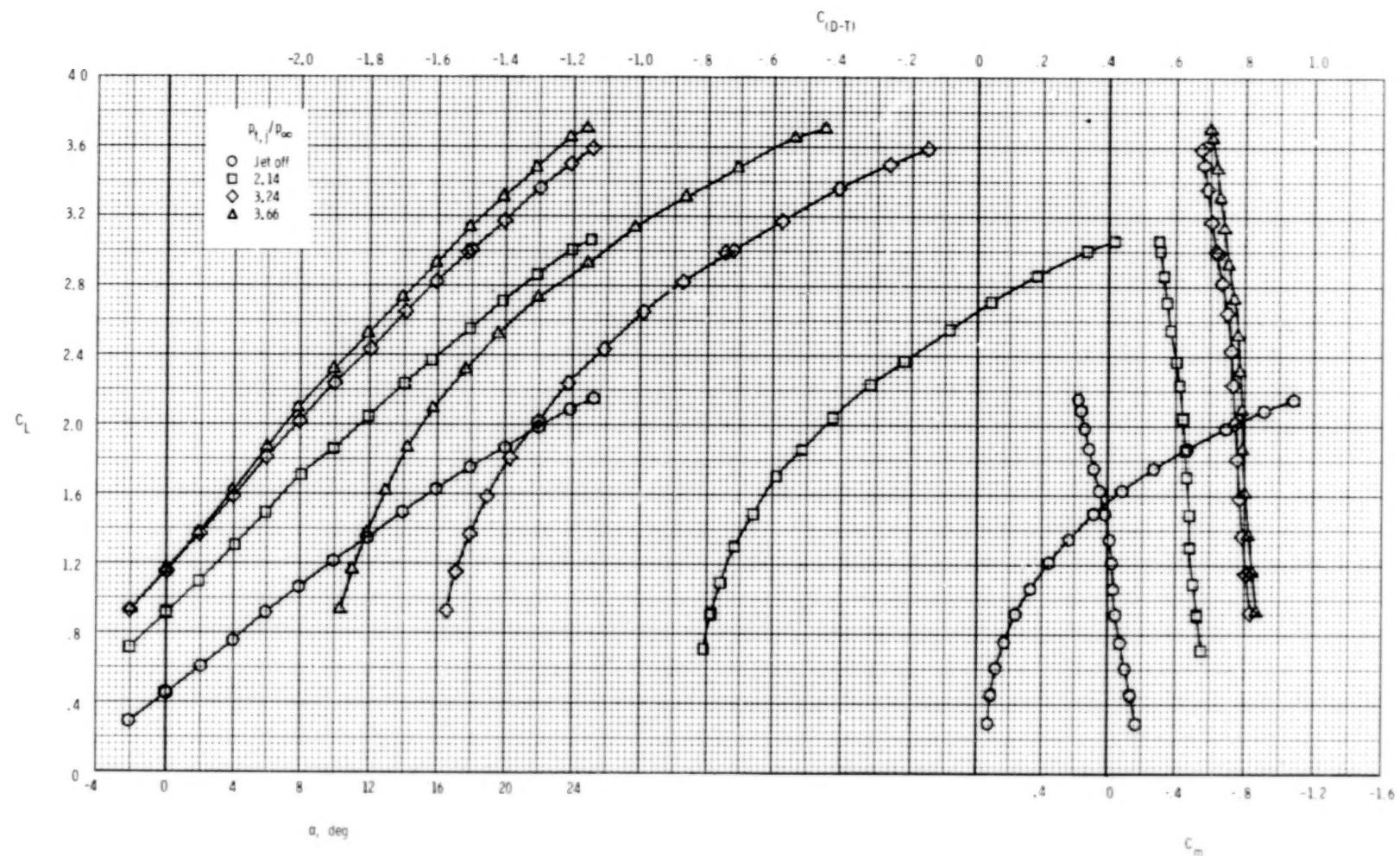
Figure 7.- Continued.

(n) $\delta_{TE} = 15^o$; $\delta_{LE} = 0^o$; $\delta_C = 20^o$; $\delta_{C,TE} = 0^o$; H_2 canard.

Figure 7.- Continued.

(o) $\delta_{TE} = \delta_{LE} = \delta_C = 0^O$; $\delta_{C,TE} = 10^O$; H_2 canard.
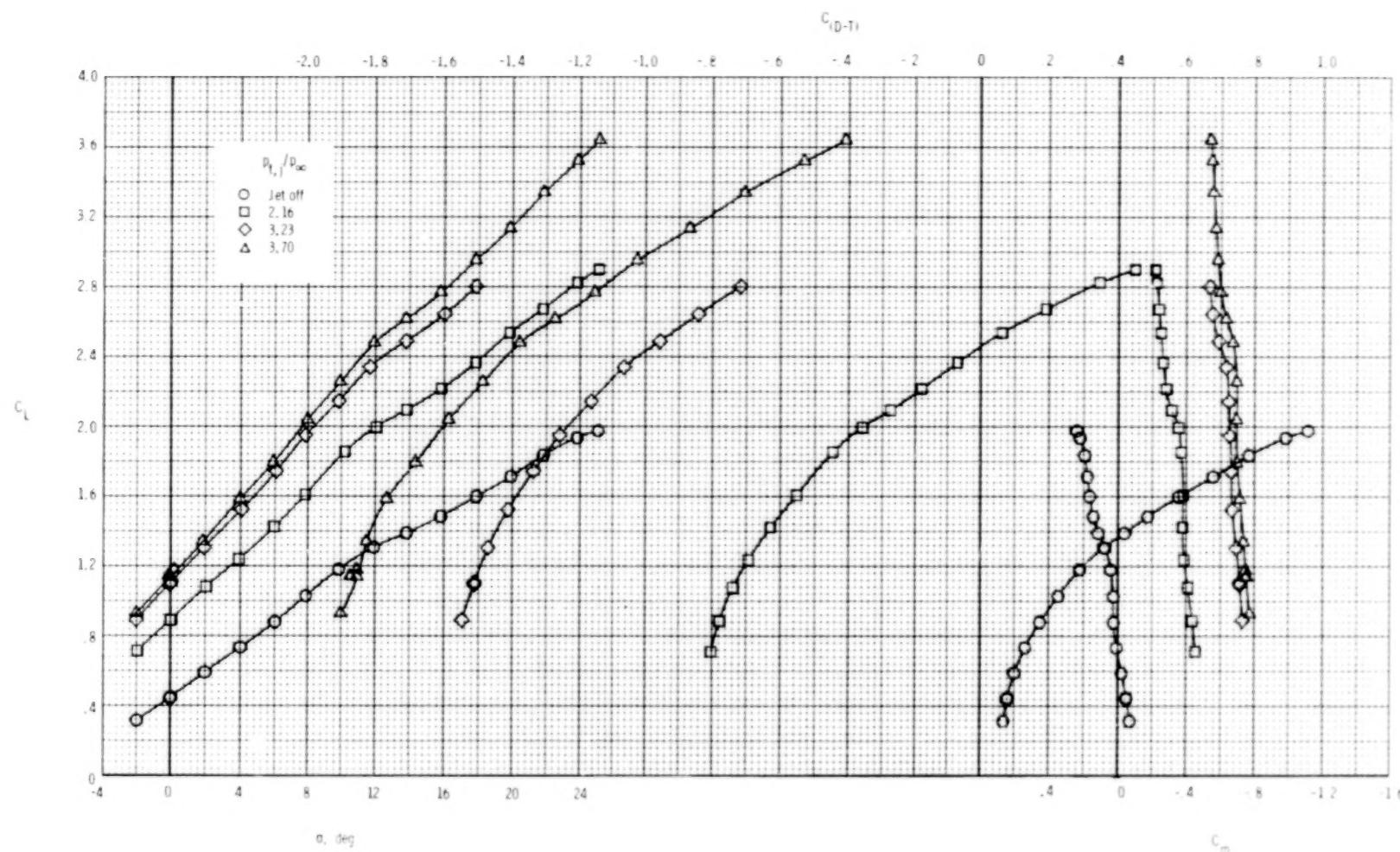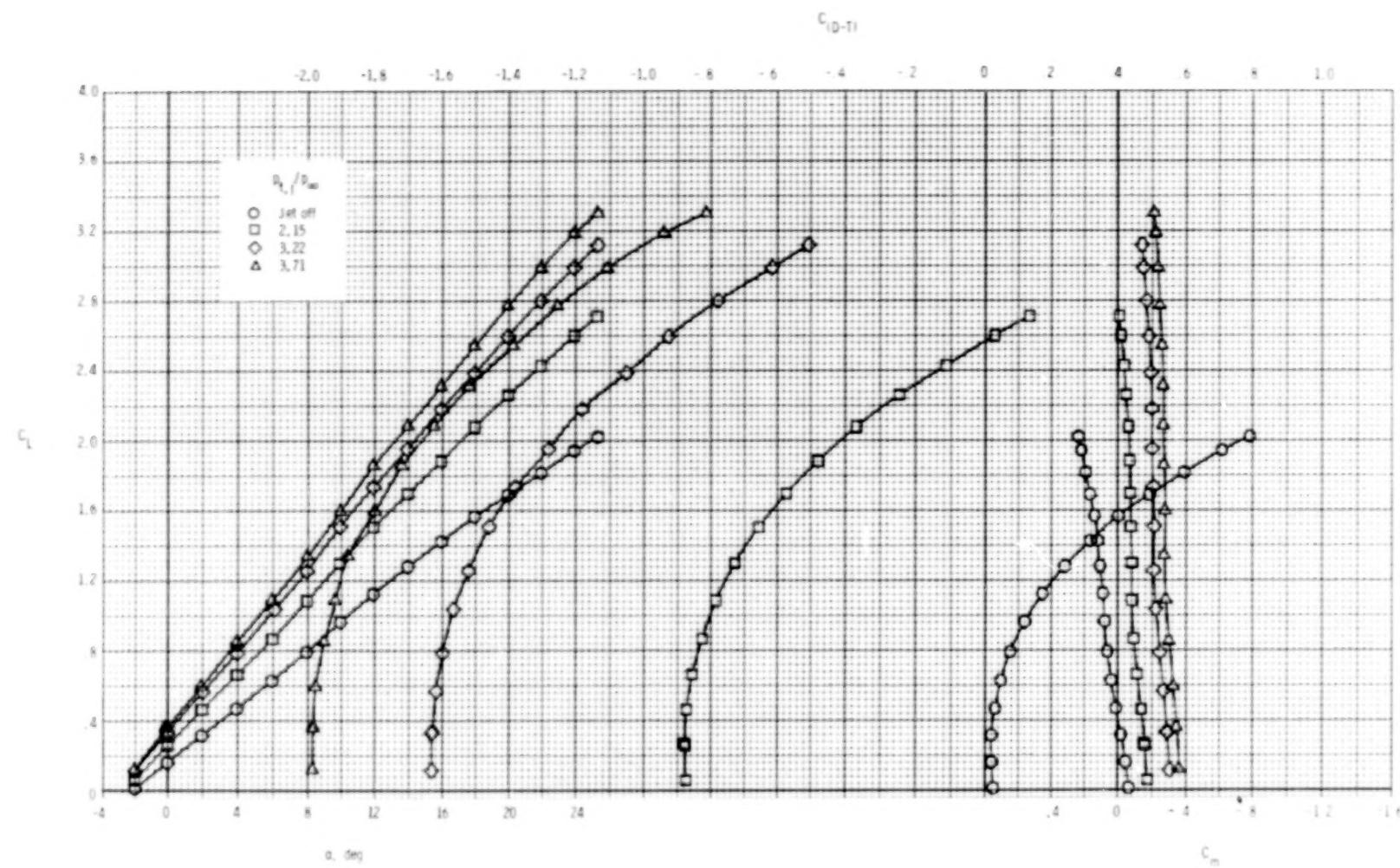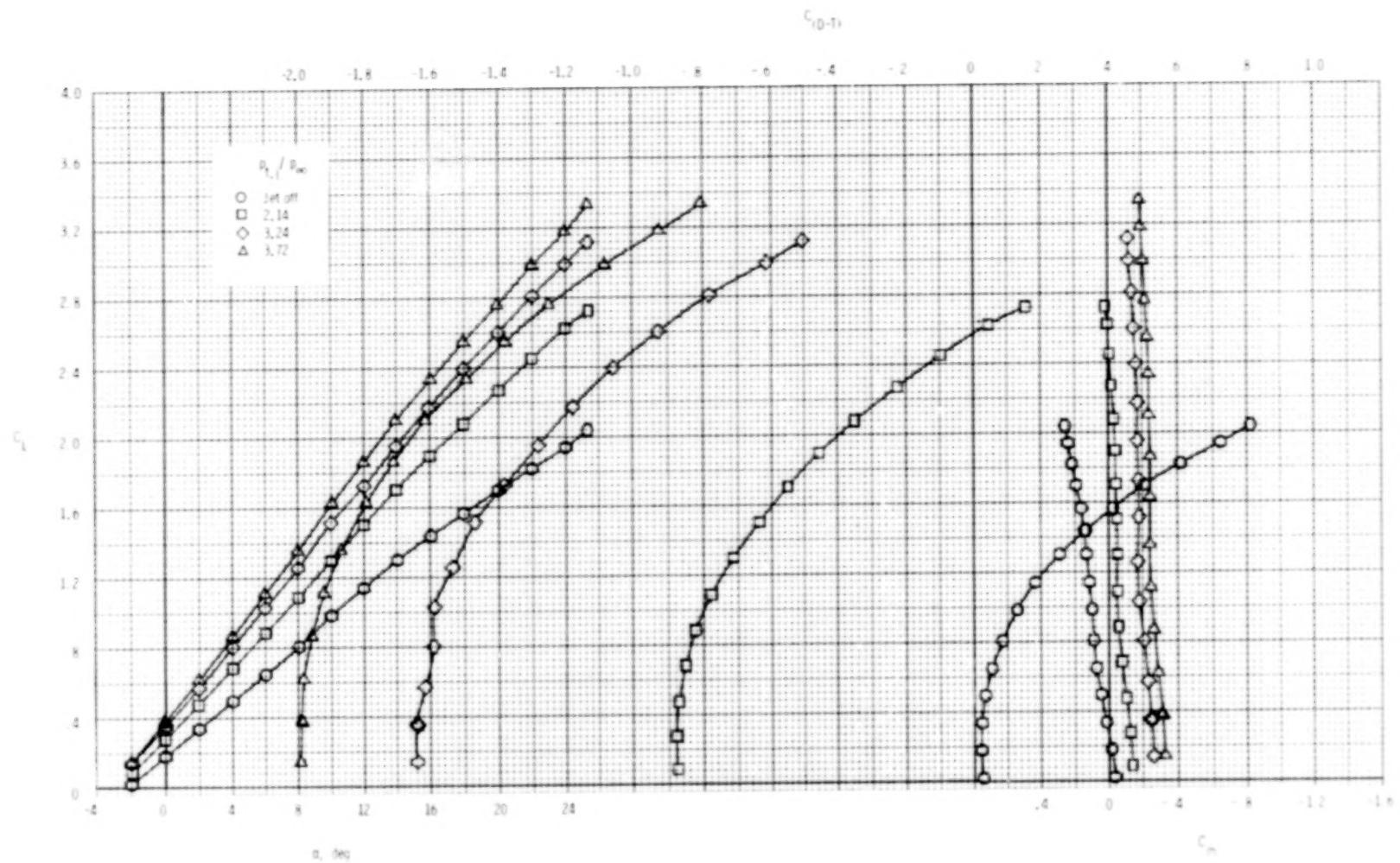
Figure 7.- Continued.

(p) $\delta_{TE} = \delta_{LE} = \delta_C = 0°$; $\delta_{C,TE} = 20°$; H_2 canard.

Figure 7.- Continued.

(q) $\delta_{TE} = \delta_{LE} = \delta_C = 0^O$; $\delta_{C,TE} = 30^O$; H_2 canard.
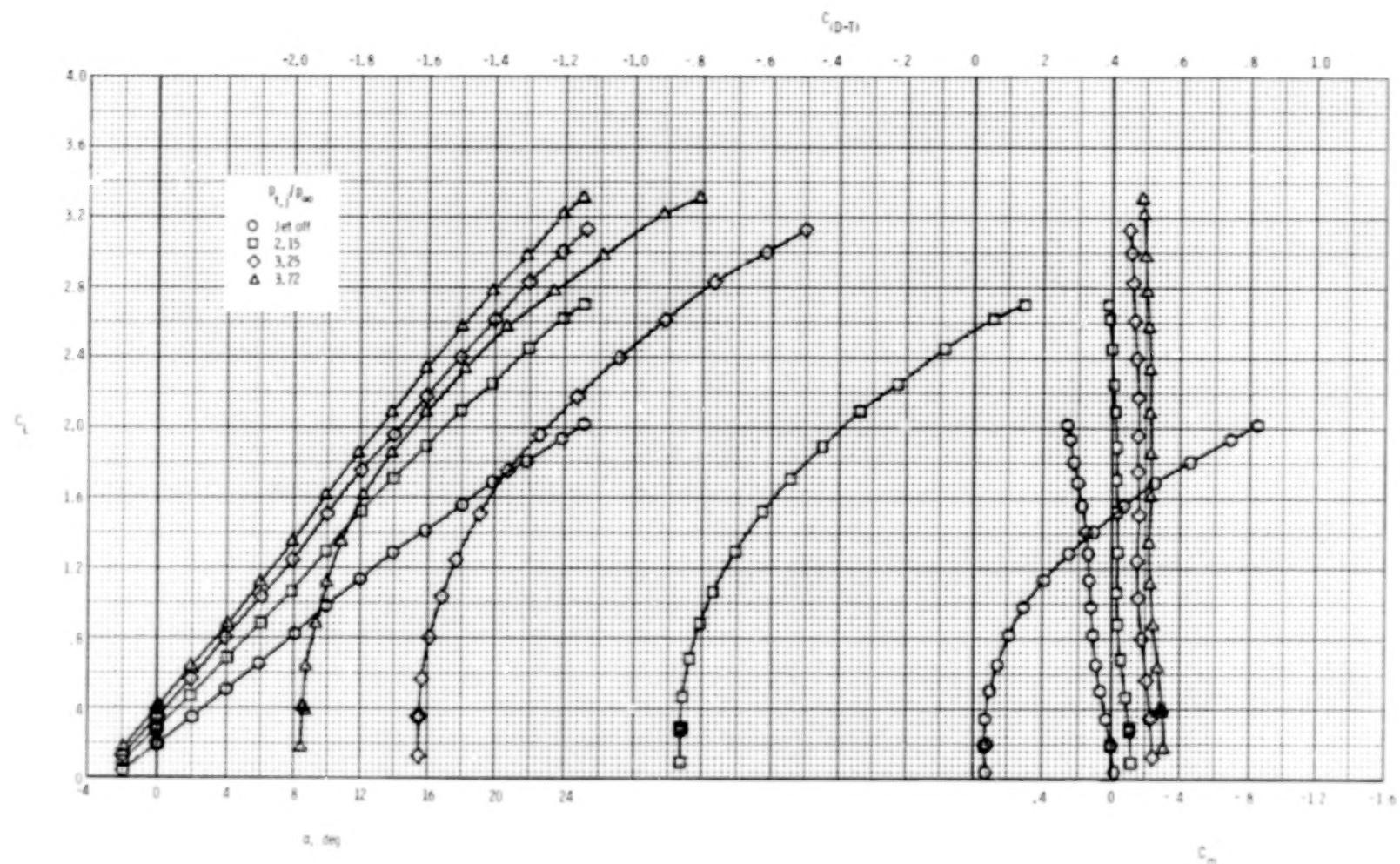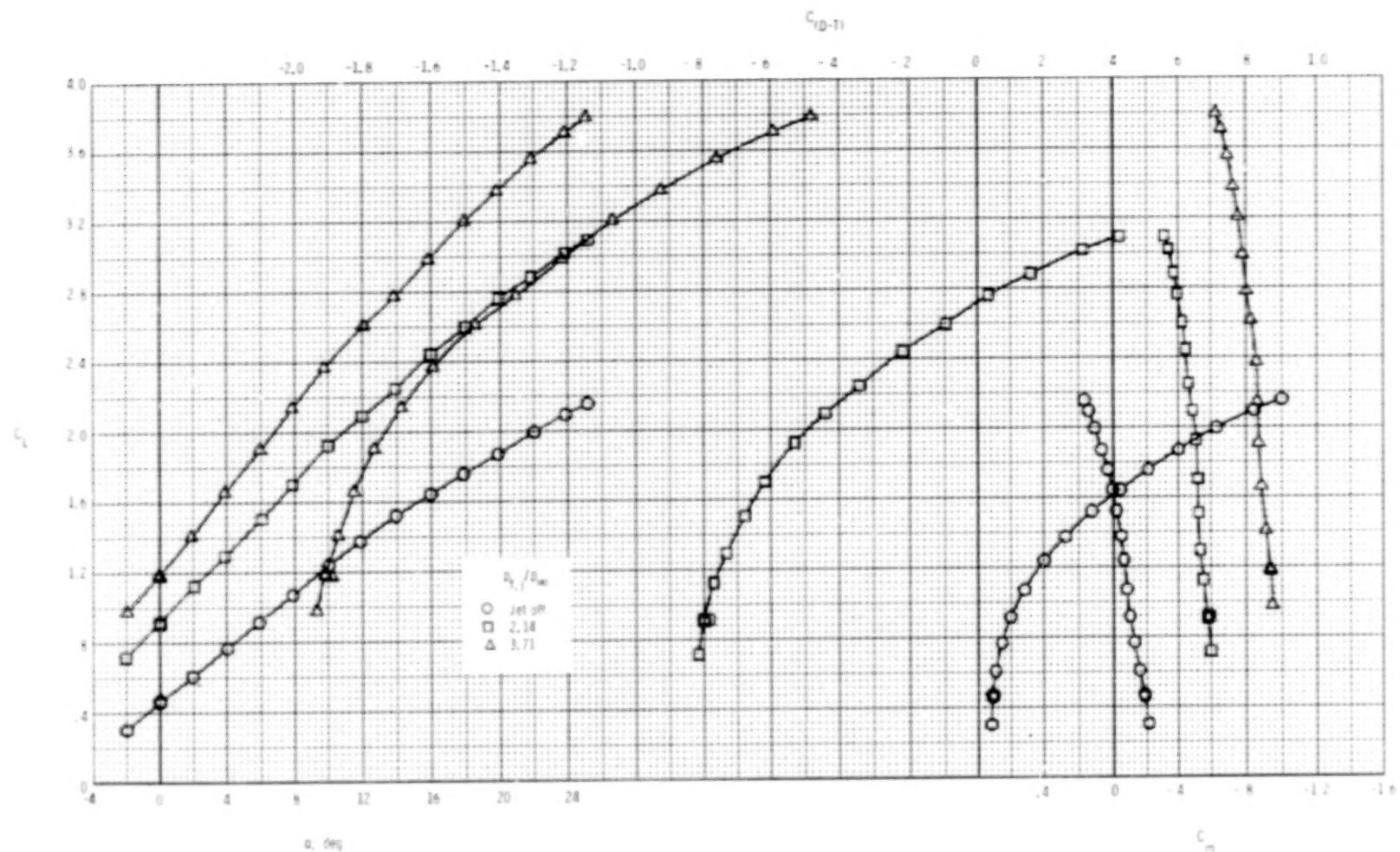
Figure 7.- Continued.

(r) $\delta_{TE} = 15^o$; $\delta_{LE} = \delta_C = 0^o$; $\delta_{C,TE} = 20^o$; H_2 canard.

Figure 7.- Continued.

57

(s) $\delta_{TE} = 15^O$; $\delta_{LE} = 0^O$; $\delta_C = 20^O$; $\delta_{C,TE} = 20^O$; H_2 canard.
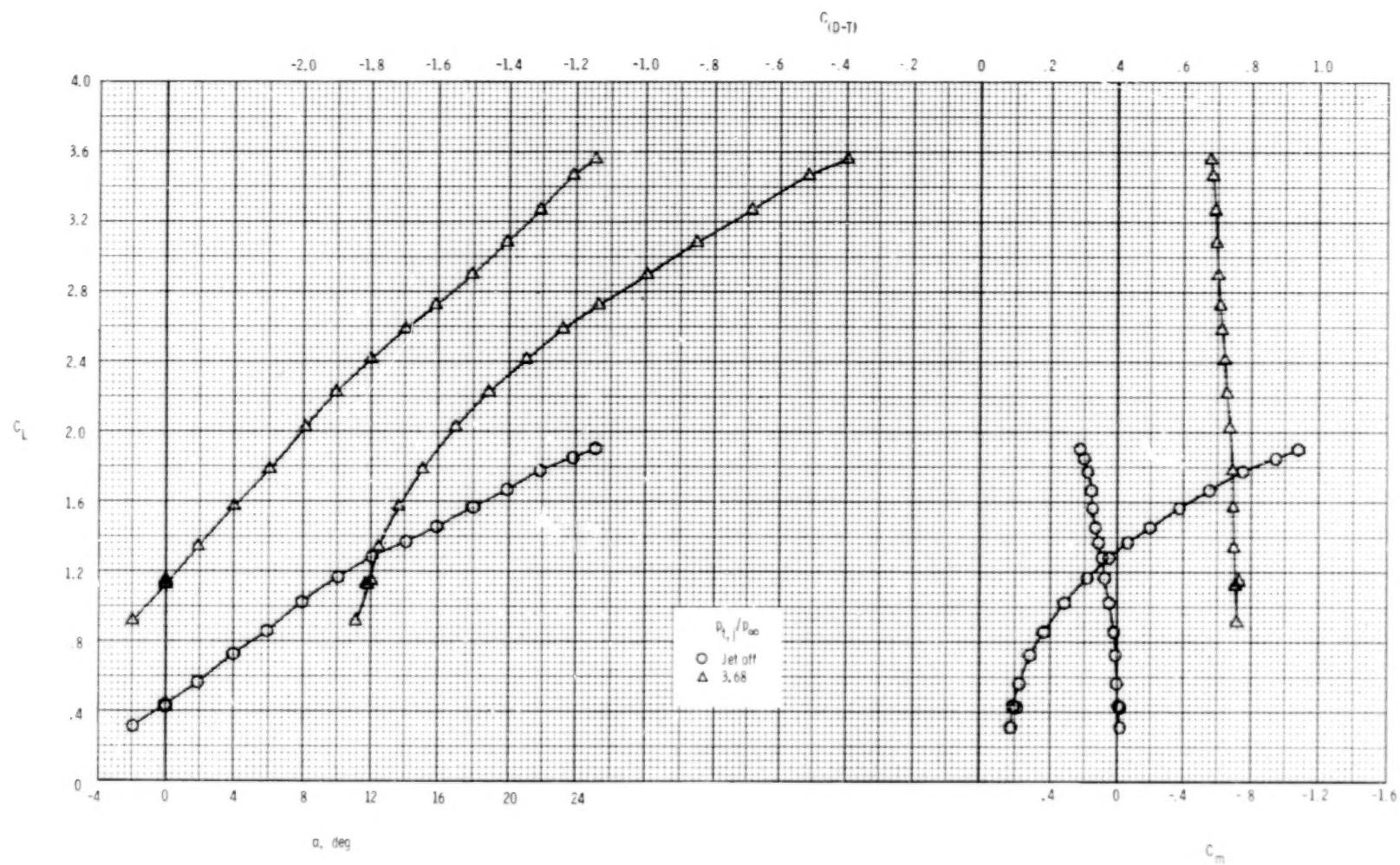
Figure 7.- Continued.

(t) $\delta_{TE} = 15^o$; $\delta_{LE} = \delta_C = \delta_{C,TE} = 0^o$; H_3 canard.
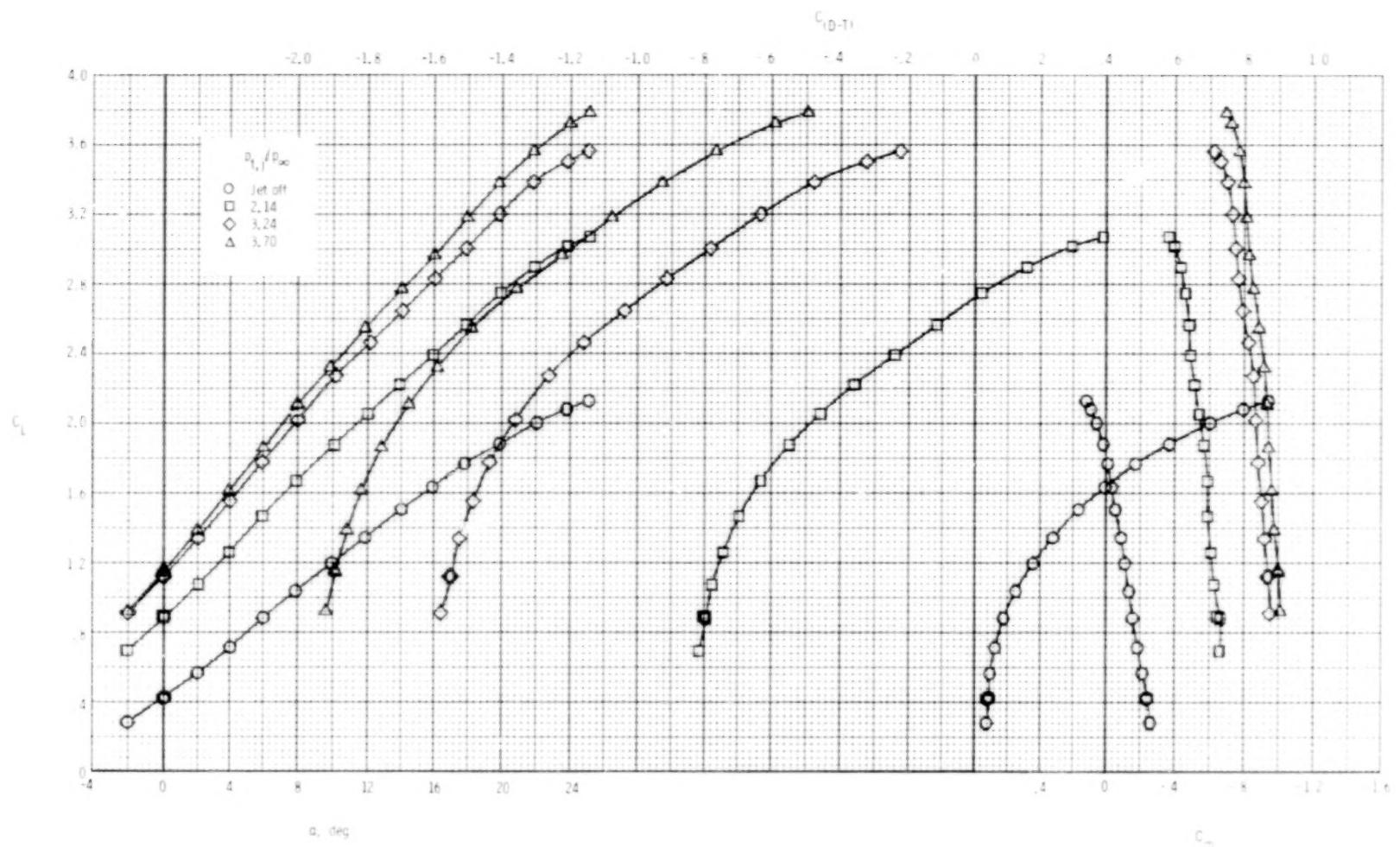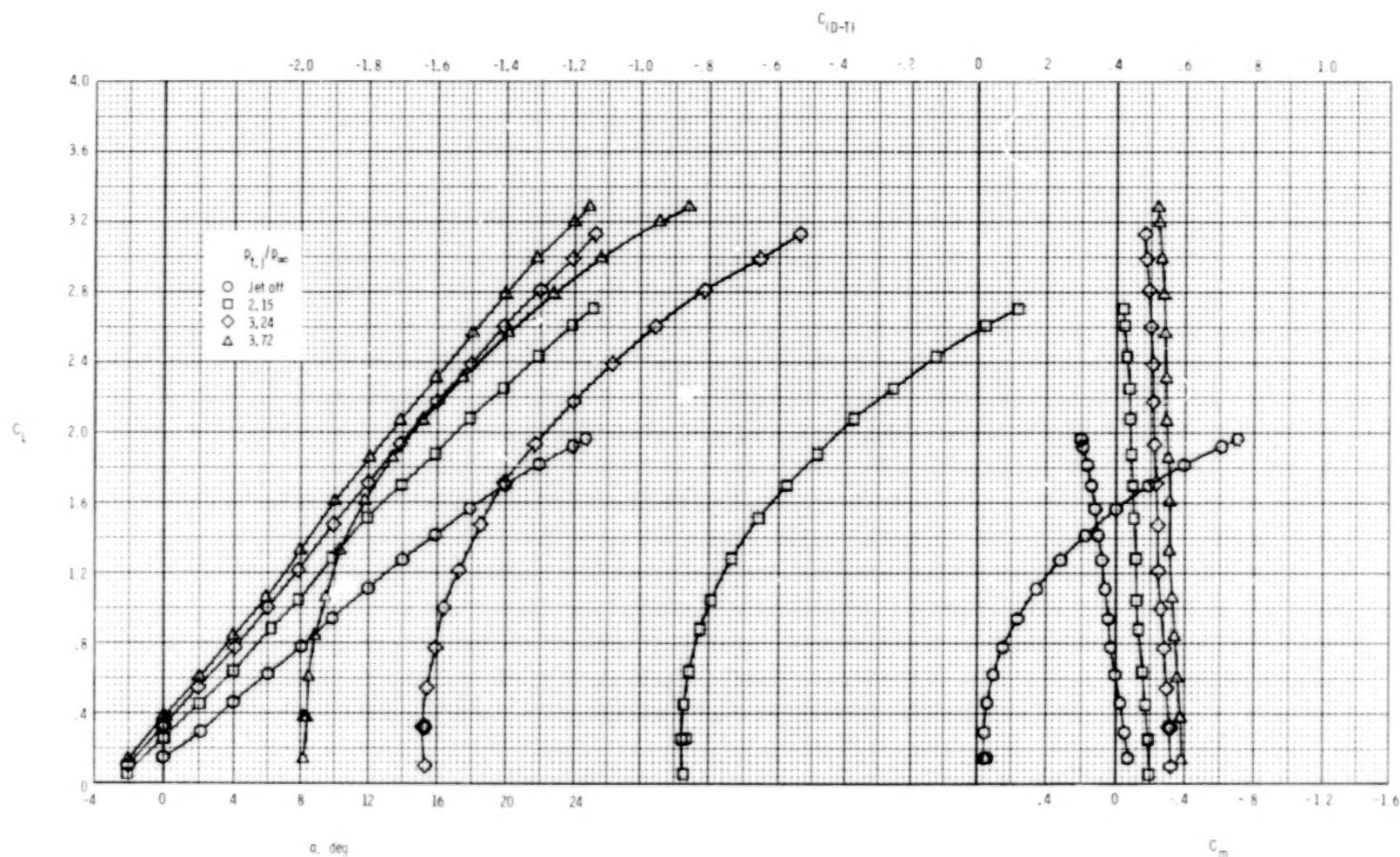
Figure 7.- Continued.

(u) $\delta_{TE} = \delta_{LE} = \delta_C = \delta_{C,TE} = 0^\circ$; H$_3$ canard.

Figure 7.- Concluded.
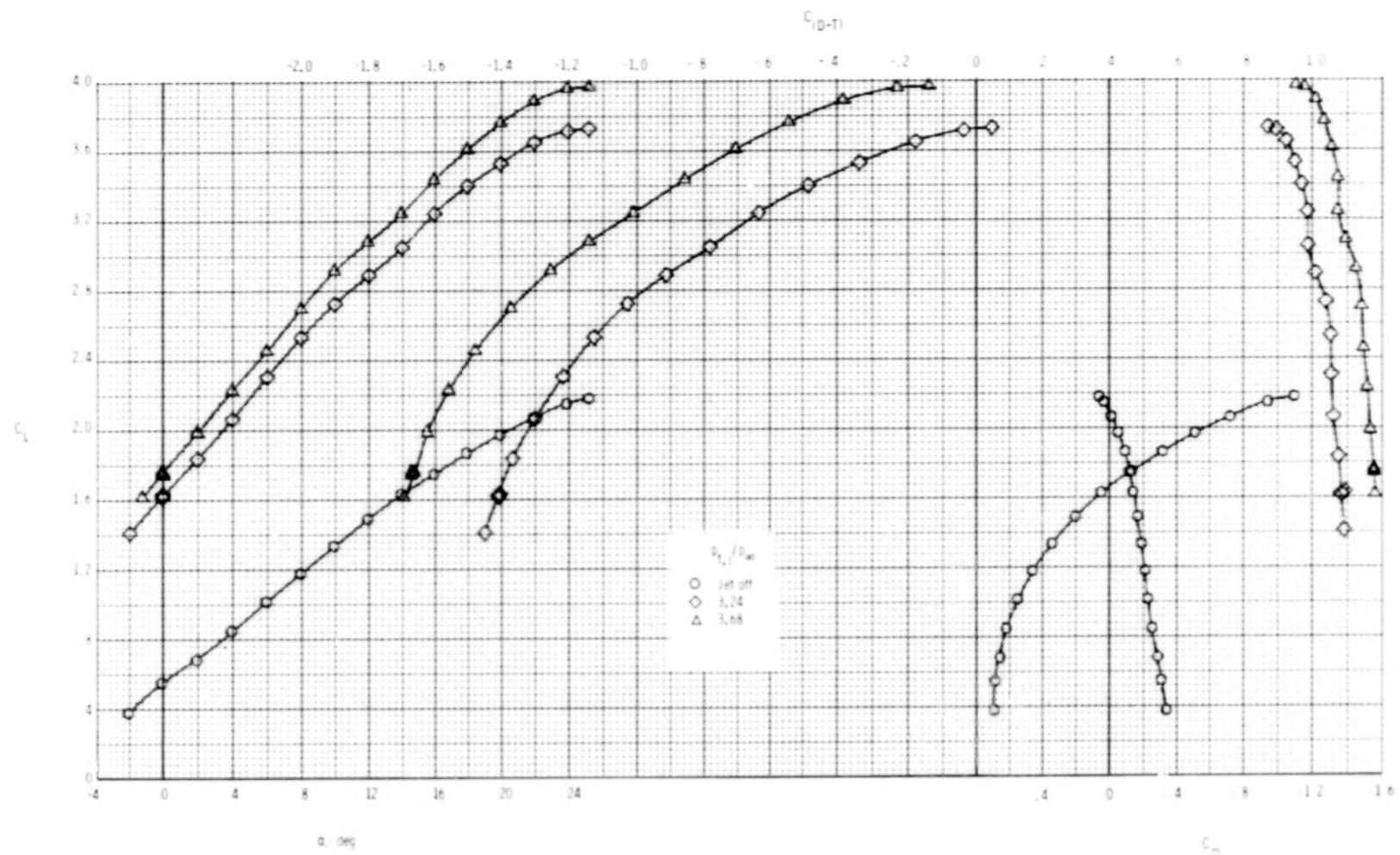
(a) $\delta_{TE} = 30^O$; $\delta_{LE} = \delta_C = \delta_{C,TE} = 0^O$; H_2 canard.

Figure 8.- Basic longitudinal aerodynamic characteristics at $M = 0.186$ for nozzle conf 2.

61

(b) $\delta_{TE} = 35^{\circ}$; $\delta_{LE} = \delta_C = \delta_{C,TE} = 0^{\circ}$; H_2 canard.

Figure 8.- Continued.

(c) $\delta_{TE} = 35^o$; $\delta_{LE} = 0^o$; $\delta_C = 20^o$; $\delta_{C,TE} = 0^o$; H_2 canard.

Figure 8.- Continued.

(d) $\delta_{TE} = 30^o$; $\delta_{LE} = \delta_C = \delta_{C,TE} = 0^o$; H_3 canard.

Figure 8.- Continued.

(e) $\delta_{TE} = 30^o$; $\delta_{LE} = 0^o$; $\delta_C = 20^o$; $\delta_{C,TE} = 0^o$; H_3 canard.
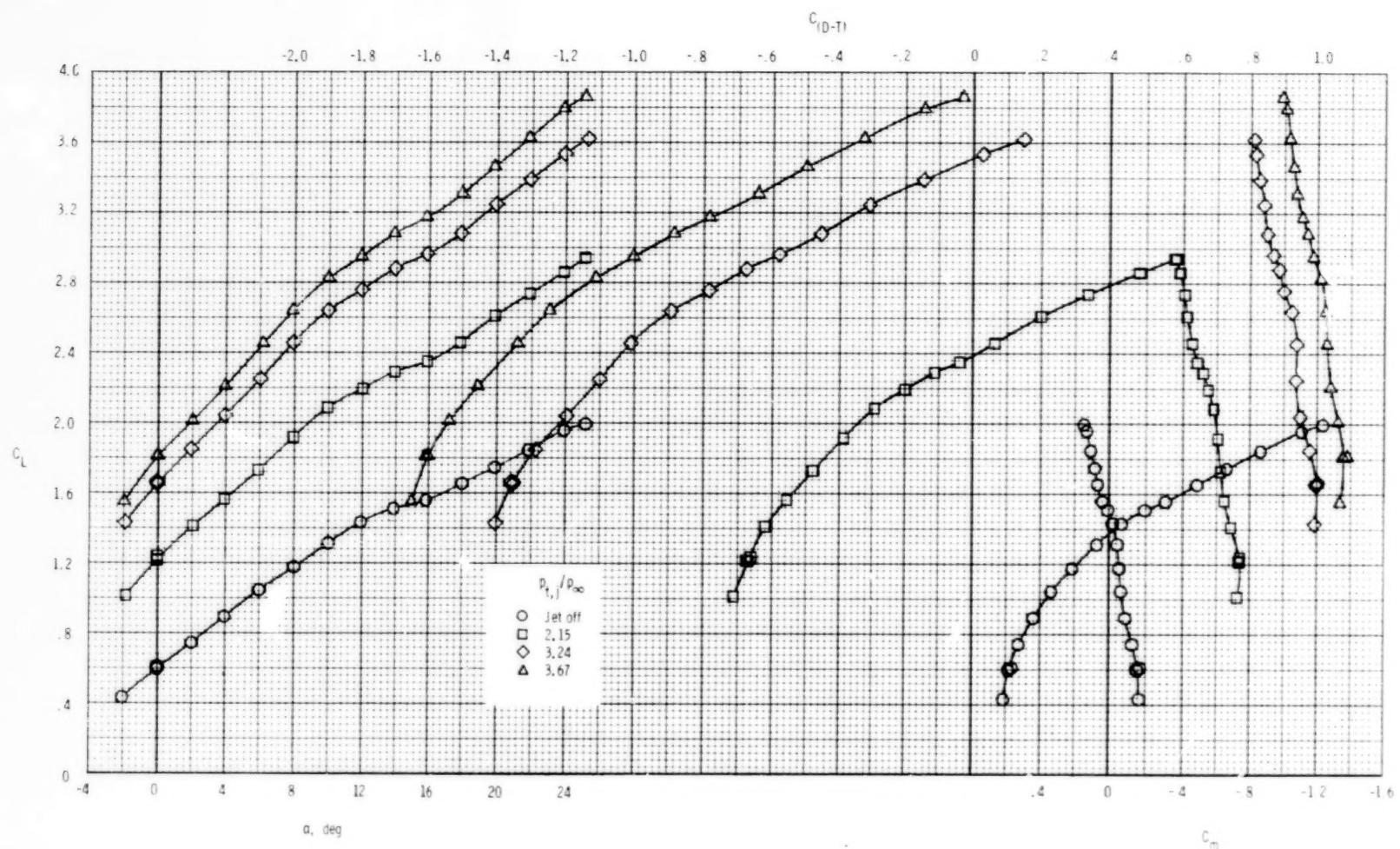
Figure 8.- Continued.

(f) $\delta_{TE} = 30^O$; $\delta_{LE} = 20^O$; $\delta_C = \delta_{C,TE} = 0^O$; H_2 canard.

Figure 8.- Continued.

(g) $\delta_{TE} = 30^{\circ}$; $\delta_{LE} = 20^{\circ}$; $\delta_{C} = 20^{\circ}$; $\delta_{C,TE} = 0^{\circ}$; H_2 canard.

Figure 8.- Continued.

(h) $\delta_{TE} = 30^o$; $\delta_{LE} = 0^o$; canard off.

Figure 8.- Concluded.

Figure 9.- Basic longitudinal aerodynamic characteristics at M = 0.186 for nozzle conf 3. $\delta_{TE} = 30^O$; $\delta_{LE} = \delta_C = \delta_{C,TE} = 0^O$; H_2 canard.
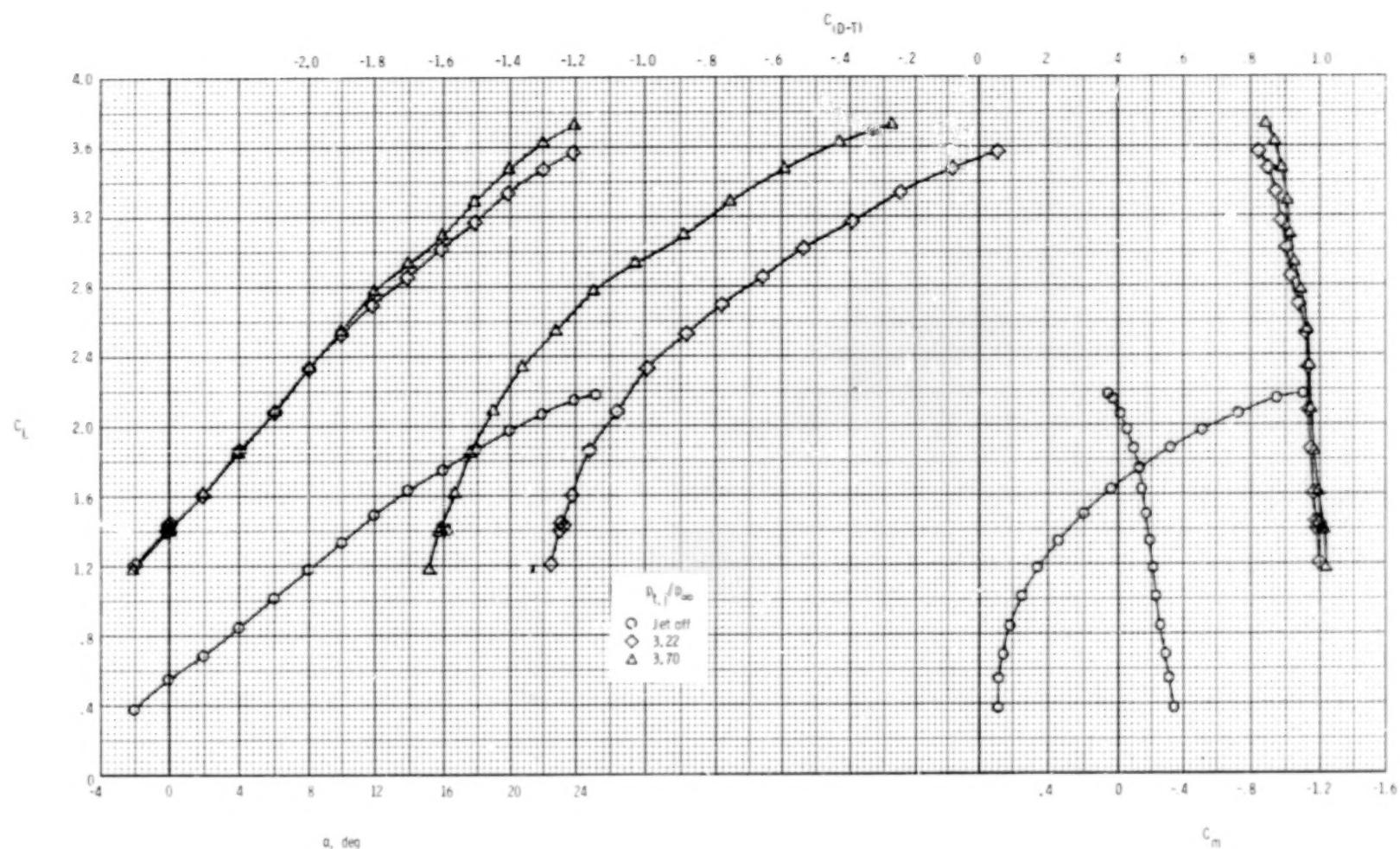
Figure 10.- Basic longitudinal aerodynamic characteristics at $M = 0.186$ for nozzle conf 4. $\delta_{TE} = 30^o$; $\delta_{LE} = \delta_C = \delta_{C,TE} = 0^o$; H_2 canard.
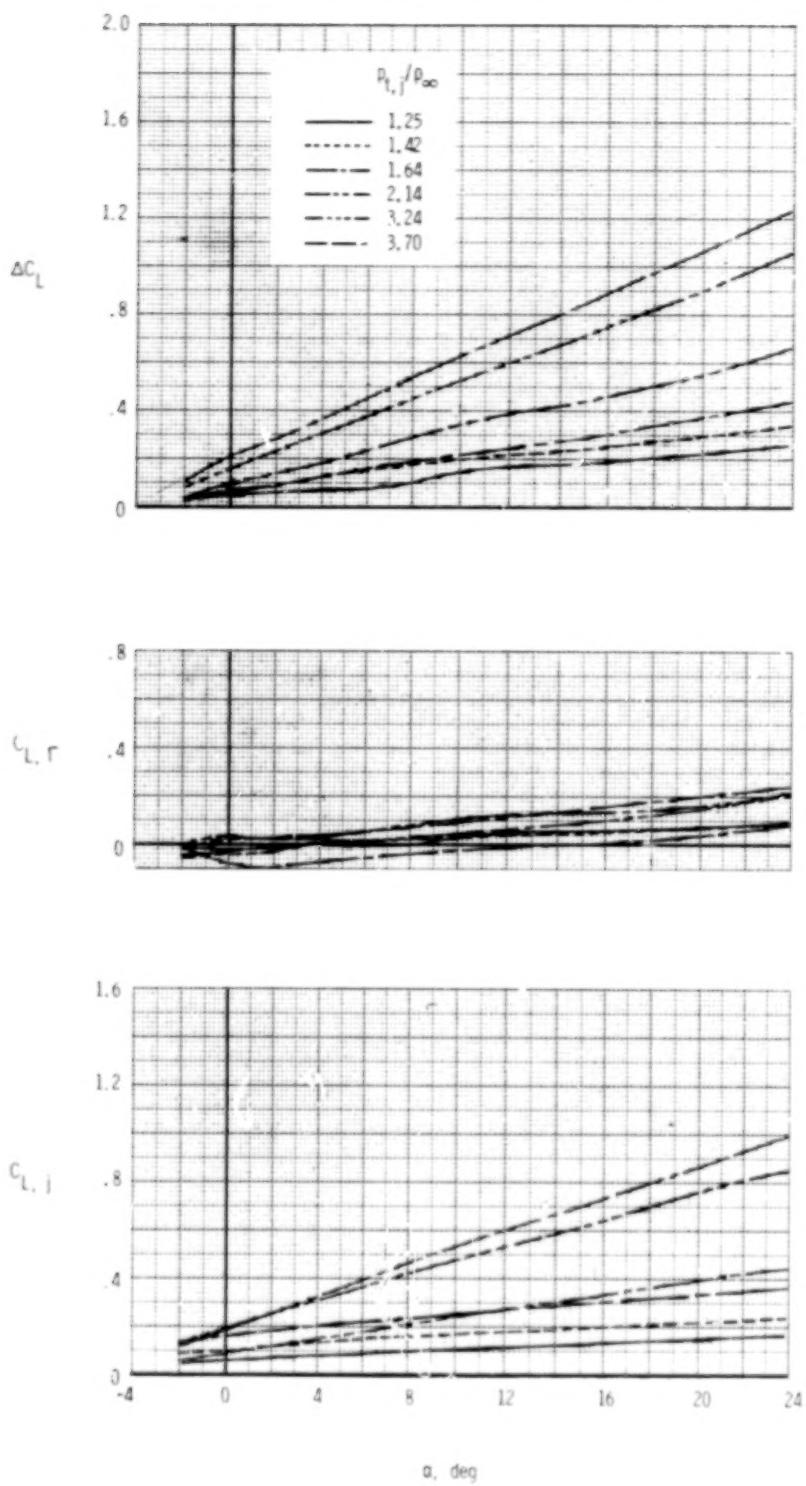
(a) $\delta_{TE} = 0^{\circ}$.

Figure 11.- Incremental lift characteristics at M = 0.186 for nozzle conf 1.
$\delta_{LE} = \delta_C = \delta_{C,TE} = 0^{\circ}$; H_2 canard.
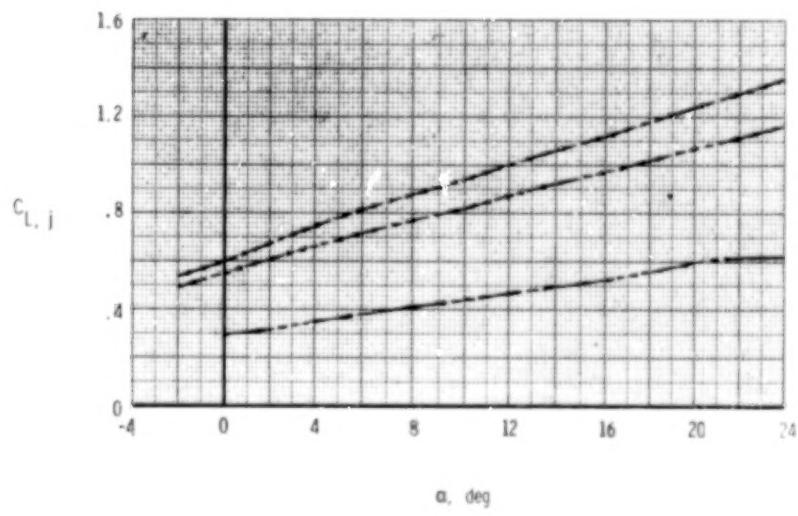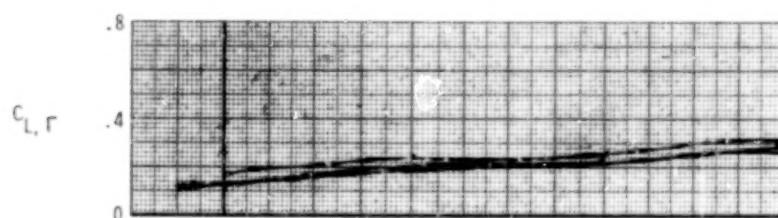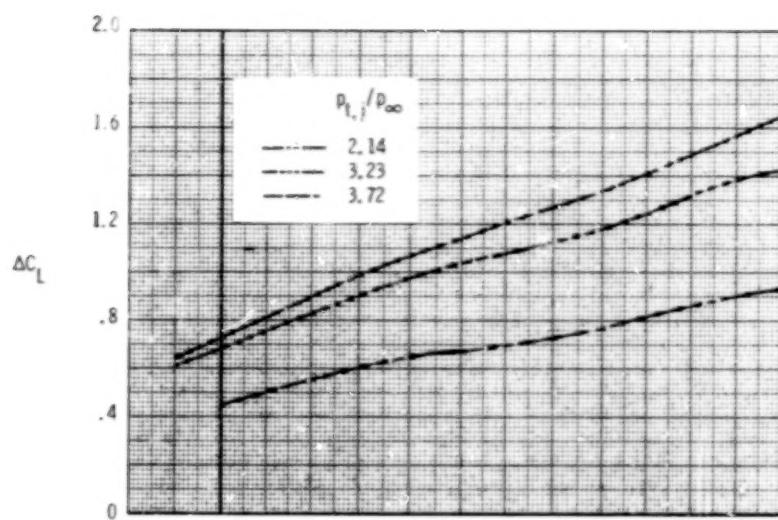
(b) $\delta_{TE} = 15°$.

Figure 11.- Continued.
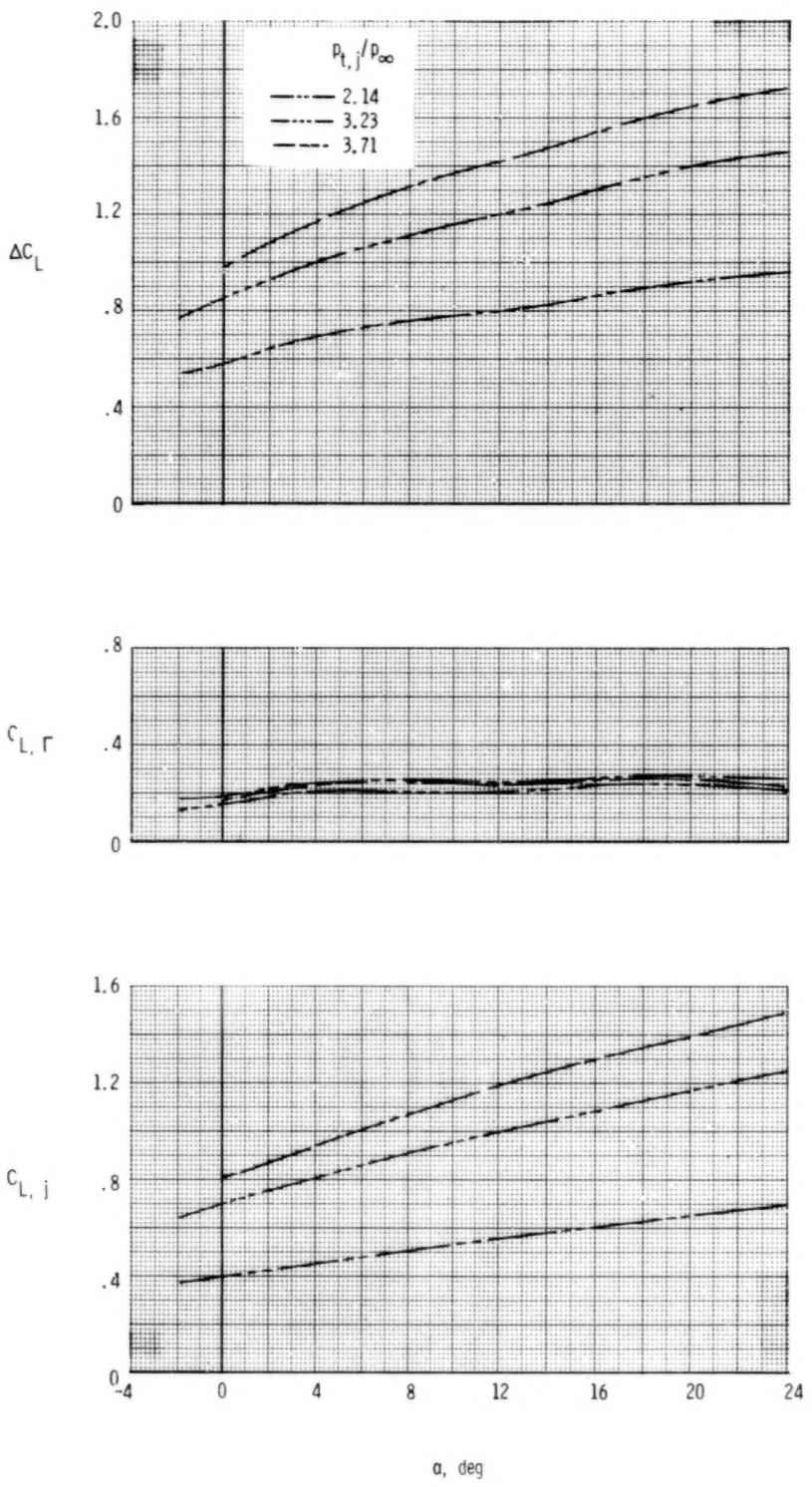
(c) $\delta_{TE} = 25^{\circ}$.

Figure 11.- Continued.
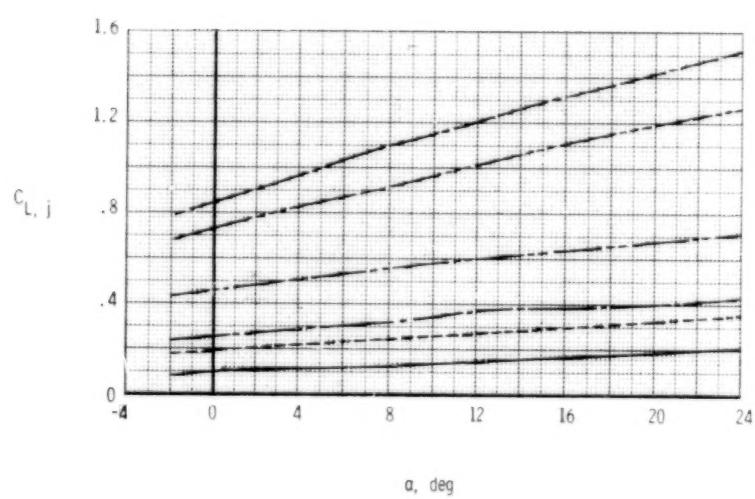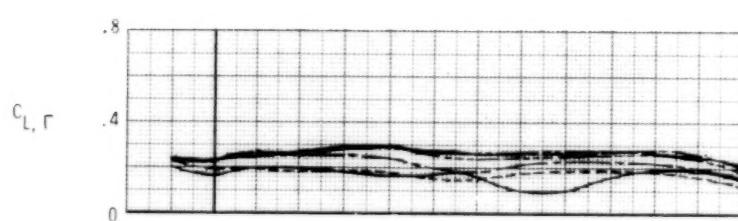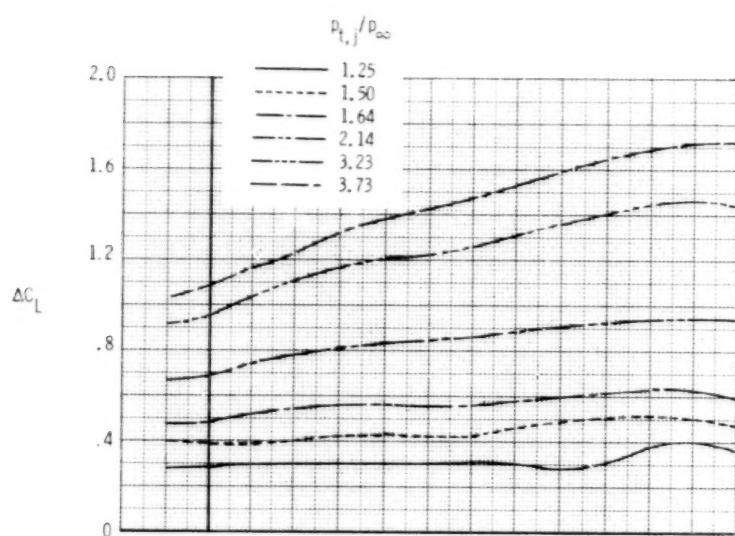
(d) $\delta_{TE} = 30^o$.

Figure 11.- Continued.
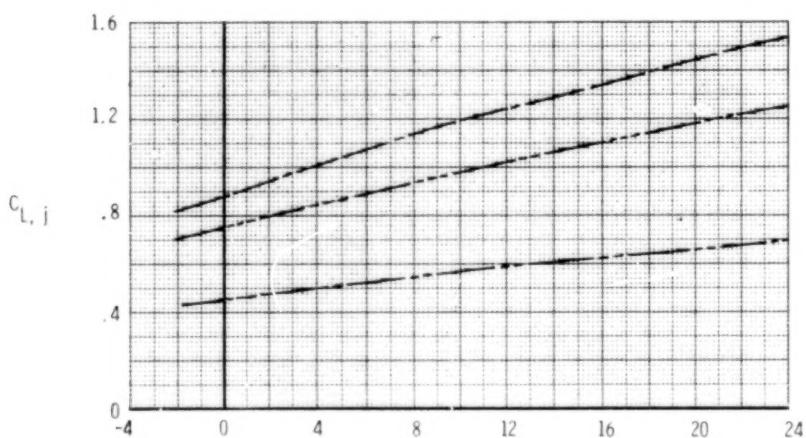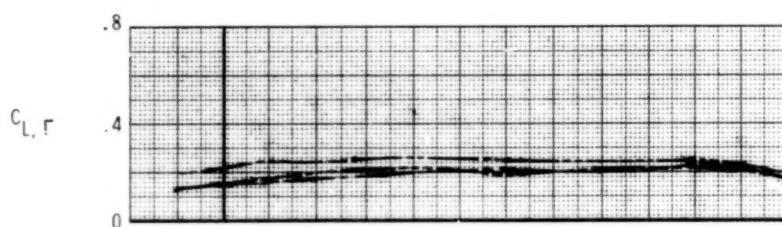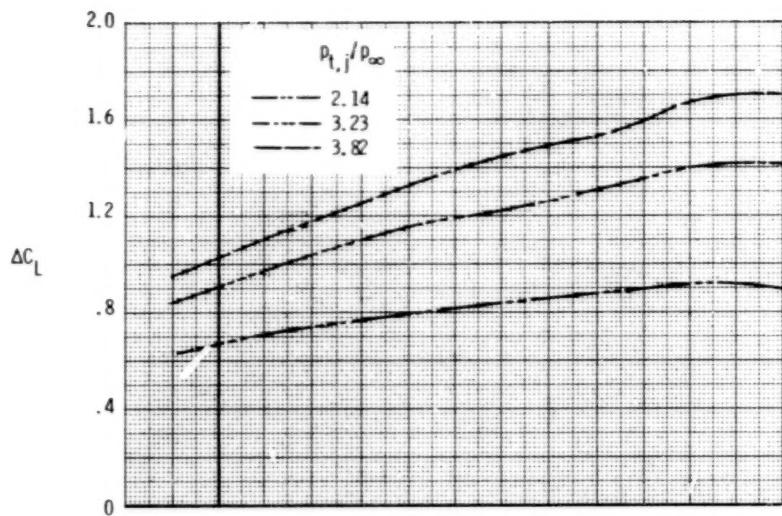
(e) $\delta_{TE} = 35^o$.

Figure 11.- Concluded.
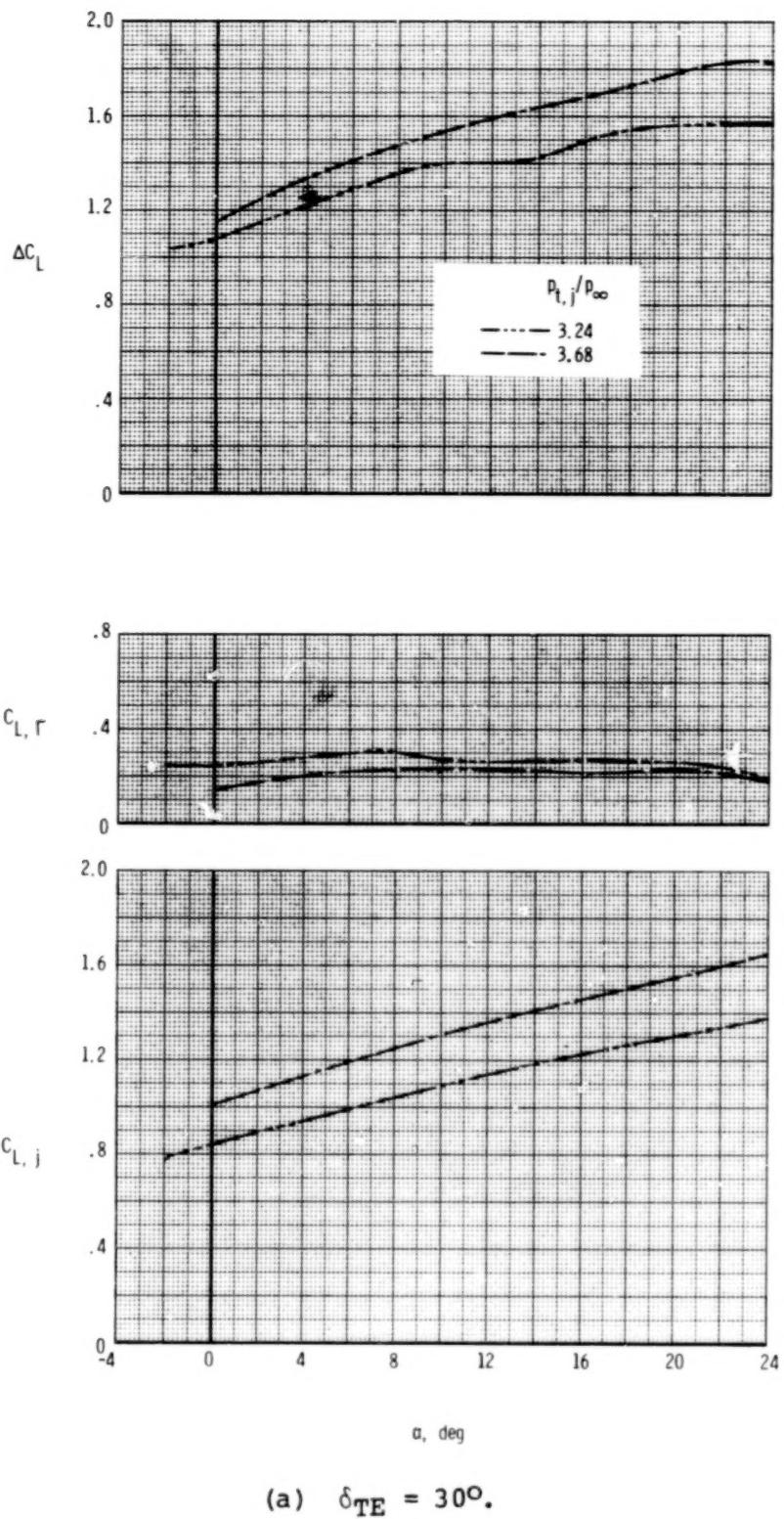
(a) $\delta_{TE} = 30°$.

Figure 12.- Incremental lift characteristics at $M = 0.186$ for nozzle conf 2.
$\delta_{LE} = \delta_C = \delta_{C,TE} = 0°$; H_2 canard.
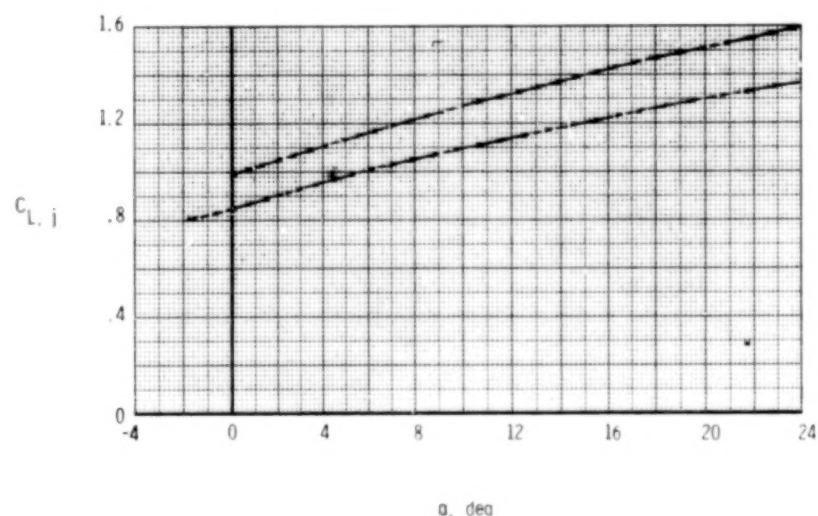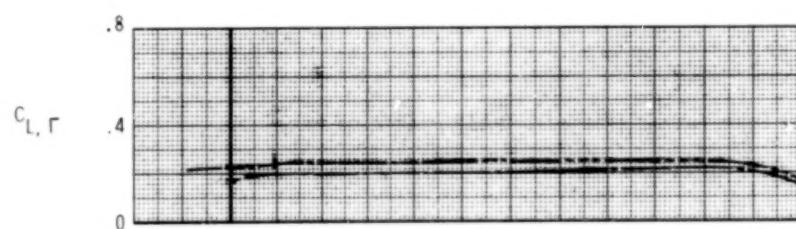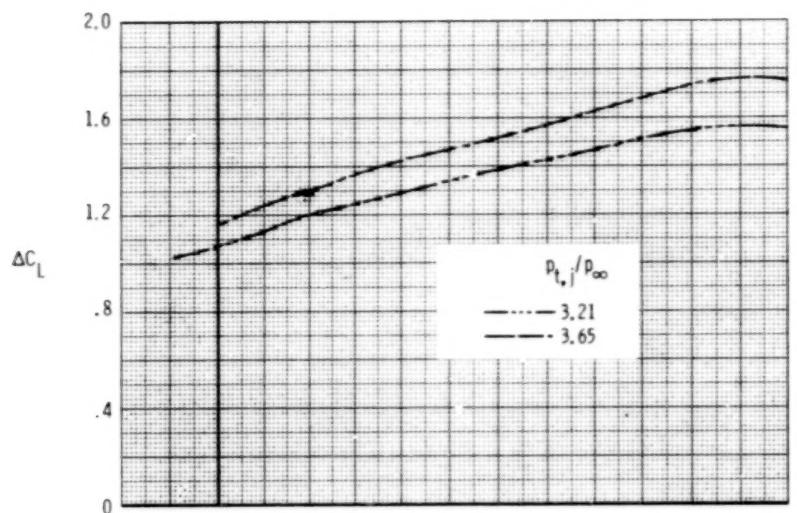
(b) $\delta_{TE} = 35^{O}$.

Figure 12.- Concluded.
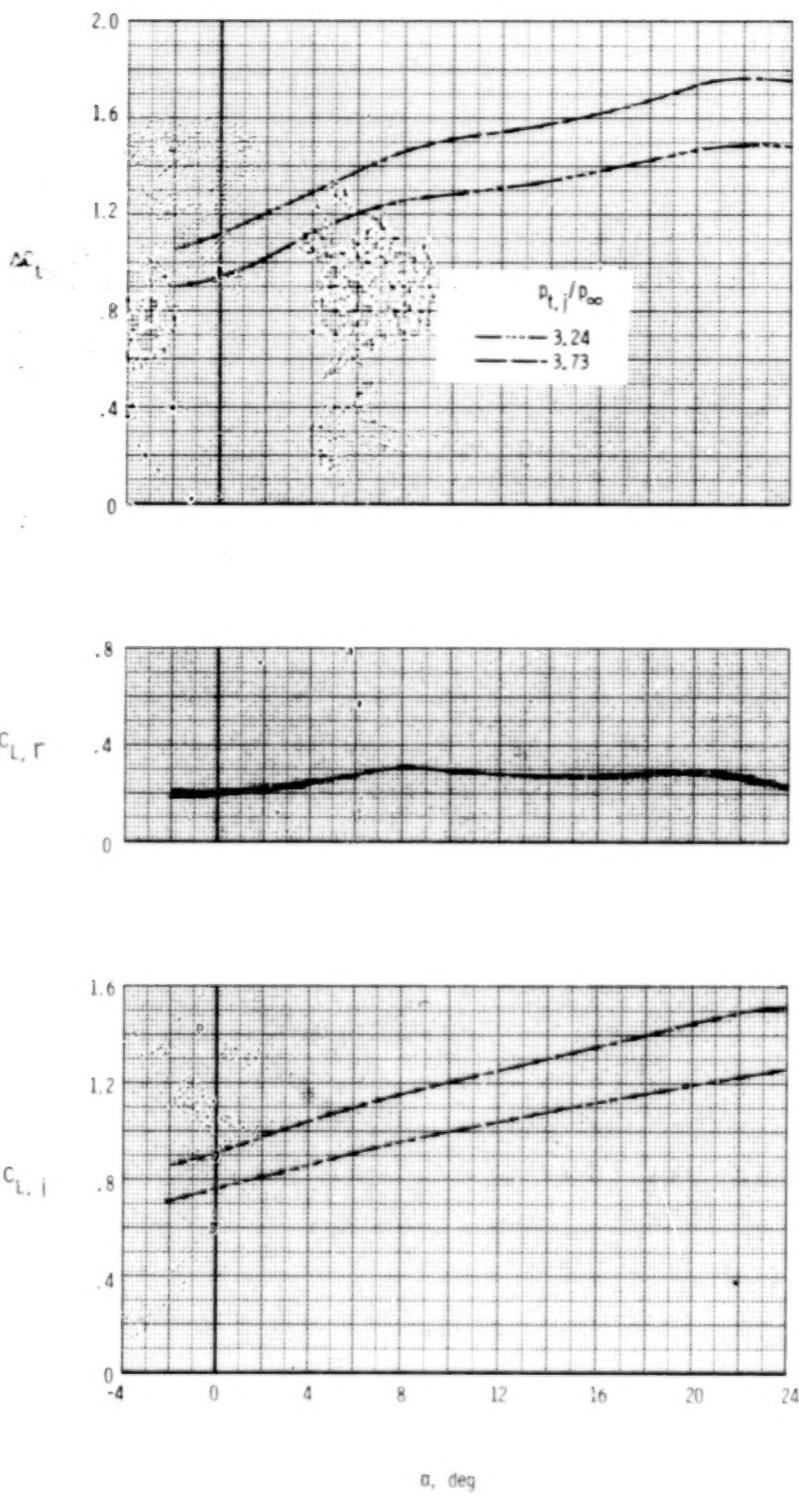
Figure 13.- Incremental lift characteristics at $M = 0.186$ for nozzle conf 3. $\delta_{TE} = 30^O$; $\delta_{LE} = \delta_C = \delta_{C,TE} = 0^O$; H_2 canard.
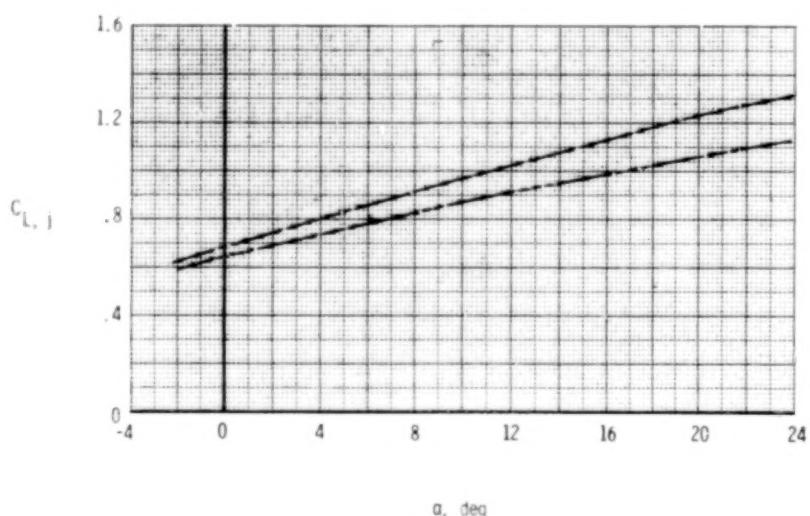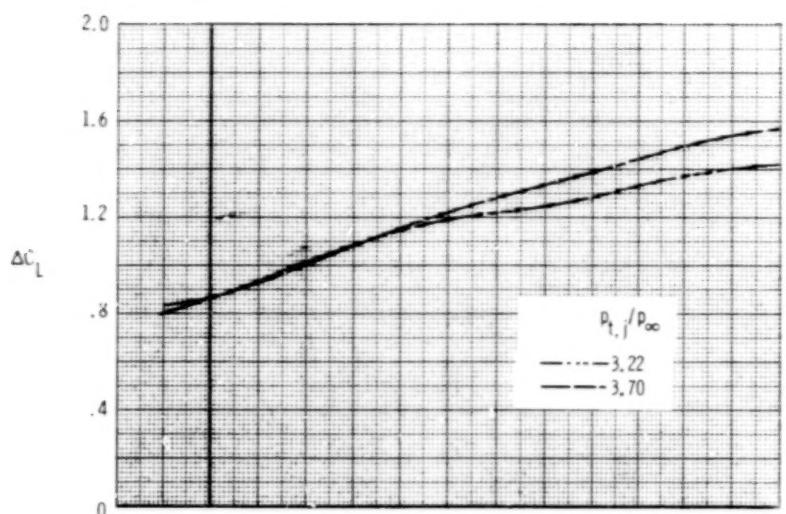
Figure 14.- Incremental lift characteristics at M = 0.186 for nozzle conf 4. $\delta_{TE} = 30^O$; $\delta_{LE} = \delta_C = \delta_{C,TE} = 0^O$; H_2 canard.
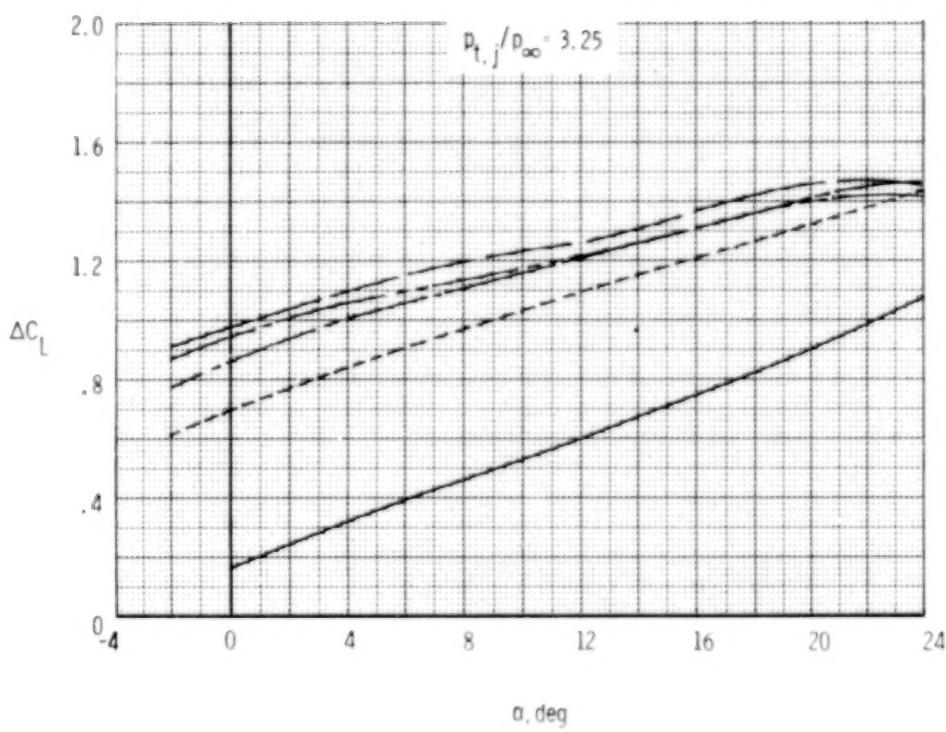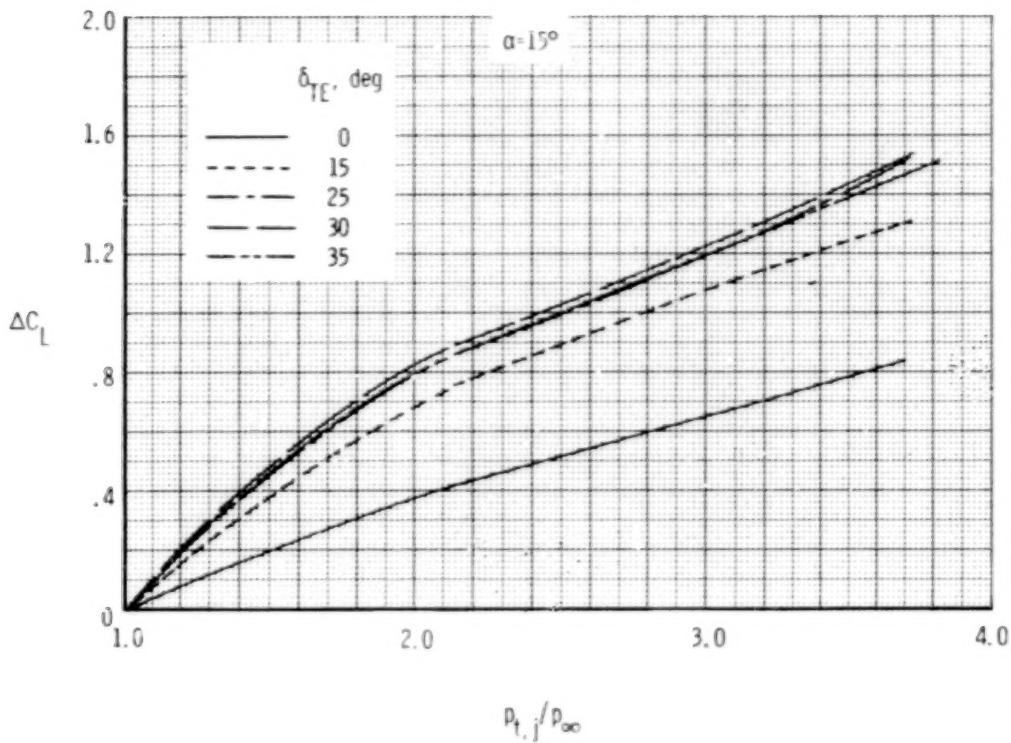
Figure 15.- Summary of incremental lift characteristics for several trailing-edge flap deflections for nozzle conf 1 at M = 0.186. $\delta_{LE} = \delta_C = \delta_{C,TE} = 0^O$; H_2 canard.
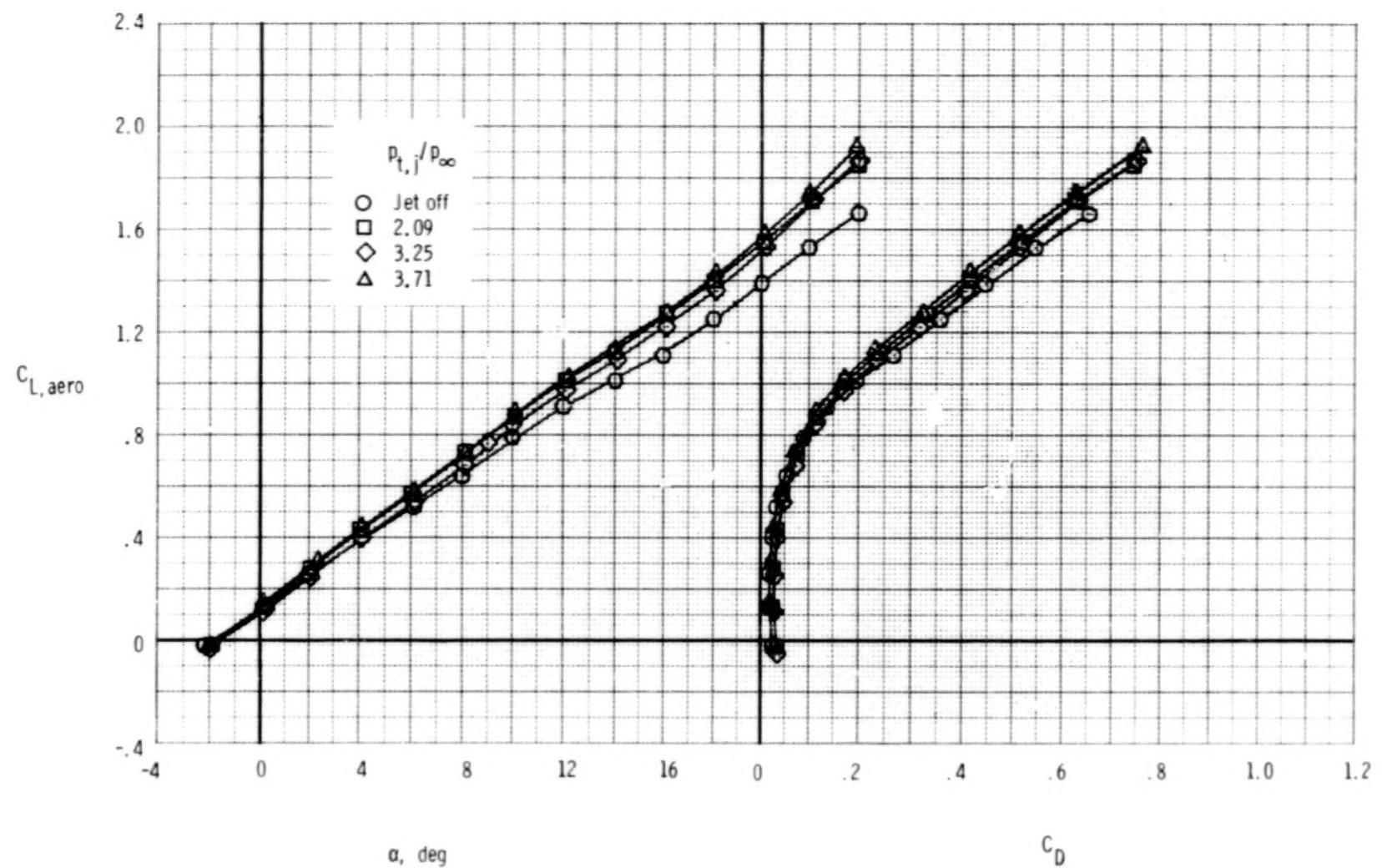
(a) $\delta_{TE} = \delta_{LE} = 0^{\circ}$; canard off.

Figure 16.- Thrust-removed lift and drag characteristics at M = 0.186 for nozzle conf 1.

81
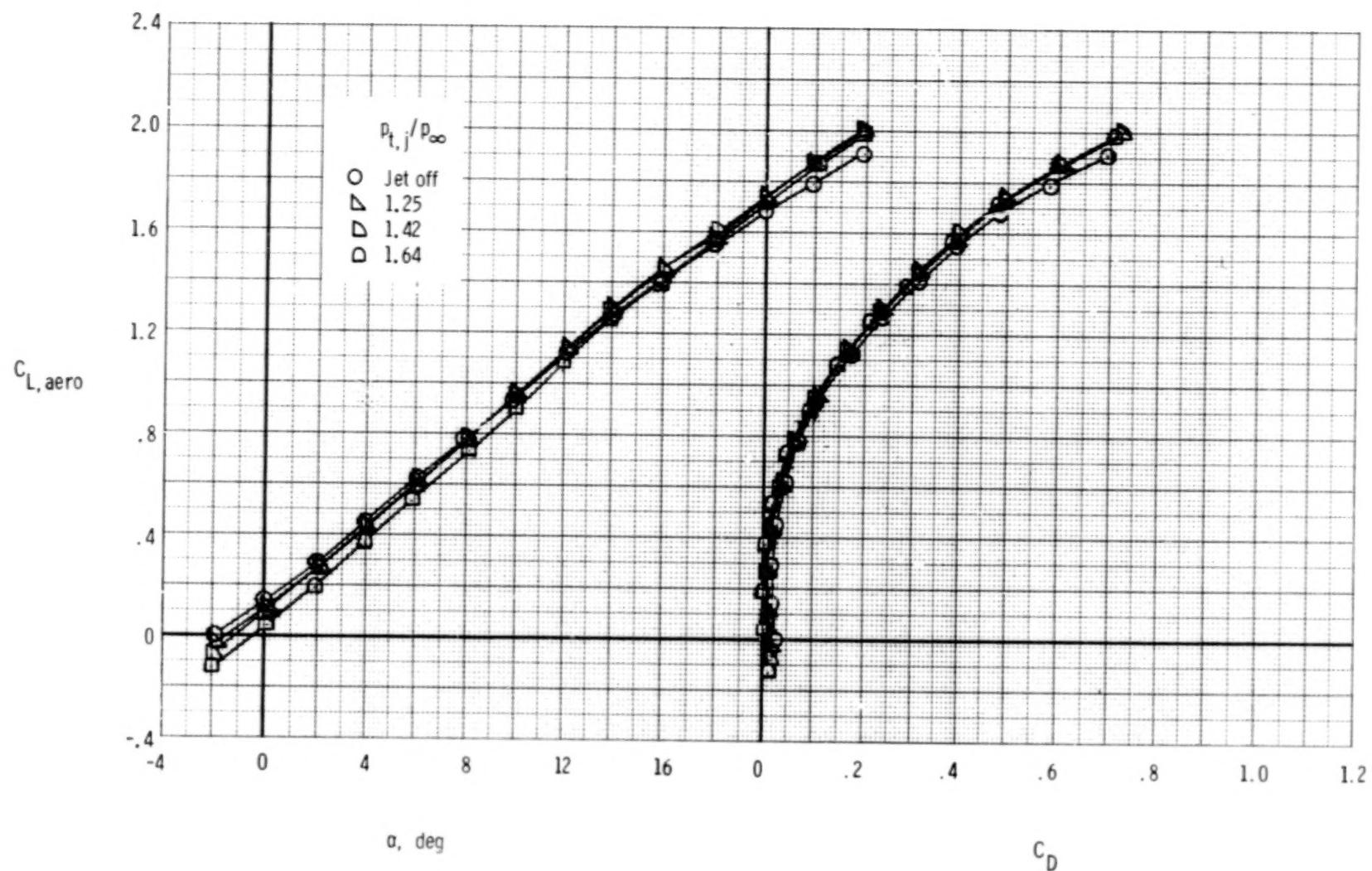
(b) $\delta_{TE} = \delta_{LE} = \delta_C = \delta_{C,TE} = 0^O$; H_2 canard; $p_{t,j}/p_\infty = 1.25$ to 1.64.

Figure 16.- Continued.
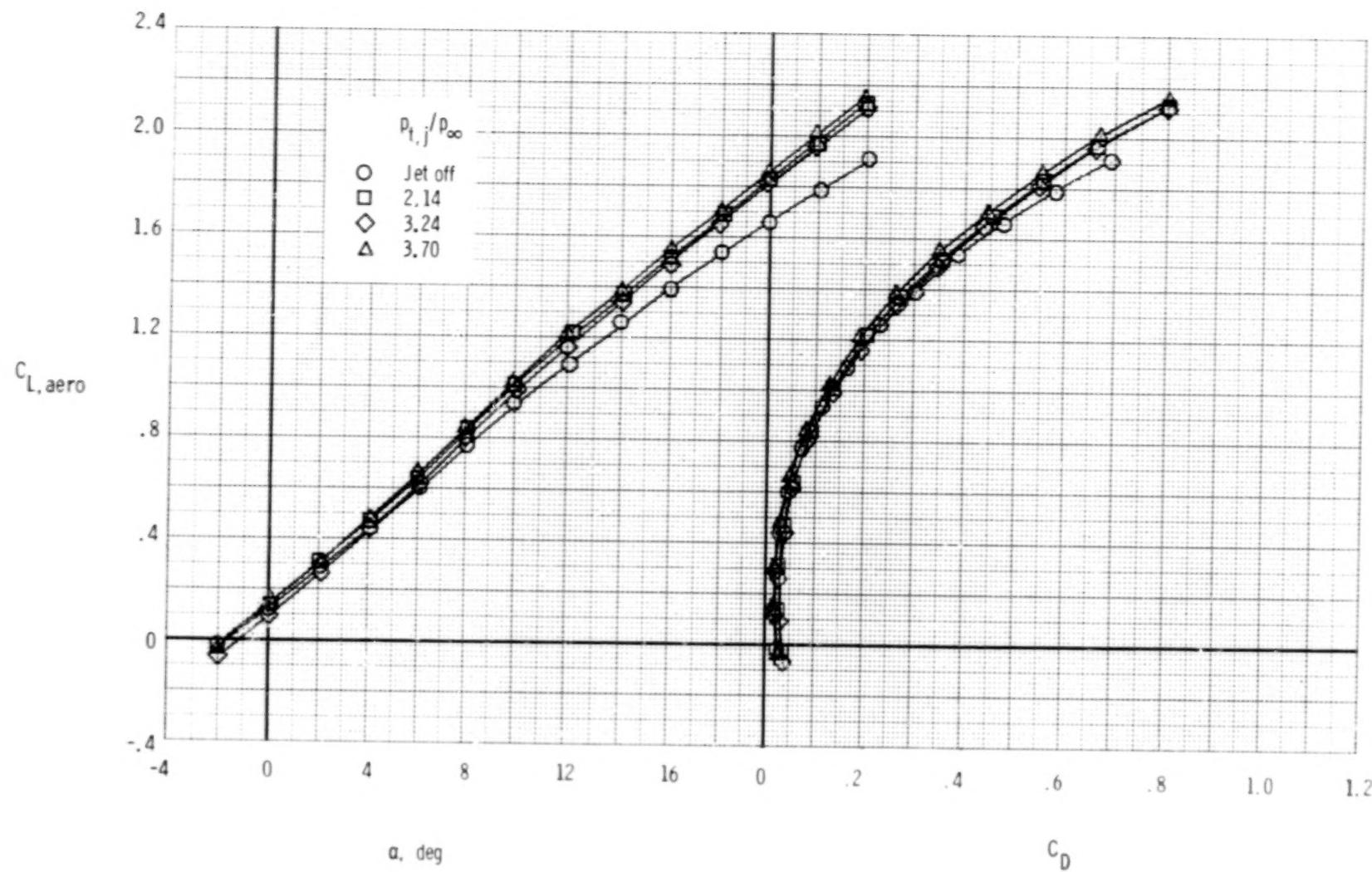
(c) $\delta_{TE} = \delta_{LE} = \delta_C = \delta_{C,TE} = 0^o$; H_2 canard; $p_{t,j}/P_\infty = 2.14$ to 3.70.

Figure 16.- Continued.
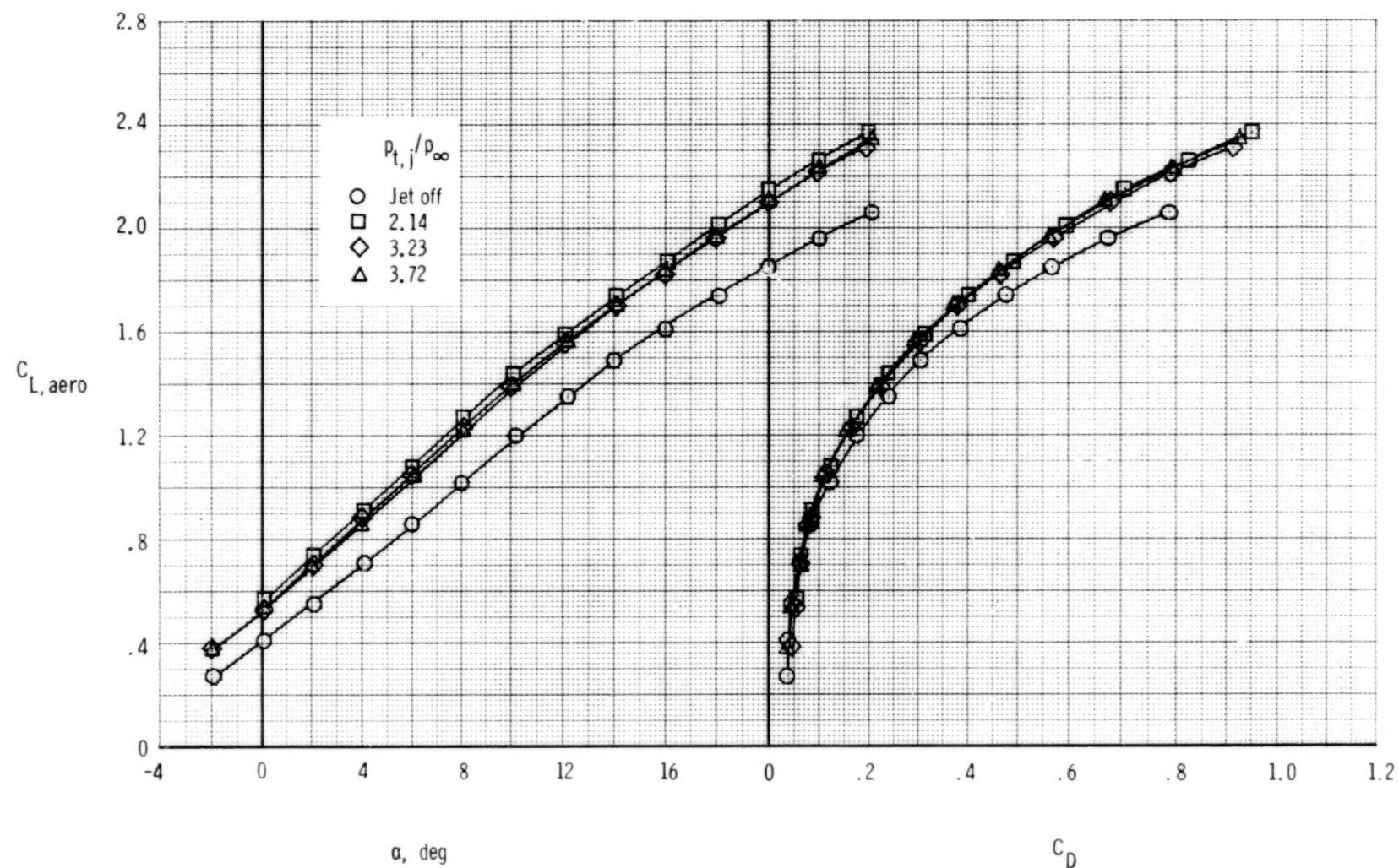
(d) $\delta_{TE} = 15°$; $\delta_{LE} = \delta_C = \delta_{C,TE} = 0°$; H_2 canard.

Figure 16.- Continued.
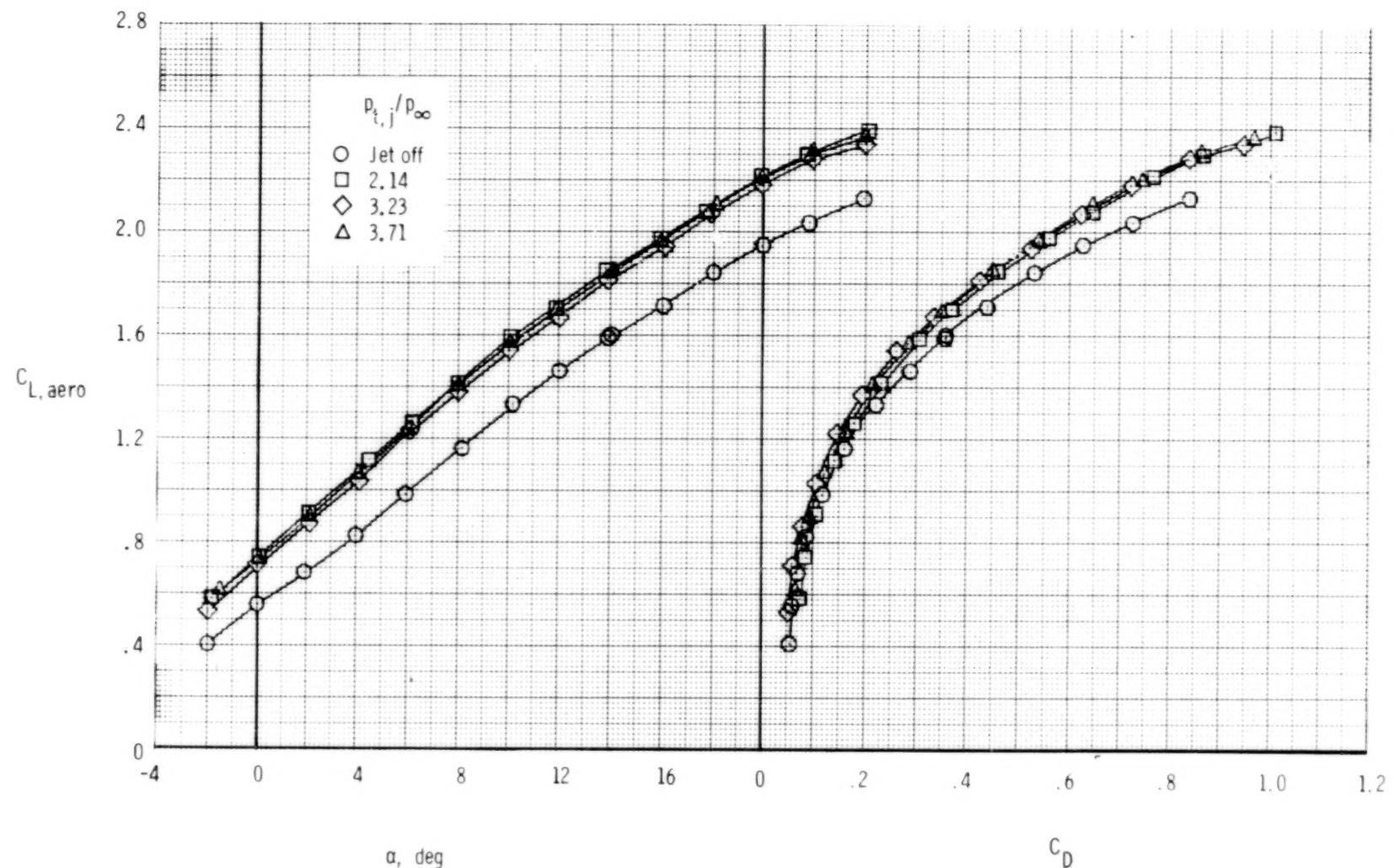
(e) $\delta_{TE} = 25°$; $\delta_{LE} = \delta_C = \delta_{C,TE} = 0°$; H_2 canard.

Figure 16.- Continued.
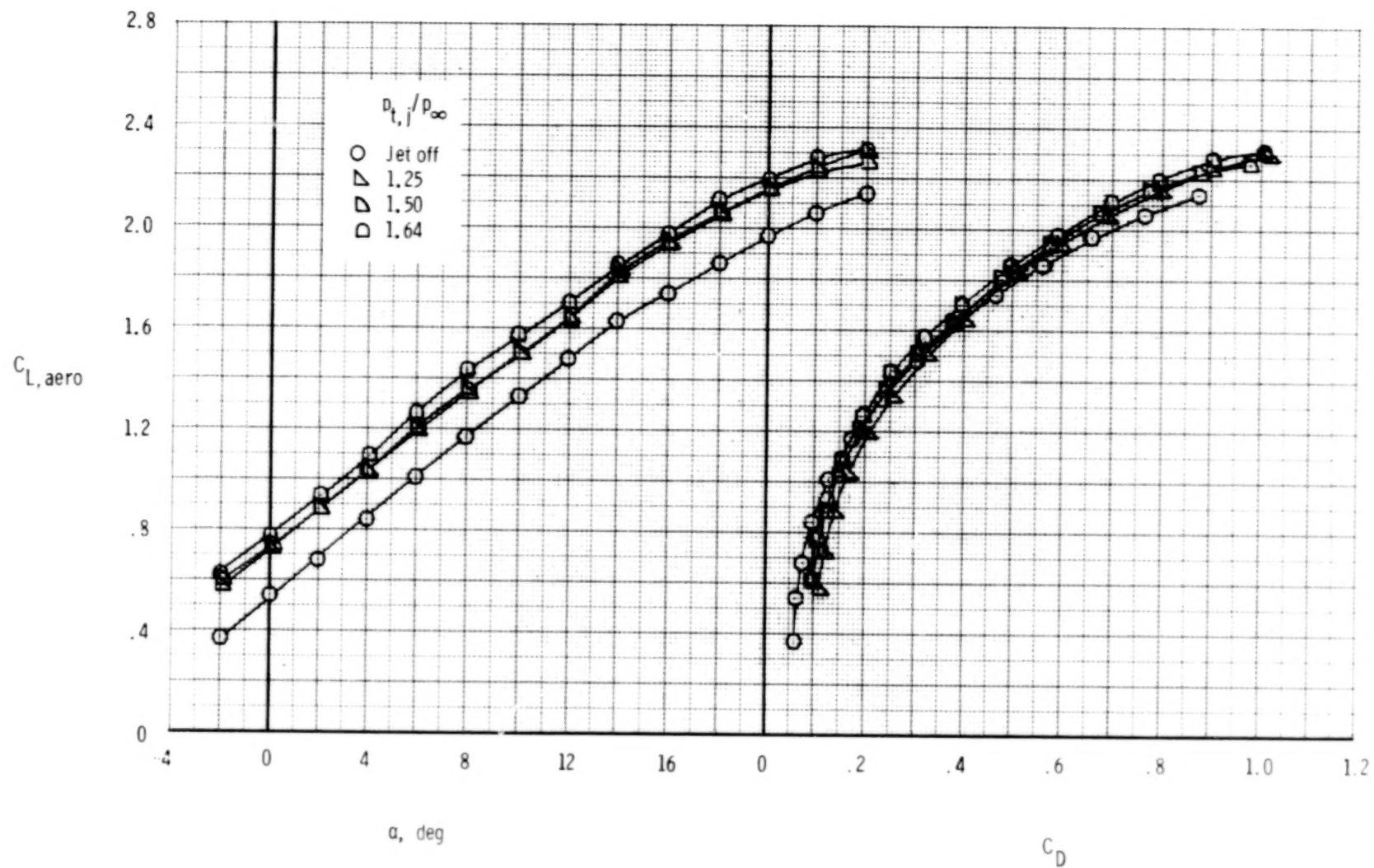
(f) $\delta_{TE} = 30^{\circ}$; $\delta_{LE} = \delta_C = \delta_{C,TE} = 0^{\circ}$; H_2 canard; $p_{t,j}/p_{\infty} = 1.25$ to 1.64.

Figure 16.- Continued.
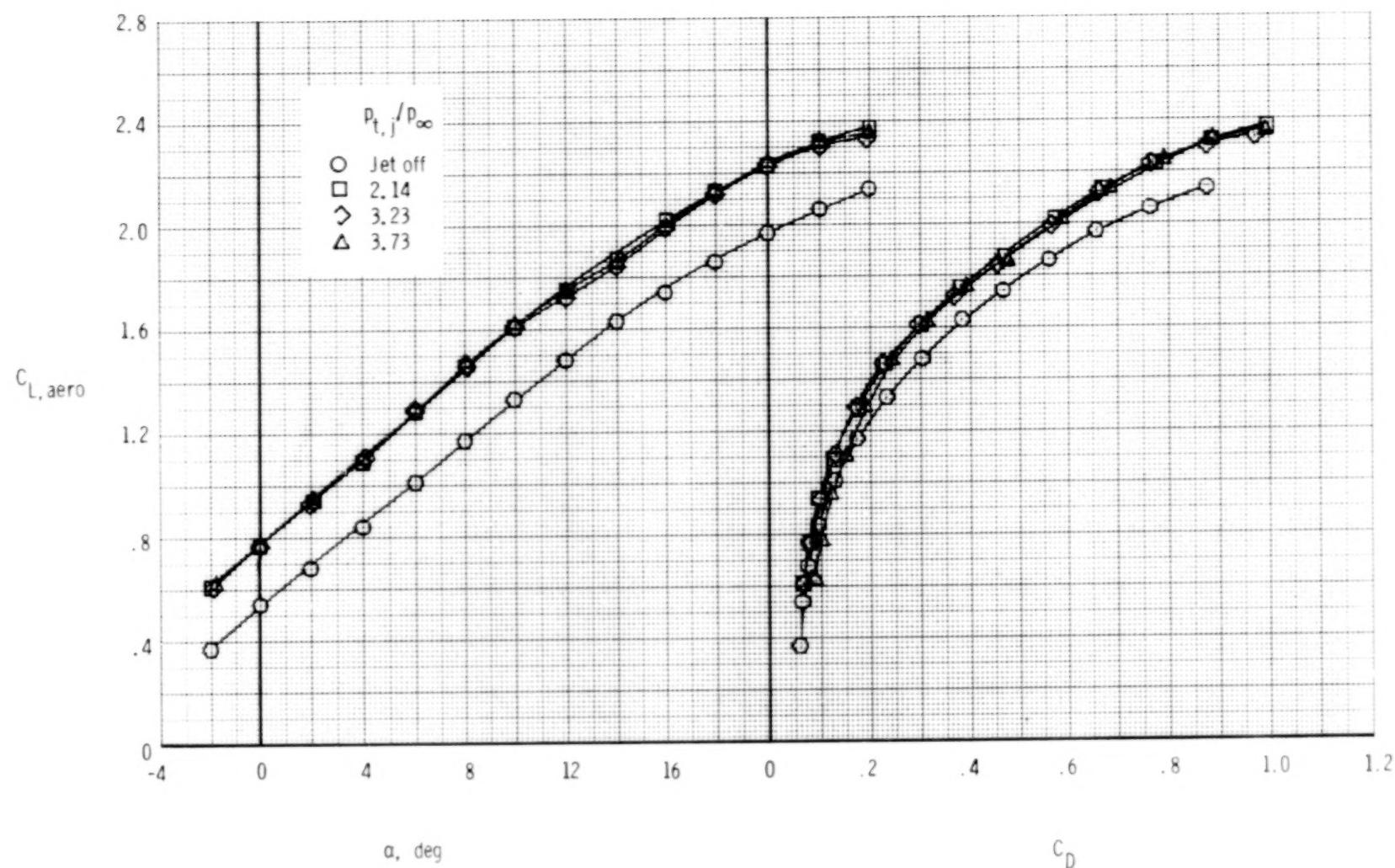
(g) $\delta_{TE} = 30^\circ$; $\delta_{LE} = \delta_C = \delta_{C,TE} = 0^\circ$; H_2 canard; $p_{t,j}/p_\infty = 2.14$ to 3.73.

Figure 16.- Continued.

(h) $\delta_{TE} = 35^{O}$; $\delta_{LE} = \delta_{C} = \delta_{C,TE} = 0^{O}$; H_2 canard.
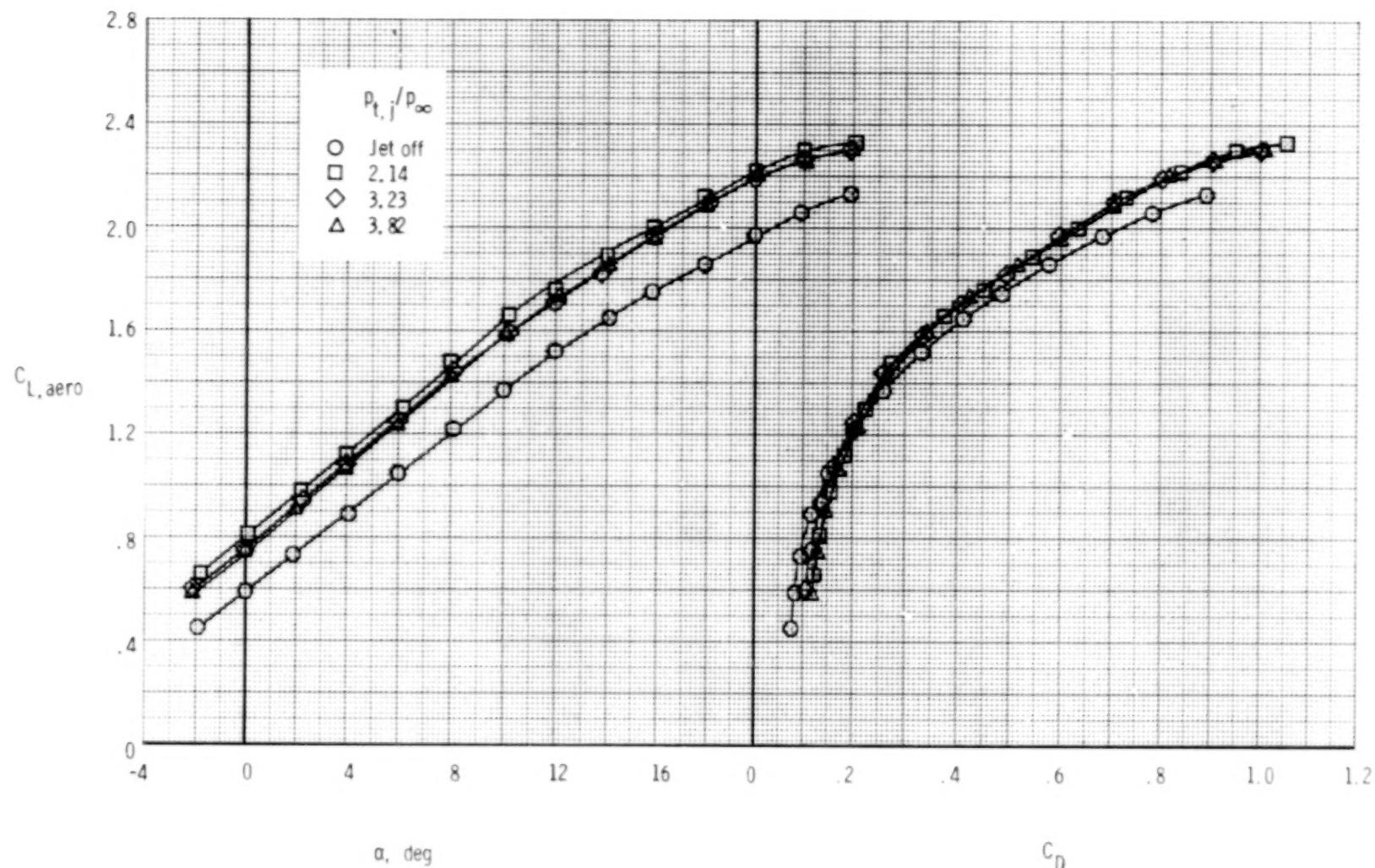
Figure 16.- Continued.

(i) $\delta_{TE} = -25^o$; $\delta_{LE} = \delta_C = \delta_{C,TE} = 0^o$; H_2 canard.
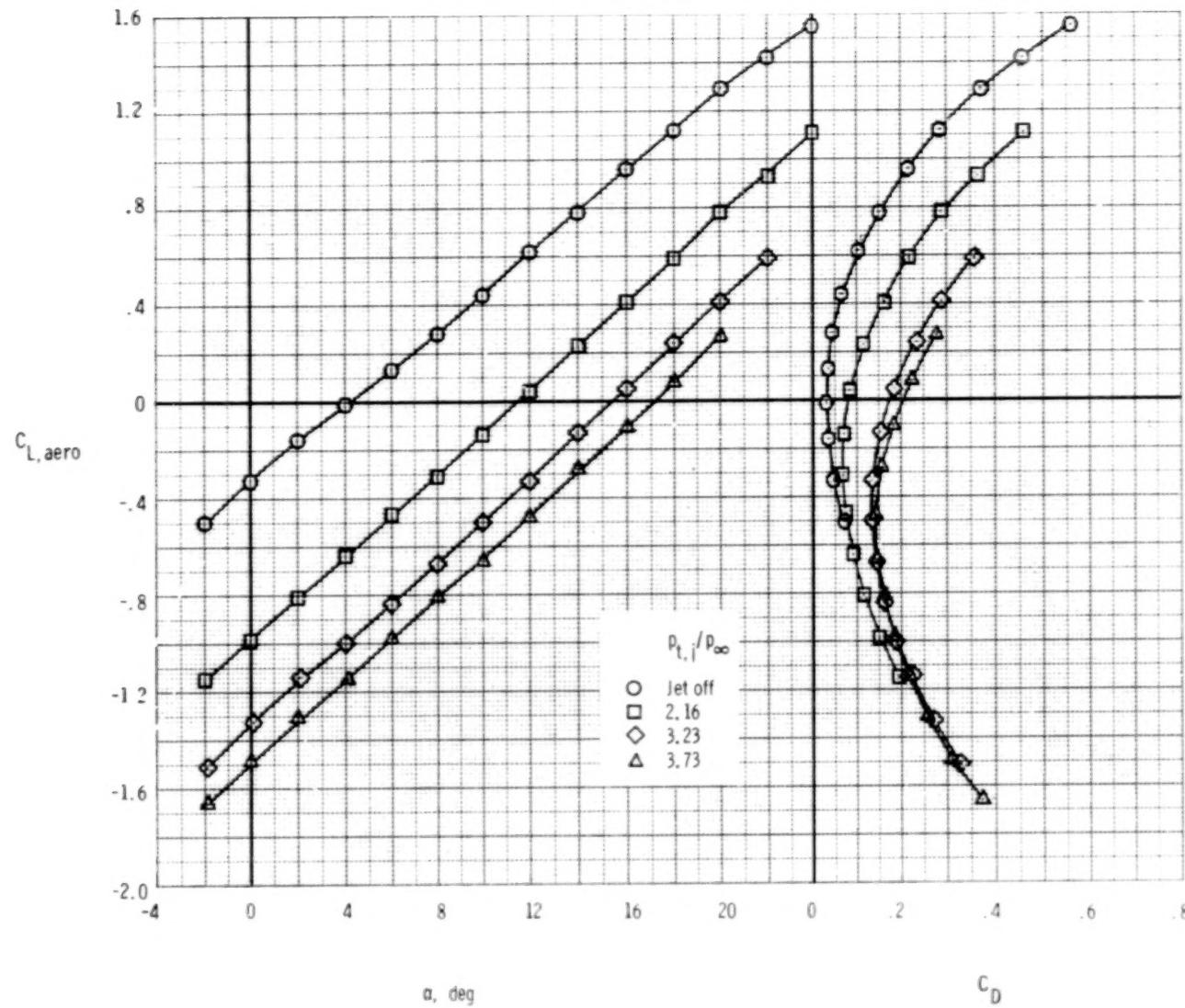
Figure 16.- Continued.
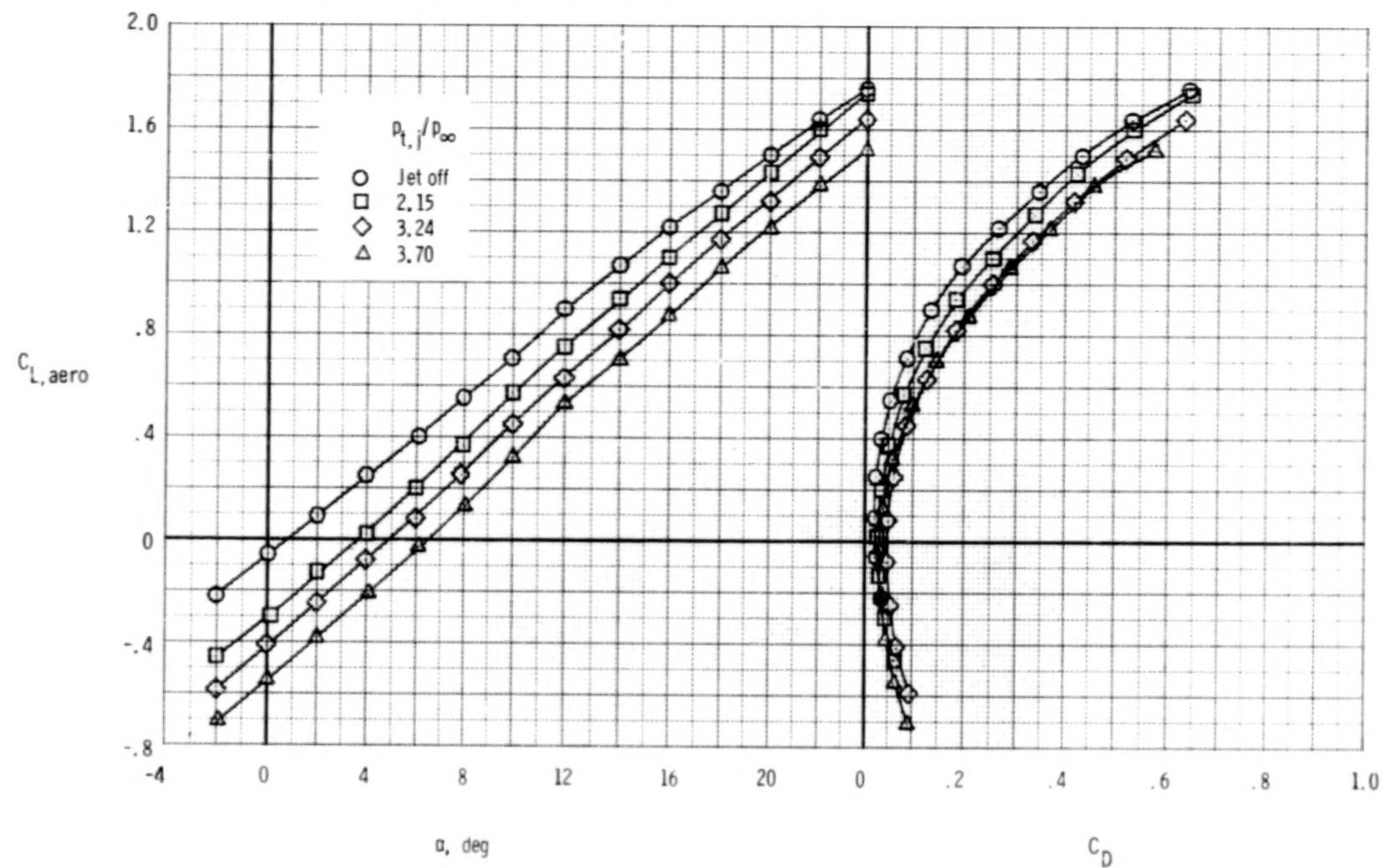
(j) $\delta_{TE} = -10^{\circ}$; $\delta_{LE} = \delta_C = \delta_{C,TE} = 0^{\circ}$; H_2 canard.

Figure 16.- Continued.
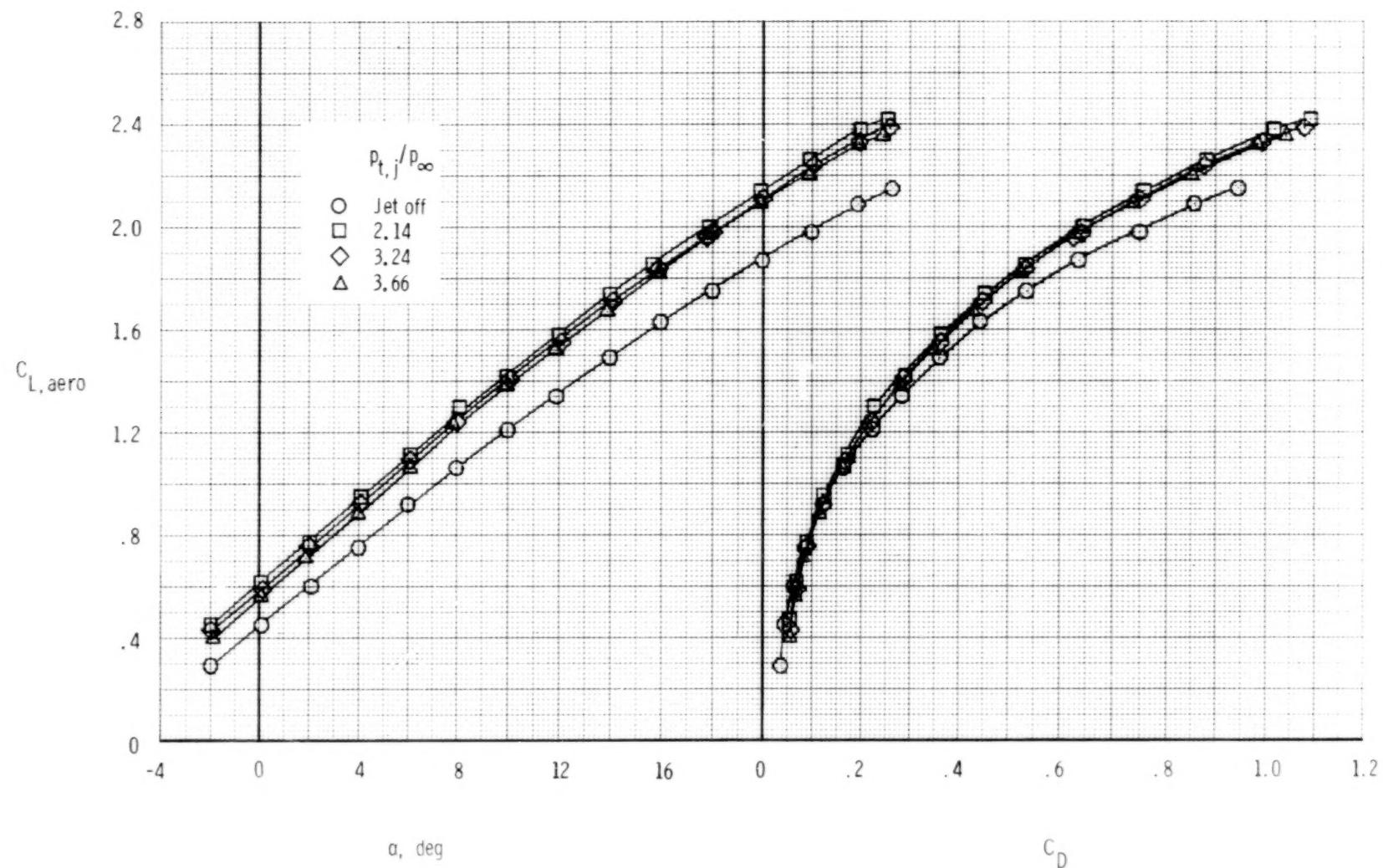
(k) $\delta_{TE} = 15^{\circ}$; $\delta_{LE} = 0^{\circ}$; $\delta_C = 10^{\circ}$; $\delta_{C,TE} = 0^{\circ}$; H_2 canard.

Figure 16.- Continued.

91

(1) $\delta_{TE} = 15^{O}$; $\delta_{LE} = 0^{O}$; $\delta_{C} = 20^{O}$; $\delta_{C,TE} = 0^{O}$; H_2 canard.

Figure 16.- Continued.
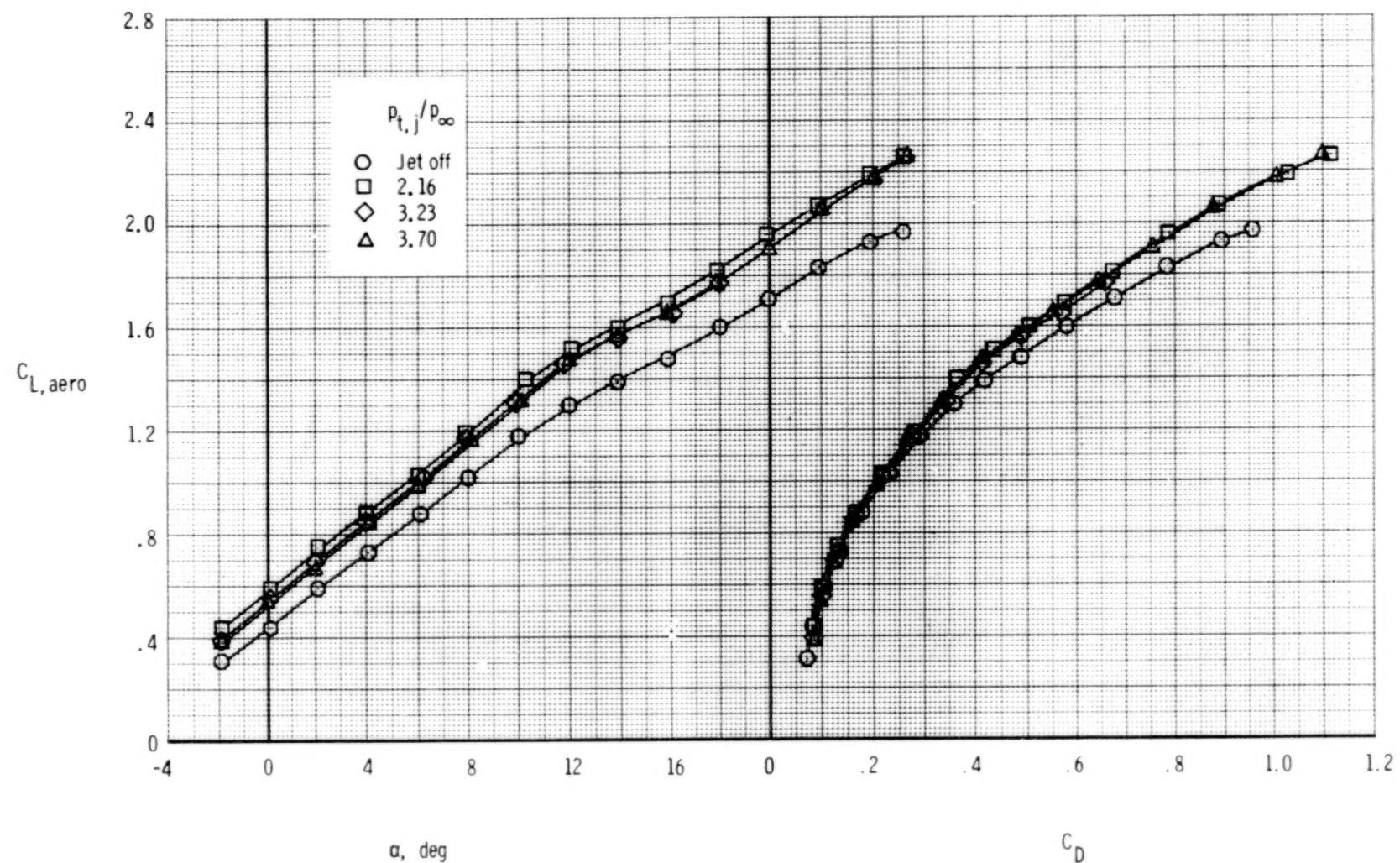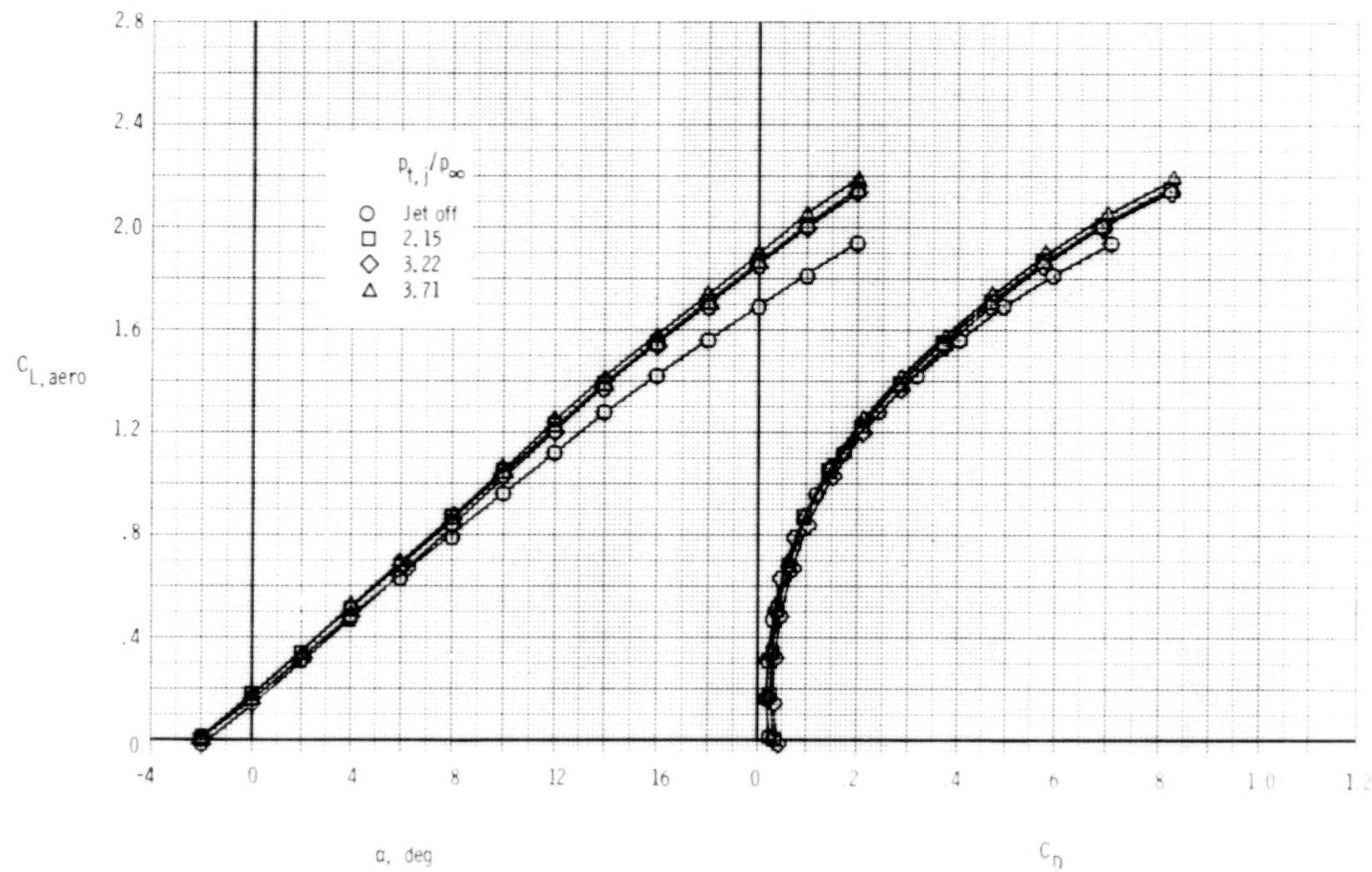
(m) $\delta_{TE} = \delta_{LE} = \delta_C = 0°$; $\delta_{C,TE} = 10°$; H_2 canard.

Figure 16.- Continued.

93

(n) $\delta_{TE} = \delta_{LE} = \delta_C = 0^o$; $\delta_{C,TE} = 20^o$; H_2 canard.
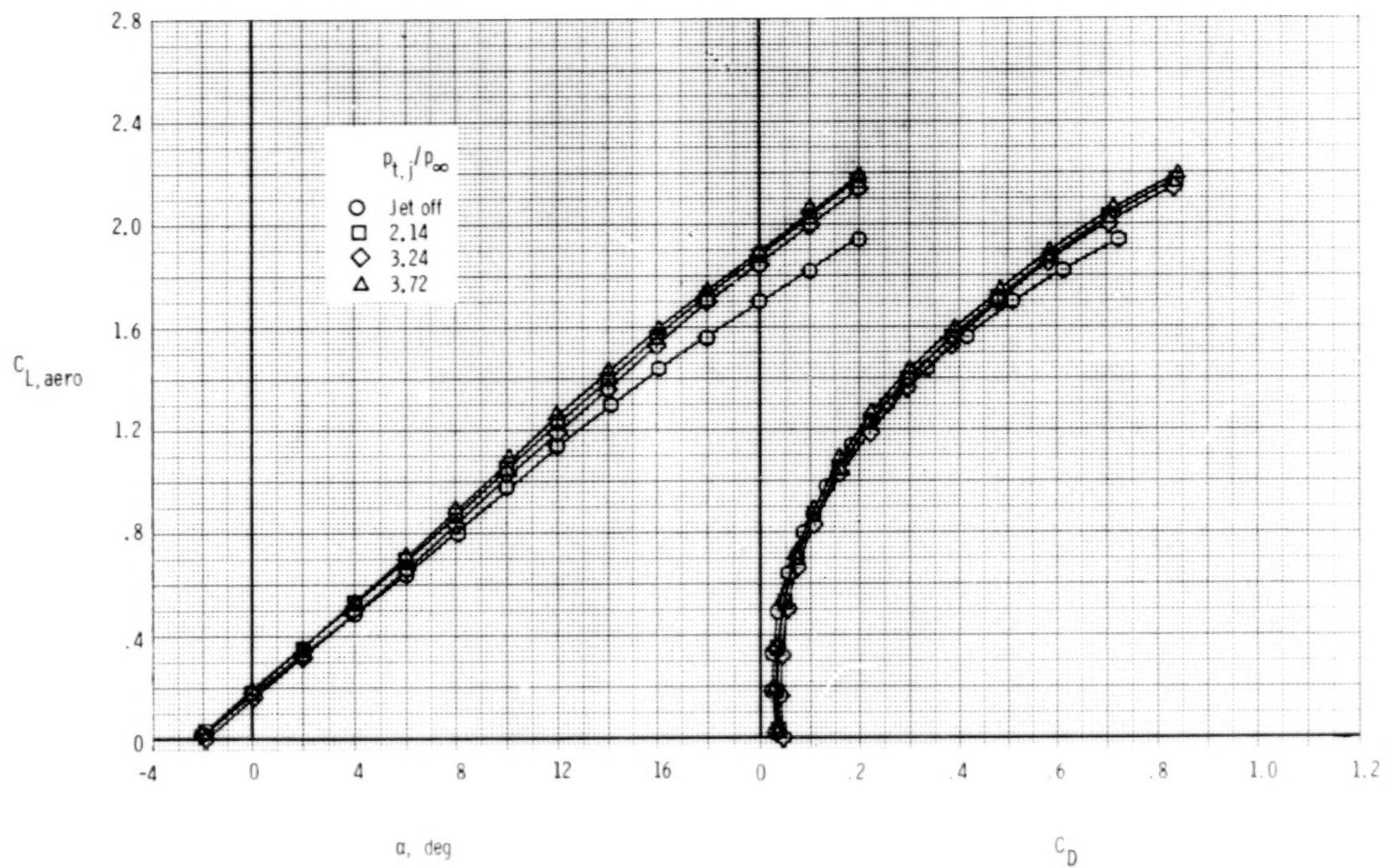
Figure 16.- Continued.

(o) $\delta_{TE} = \delta_{LE} = \delta_C = 0^O$; $\delta_{C,TE} = 30^O$; H_2 canard.
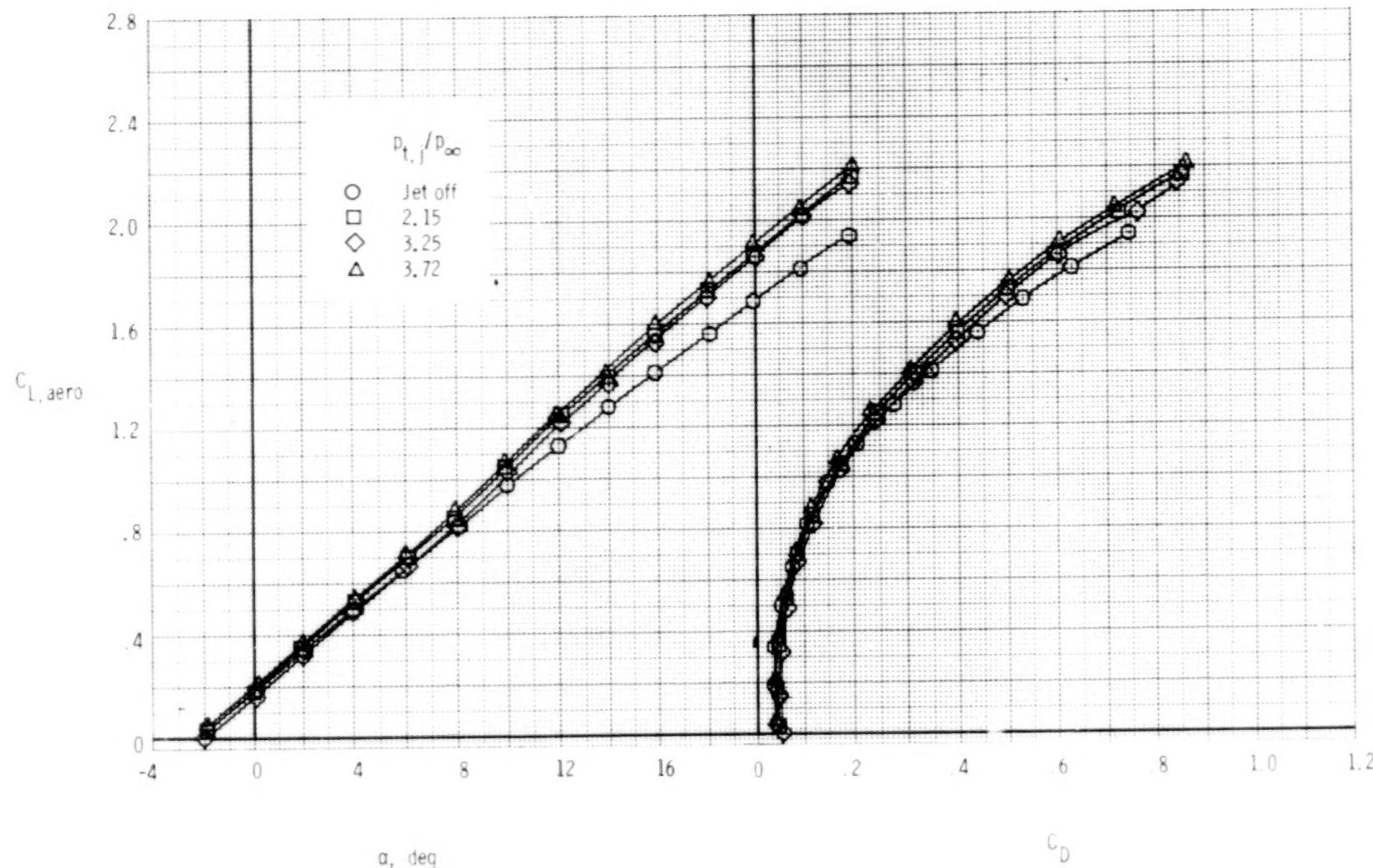
Figure 16.- Continued.
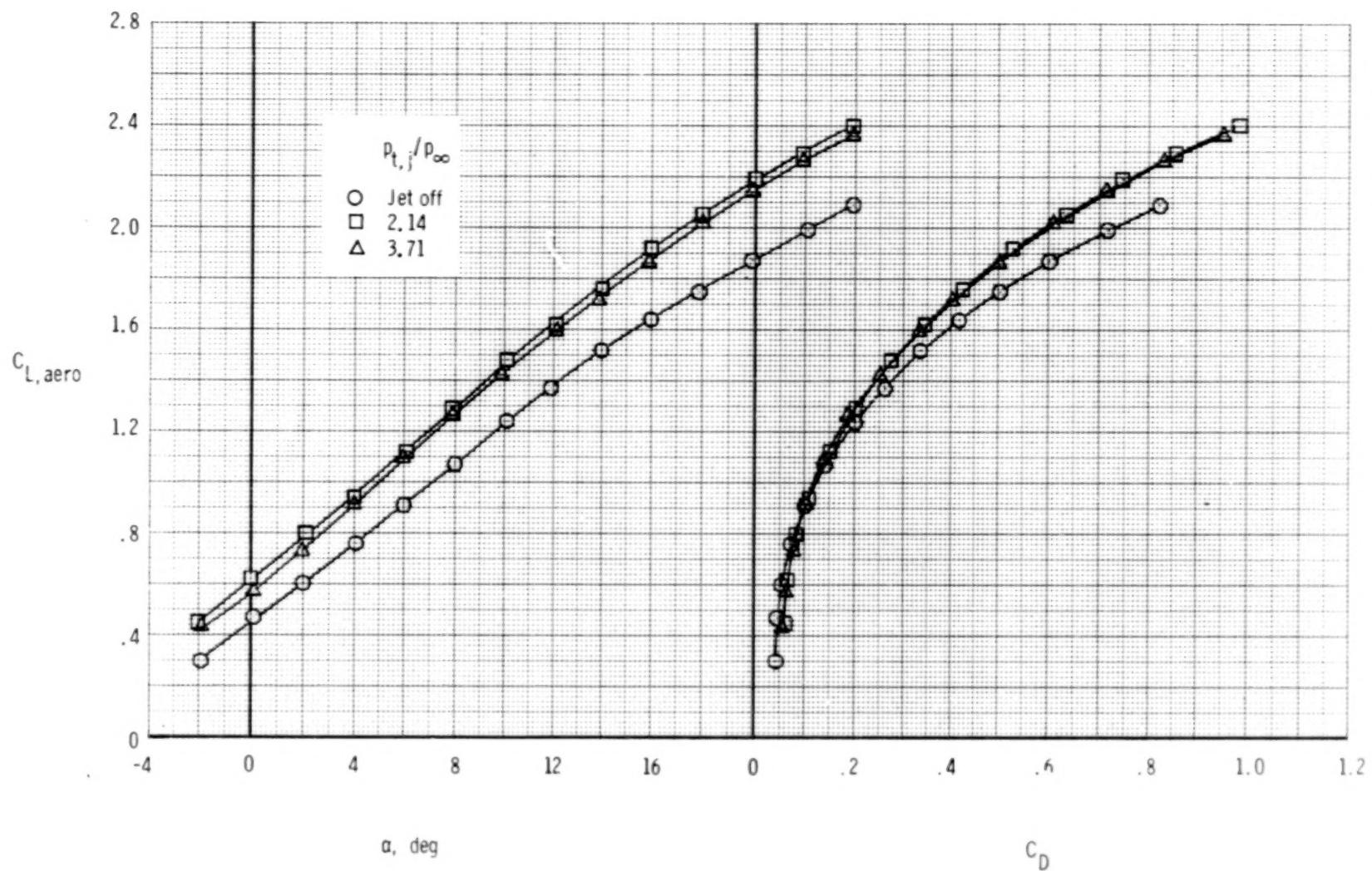
(p) $\delta_{TE} = 15^\circ$; $\delta_{LE} = \delta_C = 0^\circ$; $\delta_{C,TE} = 20^\circ$; H_2 canard.

Figure 16.- Continued.
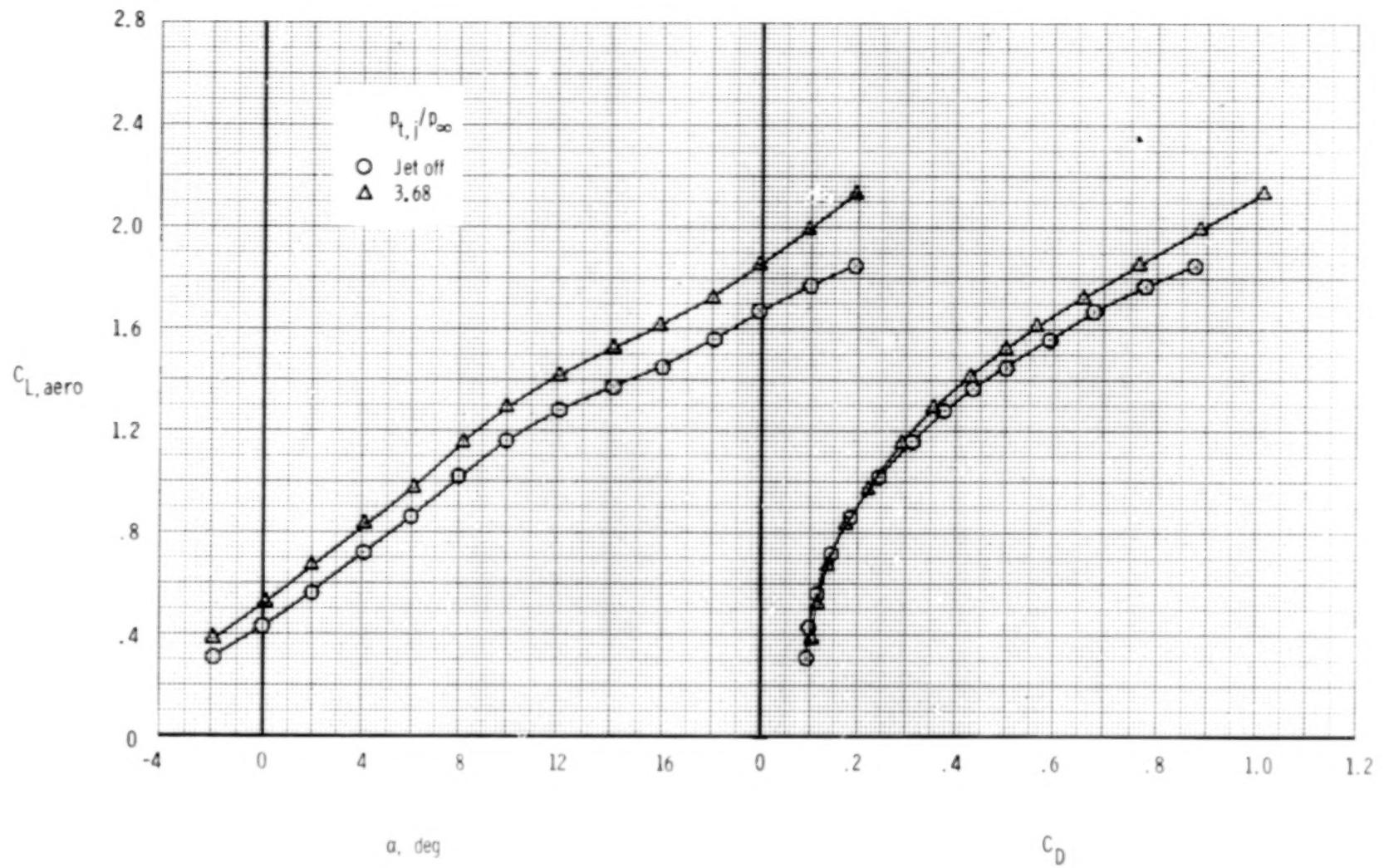
(q) $\delta_{TE} = 15^{\circ}$; $\delta_{LE} = 0^{\circ}$; $\delta_C = 20^{\circ}$; $\delta_{C,TE} = 20^{\circ}$; H_2 canard.

Figure 16.- Continued.

(r) $\delta_{TE} = 15^o;$ $\delta_{LE} = \delta_C = \delta_{C,TE} = 0^o;$ H$_3$ canard.
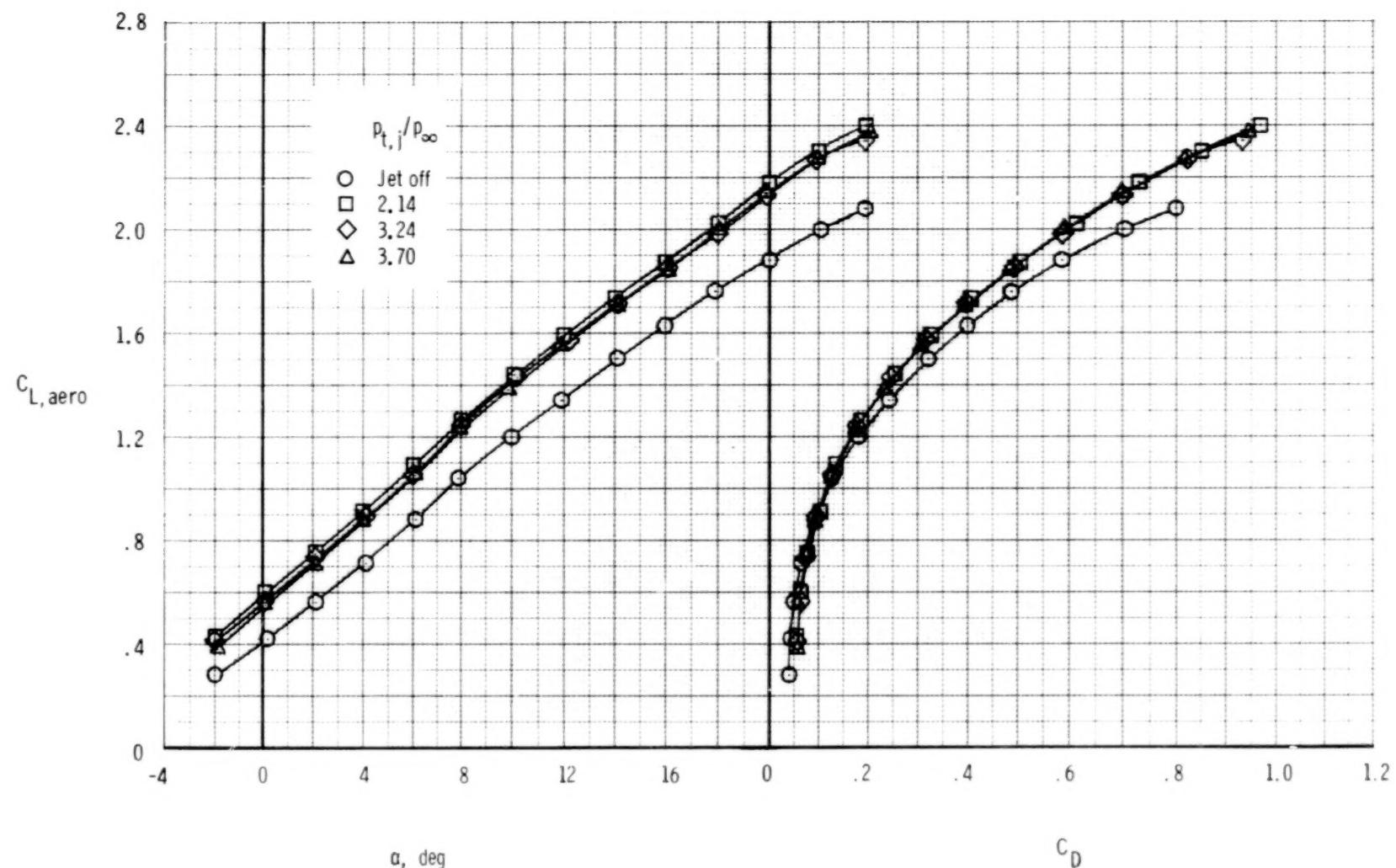
Figure 16.- Continued.
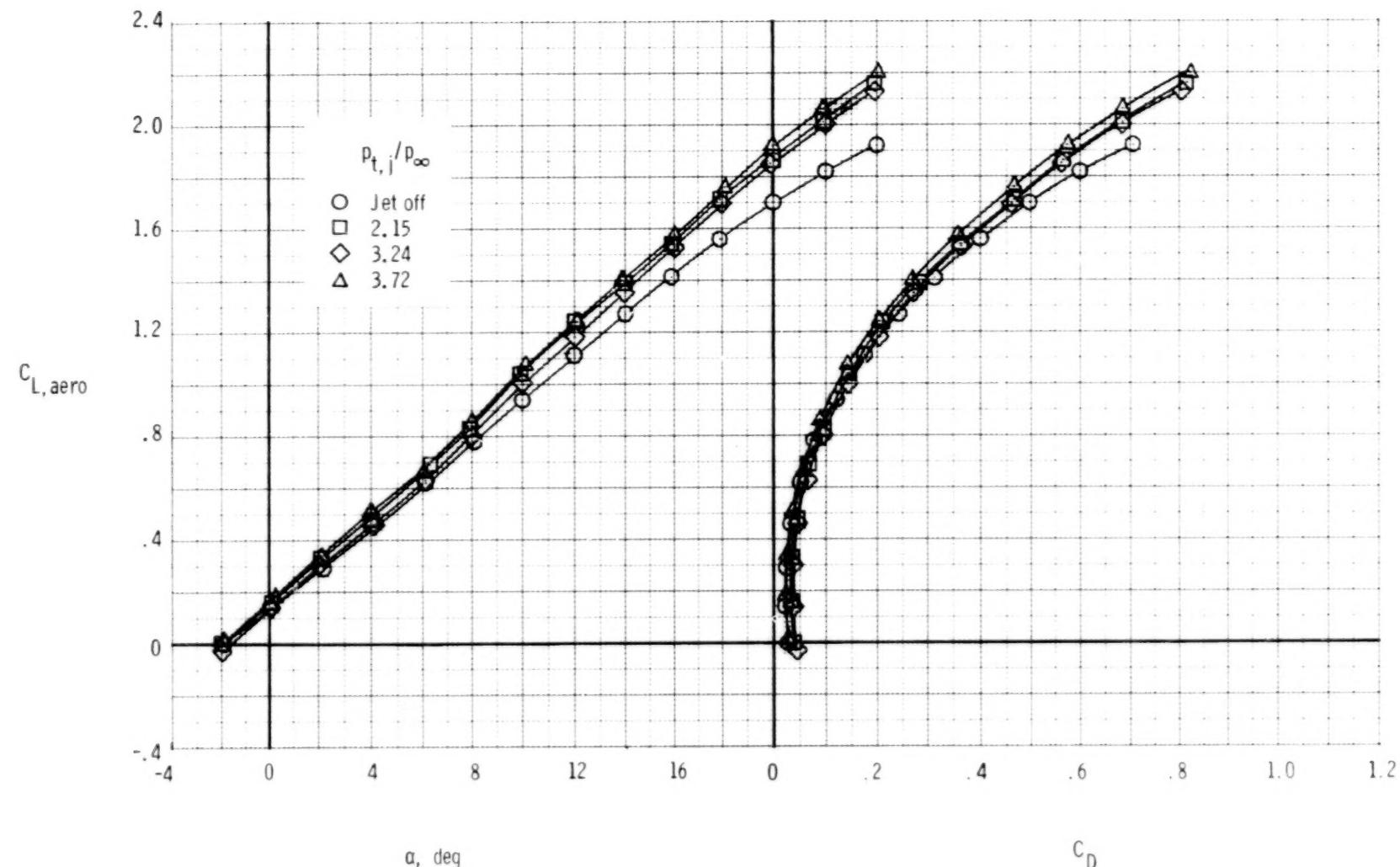
(s) $\delta_{TE} = \delta_{LE} = \delta_C = \delta_{C,TE} = 0^O$; H_3 canard.

Figure 16.- Concluded.
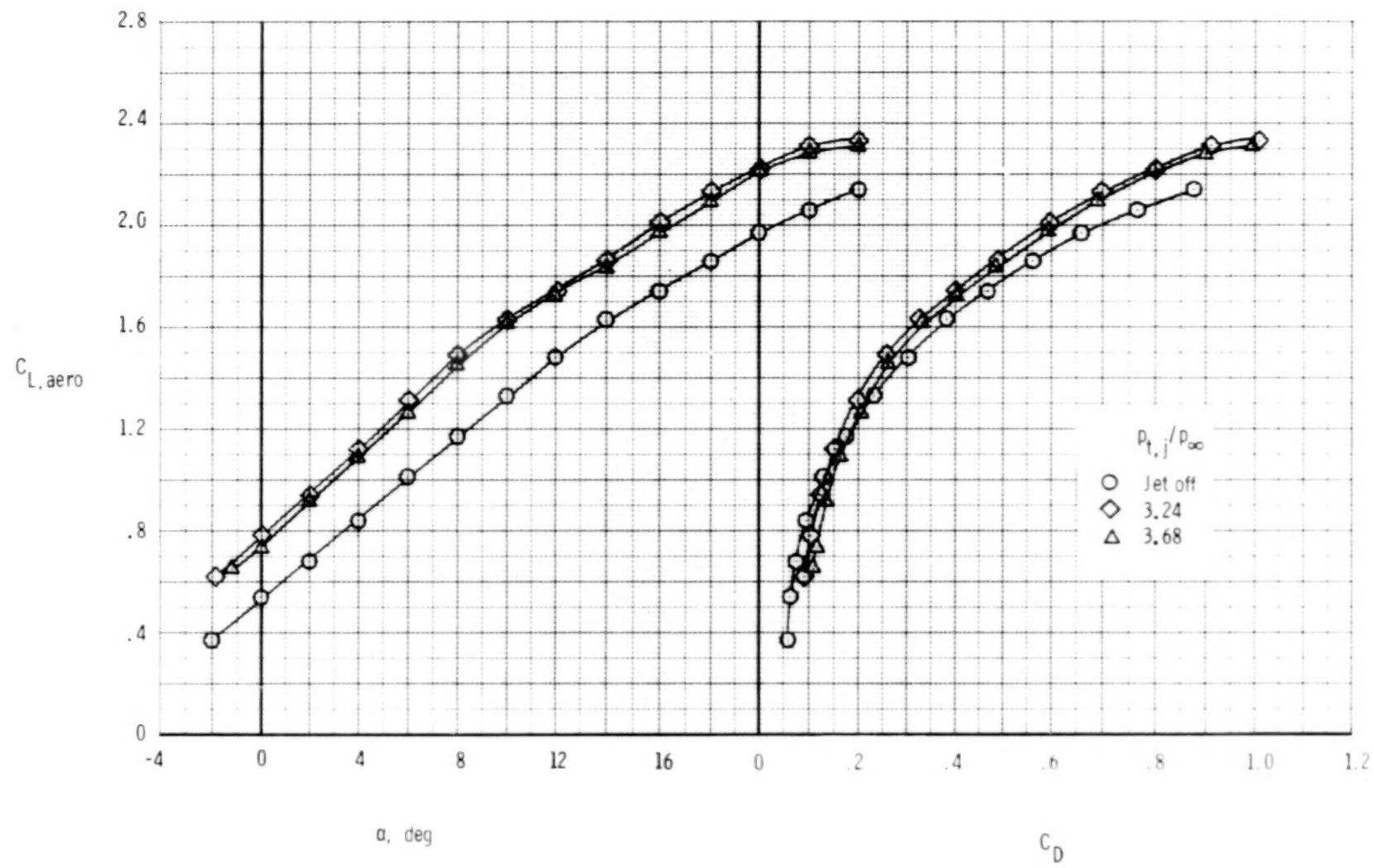
(a) $\delta_{TE} = 30^O$; $\delta_{LE} = \delta_C = \delta_{C,TE} = 0^O$; H_2 canard.

Figure 17.- Thrust-removed lift and drag characteristics at M = 0.186 for nozzle conf 2.
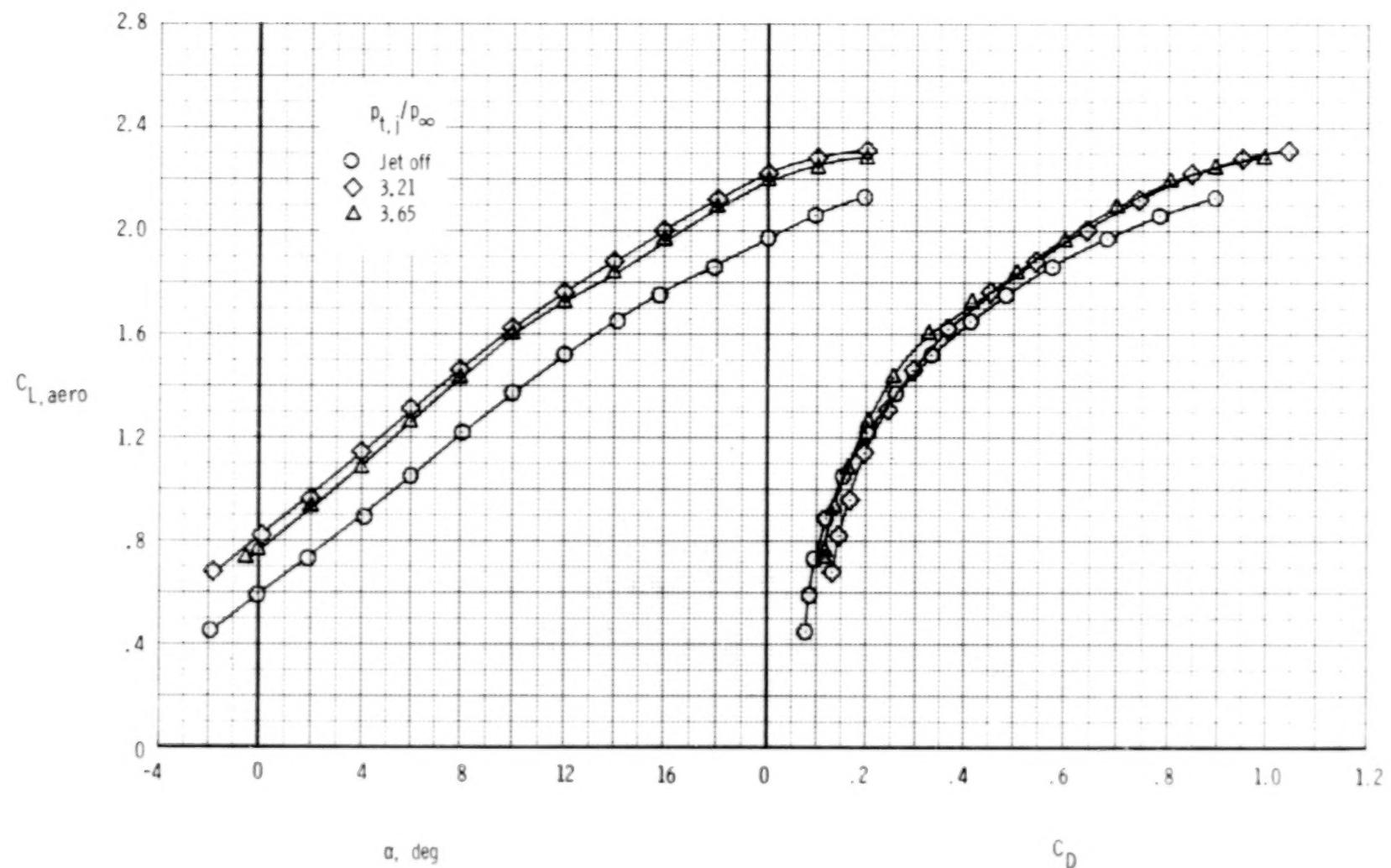
(b) $\delta_{TE} = 35^O$; $\delta_{LE} = \delta_C = \delta_{c,TE} = 0^O$; H_2 canard.

Figure 17.- Continued.

(c) $\delta_{TE} = 35^o$; $\delta_{LE} = 0^o$; $\delta_C = 20^o$; $\delta_{C,TE} = 0^o$; H_2 canard.
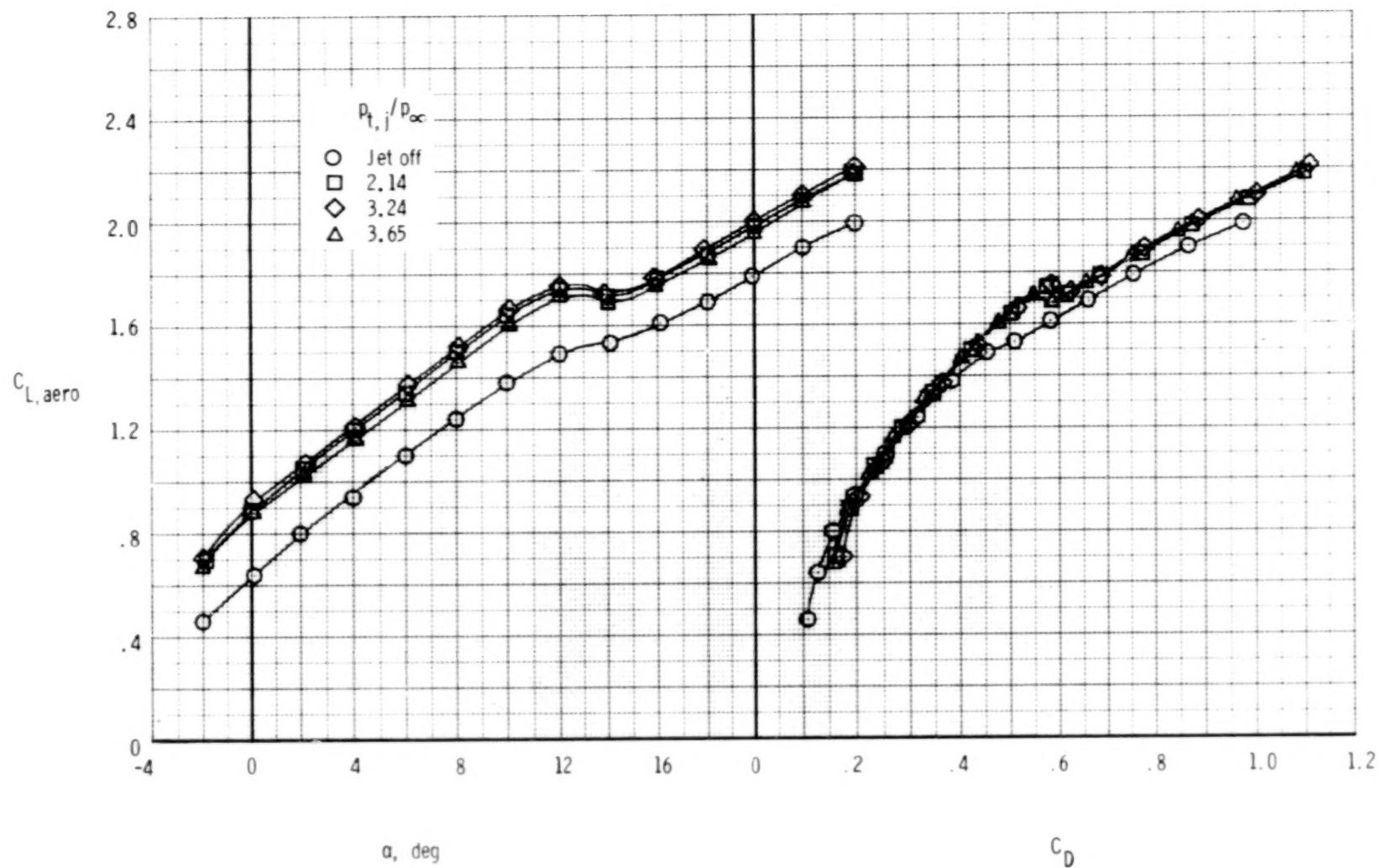
Figure 17.- Continued.

(d) $\delta_{TE} = 30°$; $\delta_{LE} = \delta_C = \delta_{C,TE} = 0°$; H_3 canard.

Figure 17.- Continued.
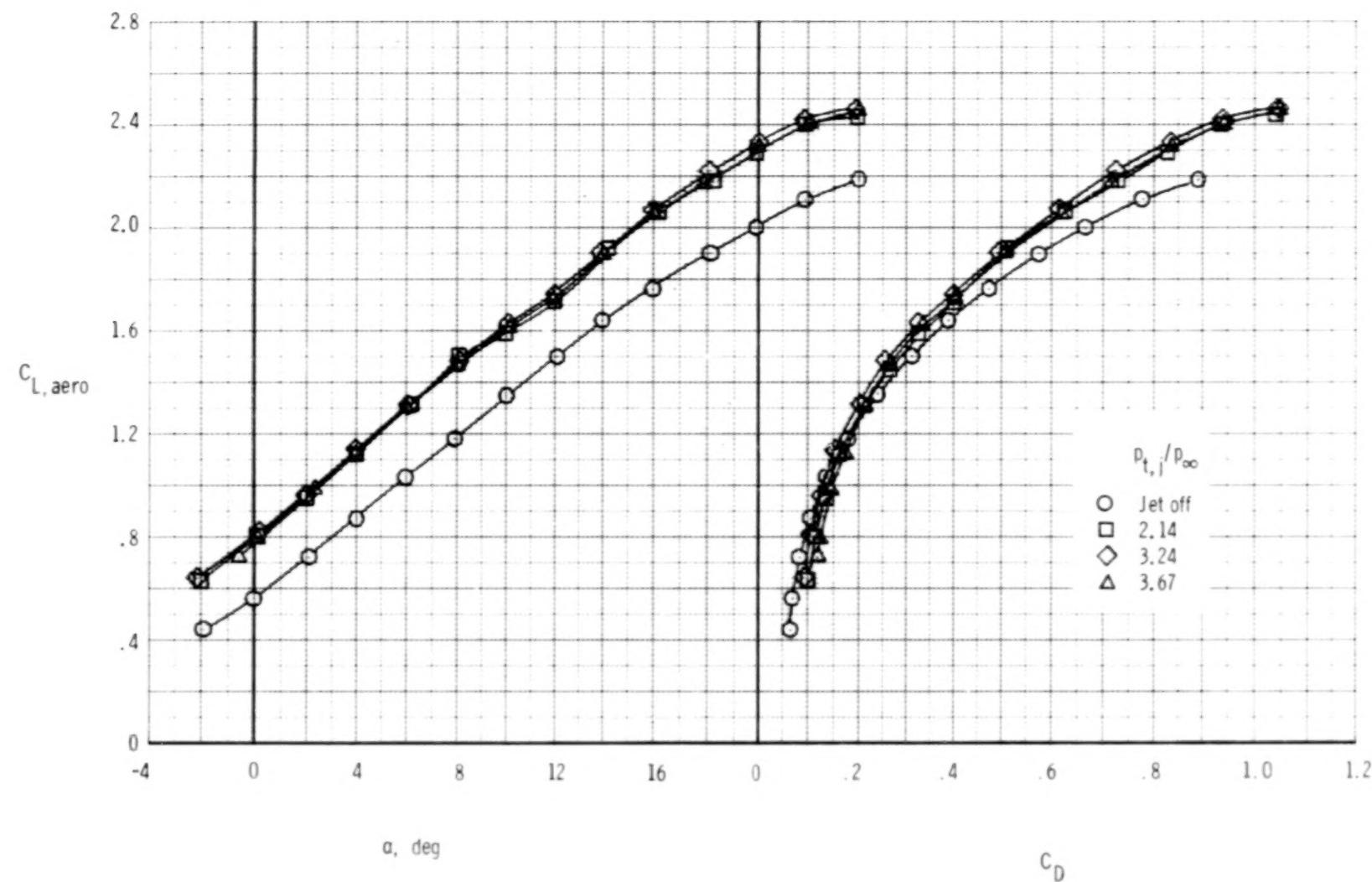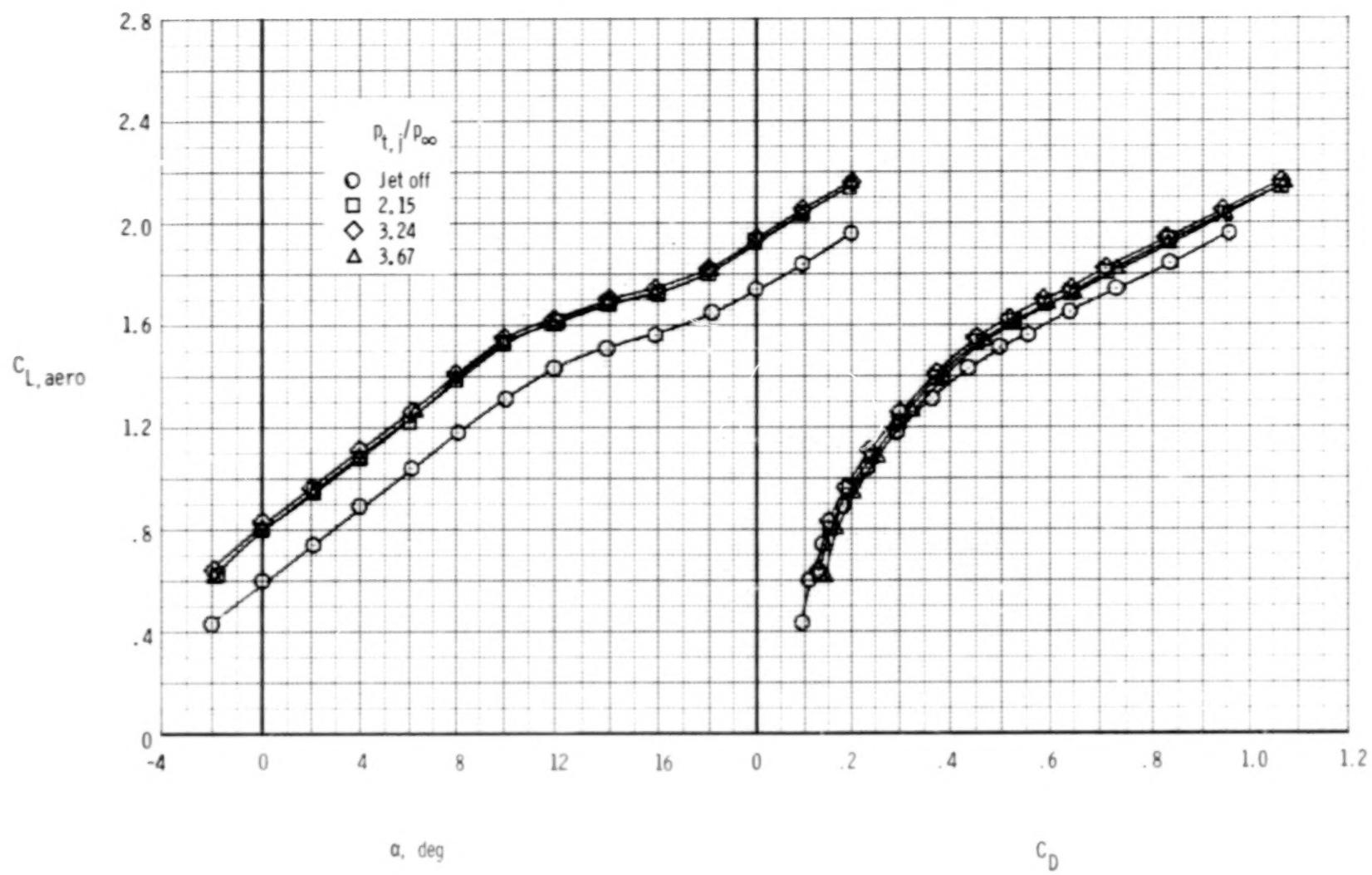
(e) $\delta_{TE} = 30^\circ$; $\delta_{LE} = 0^\circ$; $\delta_C = 20^\circ$; $\delta_{C,TE} = 0^\circ$; H_3 canard.

Figure 17.- Continued.

(f) $\delta_{TE} = 30^o$; $\delta_{LE} = 20^o$; $\delta_c = \delta_{c,TE} = 0^o$; H_2 canard.

Figure 17.- Continued.
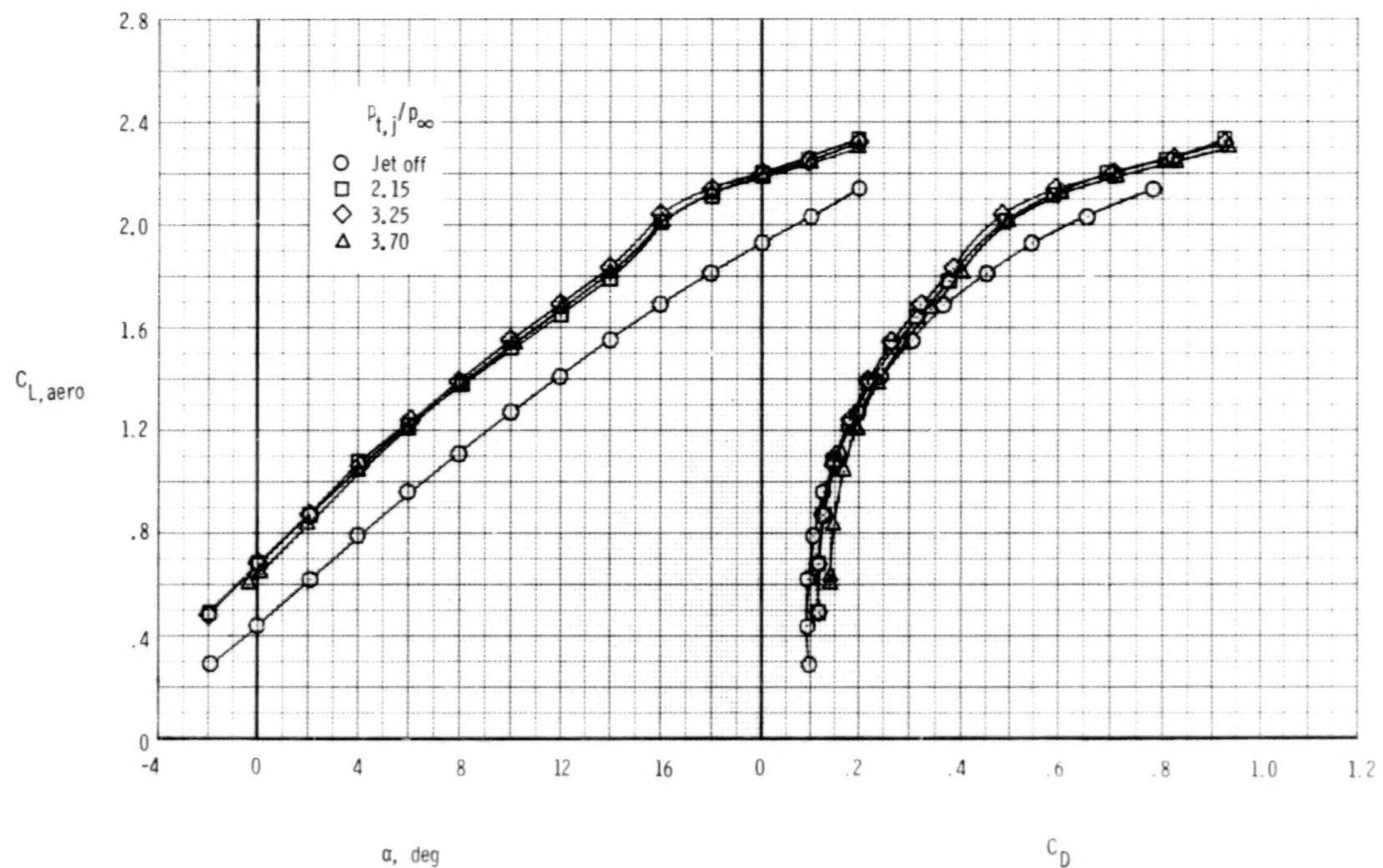
(g) $\delta_{TE} = 30°$; $\delta_{LE} = 20°$; $\delta_C = 20°$; $\delta_{C,TE} = 0°$; H_2 canard.

Figure 17.- Continued.
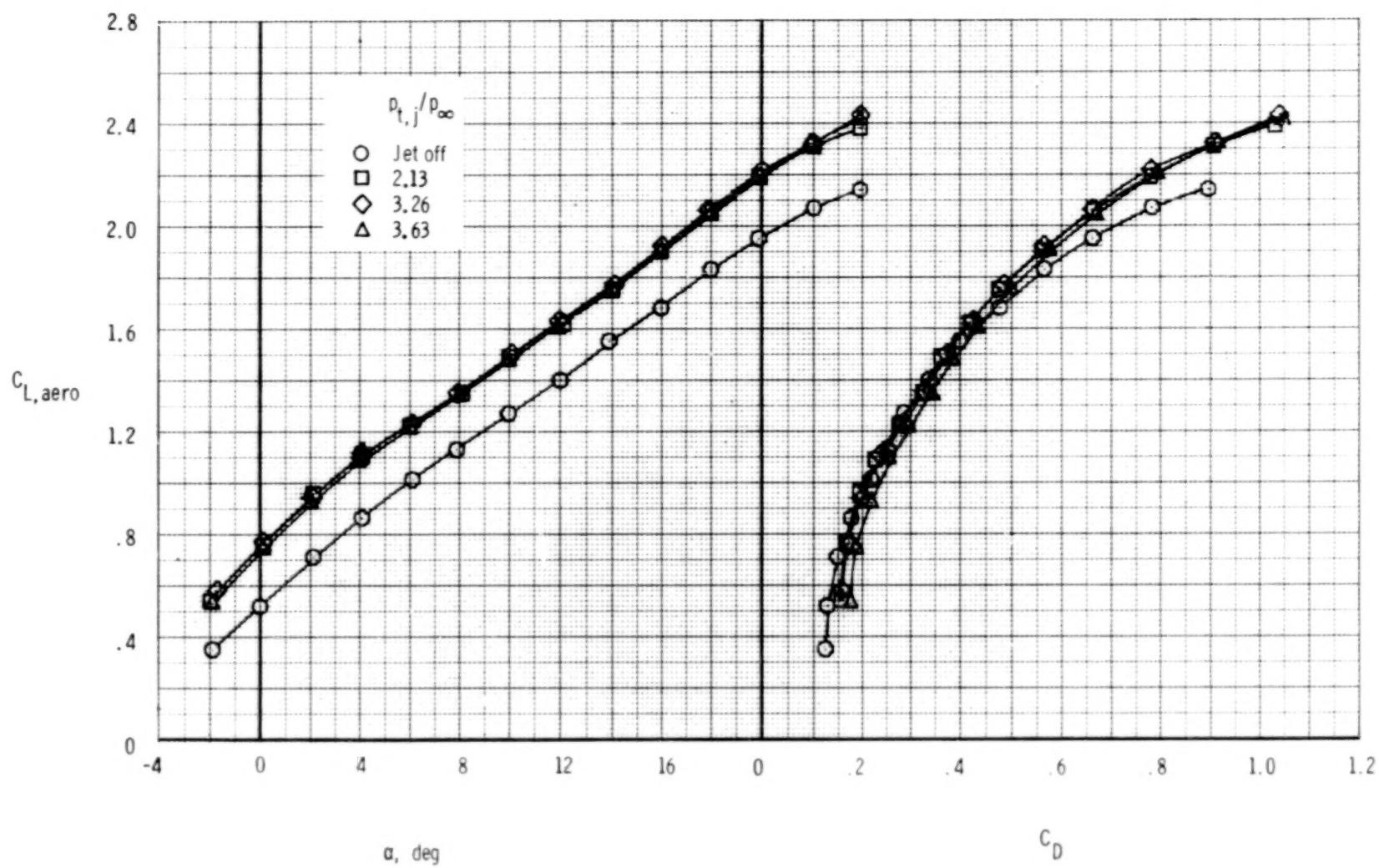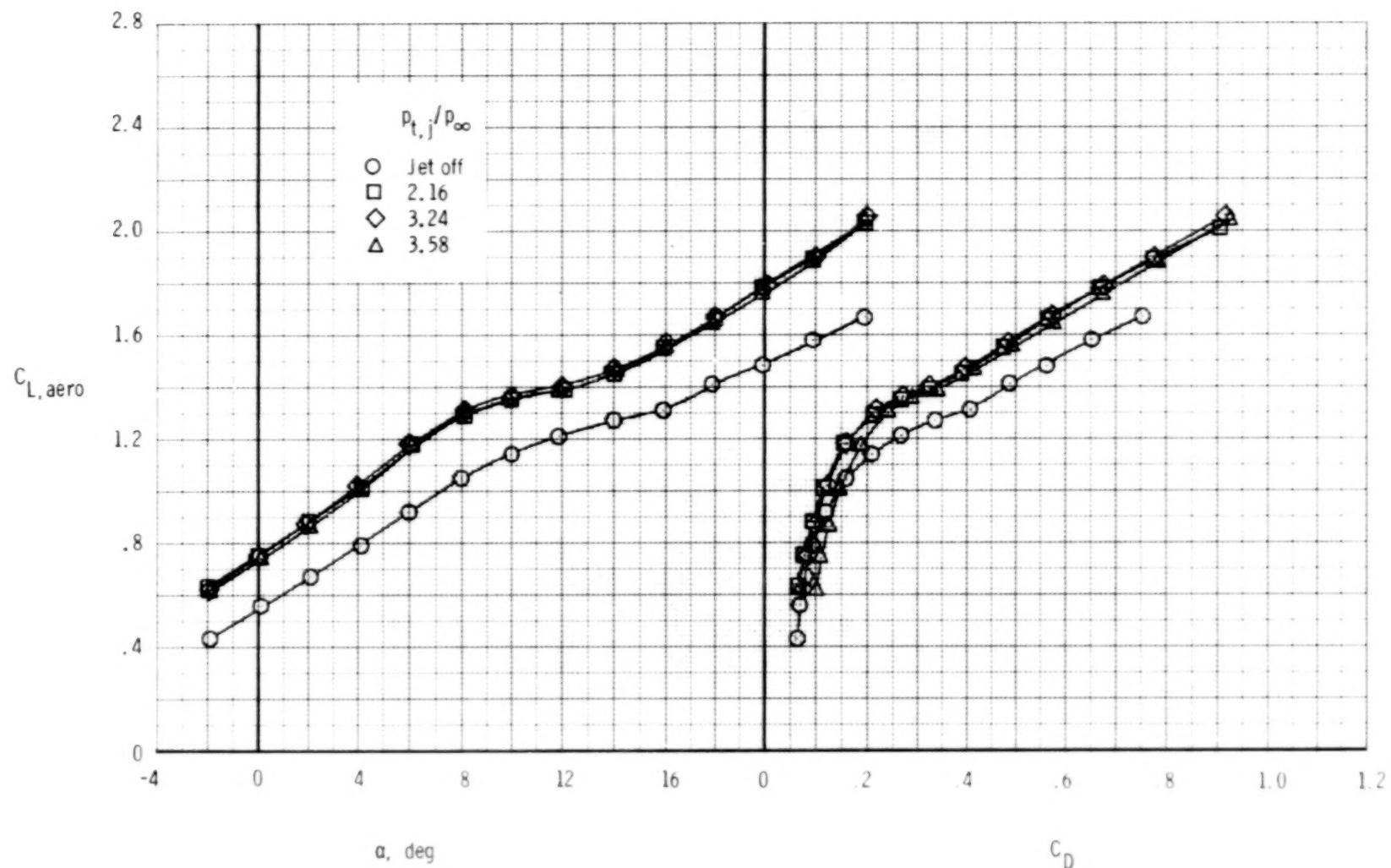
(h) $\delta_{TE} = 30°$; $\delta_{LE} = 0°$; canard off.

Figure 17.- Concluded.
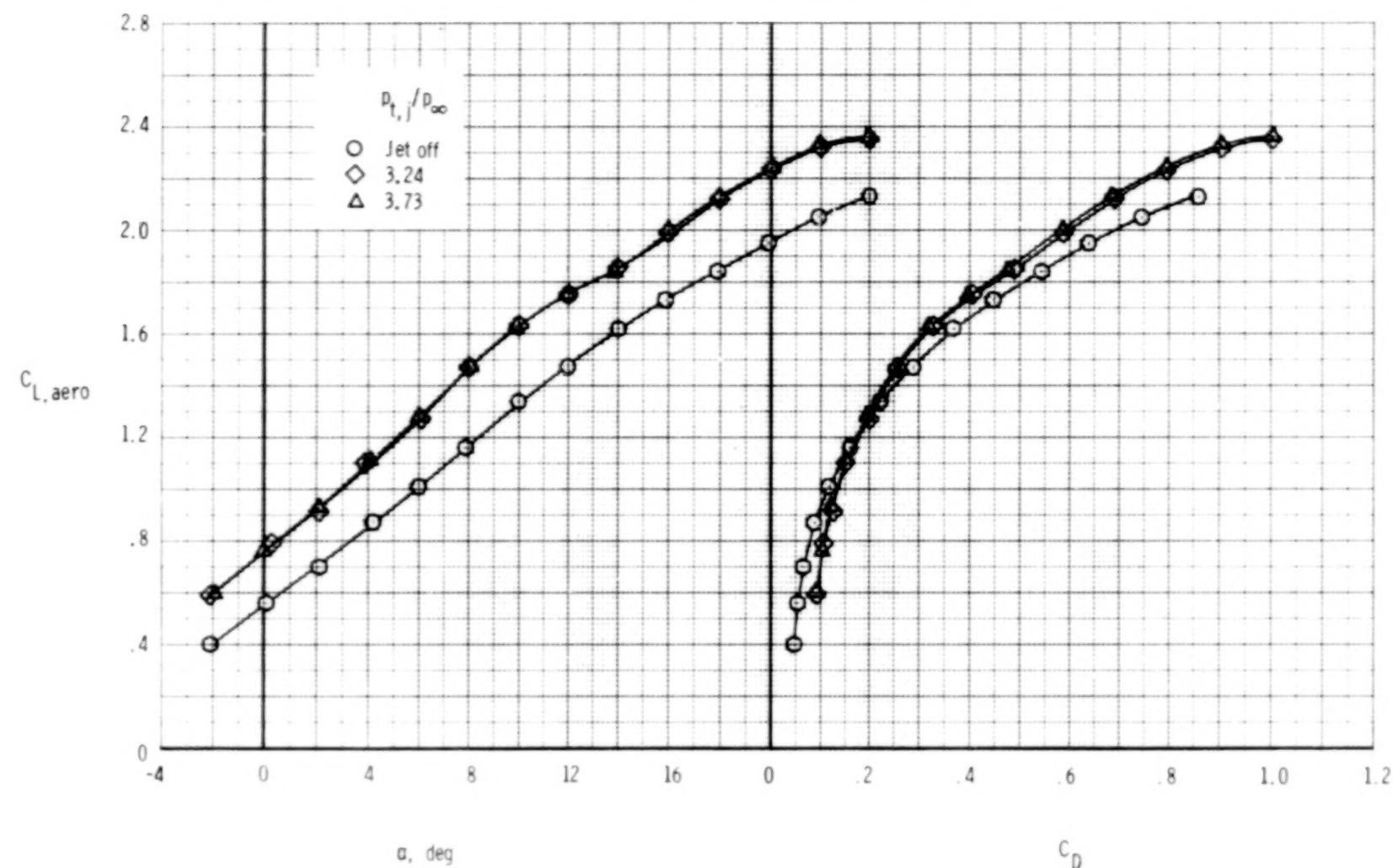
Figure 18.- Thrust-removed lift and drag characteristics at M = 0.186 for nozzle conf 3. $\delta_{TE} = 30^O$; $\delta_{LE} = \delta_C = \delta_{C,TE} = 0^O$; H_2 canard.

Figure 19.- Thrust-removed lift and drag characteristics at $M = 0.186$ for nozzle conf 4. $\delta_{TE} = 30^O$; $\delta_{LE} = \delta_C = \delta_{C,TE} = 0^O$; H_2 canard.

109
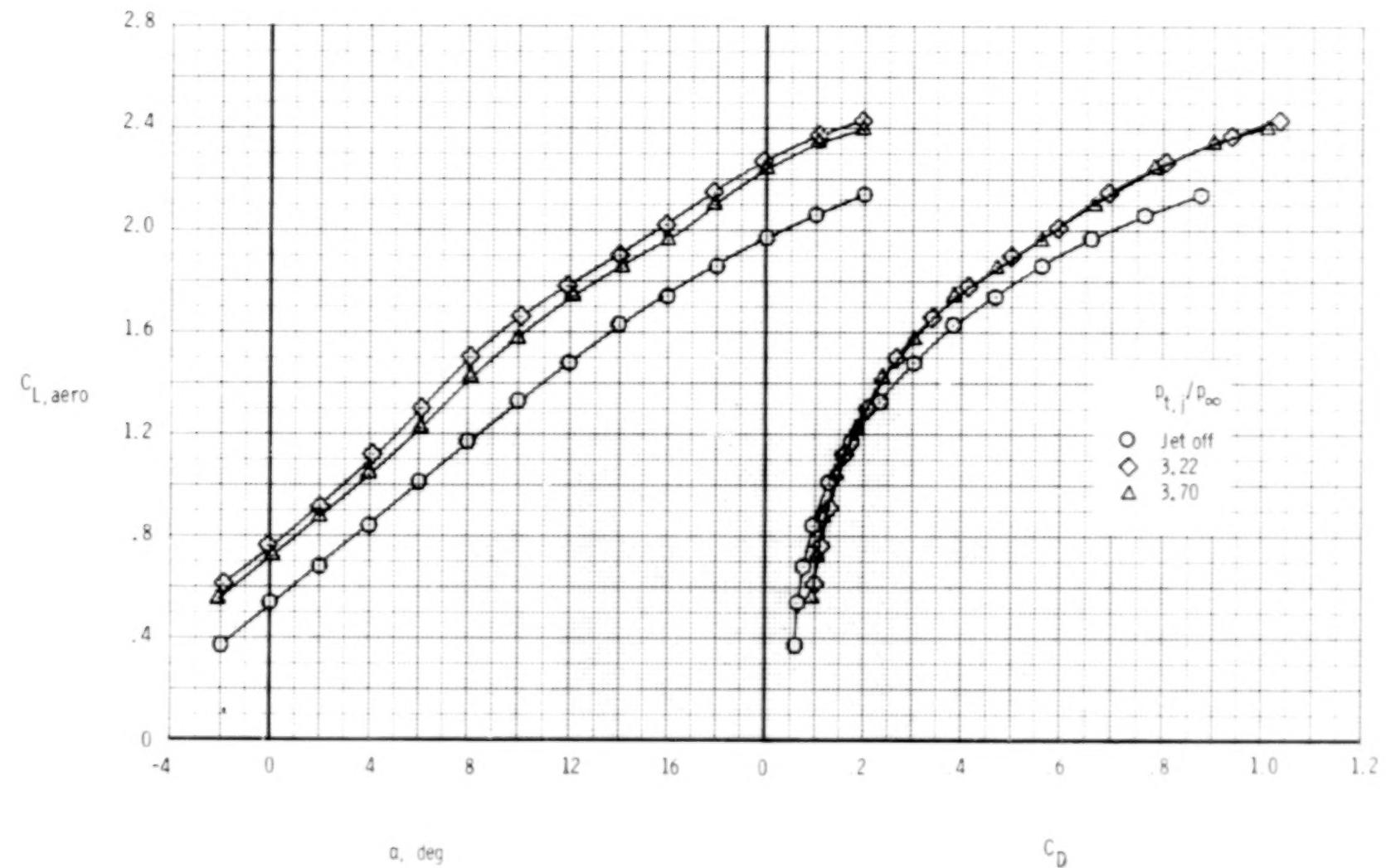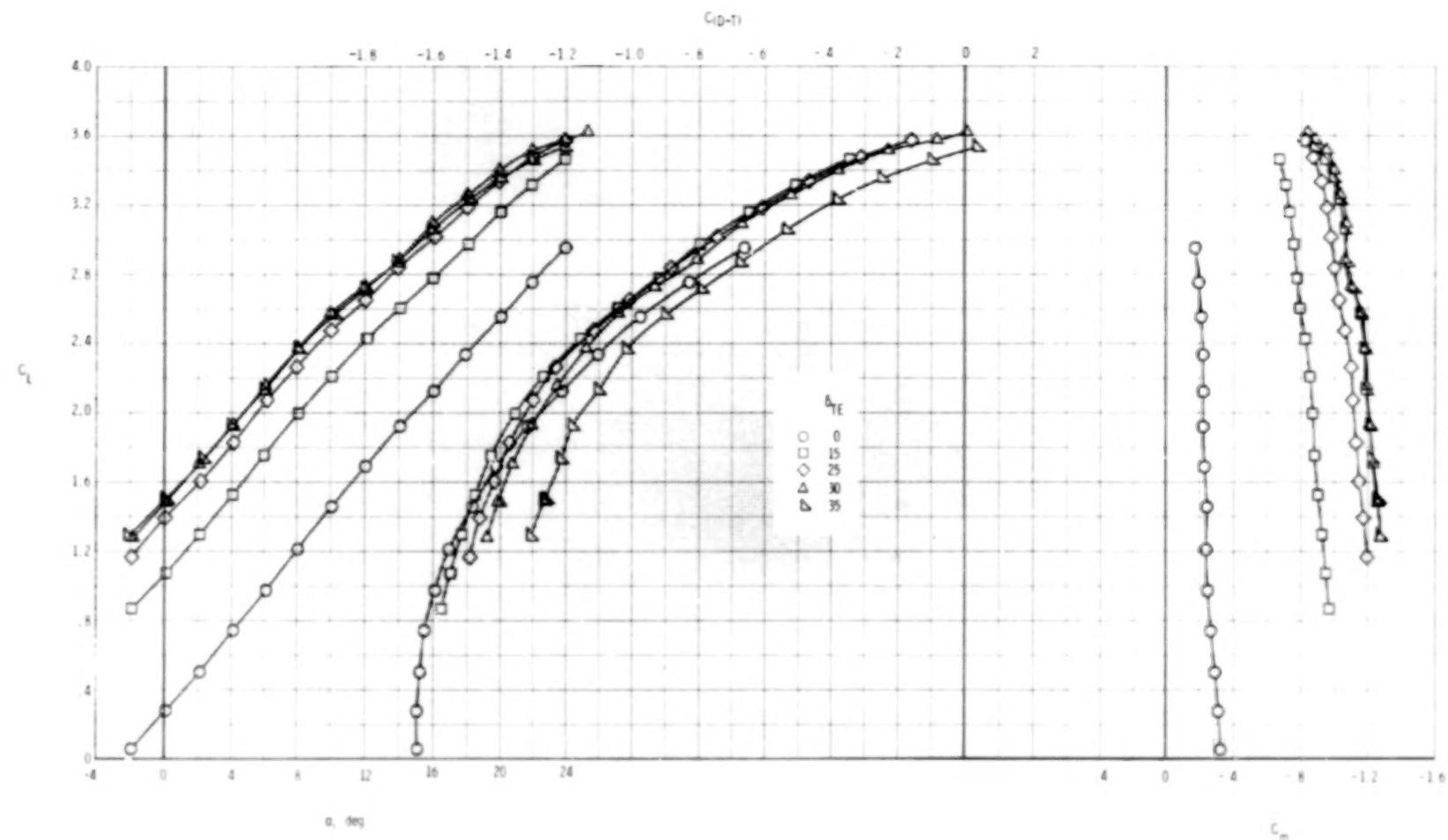
(a) Total coefficient data.

Figure 20.- Effect of trailing-edge flap deflection at $M = 0.186$ and $(p_{t,j}/p_\infty)_{av} = 3.23$ for nozzle conf 1. $\delta_{LE} = \delta_C = \delta_{C,TE} = 0^O$; H_2 canard.
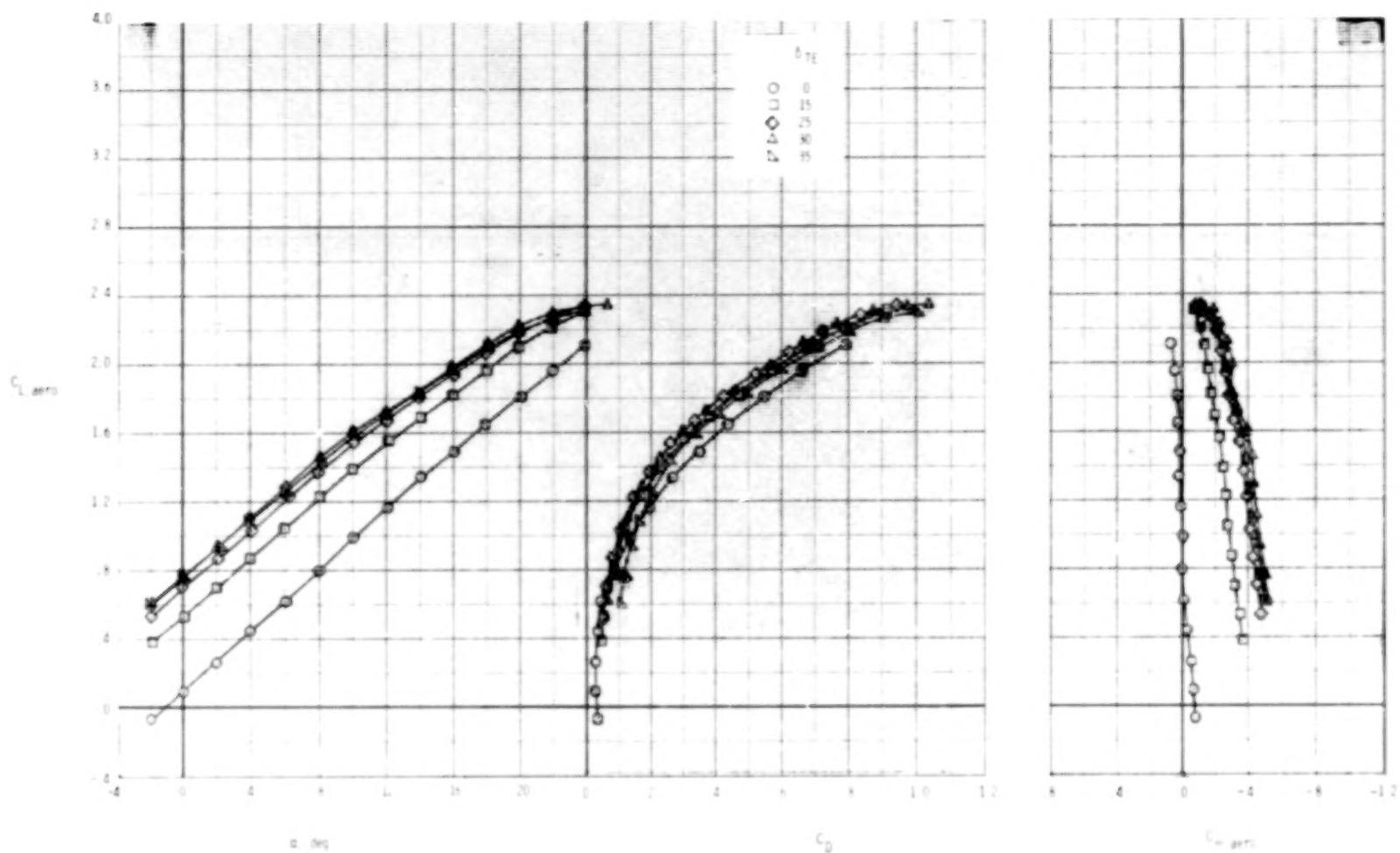
(b) Thrust-removed data.

Figure 20.- Concluded.
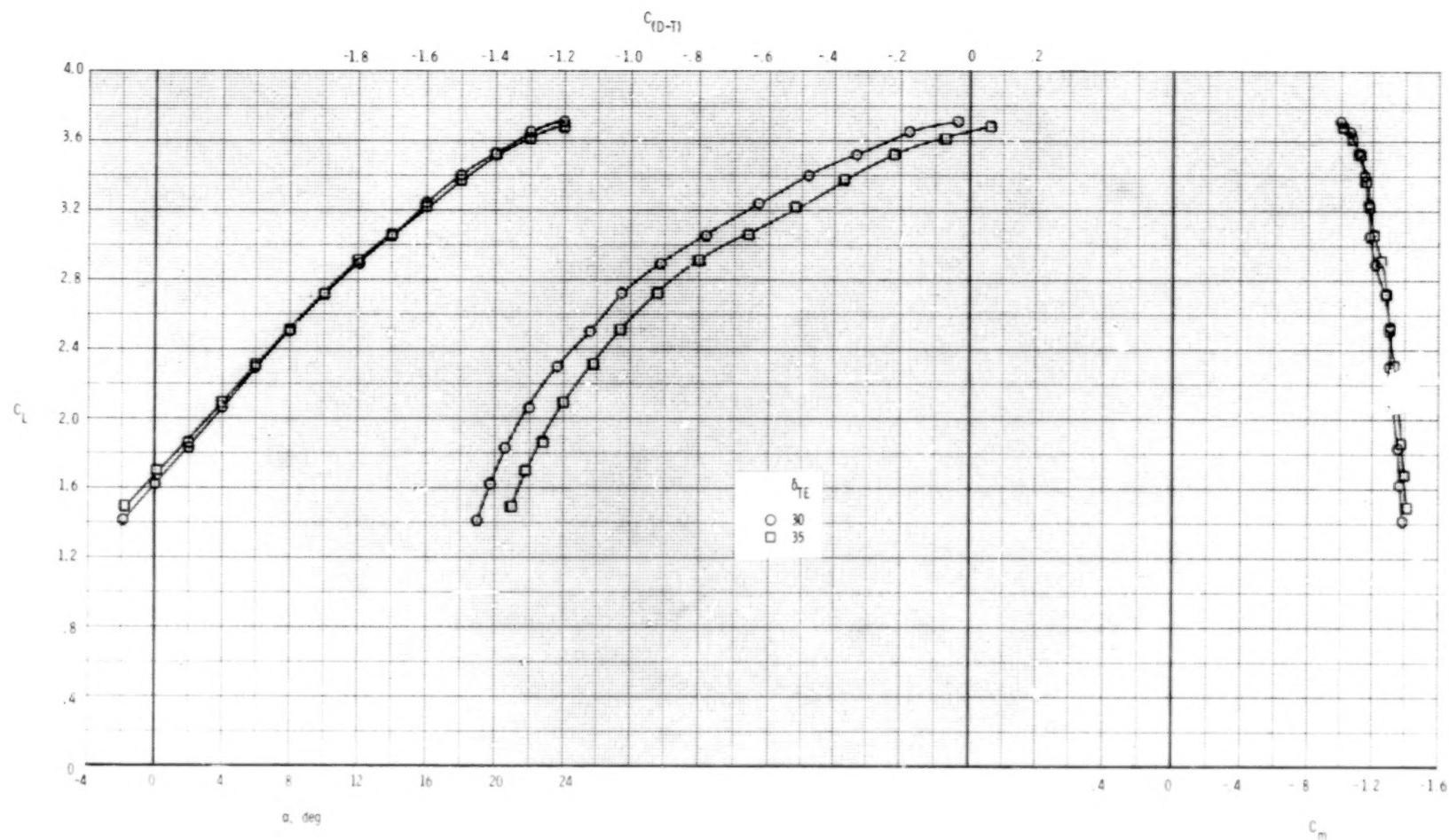
(a) Total coefficient data.

Figure 21.- Effect of trailing-edge flap deflection at $M = 0.186$ and $(p_{t,j}/p_\infty)_{av} = 3.22$ for nozzle conf 2. $\delta_{LE} = \delta_C = \delta_{C,TE} = 0°$; H_3 canard.
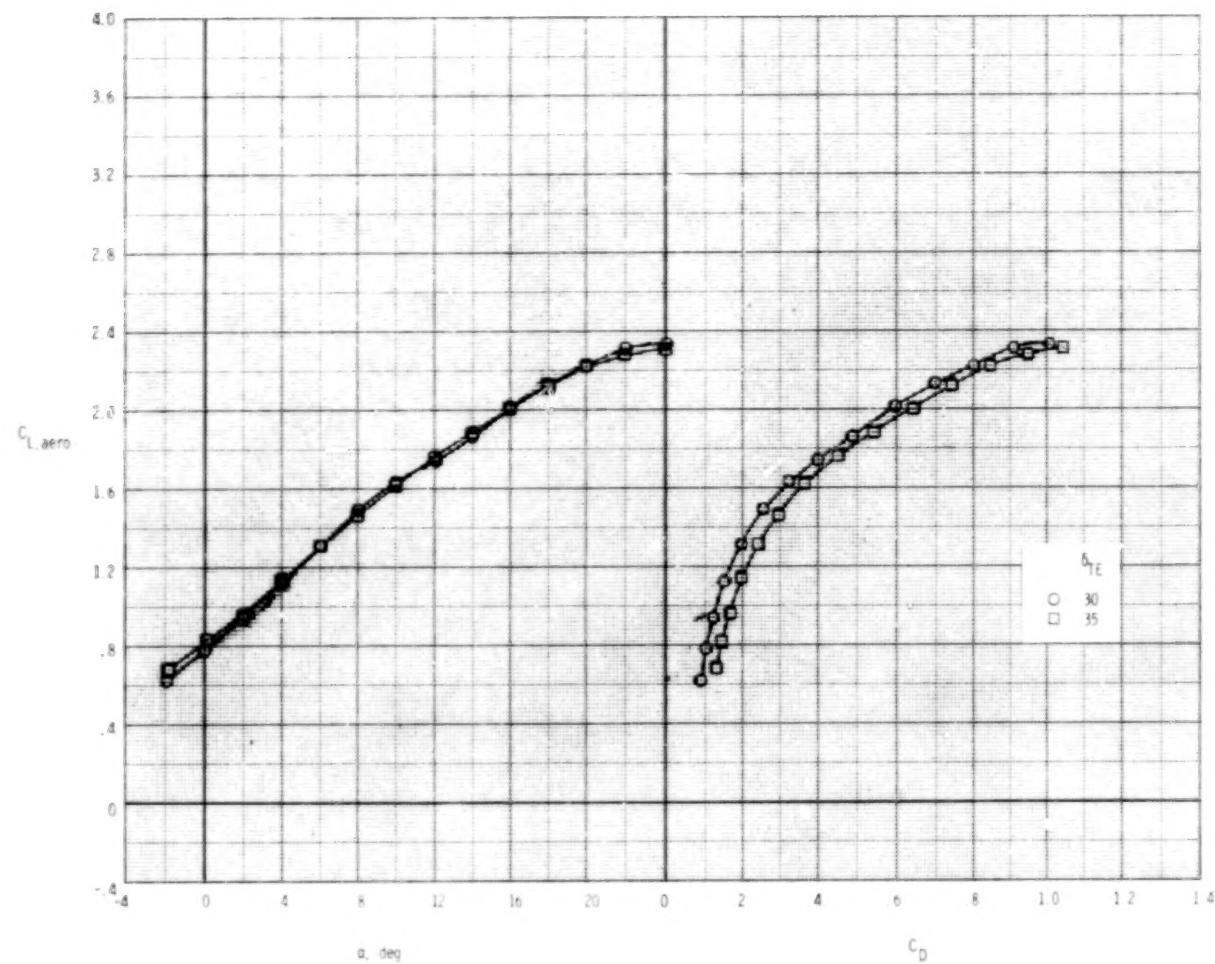
(b) Thrust-removed data.

Figure 21.- Concluded.

113
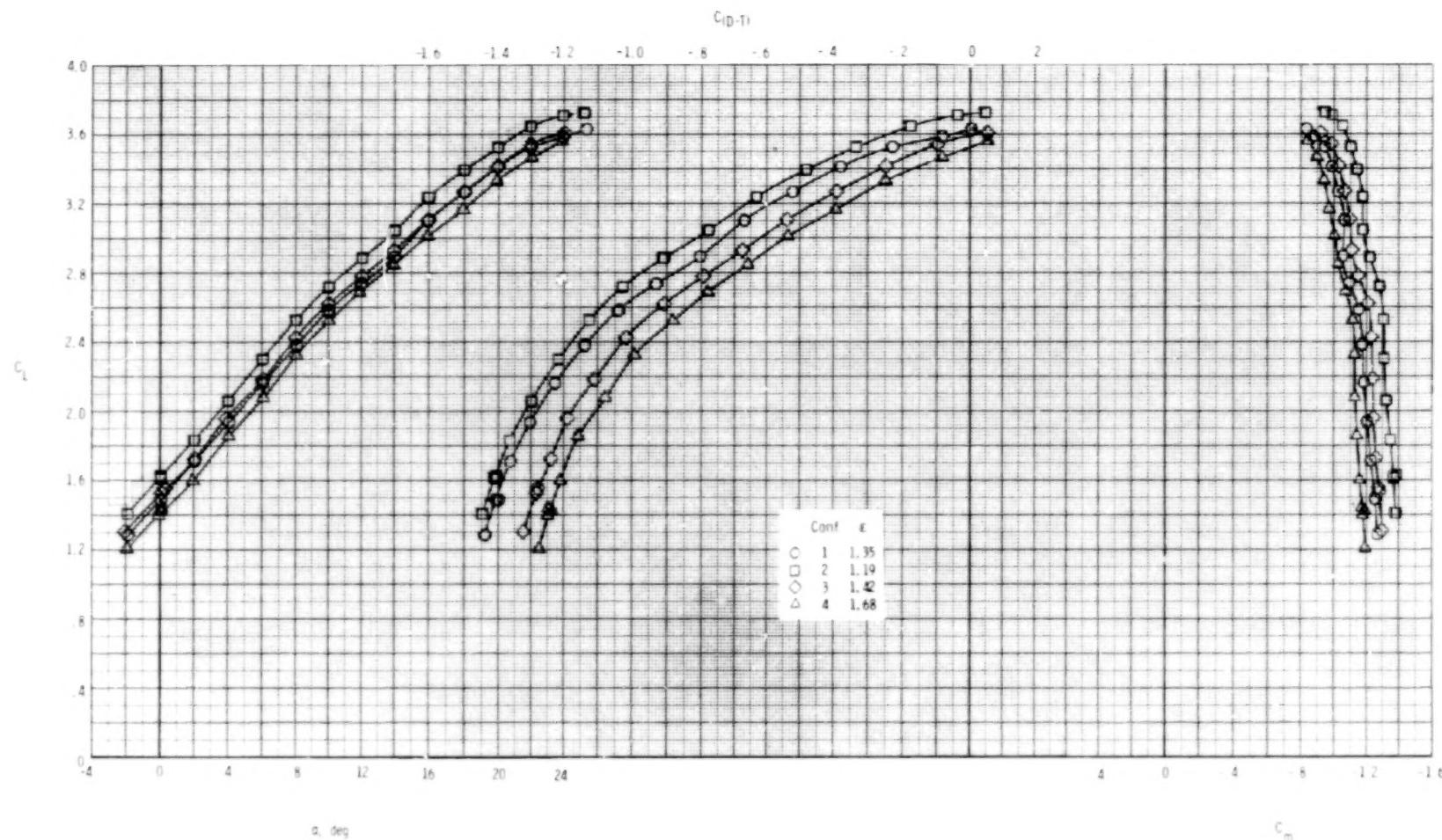
(a) Total coefficient data.

Figure 22.- Effect of nozzle configuration (nozzle expansion ratio) at $M = 0.186$ and $(p_{t,j}/p_\infty)_{av} = 3.23$ for $\delta_{TE} = 30^O$; $\delta_{LE} = \delta_C = \delta_{C,TE} = 0^O$; H_2 canard.
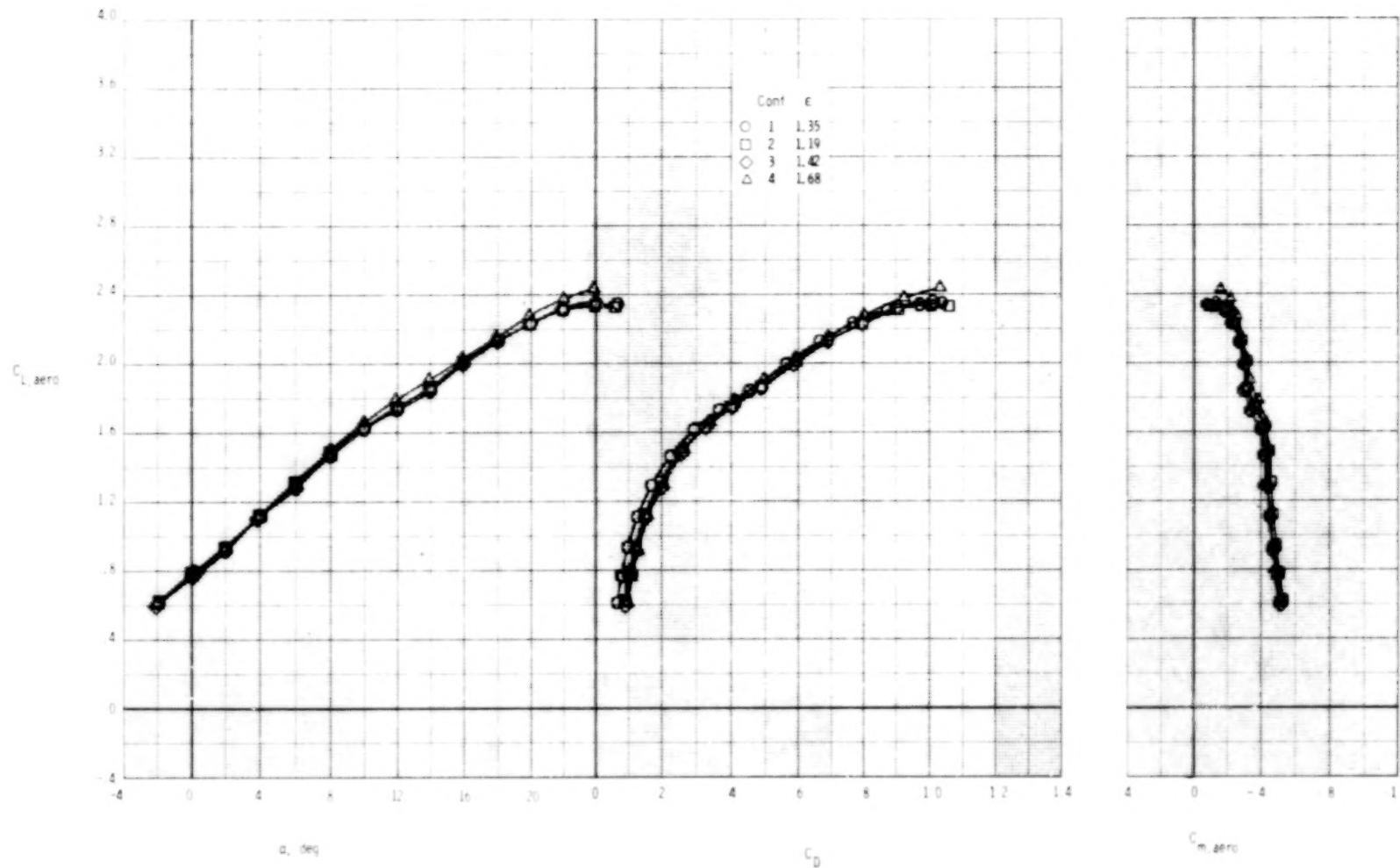
(b) Thrust-removed data.

Figure 22.- Concluded.
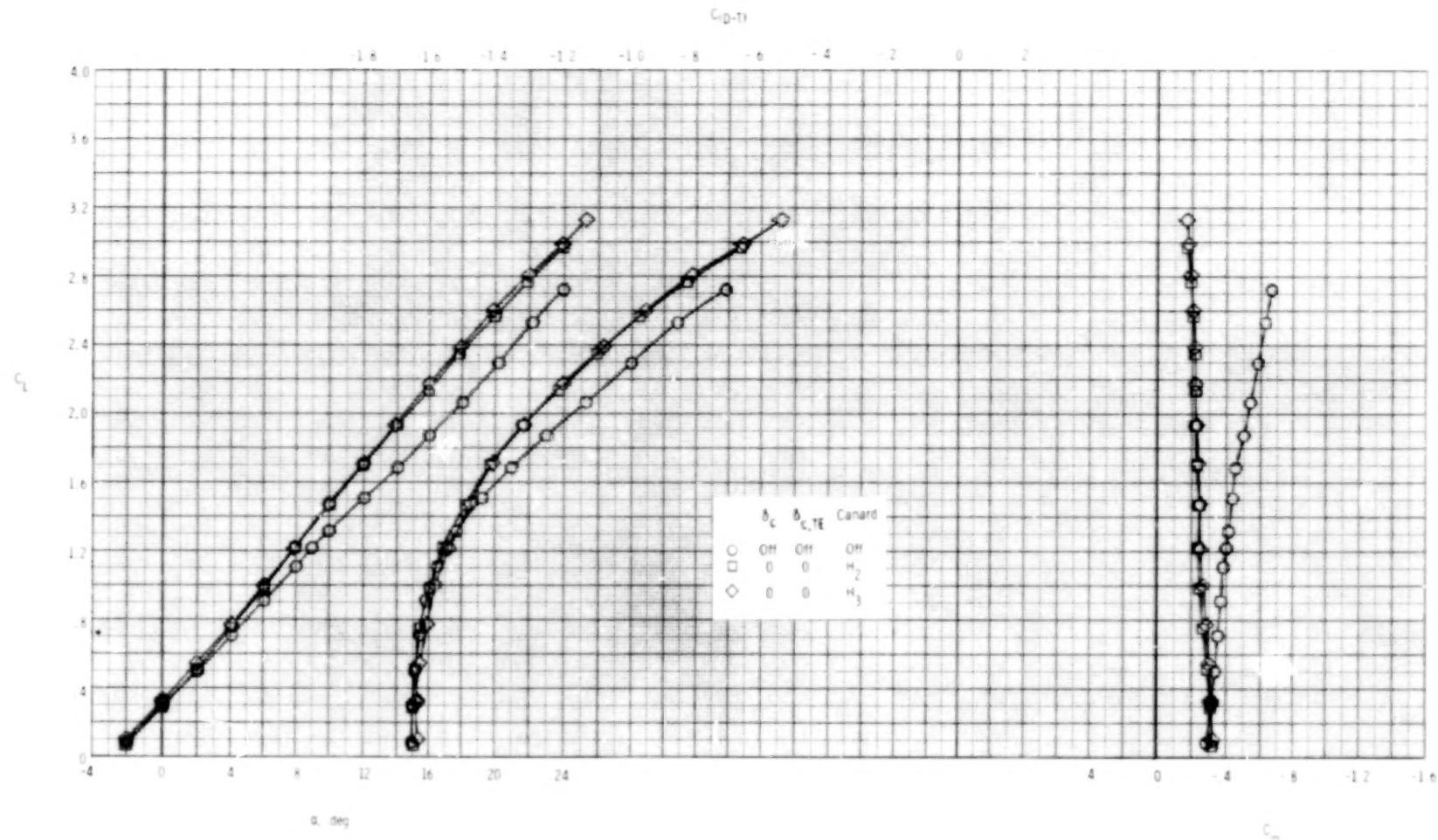
(a) Total coefficient data.

Figure 23.- Effect of canard planform at $M = 0.186$ and $(p_{t,j}/P_\infty)_{av} = 3.25$ for nozzle conf 1 and $\delta_{TE} = \delta_{LE} = 0^O$.
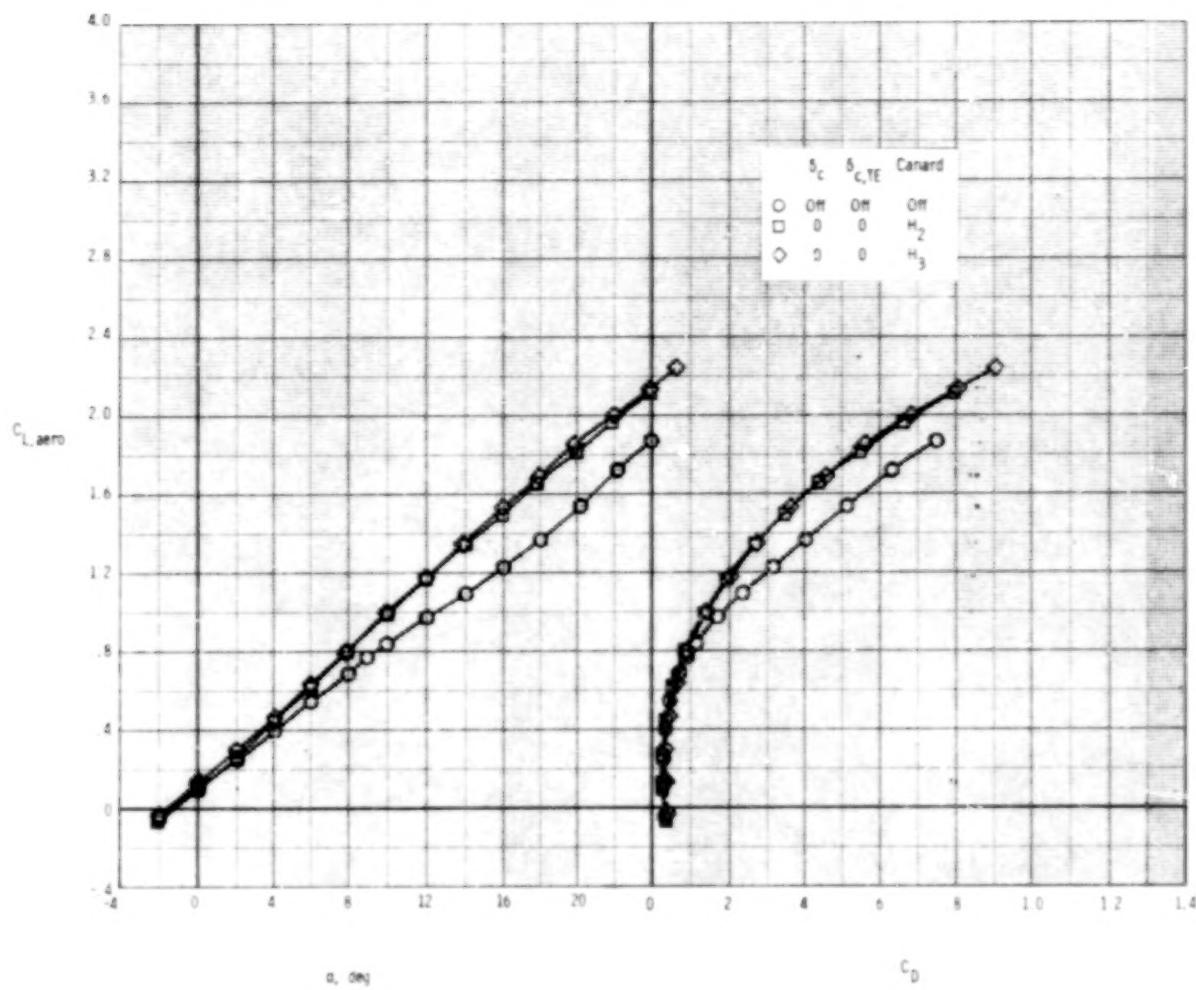
(b) Thrust-removed data.

Figure 23.- Concluded.
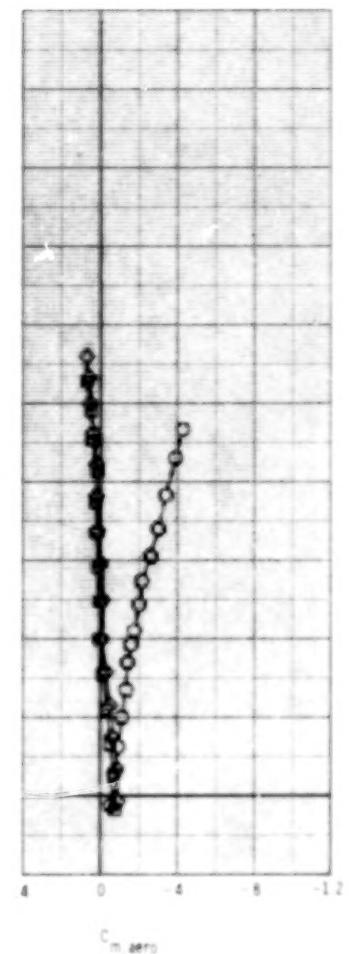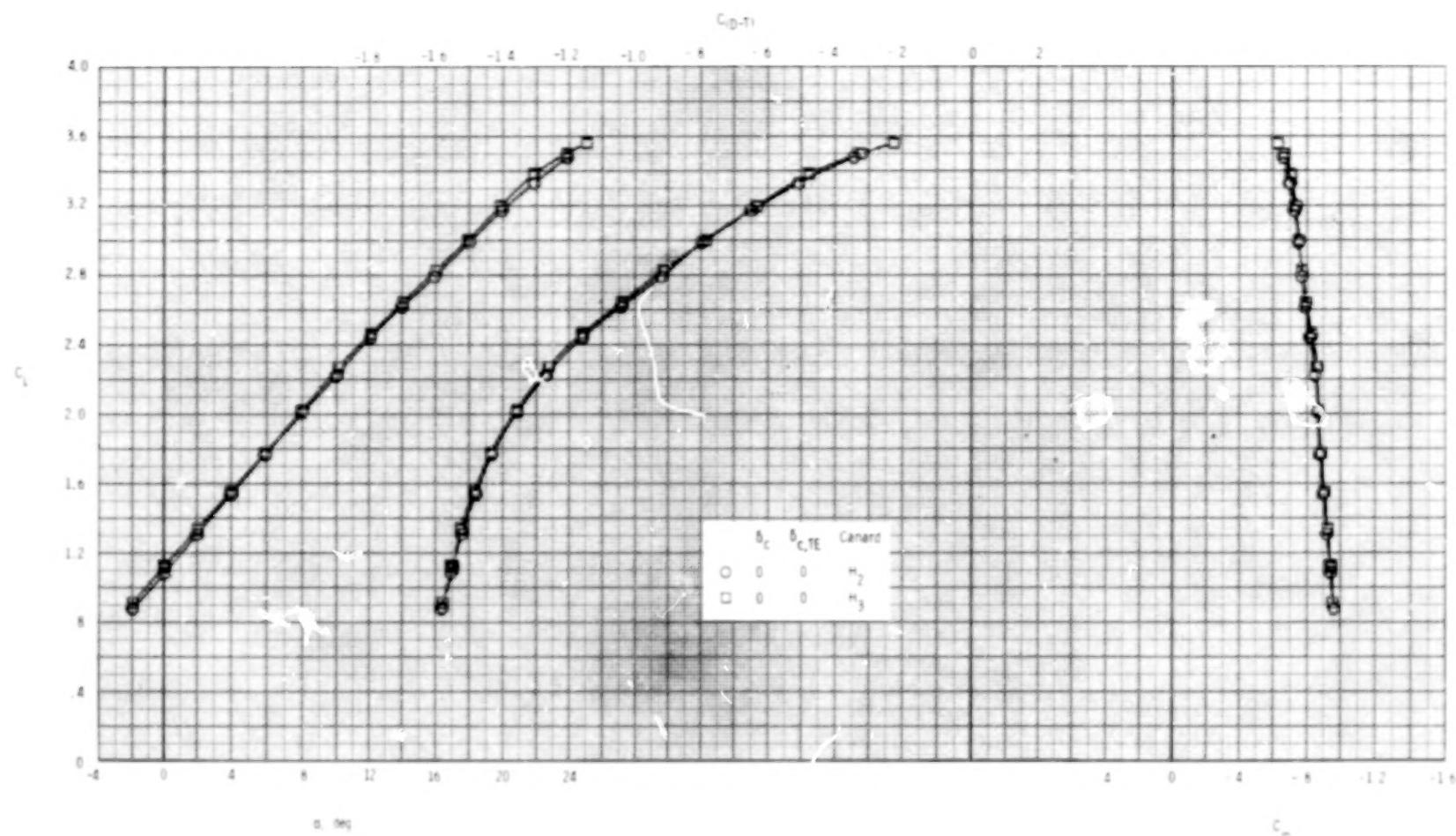
(a) Total coefficient data.

Figure 24.- Effect of canard planform at $M = 0.186$ and $(p_{t,j}/p_\infty)_{av} = 3.24$ for nozzle conf 1 and $\delta_{TE} = 15^\circ$. $\delta_{LE} = 0^\circ$.
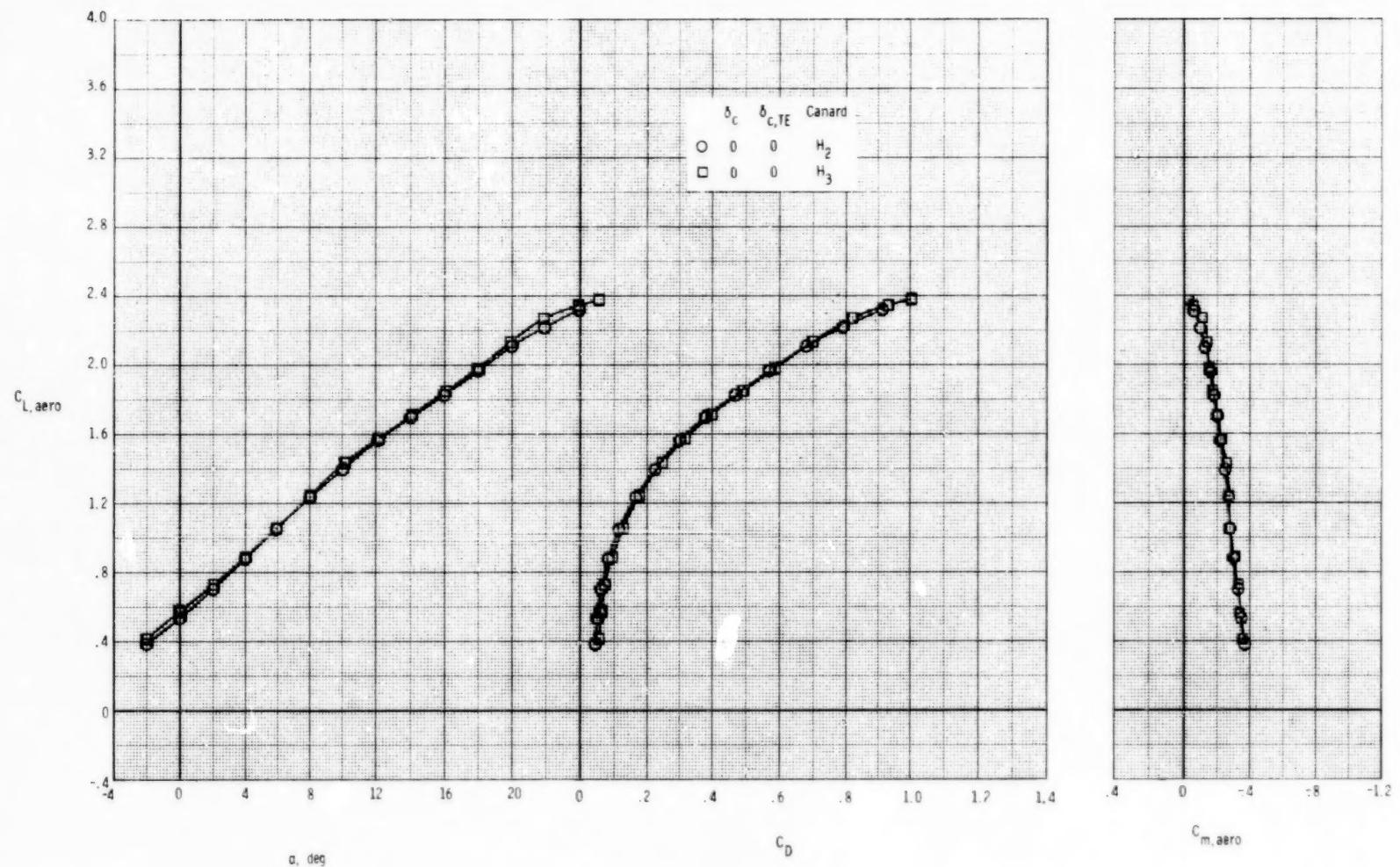
(b) Thrust-removed data.

Figure 24.- Concluded.
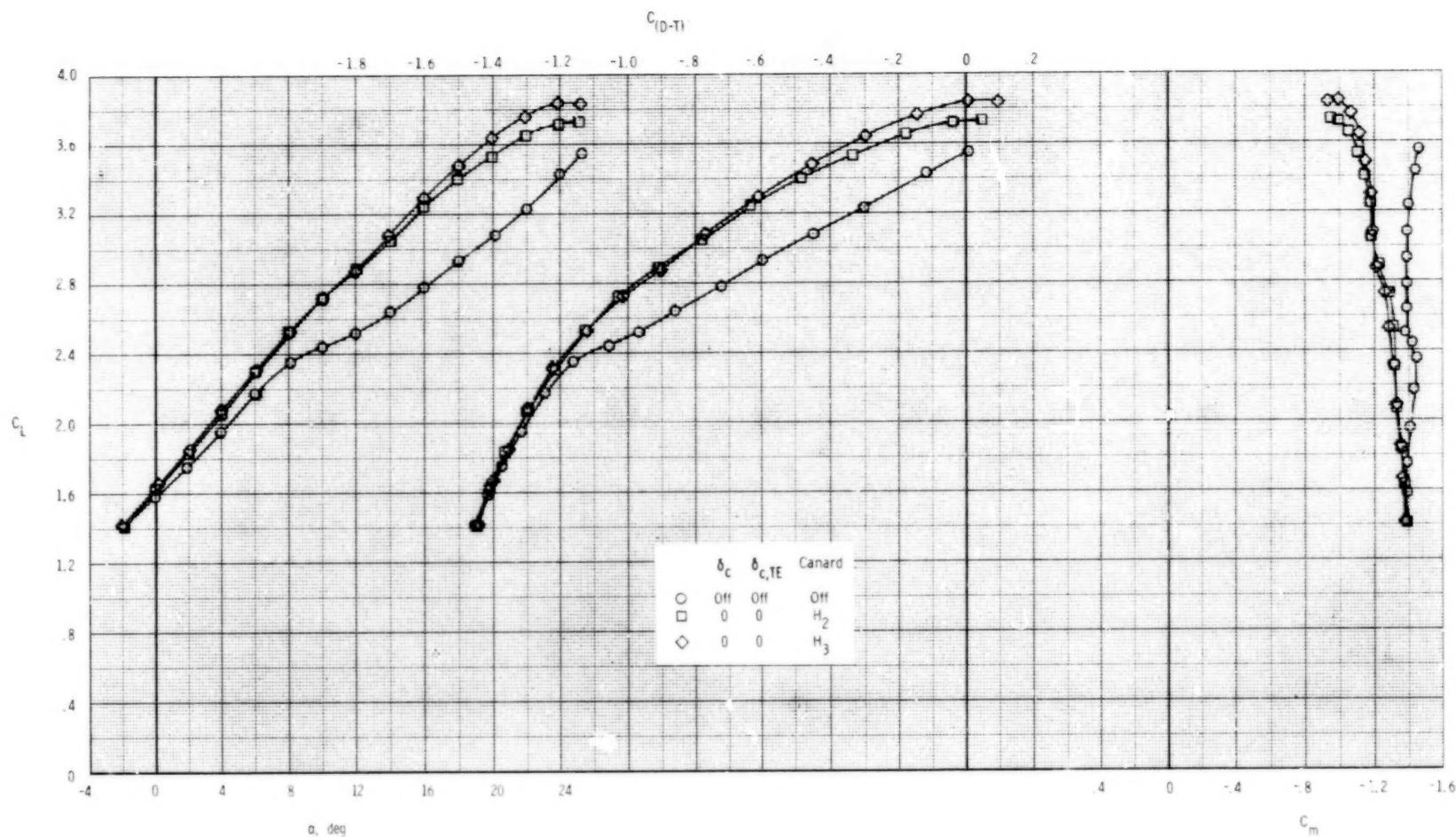
(a) Total coefficient data.

Figure 25.- Effect of canard planform at $M = 0.186$ and $(p_{t,j}/p_\infty)_{av} = 3.24$ for nozzle conf 2 and $\delta_{TE} = 30^\circ$. $\delta_{LE} = 0^\circ$.
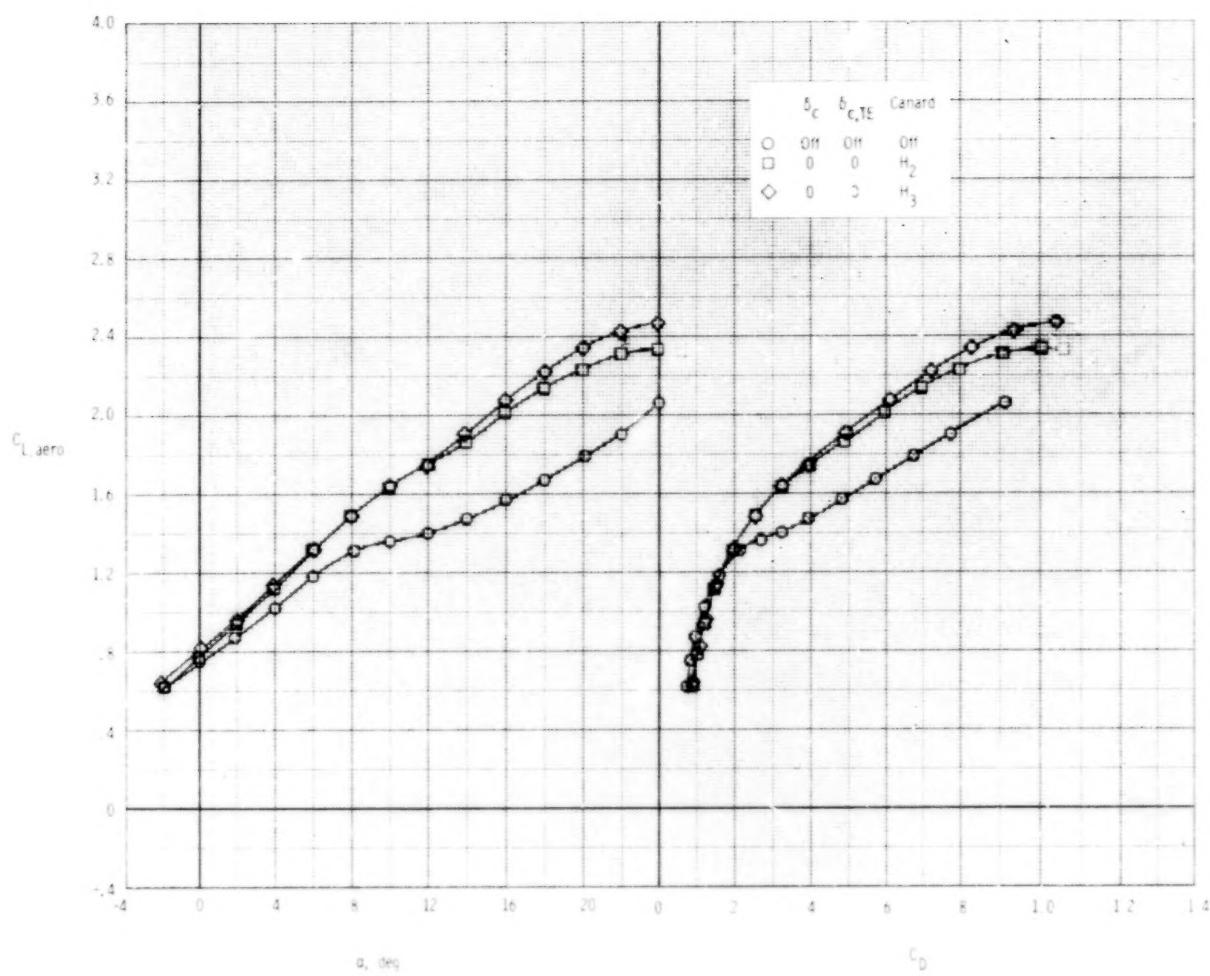
(b) Thrust-removed data.

Figure 25.- Concluded.
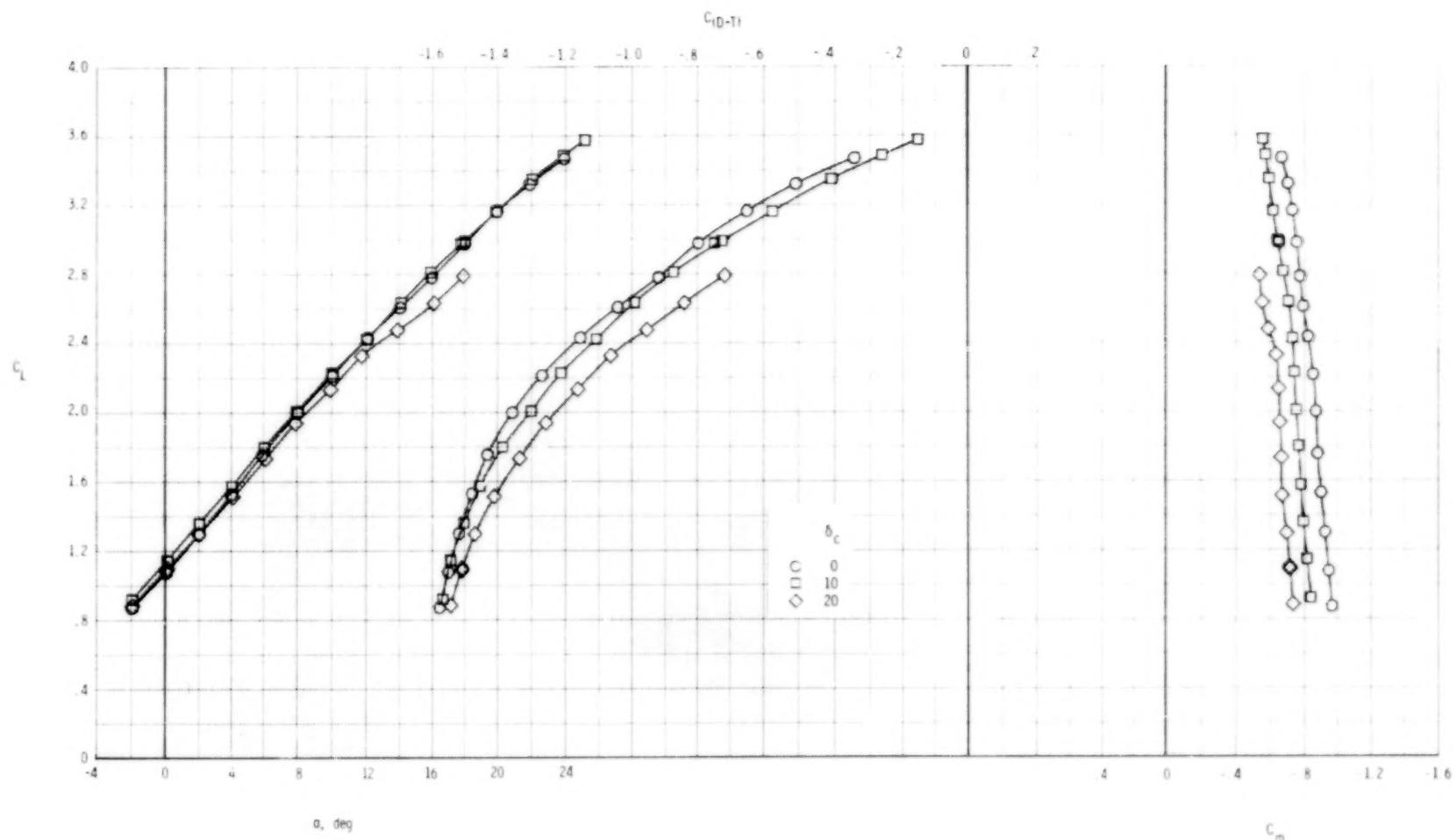
(a) Total coefficient data.

Figure 26.- Effect of canard incidence at $M = 0.186$ and $(p_{t,j}/p_\infty)_{av} = 3.23$ for nozzle conf 1 and $\delta_{TE} = 15^o$. $\delta_{LE} = \delta_{c.TE} = 0^o$; H_2 canard.
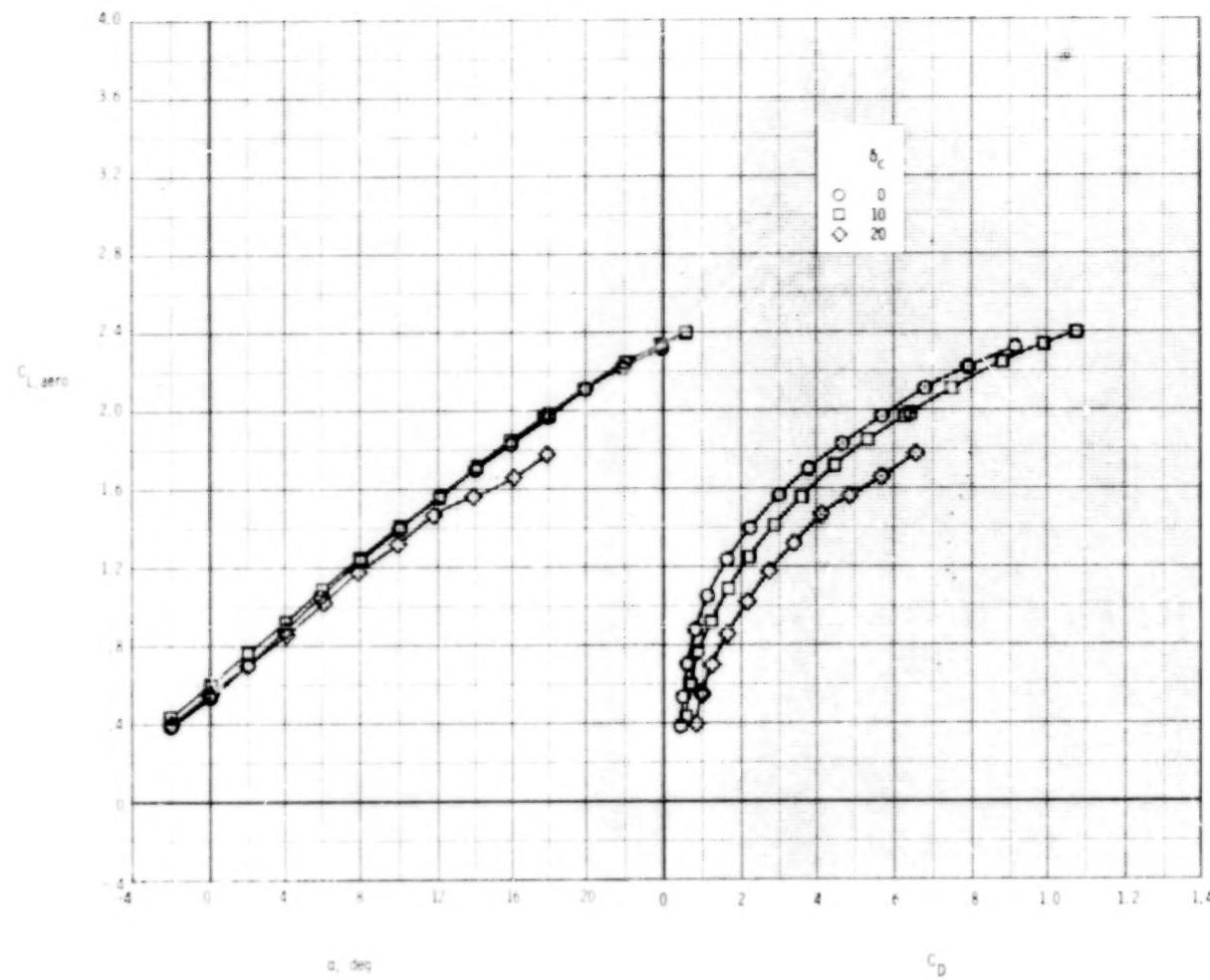
(b) Thrust-removed data.

Figure 26.- Concluded.
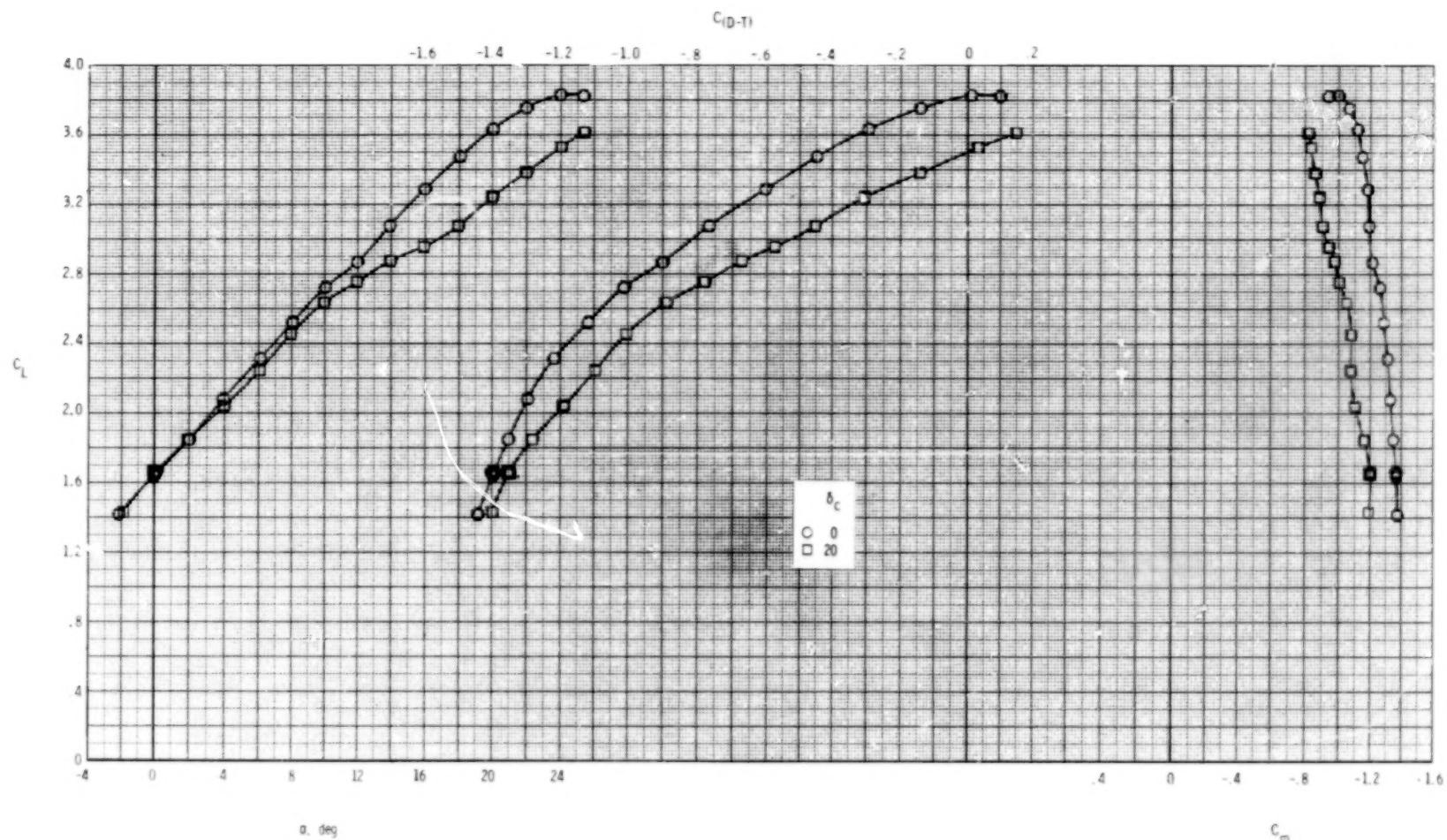
(a) Total coefficient data.

Figure 27.- Effect of canard incidence at $M = 0.186$ and $(p_{t,j}/p_\infty)_{av} = 3.24$ for nozzle conf 2 and $\delta_{TE} = 30^\circ$. $\delta_{LE} = \delta_{C,TE} = 0^\circ$; H_3 canard.
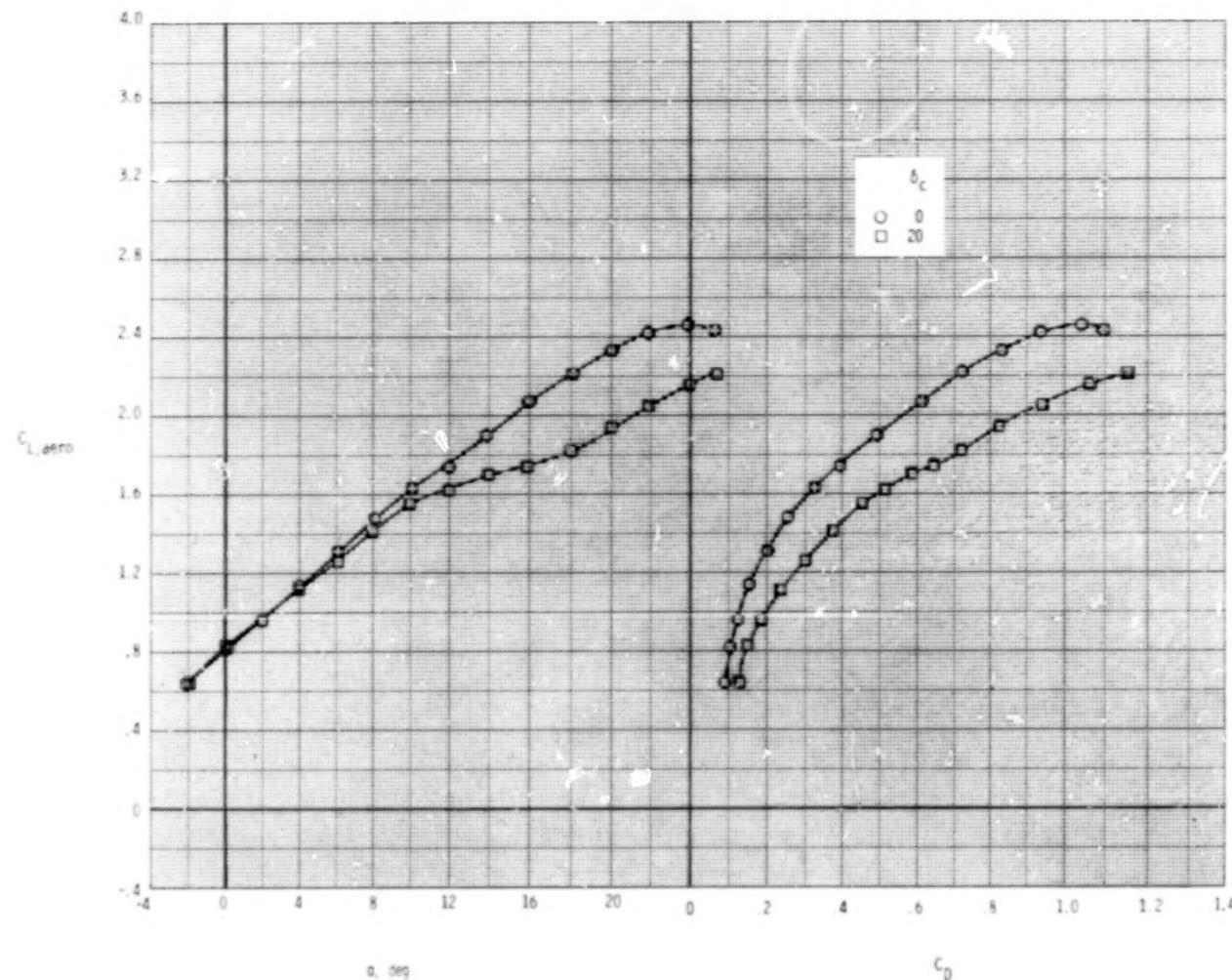
(b) Thrust-removed data.

Figure 27.- Concluded.

125

$C_{(D-T)}$
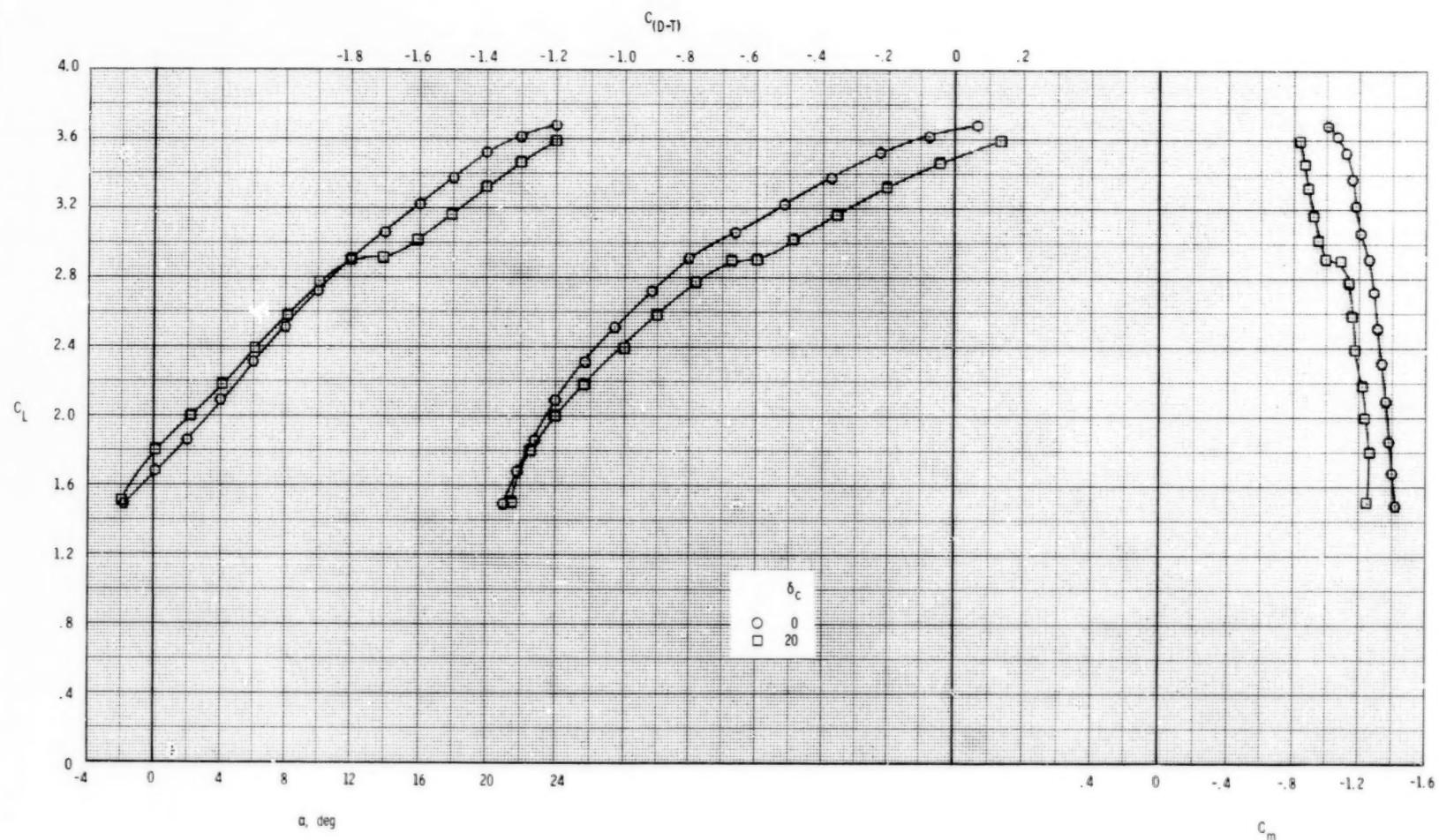
(a) Total coefficient data.

Figure 28.- Effect of canard incidence at $M = 0.186$ and $(p_{t,j}/p_\infty)_{av} = 3.22$ for nozzle conf 2 and $\delta_{TE} = 35^o$; $\delta_{LE} = \delta_{c,TE} = 0^o$; H_2 canard.
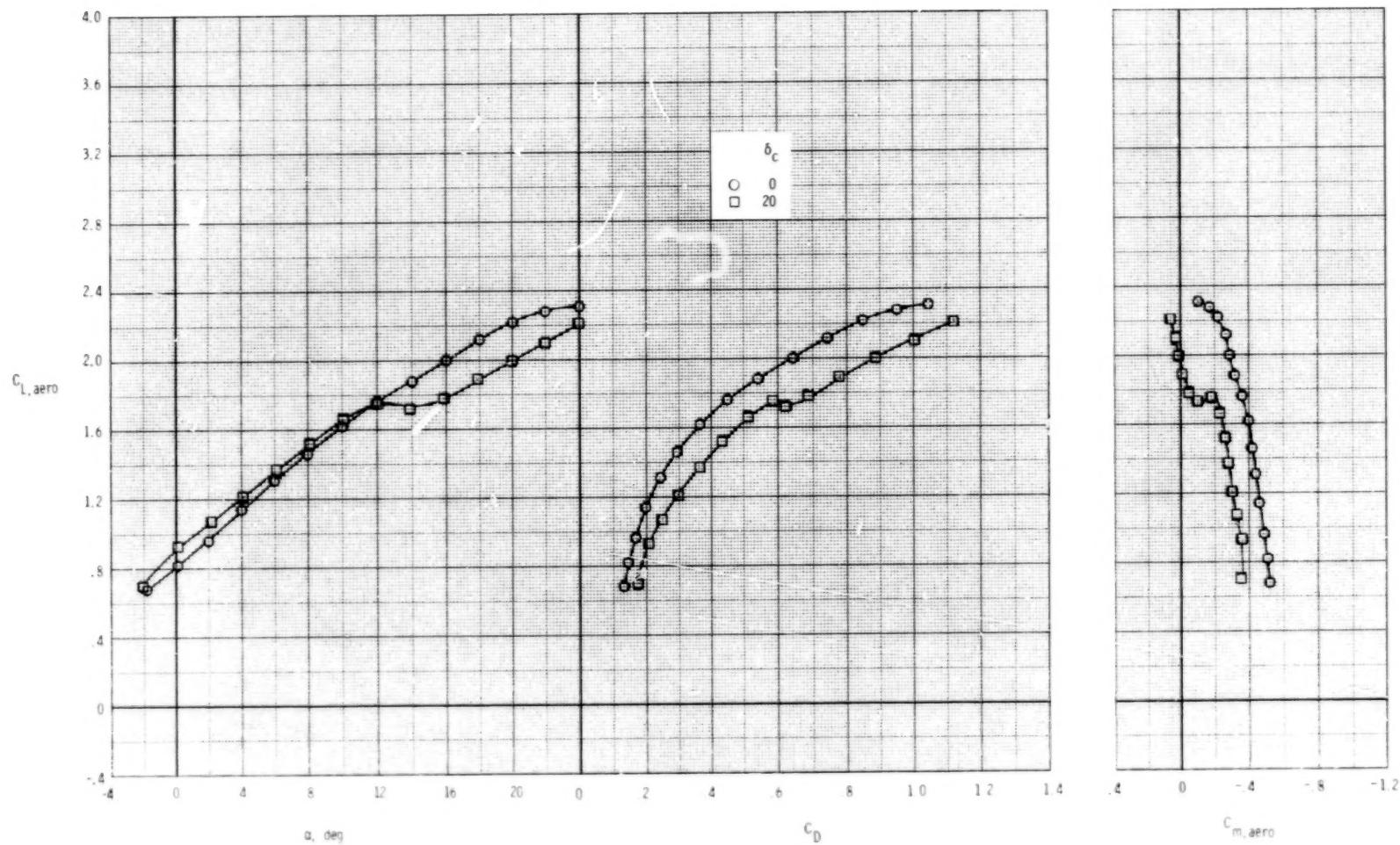
(b) Thrust-removed data.

Figure 28.- Concluded.
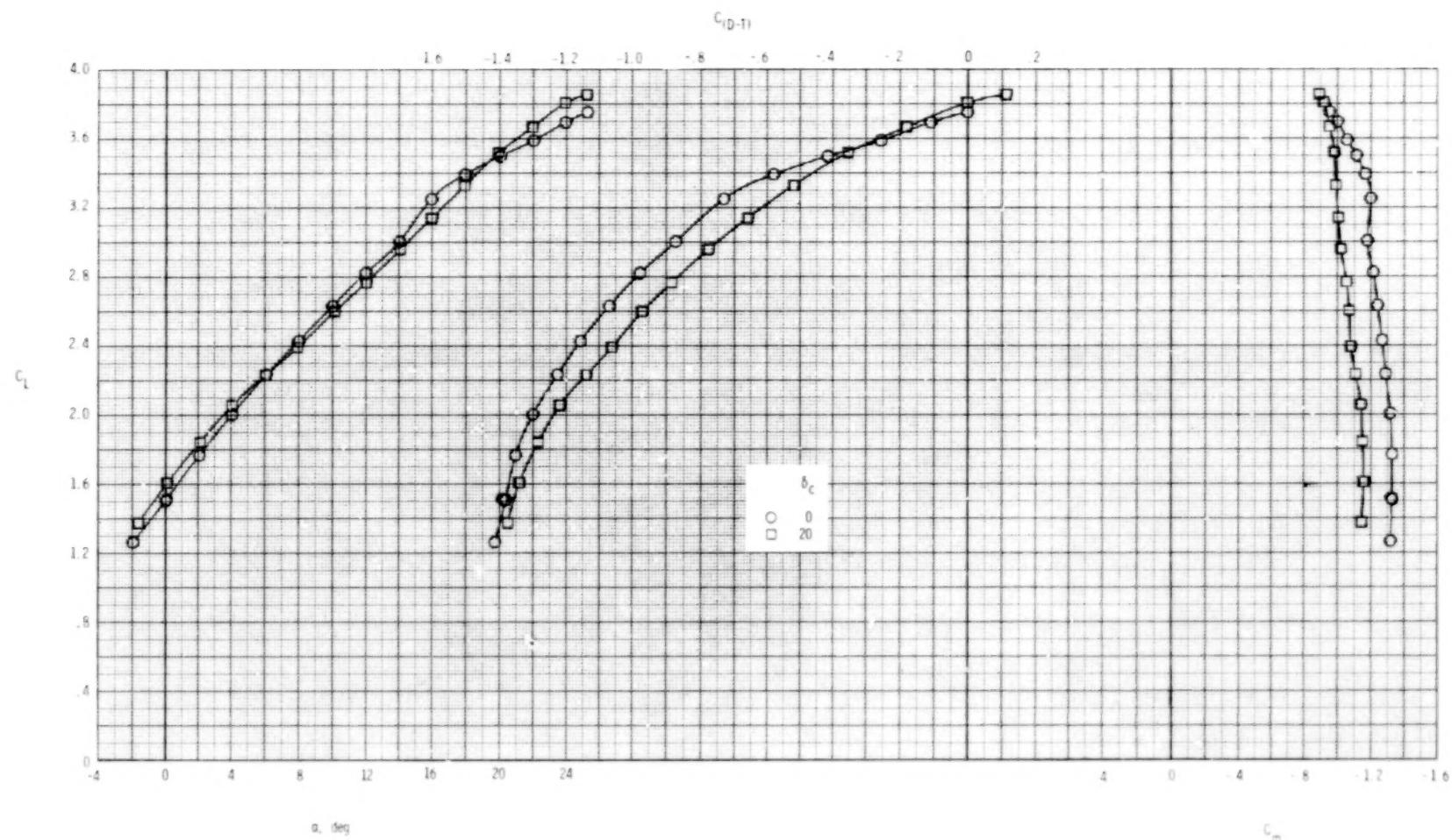
(a) Total coefficient data.

Figure 29.- Effect of canard incidence with $\delta_{LE} = 20^{\circ}$ at $M = 0.186$ and $(p_{t,j}/P_\infty)_{av} = 3.25$ for nozzle conf 2. $\delta_{TE} = 30^{\circ}$; $\delta_{c,TE} = 0^{\circ}$; H_2 canard.
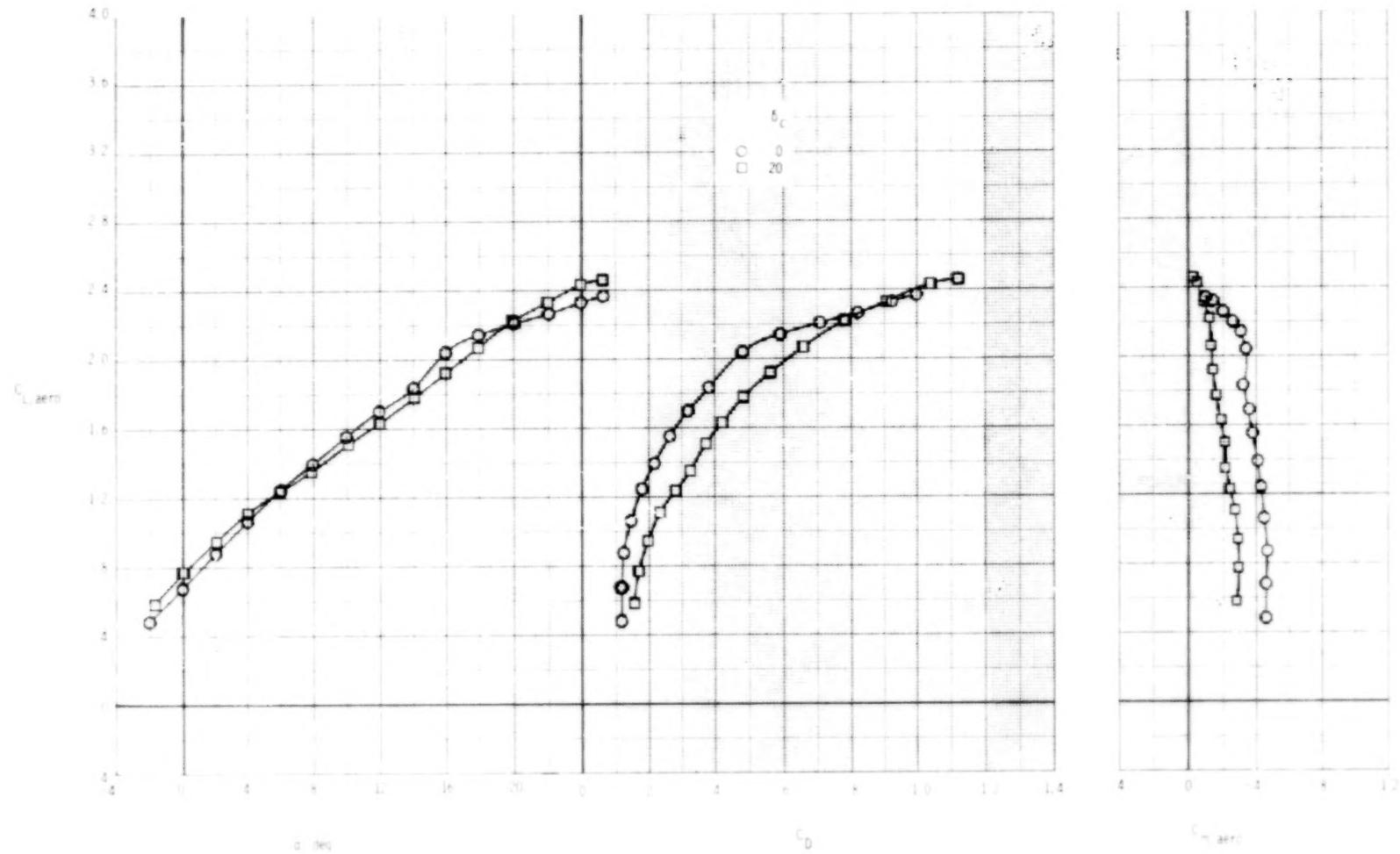
(b) Thrust-removed data.

Figure 29.- Concluded.
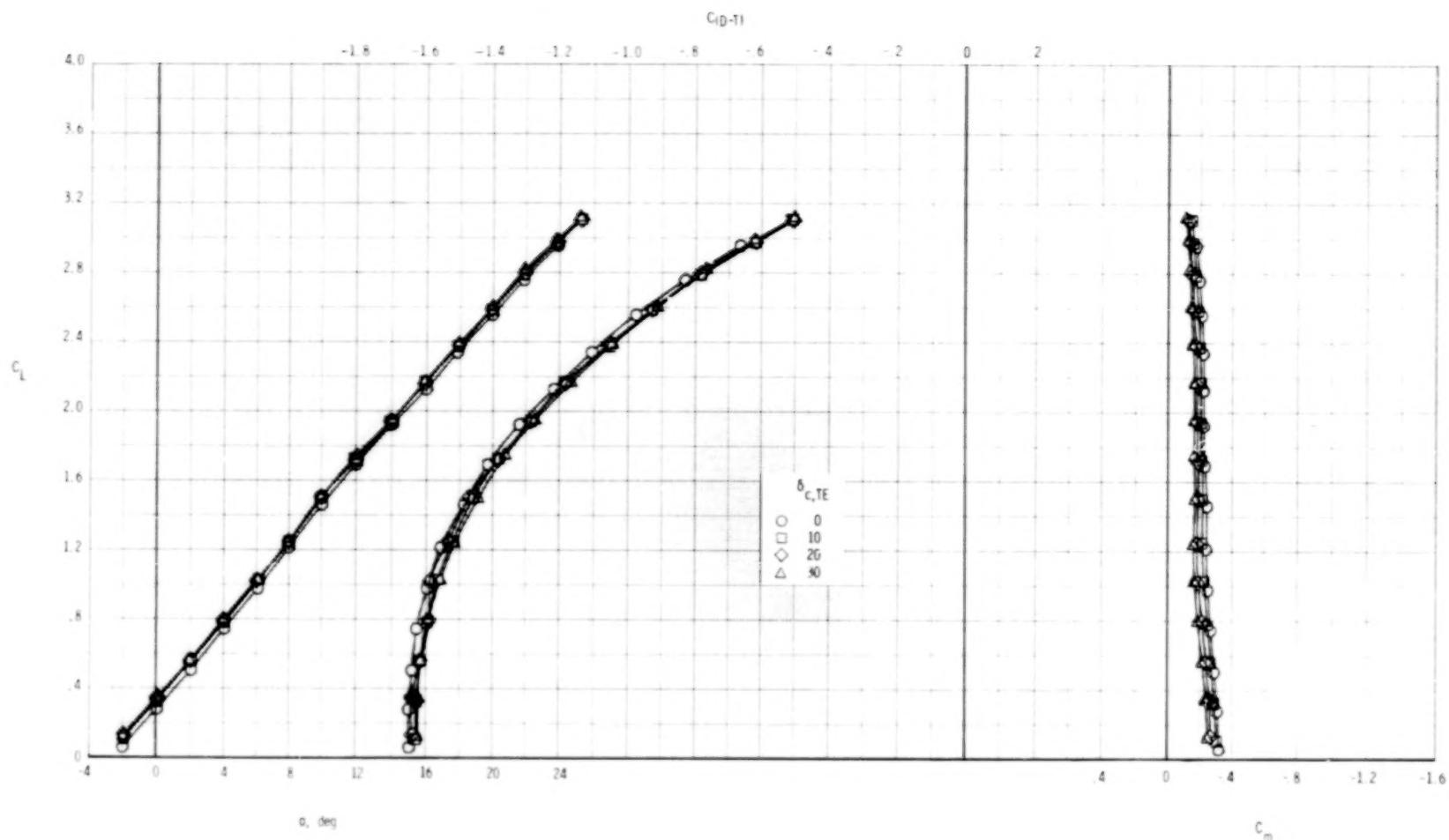
(a) Total coefficient data.

Figure 30.- Effect of canard trailing-edge flap deflection at $M = 0.186$ and $(p_{t,j}/p_\infty)_{av} = 3.24$ for nozzle conf 1. $\delta_{TE} = \delta_{LE} = \delta_C = 0°$; H_2 canard.
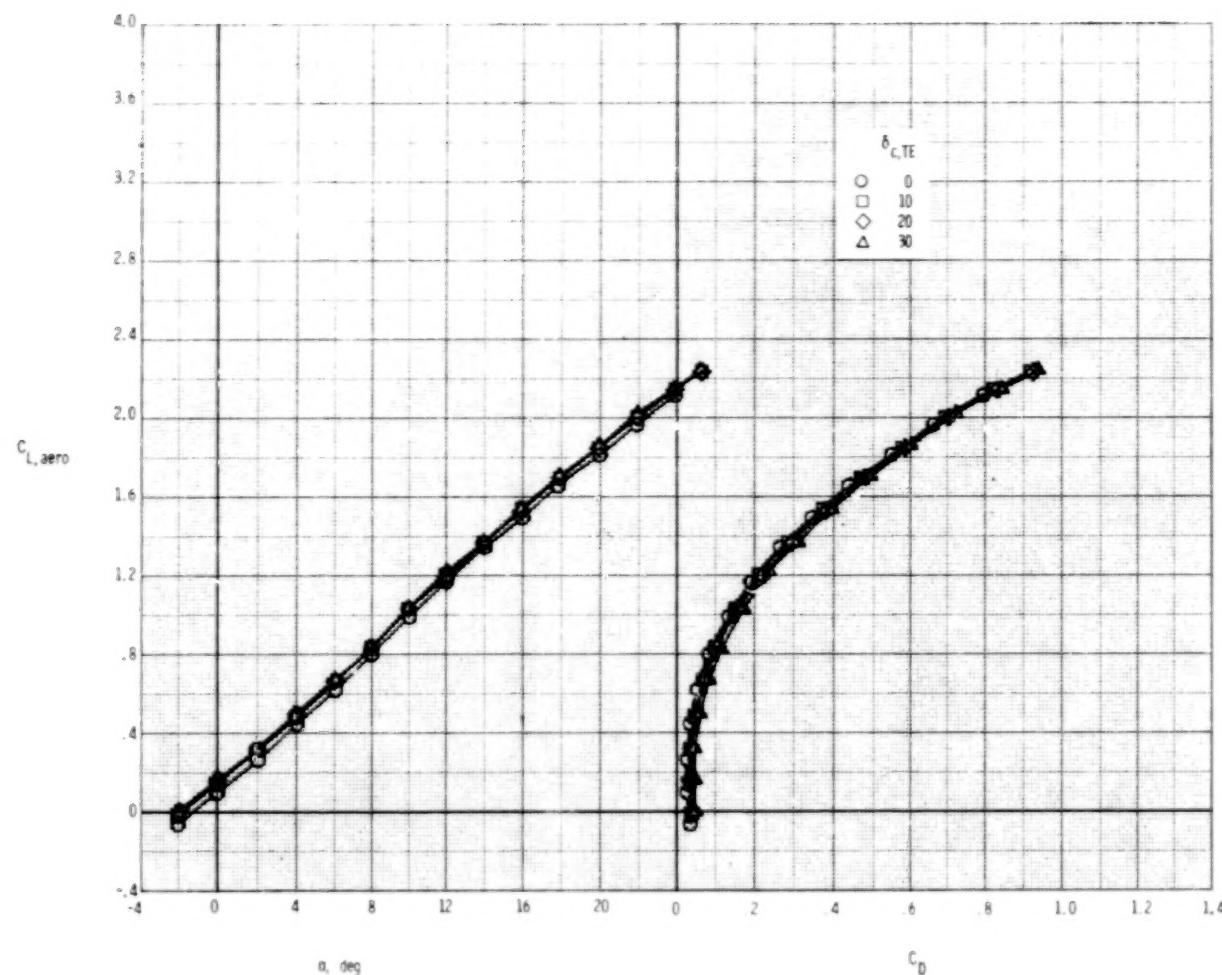
(b) Thrust-removed data.

Figure 30.- Concluded.
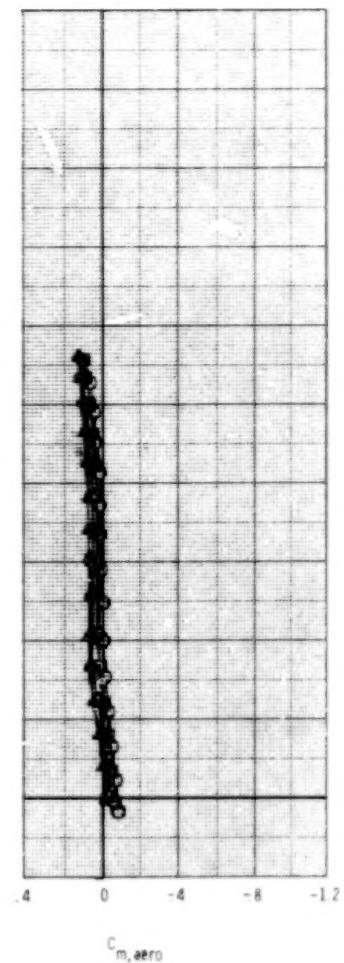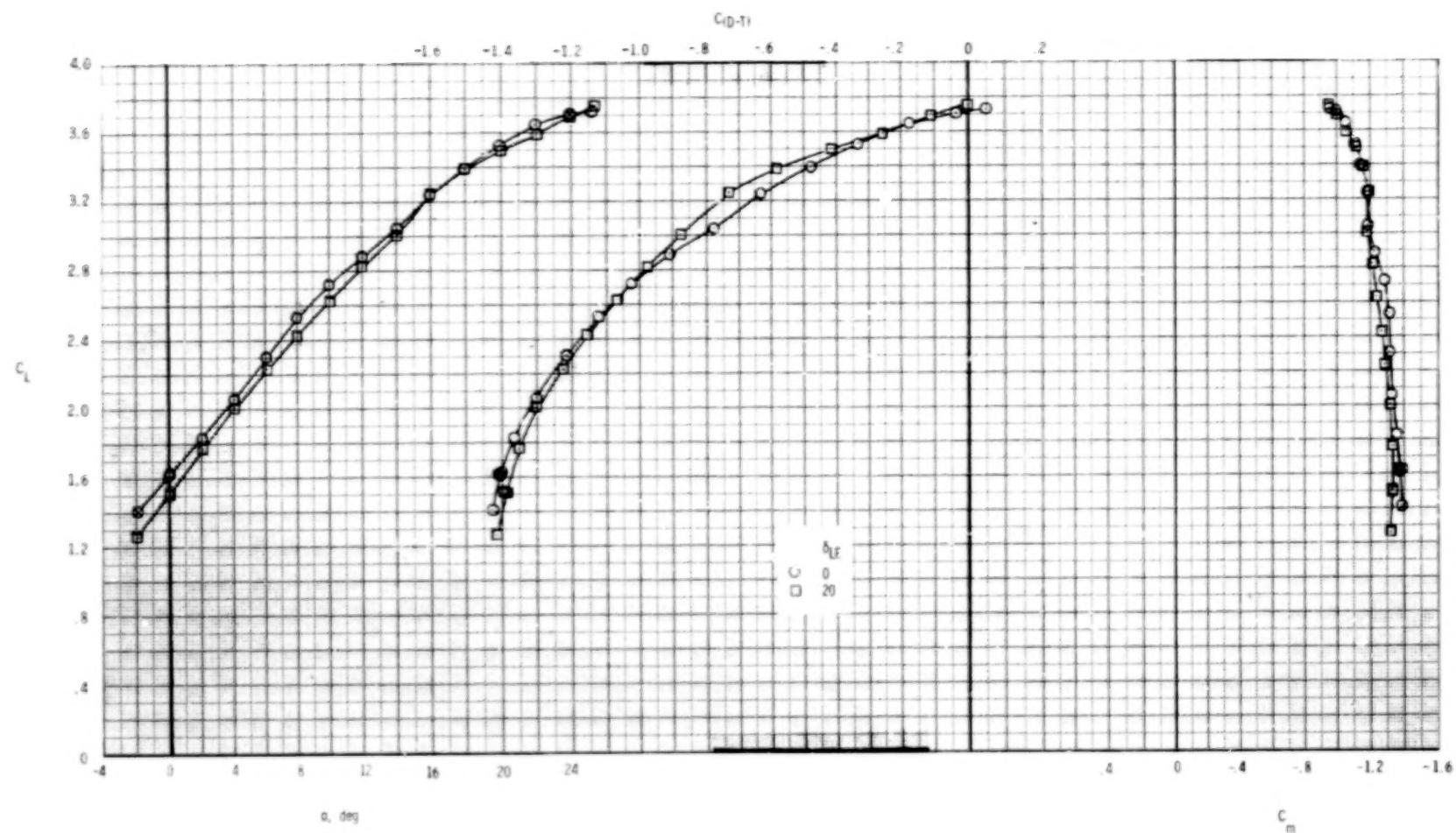
(a) Total coefficient data.

Figure 31.- Effect of wing leading-edge flap deflection at M = 0.186 and $(p_{t,j}/P_\infty)_{av}$ = 3.24 for nozzle conf 2. δ_{TE} = 30°; δ_C = $\delta_{C,TE}$ = 0°; H_2 canard.
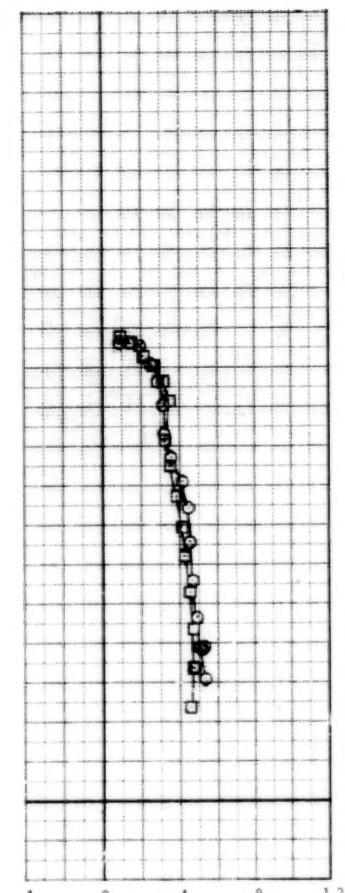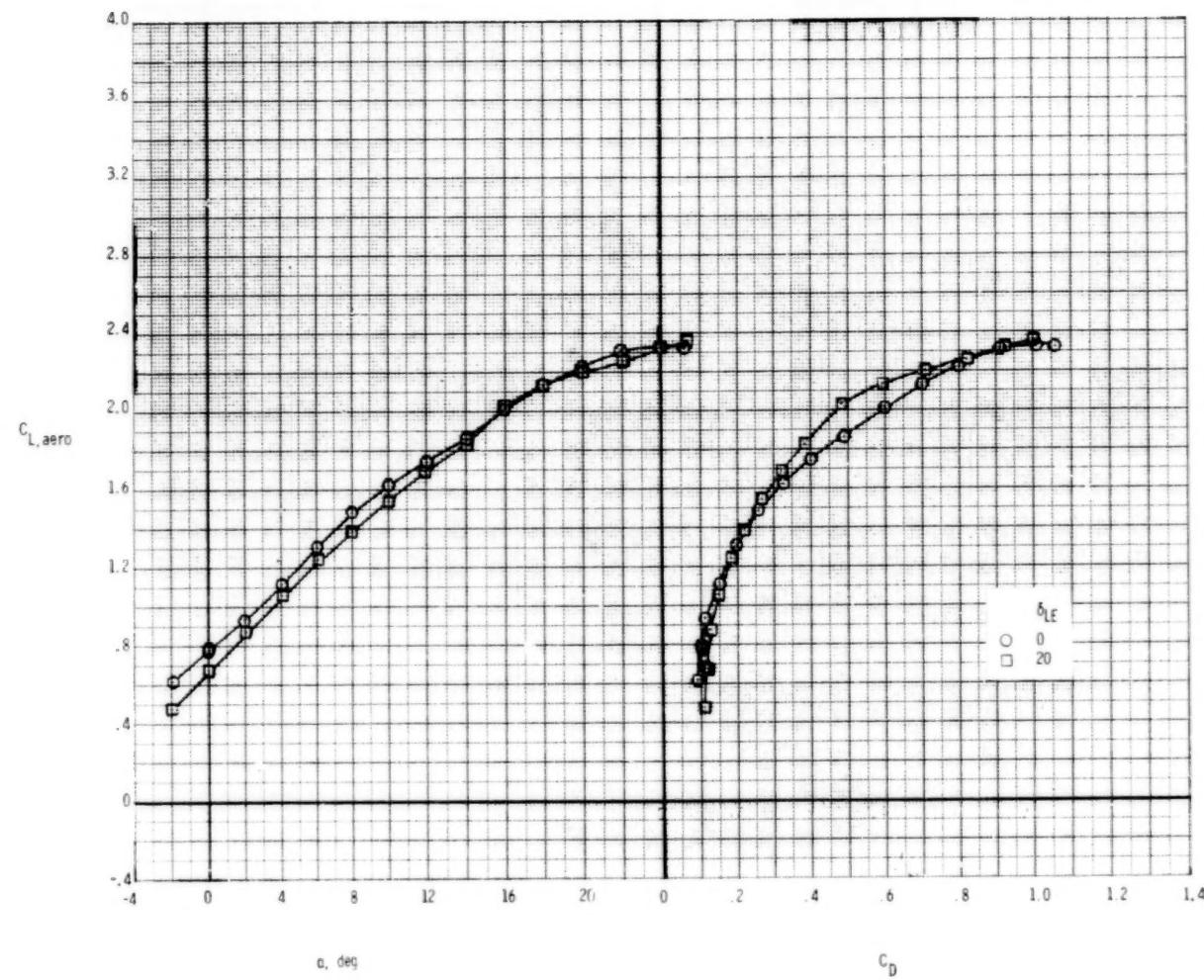
(b) Thrust-removed data.

Figure 31.- Concluded.

133

1. Report No. NASA TP-1533	2 Government Accession No.	3. Recipient's Catalog No.

4. Title and Subtitle LONGITUDINAL AERODYNAMIC CHARACTERISTICS OF A VECTORED-ENGINE-OVER-WING CONFIGURATION AT SUBSONIC SPEEDS		5. Report Date October 1979
		6. Performing Organization Code

7. Author(s) Laurence D. Leavitt	8. Performing Organization Report No. L-13108

9. Performing Organization Name and Address NASA Langley Research Center Hampton, VA 23665	10. Work Unit No. 505-04-13-02
	11. Contract or Grant No.

12. Sponsoring Agency Name and Address National Aeronautics and Space Administration Washington, DC 20546	13. Type of Report and Period Covered Technical Paper
	14 Sponsoring Agency Code

15. Supplementary Notes

16. Abstract

An investigation has been conducted in the Langley V/STOL tunnel to determine the effects of vectoring exhaust flow on the longitudinal aerodynamic characteristics of a vectored-engine-over-wing configuration. Vectoring was accomplished by blowing from over-wing-mounted engines over a variable trailing-edge flap. Effects of varying canard geometry and wing leading-edge geometry were investigated. Wind-tunnel data were obtained at a Mach number of 0.186 for an angle-of-attack range from $-2°$ to $24°$ and engine nozzle pressure ratios from 1.0 (jet off) to approximately 3.75.

17. Key Words (Suggested by Author(s)) Upper-surface blowing Vectored thrust Nonaxisymmetric nozzle Close-coupled canard wing	18. Distribution Statement Unclassified - Unlimited Subject Category 02

19. Security Classif. (of this report) Unclassified	20. Security Classif. (of this page) Unclassified	21. No. of Pages 133	22. Price* $7.25